Adaptive Fuselage Response Suppression

Jonathan Luke du Bois

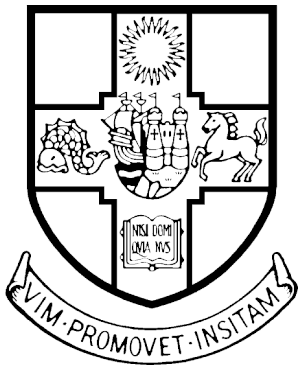

A dissertation submitted to the University of Bristol in accordance with the requirements for award of the degree of Doctor of Philosophy in the Faculty of Engineering.

Department of Aerospace Engineering

May 2009

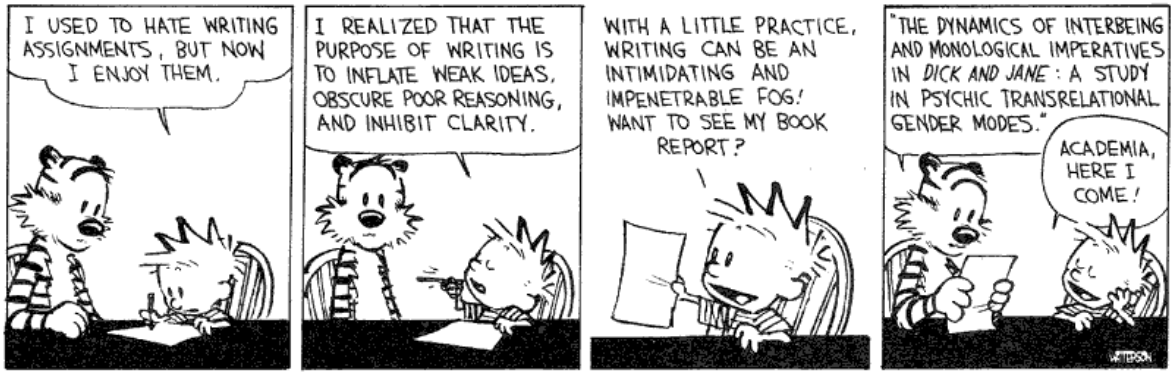

–Bill Watterson

Abstract

Vibration suppression techniques comprise a significant proportion of contemporary rotorcraft research, with much attention devoted to active methodologies. A largely overlooked class is that of adaptive-passive techniques, where instead of introducing active components to interact with the system dynamics, quasi-static adjustments are made to passive components. Such methods have the advantages of lower power requirements and inherent stability. This thesis seeks to exploit the nonlinear effect of stress stiffening, induced by static structural loading, to produce an adaptive rotorcraft response suppression system.

The stress stiffening effect is explored using analytical models and experimental results. A significant finding is that traditional stress stiffening is accompanied by an equally important change in joint parameters as a structure is loaded. Analytical tools are proposed to incorporate this effect in simple finite element models.

Parametric studies reveal the importance of a phenomenon known as eigenvalue curve veering. Instead of crossing at an intersection, two eigenvalue loci may veer abruptly away, swapping trajectories and all their properties in the transition. An explicit experimental demonstration of the effect is documented here, and a *veering index* is derived to provide a definitive criterion for its quantification. The behaviour is shown to contribute valuable information to finite element model updating methods and a novel experimental identification approach is developed, permitting the use of eigenvalues instead of the less reliable eigenvectors in symmetric updating problems.

Consolidating the preceding theory, a proof-of-concept adaptive response suppression system is implemented, demonstrating a reduction in vibrations due to variable narrowband excitation frequencies.

Finite element analyses of a Lynx helicopter lead to the proposition of a stress-based adaptive tuned vibration absorber. A cable running the length of the tail boom serves as a distributed absorber mass, and changing the tension in the cable allows tuning of the multiple absorber modes. It is shown that this configuration uses only a narrow range of cable tensions to realise the cancellation of all of the critical tail boom modes.

Acknowledgements

First and foremost I would like to offer my thanks to my supervisors, Nick Lieven and Sondipon Adhikari, whose valuable guidance and seemingly endless patience have been instrumental in the realisation of this thesis.

I am also grateful to the Engineering and Physical Sciences Research Council and AgustaWestland Helicopters for their financial support throughout my studies, and to Qinetiq for the provision of the Lynx finite element model which was adapted for the purposes of this thesis.

The Aerospace Department at the University of Bristol has proved a fantastic environment in which to work, and many of my peers and colleagues too numerous to mention have contributed to this environment. In particular, Mike Terrell and Jon Coote were a great source of information as I was embarking on my PhD studies, and Brano Titurus has always been on hand with advice to offer on every subject I have cared to enquire about. The practical assistance of Clive Rendall and Tony Griffith has been invaluable in the completion of my work, and it would be amiss not to acknowledge the sage counsel of Sandy Mitchell, who guided me through my early years at the University.

Outside of the University, I owe a debt of gratitude to my friends and flatmates for keeping me sane, barely, in the final stages of my writing up, and for all the unrequited hot meals. And, of course, I owe immeasurable thanks to my family, not only for their continued support throughout the course of my PhD, but for getting me that far in the first place.

Author's Declaration

I declare that the work in this dissertation was carried out in accordance with the requirements of the University's Regulations and Code of Practice for Research Degree Programmes and that it has not been submitted for any other academic award. Except where indicated by specific reference in the text, the work is the candidate's own work. Any views expressed in the dissertation are those of the author.

SIGNATURE

DATE

Nomenclature

Abbreviations

ADC	analogue to digital converter
CSQ	cross sensitivity quotient
DAC	digital to analogue converter
DFT	discrete Fourier transform
DOF	degree of freedom
FE	finite element
FEA	finite element analysis
FEM	finite element model
FFT	fast Fourier transform
FRF	frequency response function
IRF	impulse response function
LSCE	least squares complex exponential
LSFD	least squares frequency domain
MAC	modal assurance criterion
MDF	modal dependence factor
MDOF	multiple degree of freedom
NCO	normalised cross orthogonality
NR	Newton-Raphson
PID	proportional-integral-derivative (controller)
PSD	power spectral density
SDOF	single degree of freedom
TMD	tuned mass damper
TVA	tuned vibration absorber
VI	veering index

Symbols

$\mathbf{0}$	zero matrix
$*$	convolution operator
$\Longleftrightarrow$	Fourier function pairing

$\angle x$	argument of x
$\|x\|$	modulus of x
x^+	pseudo-inverse of x
x'	equivalent to property x but for parameter value $\delta_j{}'$ as opposed to δ_j
x^*	adapted modal property x, defined by $\mathbf{\Sigma}_j^* = \mathbf{\Lambda}^{-\frac{1}{2}}\mathbf{\Sigma}_j\mathbf{\Lambda}^{-\frac{3}{2}}$ and $\mathbf{\Lambda}^* = \mathbf{\Lambda}^{-1}$
$\overline{x}$	property x for veering datum configuration (overbar denotes veering datum)
$E[x]$	expected value of x

Greek

α	angle between two eigenvector sets in the normal basis
β	angle between the current eigenvector set and the veering datum set in the normal basis
$\gamma^2(\omega)$	coherence
δ_j	j^{th} structural parameter (or updating parameter)
η	hysteretic damping loss factor
ε	perturbation parameter
ϵ_x	normal strain
ϵ_{xy}	shear strain
$\boldsymbol{\epsilon}$	strain vector
$\boldsymbol{\varepsilon_j}$	updating variable error vector at j^{th} iteration
$\tilde{\boldsymbol{\varepsilon}}_{\boldsymbol{j}}$	predicted updating variable error vector at j^{th} iteration
κ_{ijk}	modal coupling between i^{th} and k^{th} modes with respect to parameter δ_j
λ_r	r^{th} eigenvalue
μ_λ	mean eigenvalue in a veering pair
ω	frequency (rad·s^{-1})
ω_0	undamped natural frequency (rad·s^{-1})
ω_n	natural frequency (rad·s^{-1}), where ω_r is r^{th} natural frequency for MDOF system
ϕ_{rj}	j^{th} DOF in r^{th} mass-normalised eigenvector
$\boldsymbol{\phi}_r$	r^{th} mass-normalised eigenvector
$\boldsymbol{\psi}_r$	r^{th} eigenvector, arbitrarily scaled
ρ	density
σ_{iji}	sensitivity of i^{th} eigenvalue to parameter δ_j
$\boldsymbol{\sigma}$	stress vector
τ	time, often used for delay
θ	phase difference
θ_0	rotational displacement of beam neutral axis
θ_i	rotational displacement of i^{th} element node

ζ viscous damping ratio

$\Delta\lambda_{ir}$ eigenvalue separation, $\lambda_i - \lambda_r$

$\Delta\sigma_{kji}$ sensitivity difference, $\sigma_{kKk} - \sigma_{iKi}$

Δt discrete time step

$\boldsymbol{\Delta\delta_j}$ updating parameter increment vector from j^{th} iteration

$\boldsymbol{\Delta z_j}$ updating variable increment vector for j^{th} iteration

$\boldsymbol{\Lambda}$ eigenvalue matrix, diag([λ_1 λ_2 ... λ_N])

$\boldsymbol{\Phi}$ mass-normalised eigenvector matrix, [$\boldsymbol{\phi}_1$ $\boldsymbol{\phi}_2$ ... $\boldsymbol{\phi}_N$]

$\boldsymbol{\Psi}$ eigenvector matrix, [$\boldsymbol{\psi}_1$ $\boldsymbol{\psi}_2$ ... $\boldsymbol{\psi}_N$]

$\boldsymbol{\Sigma}_j$ modal sensitivity matrix: matrix of eigenvalue sensitivities and modal couplings with respect to parameter δ_j

$\boldsymbol{\Sigma}_{ijk}$ 2×2 matrix of eigenvalue sensitivities and modal couplings for modes i and k with respect to parameter δ_j

Roman

$\mathbf{b}$ strain-displacement matrix

c viscous damping constant

d hysteretic damping constant

e 2.71828183

$f(t)$ measured force signal

$\mathbf{f}$ elemental force vector

$h_{jk}(t)$ impulse response function for DOFs j and k

$_\ell h_{jk}$ $h(\ell\Delta t)$

i imaginary unit ($\sqrt{-1}$)

k spring stiffness

k_E elastic stiffness

k_G geometric stiffness

k_T tangent stiffness

$\mathbf{k}$ elemental stiffness matrix

m mass

$\mathbf{m}$ elemental mass matrix

$\mathbf{n}$ shape function matrix

r mode number

t time

u displacement function in Cartesian x-direction

u_0 axial displacement of beam neutral axis

u_i displacement of i^{th} element node in Cartesian x-direction

$\mathbf{u}$	elemental displacement vector
v	displacement function in Cartesian y-direction
v_0	transverse displacement of beam neutral axis
v_i	displacement of i^{th} element node in Cartesian y-direction
w	displacement function in Cartesian z-direction
x	displacement *or* Cartesian x-coordinate
$\dot{x}$	velocity
$\ddot{x}$	acceleration
$\mathbf{x}$	displacement vector
$\dot{\mathbf{x}}$	velocity vector
$\ddot{\mathbf{x}}$	acceleration vector
y	Cartesian y-coordinate
z	Cartesian z-coordinate
$\mathbf{z_j}$	updating variable vector at j^{th} iteration
$\mathbf{z_m}$	updating variable vector from measured data
A	cross-sectional area
$A(\omega)$	inertance / accelerance
${}_rA_{jk}$	r^{th} modal constant for DOFs j and k
$C_{r,n}$	value of characteristic polynomial for r^{th} mode at n^{th} frequency interval
$\mathbf{C}$	global damping matrix
E	Young's modulus
$\mathbf{E}$	material property matrix
F	force
$\mathbf{F}$	global force vector
G	gauge factor
$H(\omega)$	receptance
$H_1(\omega)$	conventional receptance estimator
$H_2(\omega)$	alternative receptance estimator
$H_{jk}(\omega)$	FRF matrix element: response of DOF j to excitation of DOF k
$\mathbf{H}(\omega)$	FRF matrix
I	second moment of area
$\mathbf{I}$	identity matrix
$J(\bullet)$	penalty function
$\mathbf{K}$	global stiffness matrix
$\mathbf{K_E}$	nominal elastic stiffness matrix
$\hat{\mathbf{K}}_\mathbf{G}$	unit stress stiffening matrix (stress stiffening per unit applied force)

$\mathbf{K_T}$	tangent stiffness matrix
L	element length
$\mathbf{M}$	global mass matrix
N	number of modes
P	static force
R_{xx}	autocorrelation
R_{xf}	cross correlation
$\mathbf{R}$	effective independence matrix
$S_{xx}(\omega)$	auto-spectral density
$S_{xf}(\omega)$	cross-spectral density
$\mathbf{S}$	updating variable sensitivity matrix
T_e	kinetic energy
$\mathbf{T}$	rotational transform matrix
U_i	internal strain energy
V	volume
V_r	$e^{\lambda_r \Delta t}$
$\mathbf{W}_{\delta\delta}$	weighting matrix for updating parameters
$\mathbf{W}_{\varepsilon\varepsilon}$	weighting matrix for updating variables
X	displacement magnitude
X_n	Fourier coefficient
$Y(\omega)$	mobility

Contents

List of Figures

List of Tables

Chapter 1

Introduction

1.1 Structural Dynamics

In modern engineering the dynamic properties of a structure are every bit as important as its static characteristics and often more so. Where once the design process might only have been concerned with the primary load bearing function and static failure loads, contemporary projects must take into consideration the vibrational characteristics with regard to both function and failure. This trend is only increasing with the development of stronger, more lightweight materials, and with the higher demands of state-of-the-art constructions.

The need for dynamic analyses is prevalent across engineering disciplines. For example, traditional civil structures are faced with the potentially catastrophic effects of wind [1–3], waves [4–7] and seismic activity [8–11]. People-carrying structures such as bridges [12–14] and stadia [15–18] can even suffer from the unpredictable syncronicity of human interactions.

Fundamentally, the problem is one of resonance: all structures have natural frequencies, and if an external forcing is applied that coincides with a natural frequency then the structure will experience exceptionally high magnitudes of vibration as it resonates. These large displacements and forces can cause discomfort (in the case of people-carrying structures or vehicles), produce operational errors, and lead to structural failure either directly or through fatigue.

In many cases the dynamics of the structure will be coupled with the excitation force, further complicating the analysis. Examples can be found in the literature cited above with relation to wind, oceanic, and human excitation. One of the best known examples of this phenomenon is that of aeroelasticity in aerofoils. In this case the coupling between aerodynamic, elastic and inertial forces in wings and rotor blades can lead to oscillatory instabilities known as flutter [19–21].

In fact, aircraft are particularly susceptible to vibration problems in general. They are necessarily lightweight and flexible structures, and subject to draconian design constraints which limit the available mitigation strategies. The difficulties are compounded in rotorcraft by the disagreeable nature

of their operation: helicopters don't fly, they beat the air into submission. Whilst the former is not strictly true, the latter offers a fair appraisal; helicopters seem to fly not because of the laws of physics but despite them. In contrast to aeroplane wings, which generally encounter a steady stream of clean laminar airflow, helicopter rotor blades are constantly travelling in the wake of the preceding blade, and interacting with the trailing vortices [22]. It has been shown that this blade-vortex interaction is responsible for the majority of cabin noise created by a helicopter in descent or manouevering flight [23, 24]. Even in the absence of vortices and blade wake, a helicopter in forward flight will experience periodic airflow variation over the blades as they regularly advance into the oncoming air then retreat away from it. Supplement this environment with higher harmonic and unsteady aerodynamic excitations, and out-of-balance forces, and the scale of the difficulties to be surmounted becomes apparent.

The importance of overcoming vibration problems in rotorcraft is twofold: firstly, the large number of safety-critical parts must be protected from failure. It has been demonstrated that helicopter reliability can be directly linked with vibration levels [25]. Secondly, passengers must be kept comfortable and, more importantly, pilots must be protected from fatigue and injury [26]. A third consideration is the growing significance being attached to the adverse effects of helicopter acoustic noise levels on the spotted owl population of Mexico [27].

This thesis is concerned with the suppression of fuselage vibrations in rotorcraft. In support of these endeavours, this chapter first reviews the state of the art in general response suppression methods and discusses new avenues being opened up by smart materials before focusing on rotorcraft vibration mitigation strategies. The remaining sections of the chapter explore the open problems suitable for further investigation, detail the path taken in this thesis, and offer some comments on the work contained herein.

1.2 Response Suppression

By far the most straightforward method of vibration suppression is to avoid exciting the structure in the first place: either by eliminating the source or by ensuring its frequency does not coincide with structural resonances. In rotorcraft applications, neither of these options is available: the source of the vibration is also the thing that keeps it in the air, and the rotor frequency is fixed according to blade stressing and modal response criteria. The excitation is therefore predetermined, occurring at the rotor frequency, the blade pass frequency, and multiples thereof.

It thus falls to structural modifications and enhancements to reduce the vibration levels experienced. Vibration control methods fall under three broad headings: passive, active, and semi-active. In addition, all three may be tuned using adaptive techniques. Adaptive-passive methods will be singled out as a distinct approach in the discussions that follow, because of the fundamentally different configuration they demand compared with purely passive implementations.

1.2.1 Passive Methods

Passive methods are the simplest and generally the most robust. They can be further divided into four categories: design, damping, isolation, and undamped vibration absorption.

The first of these is seemingly trivial yet immensely important. One of the oldest tactics for redressing vibration problems is to design the structure such that the natural frequencies lie outside the range of typical excitation frequencies, and to ensure that sensitive parts are not subjected to the worst of the vibrations by careful consideration of the node locations.

Where the problem is not easily solved with such an approach, the most ubiquitous solution is to add damping. Hydraulic dampers, sometimes known as shock absorbers, are in widespread use. The damping force provided by these devices depends upon the piston configuration and the fluid velocity. More specifically, it depends upon the Reynolds number of the fluid flow: laminar flows are associated with linear force-velocity relationships, while turbulent flows tend to produce quadratic relationships [28]. As a sweeping generalisation, the former is produced by fit clearance between cylinder and piston, representing the textbook viscous dashpot, while the latter is characteristic of a piston orifice.

Another approach to damping is through the use of viscoelastic (VE) materials. Examples are given by Shen *et al.* [29], who use experimental data to model VE dampers in the form of a VE material bonded with steel plates. An obvious advantage of these dampers is their practical simplicity, although the analysis is far from simple; their mechanical properties are strongly dependent on both frequency and temperature. Two application methods are favoured: free-layer and constrained-layer damping (CLD) [30]. The former consists of a single layer of VE material bonded to a surface; energy is dissipated through the extension and compression of the VE layer as the surface bends. CLD, referred to in these circumstances as passive CLD (PCLD), is comprised of a layer of VE material sandwiched between the structural surface and a third constraining layer. In this case energy is dissipated through shear strains in the VE layer, producing higher damping levels than the free-layer configuration.

If the source of the vibrations and the structure to be protected lie in distinct regions, it may be more effective to isolate one or the other. In this way vibrations are not necessarily reduced overall but are instead confined to an acceptable locale. Examples of this approach can be seen in car engine mounts [31], industrial turbomachinery [32] and on a larger scale in buildings subject to seismic excitation [33]. This is typically achieved with elastomeric supports, although Buckle [33] discusses other options for isolating bridges and buildings including air cushions, coil springs, and mechanical configurations such as rollers, sliding plates and cable suspensions.

The undamped vibration absorber (UDVA) is alternatively refered to as a tuned vibration absorber (TVA), a dynamic vibration absorber (DVA), or a tuned vibration neutraliser (TVN). It was first patented in 1911 by Hermann Frahm [34], and its operation is outlined by Ormondroyd and Den Hartog [35]. Ozer and Royston [36] explain how the method is extended from single- to multi-degree-

of-freedom systems. In their simplest form the devices are comprised of a mass which is attached by a spring to the component to be "damped". The spring-mass arrangement can be tuned such that the resonant response peak of the component will be replaced by an antiresonance at the point of attachment, so that in theory all response will be cancelled at that frequency. The trade-off is that the vibration is transferred to the TVA. Contrary to popular misconception, however, the response of the TVA is not a resonant response and is far less severe than the component response that it suppresses. In practice, instead of using a spring the restoring force is sometimes provided by gravity, centrifugal force, or any other available method.

Tuned mass dampers (TMDs), as discussed by Sadek *et al.* [37] in the context of seismic excitation, incorporate damping in a modified TVA arrangement, offering an improved response to wideband excitation at the expense of narrowband performance. Tuned liquid column dampers (TLCDs) [38] operate on a similar principle but use a liquid for both the mass and damping element, with gravity providing the restorative force.

Other passive methods may not fall neatly into any of the above categories; for example the moment-cancelling device proposed by Nagaya *et al.* for tackling seismic vibration reduction in multistory buildings [39], which uses gearing to apply appropriate cancellation forces in response to excitations.

1.2.2 Active Methods

The drawback of passive methods is that they all involve a compromise. For example, damping reduces the resonant response at the expense of increased response away from the natural frequencies. Isolation reduces structural rigidity and strength. TVAs produce favourable results at a given excitation frequency but replace the original resonant peak with two distinct peaks either side. In summary, passive methods can only be optimised for a single set of operational conditions. Under variable excitation conditions, or changing configurations, active solutions provide unique benefits over their passive counterparts. The general principle is that, based upon some form of state feedback (usually force, acceleration or displacement), forces are fed into the system to counteract the vibrations. Wagg *et al.* [40] devote a chapter to active vibration control strategies.

There are three main configurations for the application of control forces: they can be applied between the structure and a separate, nominally rigid structure; they can be applied between two points of the structure itself; or they can be applied between the structure and a supplementary inertial element. The latter is a similar concept to that of the tuned mass dampers, and it turns out to be the most convenient to implement in many cases.

Active tuned mass dampers (ATMDs), or active mass dampers (AMDs), were first proposed by Chang and Soong [41], who placed an actuator between the mass and the structure to improve the results from a non-optimal TMD using velocity feedback. Chang and Yang [42] later showed that the results could be further improved using complete feedback (displacement, velocity and acceleration), and that

this method also demands a lesser control force of the actuator. The devices are sometimes referred to as hybrid DVAs as they will continue to function as DVAs when the actuator is inactive. Burdisso and Heilmann [43] discuss a variation on this arrangement, consisting of two parallel DVAs connected to one another via an actuator. They compare theoretical results with experiments and conclude that the modified arrangement approximately halves the control effort required to achieve a similar vibration attenuation. Olgac and Holm-Hansen [44, 45] take another novel approach, using delay and gain on a positional feedback to cancel the damping effects in an AMD, thus improving on the tuned response. In civil applications, Lee-Glauser *et al.* [46] propose a combination of passive base isolation, in the form of a laminated rubber bearing (LRB), and active forcing using a counterweight on the roof of a multistory building to reduce base displacements in response to representative seismic motion. Okada and Okashita [47] investigate the use of adaptive parameters in an active TMD to suppress elevator vibrations, and perform experimental tests of the scheme on a 1 DOF system. Gu and Peng [48] describe analytic and experimental investigations into the use of adaptive feedforward controllers in conjunction with active mass dampers on a building subject to aeroelastic wind excitation.

Placing actuators within a structure allows the manipulation of the poles to lie anywhere in the complex plane, within reason, thus determining the behaviour of the system. In this case inverse eigenvalue methods can provide an analytical framework for determining an appropriate controller. Mottershead and Ram [49] give a review of the topic with respect to both active and passive systems. Pole assignment, or eigenvalue assignment (EVA) algorithms are described in early papers by Miminis and Paige [50] and Patel and Misra [51], and numerous adaptations and improvements on the methods have been offered in the interim, including full eigenstructure assigment techniques, for example that of Inman and Kress [52]. An example of their implementation is given by Tang and Wang [53], who use active elements to provide vibration confinement. Kerber *et al.* [54] discuss other control strategies for active vibration suppression with respect to a six degree of freedom analytical model, and conclude that the H_∞ controller produces excellent results.

Using actuators as connectors between substructures presents the possibility of active vibration isolation. Bohn *et al.* [55] successfully apply active isolation to car engine and drive train mounts, using a single sensor, a state observer, a disturbance model and pre-computed observer gains. Daley *et al.* [56] use electromagnetic actuation in an active isolation scheme to prevent marine machinery from exciting hull resonances. Karnopp [57] discusses vibration isolation using both active and semi-active methods, focusing on a popular analysis method known as the *skyhook damper*. In an earlier paper [58], he considers the advantages of semi-active methods and reviews the design principles for this approach.

1.2.3 Semi-active Methods

An unappealing facet of active control systems is that the addition of forces to the system creates the possibility of negative damping and dynamic instability. This point is clearly illustrated by the ability of EVA methods to place the poles *anywhere* in the complex plane, including both sides of

the imaginary axis. An alternative option which has received much attention in recent years is that of semi-active methods. These do not directly apply forces to the structure but induce forces by modifying the behaviour of structural components: generally the damping and stiffness elements. They have more modest power requirements than active methods, and because they do not add energy to the system the techniques can guarantee stability. Jalili [59] explores the theory behind semi-active vibration control and compares some different systems. Symans and Constantinou [60] give a summary of passive, active and semi-active ideals as a background to a thorough review of semi-active control systems, with particular regard to protecting civil structures.

The tools of the trade for these methods include: variable stiffness elements, such as the variable fulcrum device proposed by Margolis and Baker [61], and the leaf spring and lead screw arrangement of Walsh and Lamancusa [62]; variable damping elements, such as variable orifice dampers [63]; and variable mass arrangements such as that employed in the adjustable inertia absorber of Jalili and Fallahi [64].

Haroun *et al.* [65] implement semi-active damping control in TLCDs using variable orifices, augmented with pressure control, to produce hybrid liquid column dampers (HLCDs). They cite numerical results showing that the HLCDs provide a marked improvement in building response suppression over TLCDs over a range of response conditions. Stammers and Sireteanu [66] demonstrate the application of a controlled friction device in vibration attenuation and consider its advantages over a variable viscous damper, including higher achievable forces at low velocities and zero forces at any velocity. Liu *et al.* [67] compare four different semi-active contol methods to an adaptive-passive damping scheme and review their performance. Their results favour the skyhook damper concept over the others presented. Some intricacies of such isolation schemes are explored by Ahmadian [68], in particular the question of how semi-active methods can achieve isolation below the passive $\sqrt{2}\omega_0$ limit. Returning to civil applications, Wongprasert and Symans [69] give experimental and analytical evaluations of a semi-active building base isolation system combining LRBs and variable-orifice fluid dampers.

Although limited in the range of forces they can apply, in many situations semi-active methods are capable of matching the performance of their fully active counterparts.

1.2.4 Adaptive-passive Methods

Adaptive-passive methods take advantage of the same physical devices used for semi-active control. While semi-active methods operate on similar principles to active methods, however, reacting with similar bandwidth to the vibrations they intend to suppress, adaptive-passive methods vary the structural configuration at a much slower rate, simply tuning it to the optimal parameter values for the prevaling excitation conditions. These have the most humble energy requirements of all three approaches, and produce a well-conditioned response. The majority of the literature on adaptive-passive methods focuses on their application to TVAs and TMDs.

Franchek *et al.* [70] present a black-box control strategy for adaptive tuning of a TVA using a variable stiffness component. Buhr *et al.* [71] extend this to a non-collocated vibration control problem. Liu and Liu [72] perform experimental studies of an online-adjustable TVA, using an electromagnet acting as a variable spring stiffness. They use frequency spectral analyses to track the excitation frequency and adaptively tune the TVA accordingly. Liu *et al.* [73] use a cantilever beam as the spring in a TVA, and vary its stiffness by positioning a support with a lead screw actuation system. They investigate two autotuning methods, differing in their excitation frequency identification approach. Bonello *et al.* [74] create a TVA using curved plates as the spring elements; the stiffness of these plates in the direction of motion is tuned by adjusting their curvature. Varadarajan and Nagarajaiah [75] create a semi-active variable stiffness device comprised of four springs in a plane rhombus configuration, where mechanically changing the aspect ratio of the rhombus varies the effective stiffness of the device. They use this to implement an adaptive-passive TVA capable of tracking the dominant response frequency of a high-rise building and present analytical results. Brennan and Dayou [76] discuss TVAs with focus on the benefits of tuned and detuned absorbers on local and global vibrations. They consider the ramifications of their findings with respect to adaptive absorbers and compare the expected results with those of an active absorber. In an aerospace application, Smith *et al.* [77] discuss the testing of adaptive stiffness floor mounts for the attenuation of general vibrations in cargo aircraft. Their method is akin to using the cargo as the reactive mass in an adaptive TMD.

Some examples of adaptive isolation can also be found in the literature. Khorrami *et al.* [78] propose an isolation system for launch vehicle payload supports, optimising the vibration isolation for varying quasi-static accelerations in different launch stages. Kim and Singh [79] discuss adaptive-passive engine mounts for automobiles and compare analytical performances with purely passive mounts. Addressing a less familiar application, Li *et al.* [80] give an analytical and experimental treatment to an adaptive method of isolating vibrations in travelling belts by means of controlling the force on a tensioning wheel.

1.2.5 Ambiguous Methods

Some vibration control methods are difficult to properly classify. A good example is that of active constained layer damping (ACLD) [81–83]. The technology is similar to standard PCLD but with the passive constraining layer replaced by an active piezoelectric element. The combination provides both passive and active vibration suppression. Although the use of the actuator in this manner technically qualifies the technique as active, its effectiveness is reduced by the VE layer. The real advantage of the method is that the actuation can increase the shear strains in the material and thus augment the damping. In this regard it bears more similarity to a semi-active method.

Another ambiguous case is proposed by Chawla *et al.* [84], in the form of axially-actuated members in truss structures. It is suggested that these are used to limit the maximum axial loads, increasing damping by simulating perfect plastic deformation above a given load. Although the devices are

capable of dynamic actuation, thus constituting an active method, Chawla *et al.* assert that no energy need be supplied by the actuators as the forces are all attributable to the structural motion. In this mode the actuators could be considered to be variable stiffness elements, resembling semi-active control methods.

Nakano *et al.* [85] investigate the possibility of creating a self-powered active vibration control device, where instead of merely dissipating vibration energy, the actuator stores any surplus energy and uses it in the parts of the cycle where power is required. Although based on active techniques, the device they construct cannot contribute energy to the system and thus is strictly speaking only semi-active. As an analogy, a spring functions in a similar manner, storing energy in one part of a cycle and releasing it in another. The experiments employ an electromechanical device which converts kinetic energy to electrical for storage. Scruggs and Iwan [86] describe a comparable device but instead of storing energy for use in active techniques, they suggest that the equipment can be switched between active and semi-active modes of operation, dependent on the availability of external power.

1.2.6 Smart Materials and Technologies

New materials and technologies are paving the way for advanced control methodologies. These developments are providing opportunies for exploiting vibration control in novel applications, such as the snowboard and mountain bike implementations of pasive piezo-electric damping and adaptive orifice hydraulic dampers discussed by Yoshikawa *et al.* [87]. Spencer and Nagarajaiah [88] review many of the available smart technolgies with regard to semi-active control.

Solid-state actuators have gained popularity in recent years due to their simplicity, light weight, low power consumption and high force capabilities. Because they contain no moving parts the devices are easily scaled, have minimal space requirements, and exhibit high reliability. Piezo-electric elements can produce extremely high forces, although only with small displacements [89]. Magnetostrictive alloys can achieve strains of 10–15 times those of piezoelectric elements [90]. Shape memory alloys (SMAs) can achieve much larger displacements, up to 50 times those of piezoelectrics [91], albeit under smaller loads. Their operation is also based upon temperature cycling, and is thus heavily dependent on external temperatures and unsuitable for high frequency applications.

Burke and Hubbard [92] demonstrated the active control of a distributed piezo-polymeric actuator layer applied to the surface of a flexible beam, improving the effective damping by varying the voltage in both the time and spatial domains. Baz *et al.* [93] perform a simlar study by attaching SMA wires to a polymethyl methacrylate sheet, and Zhang *et al.* [94] detail the fabrication and stiffness testing of composite plates with embedded SMAs. Using a comparable setup, Han *et al.* [95] employ piezo-ceramic actuators and piezo-film sensors and report improved dynamic response of the first bending and torsional modes. This is achieved with a linear quadratic Gaussian controller using a Kalman filter as observer. A less academic demonstration is provided by Guan *et al* [96], who use piezo-electric stack actuators acting on a shaft bearing in a transmission housing to reduce gearbox noise by

as much as 8dB. Demonstrating an application of magnetostrictive materials, Geng and Haynes [90] employ Terfenol-D linear actuators to create a six degree of freedom active vibration isolation device based on Stewart platforms. Using a feedforward controller in conjunction with an adaptive finite impulse response filter (FIR) and least mean squares (LMS) algorithm they report 30dB of vibration attenuation.

Focusing now on semi-active techniques, variable damping can be provided by electrorheological (ER) and magnetorheological (MR) fluid dampers, where the viscosity of the fluid may be adjusted by applying electric or magnetic fields respectively. The latter is favoured due to its superior performance in light of the limitation imposed by the electric field breakdown in ER dampers [91]. Dyke *et al.* [97] discuss the use of semi-active MR dampers in seismic response suppression in buildings. Ok *et al.* [98] incorporate MR dampers in a cable-stayed bridge simulation and use historic seismic data to test a fuzzy logic controller, obviating the need for separate adaptive and primary force controllers. Tackling some practical considerations, Sodeyama *et al.* [99] describe the development and testing of a large-scale MR damper for use in general civil structures. Another experimental demonstration is given by Christenson *et al.* [100], who use real time hybrid numerical-physical testing techniques to apply semi-active control of MR fluid dampers to a three-story steel frame structure. Opting instead for electrorheological fluid dampers, Choi and Kim demonstrate their capabilities with regard to a semi-active skyhook car damping configuration, both analytically [101] and experimentally [102].

Smart materials are equally well suited to adaptive-passive implementations. Williams *et al.* [103] describe the modelling of an adaptive TVA using the variable elastic modulus of SMAs to adjust the absorber parameters, and Rustighi *et al.* [104] present an experimental demonstration of the same. Flatau *et al.* [105] use a similar idea, this time in experimental testing of a magnetostrictive material based adaptive TVA. Taking another approach, Ketema [106] provides analytic studies to endorse the use of the temperature dependence of viscoelastic materials to create an adaptive TMD device.

1.3 Rotorcraft Implementations

Jackson and Grimster [107] give an overview of the sources of vibration and noise in helicopters. As touched upon in section 1.1, the primary source of vibration in rotorcraft comes from the main rotor assembly. The blades are subject to complex aeroelastic forces [108, 109] which are transmitted via the hub to the fuselage. The primary concern is in reducing the levels of vibration that reach the cabin. As mentioned at the outset, an obvious solution is to vary the rotor speed to achieve the best response characteristics. This is currently not an option, however, so to this end one of three methodologies can be adopted: the source of vibration can be addressed by controlling the aerodynamic forces on the blades, the vibration can be isolated at the blade root or rotor hub, or vibration control techniques can be applied in the fuselage itself.

To this day, the majority of helicopters use only passive response suppression methods. The hub

excitation is dominated by the rotor and blade pass frequencies, so the fuselage is designed with no resonances in these ranges. This alone, however, is not enough. Some efforts have been made to tackle the issue in the design of the blade assembly, for example the blade-to-blade dissimilarity approach of Tauszig and Gandhi [110]. Other passive vibration control methods include lag dampers (hydraulic [111] or elastomeric [112]) to solve the problem of ground resonance [113], bifilar vibration absorbers [25, 114, 115] to mitigate in-flight vibrations, and rotor isolation systems using traditional flexible supports [116] and more sophisticated inertial force-cancelling antiresonant suspension devices [117, 118]. TVAs are also employed in aircraft, and Fuller *et al.* [119] perform an analytical study of aircraft cabin noise to show that detuned absorbers give better noise reduction performance than tuned absorbers do in terms of reducing the propeller noise.

Pearson *et al.* [120] give a comprehensive overview of both the passive and active rotorcraft vibration suppression methods available towards the end of the twentieth century. They highlight the drawbacks of passive devices, such as their high weight penalties and performance limitations. In particular they are only capable of responding to local response conditions, and even when tuned their frequency response is usually a compromise. Active devices offer the promise of improvements over these configurations. Yu *et al.* [121] offer a review of active technologies with a focus on noise attenuation, and Fuller and von Flotow [122] give a broad perspective on the field of active noise and vibration suppression.

In rotorcraft the vibration control problem is somewhat simplified by the nature of the force generation. For steady flight conditions the predominant aerodynamic loads will be periodic at harmonics of the rotor frequency. This facilitates adaptive schemes which first measure the disturbances and then adjust to compensate. In this manner, after a brief adjustment period the controller can compensate with relative certainty, and may take advantage of methods which are not available in unpredictable transient conditions. Bittanti and Cuzzola [123] discuss this model and go one step further, introducing a gain scheduling controller to select known control parameters based on forward flight velocity. Daley *et al.* [124] also discuss an implementation of these so-called *repetitive control* approaches, and introduce an innovative use of piezo-electric actuators to create a device with variable stiffness and damping. They refer to the mechanism as a *smart spring*.

Much of the early active vibration research concentrated on controlling the aerodynamic forces on the blades. These are controllable in the flap direction by means of blade pitch variation. Helicopter flight is governed by means of collective (constant) and cyclic (once per revolution, or 1R) pitch manipulations, in addition to the yaw control which is usually achieved with tail rotor thrust. Active pitch control focuses on the vibrations above the 1R frequency, and thus should not interfere with the pilot controls.

The pilot instructions are most commonly conveyed to the rotating blade assembly by means of a swash plate. One of two schemes may be employed, applying the active control above or below the swash plate. The latter applies a proportional adjustment to each blade simultaneously and operates at harmonics of the fundamental rotor frequency. It is known as higher harmonic control (HHC).

An example is given by Nguyen and Chopra [125] who present an analytical investigation of HHC in hingeless rotors. Lovera *et al.* [126] and Patt *et al.* [127] discuss different HHC algorithms. Applying the active control above the swash plate provides the freedom to vary each blade's pitch individually, and is known as individual blade control (IBC). An advantage of IBC is that it can tackle broadband vibration problems and not just rotor harmonics. Norman *et al.* [128] and Jacklin *et al.* [129] detail wind tunnel tests of a UH-60 blackhawk rotor system with IBC actuators replacing the pitch links. Bittanti and Cuzzola [123] discuss another candidate control system for IBC.

Both HHC and IBC methods are intended to augment the main controls, although HHC may be implemented using the same actuators that apply the main control forces. Despite the theoretical separation of flight and vibration control forces, however, both systems lie in the primary control path and have the capacity to interfere with the primary control functions; if the active system were to fail or malfunction then the helicopter may become uncontrollable. This generates significant airworthiness concerns. For this reason a lot of interest has been generated by the prospect of trailing edge flaps, or flaperons, on the rotor blades. These alter the dynamics of the aerofoil enough to generate oscillatory force cancellation but without direct interference with the primary controls. They can be used to apply control as per HHC or IBC methodologies. Nixon *et al.* [130] tested HHC on a tiltrotor model in a windtunnel to demonstrate the attenuation of vibrations at the 1R and 3R frequencies (rotor frequency and blade pass frequency) using a combination of active flaps and full swash plate control. Koratkar and Chopra [131] perform open- and closed-loop wind tunnel tests on a rotor assembly with piezo-electric bender trailing edge flaps and a neural-network contol algorithm. Modern smart materials also present opportunites for morphing blades; Wilbur *et al.* [132] conduct wind tunnel experiments on rotors with embedded piezo-electric active fibre composite actuators providing blade twist. They use both collective and IBC control methodologies and report improvements in dynamic response.

Another approach which can be applied to the rotor blades is that of semi-active control. Chen *et al.* [133] implement a smart spring in a helicopter blade root and use a filtered-x LMS algorithm to test the effects of semi-active control on the torsional (pitch) response to mechanical excitation. Anusontri-Inthra and Gandhi [134] show that reductions in response levels can be achieved with semi-active stiffness elements at the blade root in both the flap and lag directions.

The discussion thus far has concentrated on rotor flap motion, with little regard for lead/lag motion. Lag dampers are included on articulated rotors with more than two blades, primarily to inhibit ground resonance. They are not helpful in general flight conditions however, and can lead to unnecessary periodic forcing. This arises mainly from the Coriolis forces that couple the flap and lag motions. Gandhi *et al.* [135] investigate a semi-active treatment using magnetorheological (MR) dampers to improve the response while maintaining the necessary damping for ground and flight transition conditions. Wei and Pinqi [136] also use MR dampers but they focus on improving ground resonance attenuation with an adaptive feedforward controller in the form of a neural network adaptive filter and adaptive inverse control [137]. A practical demonstration is provided by Hu and Wereley [138], who detail the

laboratory implementation of a hybrid MR-elastomeric damper designed for rotorcraft deployment.

Isolation methods have received less attention than the technologies described above. An early patent for an active isolation device between the rotor shaft and the fuselage was filed by Scharton and Bies [139]. Due to actuator limitations of the era they cite a need for a hybrid active-passive system with the passive system compensating for actuator deficiencies. Modern actuators, smart materials and semi-active approaches could eliminate the need for passive elements. Choi *et al.* [140] implement a semi-active MR vibration isolator and report marked response attenuation at resonant frequencies. Hiemenz *et al.* [141] again use semi-active MR dampers to provide vibration isolation in helicopter crew seats. Sutton *et al.* [142] attach magnetostrictive actuators to a helicopter gearbox support strut and give a laboratory demonstration of active isolation, achieving up to 40dB attenuation in the 250-1250Hz range. Despite the success demonstrated in these publications, isolation methods remain unpopular. In practice, even with active control, it is difficult to fully isolate the fuselage; to do so necessitates the isolation of the rotor shaft, gearbox, engines and drive train. Each of these elements demands isolation in six degrees of freedom such that even where the design permits the space for the components, the weight penalty is prohibitive.

All of the above methods attempt to mitigate vibrations at the source or in the transmission path. In contrast, the method that follows takes advantage of superposition principles in linearised systems to cancel the vibrations within the fuselage. Known as active control of structural response (ACSR) [143], the technique uses actuators in the fuselage to create forces and displacements which, when summed with the rotor excitation, reduce the cabin vibrations. Because the actuators are housed in the fuseage and are not directly connected to the flight systems the airworthiness concerns are much lower than in the other technologies described. The method is typically implemented with the actuators connected to a rigid platform, but another system known as active vibration reduction (AVR) [144, 145] instead reacts against the gearbox mass. Chiu and Friedmann [146] describe simulations of a standard ACSR configuration in a coupled rotor-flexible fuselage aeroelastic response model: one of few in existence at the time. Mathews *et al.* [147] present a more recent reduced-order model, and offer comments on the choice of sensor locations for the ACSR controller. A comparison of frequency- and time-domain control methods is offered by Pearson and Goodall [148]: they assert that the former performs well in steady flight conditions while the latter performs better in transient manouevers, and proceed to develop a hybrid method to produce good steady-state *and* transient attenuation. Huggin *et al.* [149] report analytic studies to determine optimal actuator placements in a Lynx airframe using an FE model and mathematical models based on modal test data. They also report an ACSR experiment conducted on the airframe using a filtered-x LMS algorithm.

1.4 Open Problems

Despite the myriad strategies that have been tested for the mitigation of rotorcraft vibrations, adaptive-passive methods are all but overlooked. While local suppression may be achieved with con-

ventional adaptive TVAs there is little mention in the literature of globally applicable adaptive-passive vibration control in rotorcraft. The advantages of such an approach are several:

- Adaptive-passive control offers an improvement over standard passive control in changeable operating conditions.
- The power consumption is minimal, even compared to semi-active methods.
- As with semi-active control there is no possibility of inducing instabilities.
- The method would not suffer the same difficulties encountered by active and semi-active methods in transient flight conditions.

Many avenues have been explored for inducing the variable stiffness and damping required for adaptive-passive control; these range from geometry and orifice manipulations to smart materials. A common drawback of the devices reviewed here is that they are only capable of producing local changes in stiffness and damping. There is a well-known but rarely-exploited effect which can alter the global stiffness characteristics of any structure using quasi-static actuation, and that effect is *stress stiffening*. Stress stiffening effects are a subset of the geometric nonlinearity observed in thin or slender structures subject to loading, whereby the transverse stiffness is effectively reduced by compressive in-plane or axial loading. It is expected that careful actuator placement will facilitate the transmission of load throughout an airframe, which is expected to have a significant effect on the many slender members employed in such structures. This approach appears to be undocumented in the literature.

1.5 Scope of Thesis

The focus of the research covered in this manuscript is to investigate the potential of structural loading as a means of adaptive response tuning in rotorcraft fuselages. The task is split into three key stages: general investigations of stress stiffening behaviour, proof-of-concept demonstrations of automated response suppression, and development of rotorcraft-specific response suppression strategies. The general stress stiffening investigations also prompt some new lines of inquiry regarding eigenstructure response under parametric variation, which are given due attention.

Before tackling the specifics of these tasks, chapter 2 undertakes a thorough discussion of the background theory supporting the work. Starting from fundamental physics, a concise coverage of the field progresses quickly to describe all of the techniques drawn upon in the course of these studies. Both analytical and experimental considerations are reviewed.

Chapter 3 begins the narration of the new work, describing a set of experiments to investigate stress stiffening effects and the correlation of analytical methods. Features of the behaviour are highlighted as potential exploitation routes, and curiosities are noted for the refinement of later studies.

One such curiosity is the phenomenon of eigenvalue curve veering. This ostensibly bizarre feature of parametric eigenstructure variation is investigated further in chapter 4, where it is found to be an inevitable consequence of converging modes in a wide class of systems, and surprisingly commonplace. Experimental results are shown, and a novel method for quantifying the behaviour is derived.

The approach offered by chapter 4 gives insight into previously tenebrous characteristics of a system subject to parameter changes, and the techniques permit new and computationally efficient means for calculating the extremums of modal properties over a parameter range. These are detailed in chapter 5, along with a practical demonstration of the advantages offered by the tools developed in these two chapters.

The fresh insight into system properties has an immediate application in finite element model updating, and chapter 6 takes the opportunity to describe a practical implementation of the ideas developed in the preceding chapters. The new theory required to conduct such a scheme is outlined, including an innovative experimental identification method. The technique is used to identify joint characteristics in one of the early experimental configurations.

Chapter 7 covers the implementation of the proof-of-concept adaptive response suppression system. Here a new structure is introduced, an FE model presented, and the practical considerations attended to. The approach taken is that of adaptively tuning the natural frequencies in response to a given external drive frequency, using an embedded electromechanical actuator. Test results are given and the system is refined to present improved and more general results.

With a solid grounding firmly established, the problem of repsonse tuning in rotorcraft is addressed in chapter 8. The chapter starts with a discussion of acutator locations, developing methods for optimising the placement. Finite element studies investigate the potential for simple tuning of the natural frequencies in a helicopter tail boom, as well as more sophisticated attenuation methods based on adaptive tuned vibration absorber principles.

Chapter 9 concludes with a summary of the new findings and suggestions for future developments.

1.6 Notes on Thesis

As far as possible, the supporting theory from existing work is all confined to chapter 2, leaving the remaining chapters free to discuss the author's own work. All of the theory outlined in chapter 2 appears there because it has been applied directly by the author, usually in the form of code or computations. Although there is nothing novel in the application of these methods themselves, it is a non-trivial task which is belied by the brevity of the descriptions in the later chapters.

Several commercial hardware and software suites were employed to facilitate the studies described herein. The most important of these is the matrix algebra oriented programing language MAT-

LAB [150]. An LMS modal testing suite [151] was employed extensively, although all of the software functionality contributed by this package was also duplicated in the author's MATLAB code. While the early finite element models were constructed in MATLAB using a purpose-built FE package created by the author, the larger finite element models were processed using the ANSYS [152] finite element code, using custom scripting to facilitate the parametric analyses and model updating.

The penultimate chapter of the thesis explores ideas for vibration suppression in rotorcraft. It was always the intention to perform tests on physical rotorcraft hardware: a lynx helicopter tail boom was earmarked as the test subject [153]. Unfortunately the tail, along with the rest of the helicopter, was required for testing at another facility and it was not possible to perform the anticipated experiments. As a result the final chapter of the thesis is limited to finite element analyses of the structure, validated only in part by comparisons with preliminary experimental data obtained from the tail boom.

1.7 Publications Arising from Thesis

To date, two refereed journal papers and five conference papers have been published based on work carried out in the course of this thesis. A third journal paper is currently under review.

The first of the journal papers investigates the propagation of measurement errors in trifilar inertia determination techniques, in particular highlighting the insensitivity of the results to exact alignment of the centre of mass of the test specimen [154].

The second journal paper details an explicit experimental demonstration of the effect of eigenvalue curve veering and the associated mode shape transformations, and compares the results with those from a numerical study [155].

Four of the five conference papers are once more concerned with frequency veering and the related manifestations, the first providing a broad overview of the behaviour [156], the second offering an objective method of quantifying the effects [157], the third discussing the exploitation of these ideas in finite element model updating [158], and the fourth addressing the practical considerations in the planning of suitable modal tests [159].

The remaining conference paper presents the proof-of-concept demonstration of an adaptive stress-stiffening based response suppression system [160]. Experimental results are presented along with a general discussion of the subject.

Chapter 2

Supporting Theory and Tools

The chapters that follow are built upon a body of research stretching back to the beginnings of natural philosophy. They use myriad theories and techniques developed over the history of structural analysis; some of these are well known textbook approaches and others are more recent developments. This chapter does not provide an exhaustive foundation in structural dynamics, but outlines the background theory and describes the methods used in this manuscript.

The chapter is intended as a reference covering the existing body of research, leaving the remainder of the thesis free to discuss the new contributions to the field. All of the techniques elaborated below appear here because they have been directly applied in code or computations in the course of the present work.

2.1 Structural Dynamics

The study of structural dynamics in academic pursuits is usually referred to some form of analytical model. The problem is formulated using the equations of motion. Newton's Second Law of Motion balances the structural and inertial forces of a body so that

$$F = m\ddot{x} \tag{2.1}$$

where the body's displacement is represented by x and the velocity and acceleration are given by the first and second derivatives $\dot{x}$ and $\ddot{x}$. The structural forces are generally a function of the displacement and velocity so that $F = F(x, \dot{x})$. For example, Hooke's law gives a linear relationship between force and displacement for elastic materials and is typified by a spring. Damping is commonly modelled using a linear variation of force with velocity, as would be seen in an ideal viscous dashpot. Thus the simple one degree of freedom (DOF) system seen in figure 2.1, consisting of a mass, a spring and a damper, is described by

$$m\ddot{x} + c\dot{x} + kx = 0 \tag{2.2}$$

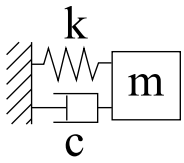

Figure 2.1: One DOF mass-spring-damper system.

where m is the mass, k is the spring stiffness and c is the viscous damping constant. A harmonic motion is assumed such that

$$x = Xe^{i\omega t} \tag{2.3}$$

and thus

$$\dot{x} = i\omega Xe^{i\omega t} \qquad \text{and} \qquad \ddot{x} = -\omega^2 Xe^{i\omega t}. \tag{2.4}$$

Substituting eqns. (2.3) and (2.4) into eqn. (2.2) and dividing by $Xe^{i\omega t}$, the natural frequency is found as the roots of the equation

$$-\omega^2 m + i\omega c + k = 0. \tag{2.5}$$

The undamped natural frequency, found by setting $c = 0$ in eqn. (2.5), is

$$\omega_0 = \sqrt{\frac{k}{m}}. \tag{2.6}$$

Solving eqn. (2.5) for non-zero values of c gives complex roots, and it is useful at this stage to define the damping ratio as

$$\zeta = \frac{c}{2\sqrt{mk}}. \tag{2.7}$$

The damping ratio is unity for critical damping such that values above one produce an overdamped response represented by purely imaginary roots. Values below one produce an oscillatory response whose frequency is described by the real part of the roots as

$$\omega_n = \omega_0\sqrt{1-\zeta^2} \tag{2.8}$$

and whose decay rate is determined by the imaginary part of the roots, giving

$$|x| = Xe^{-\zeta\omega_0 t}. \tag{2.9}$$

Considering the case of external harmonic excitation, eqn. (2.2) becomes

$$m\ddot{x} + c\dot{x} + kx = Fe^{i(\omega t+\theta)} \tag{2.10}$$

where F is a real constant representing the magnitude of the force, analogous to the real constant X representing the displacement amplitude, and the value of θ determines the phase difference between

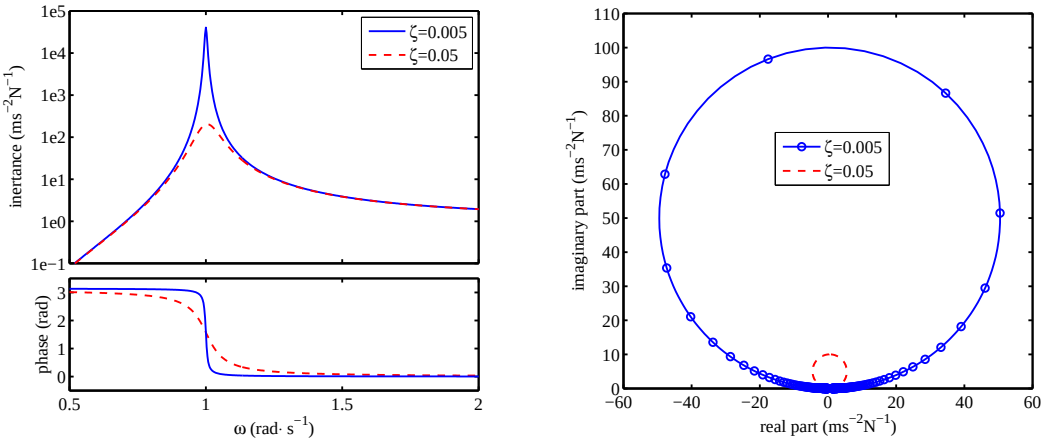

(a) Bode (b) Nyquist

Figure 2.2: Bode and Nyquist plots for the one DOF system in figure 2.1, using unity values for k and m. Markers on the lightly damped Nyquist plot are spaced at constant frequency intervals for illustrative purposes.

the two. Once more substituting eqns. (2.3) and (2.4) yields

$$\frac{X}{Fe^{i\theta}} = H(\omega) = \frac{1}{-\omega^2 m + i\omega c + k}. \tag{2.11}$$

This ratio of response amplitude to excitation force is given in terms of the frequency and is called the frequency response function (FRF). In fact, there are three variations on the FRF, describing the response in terms of the displacement, velocity and acceleration. The former is called the receptance $H(\omega)$ and is described by eqn. (2.11) whilst equivalent velocity and acceleration terms are called the mobility $Y(\omega)$ and inertance, or accelerance, $A(\omega)$; these may be derived from the relationships in eqns. (2.4) as

$$Y(\omega) = \frac{i\omega}{-\omega^2 m + i\omega c + k} \tag{2.12}$$

and

$$A(\omega) = \frac{-\omega^2}{-\omega^2 m + i\omega c + k}. \tag{2.13}$$

The values obtained from the FRF are complex and convey both the magnitude and phase of the response. These are commonly depicted using Bode (figure 2.2(a)) or Nyquist (figure 2.2(b)) plots. The former gives a clear representation of the response variation with frequency while the latter gives an appreciation of the variation in the complex plane, particularly useful in curve-fitting procedures. Two damping cases have been illustrated; for lightly-damped structures the FRF is approximately real everywhere except in the close vicinity of resonance, where extremely high amplitudes are encountered and the phase shifts through 180° in a short frequency interval. Heavier damping produces smaller resonant responses, lowers the natural frequency and produces a more gradual phase variation.

This example has been confined to viscous damping but many and varied damping models exist. Common representations are Coulomb damping, or dry damping, where the magnitude of the force is constant but its direction always opposes the motion, and hysteretic damping: similar to viscous

damping in that the force is in phase with the velocity but with the magnitude proportional to the displacement. In the latter case, eqn. (2.5) is usually written

$$-\omega^2 m + id + k = 0 \tag{2.14}$$

or

$$-\omega^2 m + k(1 + i\eta) = 0 \tag{2.15}$$

where d is the hysteretic damping constant and η is called the *damping loss factor*, given by $\eta = d/k$. Noting that eqn. (2.14) is equivalent to setting $c = d/\omega$ in the viscous damping model, the damping ratio is seen to be related to the loss factor by

$$\eta = 2\zeta\frac{\omega}{\omega_0} \tag{2.16}$$

so that near resonance

$$\eta \approx 2\zeta \tag{2.17}$$

Further reading on the subject of damping may be found in texts such as Meirovitch [161].

The discussion above has also assumed linear relationships between the structural forces, the displacement and its derivatives. In practice this assumption is not always valid, however, and it is prudent to be aware of the manifestations as they will corrupt computational results depending on linear theory. Typical hydraulic orifice dampers, for example, produce a force proportional to the square of the velocity, and cubic stiffness characteristics are also common in real-world engineering. Furthermore, at sufficient response magnitudes almost every structure will exhibit non-linear behaviour. This thesis does not deal explicitly with nonlinearities, so only a brief description follows:

The consequence of nonlinearities with regard to dynamic analyses is that the frequency response functions will vary with the response amplitude. To illustrate this concept, figure 2.3 shows the variation of an FRF for a system with cubic stiffness properties, plotted using an approximate solution to Duffing's equation. With increasing excitation amplitudes the resonant peak is seen to 'lean over' to the right. Further increases in amplitude lead to multiple solutions to the response equation for some frequencies, and the observed response will be path dependent. It should be noted that, unlike linear systems, the response spectrum of a nonlinear system subjected to a harmonic excitation will not be confined to the excitation frequency. In addition to these peculiarities, nonlinearity invalidates the principle of superposition and requires different experimental and analytical methodologies to those used with linear systems. In particular, modal analysis (discussed below and used extensively in this thesis) is rendered largely redundant in the presence of nonlinearity. Once again Meirovitch [161] provides an in-depth discussion on this subject, and Ewins [162] considers the behaviour from an experimental perspective.

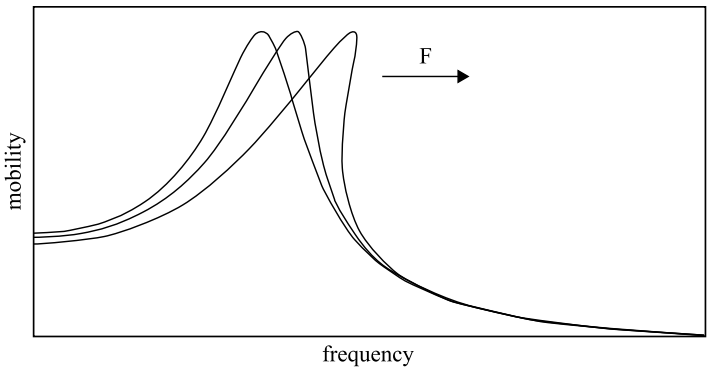

Figure 2.3: Variation of frequency response with increasing excitation force (F) for a system exhibiting a cubic stiffness characteristic.

2.2 The Finite Element Method

2.2.1 Background and General Approach

Thus far, vibrations have been considered only for single degree of freedom (DOF) systems. Such systems have just one natural frequency and their movement is easily described in terms of a simple sinusoid. In practice, structures are comprised of a collection of parts, and these parts themselves are formed of a continuum. For simple configurations it is possible to formulate expressions for the continuous forces and displacements, and obtain an exact solution for the dynamic response; the example of a single beam is examined in appendix A. In general, however, exact solutions are difficult to obtain and some form of discretisation must be applied. Perhaps the most famous technique is the Rayleigh-Ritz method, where the exact differential eigenproblem is reformed as an approximate algebraic eigenproblem by expressing the displacement function in terms of a series of trial functions. The coefficients of these trial functions become the discrete DOFs to be solved for. One of the primary attractions of this method is the mathematical rigour on which it is based, providing an unequivocal upper bound on the natural frequency estimates. Meirovitch [161] provides a full description of the method, as well as the related assumed-modes, Galerkin and collocation methods.

A different approach lies in the more intuitive spatial discretisation of a structure. The premise is to represent the structure with a set of simple elements, and the motion of the structure is then described in terms of the displacements at the element interfaces. This approach is referred to as the Finite Element (FE) method. It is widely used due to its general applicability, and its suitability for automated computations.

The number of degrees of freedom at each element interface depends upon the nature of the element and the spatial dimensionality of the analysis. Typically a three dimensional model will have six degrees of freedom at each point, or *node*: three translational and three rotational displacements. Common elements used in FE models include rods, beams, plates, shells and solid elements. Rods and beams are associated with only two nodes, although some formulations allow for the definition of intermediate stations where the material properties and beam section vary along the length. These are

not used directly in the structural computations but forces and displacements for these locations may be derived in the postprocessing analysis. Plates and shells typically employ triangular or quadrilateral geometries; it's usual to have one node for each vertex in the geometry but nodes are also sometimes positioned along edges to provide a better description of the element's distortion. Popular solid geometries are cuboids and tetrahedra.

To employ the FE method it is necessary to reduce the distributed mass and stiffness properties (and where appropriate the damping properties) to discrete quantities for each DOF. The problem is then formulated as a set of simultaneous equations, each equation describing the forces for one DOF. The solution is obtained using linear algebraic methods, most commonly expressed in the form of matrix manipulations. The simplest means of achieving this is to 'lump' the parameters. This process is most commonly adopted for the mass, dividing each element's mass and distributing it amongst the constituent nodes. The accuracy of the method is heavily dependent upon the degree of discretisation and thus the number of elements employed. Acceptable results may demand prohibitive computational effort.

A more rigorous approach is to derive *consistent* mass and stiffness parameters, where the elastic and inertial forces are balanced. This derivation is achieved by effectively applying the Rayleigh-Ritz procedure locally to each element, as described by Cook [163]. While the trial functions used in the classical Rayleigh-Ritz method are intended to mimic the true displacement with a great deal of accuracy, those used in the finite element method serve mainly as interpolation functions for the spatial discretisation. As such it is common to apply the simplest permissible functions, in the form of low order polynomials. It is considered sufficient that these functions satisfy the boundary conditions for the element. The polynomial coefficients are then transformed into nodal displacements through the stress-strain relationships, allowing for intuitive coupling of the elemental functions at their interfaces. The result is a series of elemental stiffness matrices, $\mathbf{k}$, satisfying the static equilibrium equation

$$\mathbf{f} = \mathbf{ku} \tag{2.18}$$

and a series of elemental mass matrices, $\mathbf{m}$, satisfying the inertia equation

$$\mathbf{f} = \mathbf{m\ddot{u}} \tag{2.19}$$

where $\mathbf{f}$ is the vector of forces, $\mathbf{u}$ is the vector of displacements and $\ddot{\mathbf{u}}$ is the vector of accelerations for the elemental DOFs. The derivation of these matrices will be described in the sections that follow. To begin with the analysis will be given in terms of generalised stress, strain and displacement vectors: $\boldsymbol{\sigma}$, $\boldsymbol{\epsilon}$ and $\mathbf{d}$, constituting multidimensional functions throughout the spatial domain of the element. A discussion of the common coordinate systems and corresponding spatial functions is then given in section 2.2.4 to provide a more physical understanding of the technique. Finally a two-dimensional beam is used as an example, demonstrating the derivation of the polynomial shape functions and the computation of the system matrices.

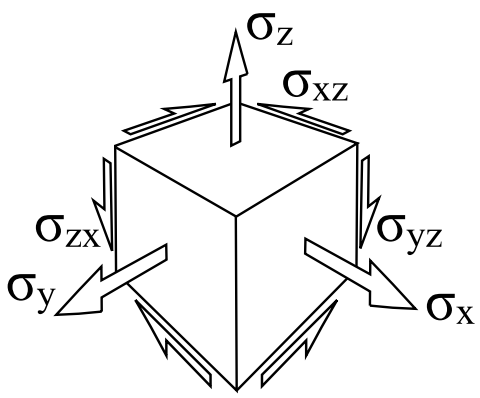

Figure 2.4: Shear stresses and normal stresses in three dimensions.

2.2.2 Stiffness Matrices

Przemieniecki [164] develops the stiffness matrices in a structural mechanics context. He uses Castigliano's theorem (closely related to the principle of virtual work) to express the external forces on an element in terms of the derivative of the internal strain energy:

$$\mathbf{f} = \frac{\partial}{\partial \mathbf{u}} U_i \tag{2.20}$$

where U_i is the internal strain energy, $\mathbf{u}$ is the elemental DOF displacement vector and $\mathbf{f}$ is the force vector for the n elemental DOFs. The strain energy is given by

$$U_i = \frac{1}{2} \int \boldsymbol{\epsilon}^T \boldsymbol{\sigma} dV \tag{2.21}$$

where V is the element volume, $\boldsymbol{\sigma}$ is the stress vector and $\boldsymbol{\epsilon}$ is the strain vector. From Hooke's Law,

$$\boldsymbol{\sigma} = \mathbf{E}\boldsymbol{\epsilon} \tag{2.22}$$

where $\mathbf{E}$ is the material property matrix. The strain vector is related to the elemental DOF displacements by

$$\boldsymbol{\epsilon} = \mathbf{bu}. \tag{2.23}$$

where $\mathbf{b}$ is the strain-displacement matrix, the derivation of which will be discussed presently. Combining eqns. (2.21), (2.22) and (2.23),

$$U_i = \frac{1}{2} \int \mathbf{u}^T \mathbf{b}^T \mathbf{Ebu}\, dV\ . \tag{2.24}$$

Putting this result back into eqn. (2.20), it is found that

$$\mathbf{f} = \int \mathbf{b}^T \mathbf{Eb}\, dV\ \mathbf{u}. \tag{2.25}$$

Thus, by analogy with eqn. (2.18), the stiffness matrix is given by

$$\mathbf{k} = \int \mathbf{b}^T \mathbf{E} \mathbf{b} \, dV \ . \tag{2.26}$$

2.2.3 Mass Matrices

Analogous to the stiffness matrices, an energy method is used to deduce the appropriate mass matrix. Recasting Castigliano's theorem,

$$\mathbf{f} = \frac{\partial}{\partial \mathbf{u}} T_e \tag{2.27}$$

where T_e is the kinetic energy. This can be expressed in terms of the velocity by

$$\mathbf{f} = \frac{\partial}{\partial t} \frac{\partial}{\partial \dot{\mathbf{u}}} T_e \tag{2.28}$$

where t is time. The kinetic energy is given by

$$T_e = \frac{1}{2} \rho \int \dot{\mathbf{d}}^T \dot{\mathbf{d}} \, dV \tag{2.29}$$

where ρ is the density and $\dot{\mathbf{d}}$ is the general velocity vector. A shape function $\mathbf{n}$ is used to relate the general displacement to the element DOF displacements

$$\mathbf{d} = \mathbf{n}\mathbf{u} \tag{2.30}$$

where $\mathbf{n}$ and thus $\mathbf{d}$ are spatial functions. Differentiating with respect to time,

$$\dot{\mathbf{d}} = \mathbf{n}\dot{\mathbf{u}}. \tag{2.31}$$

Accordingly, the kinetic energy is given by

$$T_e = \frac{1}{2} \rho \int \dot{\mathbf{u}}^T \mathbf{n}^T \mathbf{n} \dot{\mathbf{u}} \, dV. \tag{2.32}$$

Putting this into eqn. (2.28) produces

$$\begin{aligned} \mathbf{f} &= \frac{\partial}{\partial t} \rho \int \mathbf{n}^T \mathbf{n} \, dV \dot{\mathbf{u}} \\ &= \rho \int \mathbf{n}^T \mathbf{n} \, dV \ddot{\mathbf{u}}. \end{aligned} \tag{2.33}$$

Thus the mass matrix is given by

$$\mathbf{m} = \rho \int \mathbf{n}^T \mathbf{n} \, dV. \tag{2.34}$$

2.2.4 Spatial Functions

If a three-dimensional Cartesian coordinate system is employed with the three axes denoted by x, y, and z, the displacement vector is defined as

$$\mathbf{d} = \left\{ \begin{array}{ccc} u(x,y,z) & v(x,y,z) & w(x,y,z) \end{array} \right\}^T \tag{2.35}$$

where u, v, and w are functions of x, y, and z. The stress and strain vectors are

$$\boldsymbol{\epsilon} = \left\{ \begin{array}{cccccc} \epsilon_x & \epsilon_y & \epsilon_z & \epsilon_{xy} & \epsilon_{yz} & \epsilon_{zx} \end{array} \right\}^T \tag{2.36}$$

$$\boldsymbol{\sigma} = \left\{ \begin{array}{cccccc} \sigma_x & \sigma_y & \sigma_z & \sigma_{xy} & \sigma_{yz} & \sigma_{zx} \end{array} \right\}^T . \tag{2.37}$$

These vectors are each comprised of three normal quantities followed by three shear quantities, as illustrated in figure 2.4. In such a system, for an isotropic material, the material property matrix is given by

$$\mathbf{E} = \frac{E}{(1+\nu)(1-2\nu)} \begin{bmatrix} 1-\nu & \nu & \nu & 0 & 0 & 0 \\ \nu & 1-\nu & \nu & 0 & 0 & 0 \\ \nu & \nu & 1-\nu & 0 & 0 & 0 \\ 0 & 0 & 0 & \frac{1-2\nu}{2} & 0 & 0 \\ 0 & 0 & 0 & 0 & \frac{1-2\nu}{2} & 0 \\ 0 & 0 & 0 & 0 & 0 & \frac{1-2\nu}{2} \end{bmatrix} \tag{2.38}$$

where E is the Young's modulus and ν is the Poisson's ratio.

The derivation of the shape function, $\mathbf{n}$, is where the main differences between element formulations are introduced. The key step is in deciding on a function relating the displacements at a general point to those of the elemental DOFs; the strain-displacement matrix then follows on using partial derivatives of the shape function:

$$\mathbf{b} = \begin{bmatrix} \frac{\partial}{\partial x} & 0 & 0 \\ 0 & \frac{\partial}{\partial y} & 0 \\ 0 & 0 & \frac{\partial}{\partial z} \\ \frac{\partial}{\partial y} & \frac{\partial}{\partial x} & 0 \\ 0 & \frac{\partial}{\partial z} & \frac{\partial}{\partial y} \\ \frac{\partial}{\partial z} & 0 & \frac{\partial}{\partial x} \end{bmatrix} \mathbf{n}. \tag{2.39}$$

If the dimensionality of the system being considered is restricted to two, then the equations may be

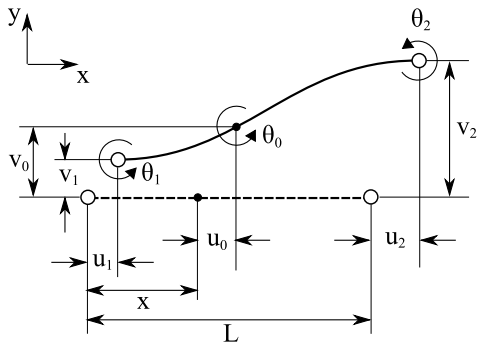

Figure 2.5: Two dimensional beam (–) deflected from its nominal position (- -).

abbreviated to

$$\mathbf{d} = \left\{ \begin{array}{cc} u & v \end{array} \right\}^T \tag{2.40}$$

$$\boldsymbol{\epsilon} = \left\{ \begin{array}{ccc} \epsilon_x & \epsilon_y & \epsilon_{xy} \end{array} \right\}^T \tag{2.41}$$

$$\boldsymbol{\sigma} = \left\{ \begin{array}{ccc} \sigma_x & \sigma_y & \sigma_{xy} \end{array} \right\}^T \tag{2.42}$$

$$\mathbf{E} = \frac{E}{(1+\nu)(1-2\nu)} \left[\begin{array}{ccc} 1-\nu & \nu & 0 \\ \nu & 1-\nu & 0 \\ 0 & 0 & \frac{1-2\nu}{2} \end{array} \right] \tag{2.43}$$

$$\mathbf{b} = \left[\begin{array}{cc} \frac{\partial}{\partial x} & 0 \\ 0 & \frac{\partial}{\partial y} \\ \frac{\partial}{\partial y} & \frac{\partial}{\partial x} \end{array} \right] \mathbf{n}. \tag{2.44}$$

2.2.5 Beam Element Derivation

Shape Function

A two dimensional beam is shown in figure 2.5. The deflection is described in terms of the neutral axis displacement, represented at any point along its length by three displacements: two translational and one rotational. These are denoted $u_0(x)$, $v_0(x)$, and $\theta_0(x)$, where x is the position along the element length and $0 \leq x \leq L$. The element has two nodes, one at each end, giving a total of six DOFS, collected together in vector form as

$$\mathbf{u} = \left\{ \begin{array}{cccccc} u_1 & v_1 & \theta_1 & u_2 & v_2 & \theta_2 \end{array} \right\}^T. \tag{2.45}$$

These form the boundary conditions for the generation of the shape function. Assuming small rotations, θ_0, the neutral axis displacements are related to the general displacements by

$$u = u_0 - \theta_0 y \tag{2.46}$$

$$v = v_0 \tag{2.47}$$

or

$$\mathbf{d} = \begin{bmatrix} 1 & 0 & -y \\ 0 & 1 & 0 \end{bmatrix} \begin{Bmatrix} u_0 \\ v_0 \\ \theta_0 \end{Bmatrix} \tag{2.48}$$

For simplicity the axial and transverse neutral axis displacements are assumed to be uncoupled. This allows the shape functions to be condsidered separately. Addressing first the axial displacement, u_0, a suitable shape function need only satisfy two boundary conditions, so a linear function is employed:

$$u_0 = \begin{bmatrix} 1 & x \end{bmatrix} \begin{Bmatrix} a_1 \\ a_2 \end{Bmatrix} \tag{2.49}$$

where a_1 and a_2 are coefficients to be determined. Applying the boundary conditions $u_0(0) = u_1$ and $u_0(L) = u_2$ produces

$$\begin{Bmatrix} u_1 \\ u_2 \end{Bmatrix} = \begin{bmatrix} 1 & 0 \\ 1 & L \end{bmatrix} \begin{Bmatrix} a_1 \\ a_2 \end{Bmatrix}. \tag{2.50}$$

Inverting eqn. (2.50) gives the coefficients as

$$\begin{Bmatrix} a_1 \\ a_2 \end{Bmatrix} = \begin{bmatrix} 1 & 0 \\ -1/L & 1/L \end{bmatrix} \begin{Bmatrix} u_1 \\ u_2 \end{Bmatrix}. \tag{2.51}$$

so from eqns. (2.49) and (2.51) the axial displacement is

$$\begin{aligned} u_0 &= \begin{bmatrix} 1 & x \end{bmatrix} \begin{bmatrix} 1 & 0 \\ -1/L & 1/L \end{bmatrix} \begin{Bmatrix} u_1 \\ u_2 \end{Bmatrix} \\ &= \begin{bmatrix} (1-\xi) & \xi \end{bmatrix} \begin{Bmatrix} u_1 \\ u_2 \end{Bmatrix} \end{aligned} \tag{2.52}$$

where $\xi = x/L$. Now addressing the transverse displacement, four boundary conditions must be met: $v_0(0) = v_1$, $v_0(L) = v_2$, $\theta_0(0) = \theta_1$ and $\theta_0(L) = \theta_2$. Accordingly, a cubic equation is applied so that

$$v_0 = \begin{bmatrix} 1 & x & x^2 & x^3 \end{bmatrix} \begin{Bmatrix} a_1 \\ a_2 \\ a_3 \\ a_4 \end{Bmatrix}. \tag{2.53}$$

Differentiating gives

$$\theta_0 = \begin{bmatrix} 0 & 1 & 2x & 3x^2 \end{bmatrix} \begin{Bmatrix} a_1 \\ a_2 \\ a_3 \\ a_4 \end{Bmatrix} \tag{2.54}$$

and with the boundary conditions this produces

$$\begin{Bmatrix} v_1 \\ \theta_1 \\ v_2 \\ \theta_2 \end{Bmatrix} = \begin{bmatrix} 1 & 0 & 0 & 0 \\ 0 & 1 & 0 & 0 \\ 1 & L & L^2 & L^3 \\ 0 & 1 & 2L & 3L^2 \end{bmatrix} \begin{Bmatrix} a_1 \\ a_2 \\ a_3 \\ a_4 \end{Bmatrix}. \tag{2.55}$$

As before, inverting the transform yields

$$\begin{Bmatrix} a_1 \\ a_2 \\ a_3 \\ a_4 \end{Bmatrix} = \begin{bmatrix} 1 & 0 & 0 & 0 \\ 0 & 1 & 0 & 0 \\ -3/L^2 & -2/L & 3/L^2 & -1/L \\ 2/L^3 & 1/L^2 & -2/L^3 & 1/L^2 \end{bmatrix} \begin{Bmatrix} v_1 \\ \theta_1 \\ v_2 \\ \theta_2 \end{Bmatrix} \tag{2.56}$$

and combining with eqns. (2.53) and (2.54),

$$\begin{Bmatrix} v_0 \\ \theta_0 \end{Bmatrix} = \begin{bmatrix} 1-3\xi^2+2\xi^3 & \left(\xi-2\xi^2+\xi^3\right)L & 3\xi^2-2\xi^3 & \left(-\xi^2+\xi^3\right)L \\ 6(-\xi+\xi^2)L & \left(1-4\xi+3\xi^2\right)L^2 & 6(\xi-\xi^2)L & \left(-2\xi+3\xi^2\right)L^2 \end{bmatrix} \begin{Bmatrix} v_1 \\ \theta_1 \\ v_2 \\ \theta_2 \end{Bmatrix}. \tag{2.57}$$

Amalgamating eqns. (2.52) and (2.57) yields

$$\begin{Bmatrix} u_0 \\ v_0 \\ \theta_0 \end{Bmatrix} = \begin{bmatrix} (1-\xi) & 0 & 0 \\ 0 & 1-3\xi^2+2\xi^3 & 6(-\xi+\xi^2)L \\ 0 & \left(\xi-2\xi^2+\xi^3\right)L & \left(1-4\xi+3\xi^2\right)L^2 \\ \xi & 0 & 0 \\ 0 & 3\xi^2-2\xi^3 & 6(\xi-\xi^2)L \\ 0 & \left(-\xi^2+\xi^3\right)L & \left(-2\xi+3\xi^2\right)L^2 \end{bmatrix}^T \begin{Bmatrix} u_1 \\ v_1 \\ \theta_1 \\ u_2 \\ v_2 \\ \theta_2 \end{Bmatrix}. \tag{2.58}$$

and putting this into eqn. (2.48) gives

$$\mathbf{d} = \begin{bmatrix} 1-\xi & 0 \\ 6(\xi-\xi^2)\varsigma & 1-3\xi^2+2\xi^3 \\ (-1+4\xi-3\xi^2)L\varsigma & (\xi-2\xi^2+\xi^3)L \\ \xi & 0 \\ 6(-\xi+\xi^2)\varsigma & 3\xi^2-2\xi^3 \\ (2\xi-3\xi^2)L\varsigma & (-\xi^2+\xi^3)L \end{bmatrix}^T \begin{Bmatrix} u_1 \\ v_1 \\ \theta_1 \\ u_2 \\ v_2 \\ \theta_2 \end{Bmatrix} \tag{2.59}$$

where once again $\xi = x/L$, and $\varsigma = y/L$. This can be recognised as eqn. (2.30) so the shape function

is

$$\mathbf{n} = \begin{bmatrix} 1-\xi & 0 \\ 6(\xi-\xi^2)\varsigma & 1-3\xi^2+2\xi^3 \\ (-1+4\xi-3\xi^2)L\varsigma & (\xi-2\xi^2+\xi^3)L \\ \xi & 0 \\ 6(-\xi+\xi^2)\varsigma & 3\xi^2-2\xi^3 \\ (2\xi-3\xi^2)L\varsigma & (-\xi^2+\xi^3)L \end{bmatrix}^T \tag{2.60}$$

Strain-Displacement Matrix

In the derivation of the shape function, transverse strain (ϵ_y) has been neglected; this is because it is unconstrained. A further approximation will now be made by omitting the shear strain. All that remains is the normal strain, so the strain-displacement matrix in eqn. (2.44) is reduced to

$$\mathbf{b} = \begin{bmatrix} \frac{\partial}{\partial x} & 0 \end{bmatrix} \mathbf{n}. \tag{2.61}$$

Applying this to eqn. (2.60) produces

$$\mathbf{b} = \begin{bmatrix} -\frac{1}{L} & (-6+12\xi)\varsigma/L & (-4+6\xi)\varsigma & \frac{1}{L} & (6-12\xi)\varsigma/L & (-2+6\xi)\varsigma \end{bmatrix}. \tag{2.62}$$

Stiffness Matrix

The material property matrix for a pure normal strain expression is simply the Young's modulus, E, so in this case eqn. (2.26) becomes

$$\mathbf{k} = E\int \mathbf{b}^T\mathbf{b}\,dV = E\int_0^L\int \mathbf{b}^T\mathbf{b}\,dA\,dx. \tag{2.63}$$

At this point it is convenient to express the strain-displacement matrix as

$$\mathbf{b} = \mathbf{b_0} + \mathbf{b_y}y \tag{2.64}$$

$$\mathbf{b_0} = \begin{bmatrix} -\frac{1}{L} & 0 & 0 & \frac{1}{L} & 0 & 0 \end{bmatrix} \tag{2.65}$$

$$\mathbf{b_y} = \begin{bmatrix} 0 & (-6+12\xi)/L^2 & (-4+6\xi)/L & 0 & (6-12\xi)/L^2 & (-2+6\xi)/L \end{bmatrix} \tag{2.66}$$

so that

$$\mathbf{k} = E\int_0^L\int (\mathbf{b_0}+y\mathbf{b_y})^T(\mathbf{b_0}+y\mathbf{b_y})\,dA\,dx. \tag{2.67}$$

$$= E\int_0^L\int (\mathbf{b_0}^T\mathbf{b_0} + y(\mathbf{b_y}^T\mathbf{b_0}+\mathbf{b_0}^T\mathbf{b_y}) + y^2\mathbf{b_y}^T\mathbf{b_y})\,dA\,dx. \tag{2.68}$$

$$= EA\int_0^L \mathbf{b_0}^T\mathbf{b_0}\,dx + EI\int_0^L \mathbf{b_y}^T\mathbf{b_y}\,dx. \tag{2.69}$$

where A is the cross-sectional area of the beam and I is the second moment of inertia. Performing the matrix multiplication and integrating yields

$$\mathbf{k} = \frac{EI}{L}\begin{bmatrix} \frac{A}{I} & 0 & 0 & \frac{-A}{I} & 0 & 0 \\ 0 & \frac{12}{L^2} & \frac{6}{L} & 0 & \frac{-12}{L^2} & \frac{6}{L} \\ 0 & \frac{6}{L} & 4 & 0 & \frac{-6}{L} & 2 \\ \frac{-A}{I} & 0 & 0 & \frac{A}{I} & 0 & 0 \\ 0 & \frac{-12}{L^2} & \frac{-6}{L} & 0 & \frac{12}{L^2} & \frac{-6}{L} \\ 0 & \frac{6}{L} & 2 & 0 & \frac{-6}{L} & 4 \end{bmatrix} \tag{2.70}$$

The stiffness matrix can be recognised as the well-known Euler-Bernoulli beam element.

Mass Matrix

Following the same methodology as for the stiffness matrix, the shape function is expressed

$$\mathbf{n} = \mathbf{n_0} + \mathbf{n_y} y \tag{2.71}$$

$$\mathbf{n_0} = \begin{bmatrix} 1-\xi & 0 \\ 0 & 1-3\xi^2+2\xi^3 \\ 0 & (\xi-2\xi^2+\xi^3)L \\ \xi & 0 \\ 0 & 3\xi^2-2\xi^3 \\ 0 & (-\xi^2+\xi^3)L \end{bmatrix}^T \qquad \mathbf{n_y} = \begin{bmatrix} 0 & 0 \\ 6(\xi-\xi^2)\varsigma & 0 \\ (-1+4\xi-3\xi^2)L\varsigma & 0 \\ 0 & 0 \\ 6(-\xi+\xi^2)\varsigma & 0 \\ (2\xi-3\xi^2)L\varsigma & 0 \end{bmatrix}^T \tag{2.72}$$

Here the second matrix gives the inertial effects of a rotation of the beam cross-section about its neutral axis. It is often assumed that the beam is sufficiently slender that y will be negligible in this context, and the mass matrix is taken to be (from eqn. (2.34))

$$\mathbf{m} = \rho \int \mathbf{n_0}^T \mathbf{n_0}\, dV \tag{2.73}$$

$$= \rho A \int_0^L \mathbf{n_0}^T \mathbf{n_0}\, dx. \tag{2.74}$$

This evaluates to

$$\mathbf{m} = \rho A L \begin{bmatrix} \frac{1}{3} & 0 & 0 & \frac{1}{6} & 0 & 0 \\ 0 & \frac{13}{35} & \frac{11}{210}L & 0 & \frac{9}{70} & \frac{-13}{420}L \\ 0 & \frac{11}{210}L & \frac{1}{105}L^2 & 0 & \frac{13}{420}L & \frac{-1}{140}L^2 \\ \frac{1}{6} & 0 & 0 & \frac{1}{3} & 0 & 0 \\ 0 & \frac{9}{70} & \frac{13}{420}L & 0 & \frac{13}{35} & \frac{-11}{210}L \\ 0 & \frac{-13}{420}L & \frac{-1}{140}L^2 & 0 & \frac{-11}{210}L & \frac{1}{105}L^2 \end{bmatrix} \tag{2.75}$$

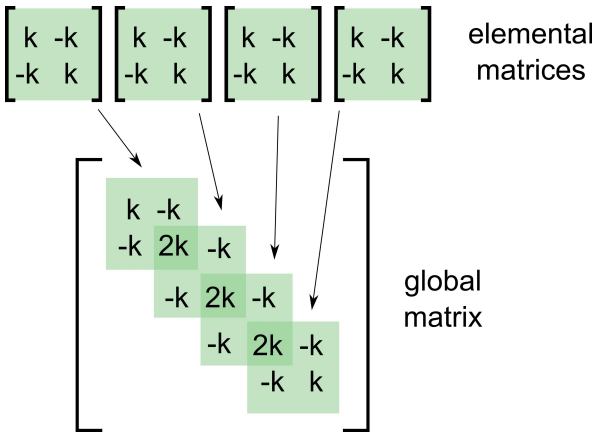

Figure 2.6: Assembly of elemental stiffness matrices into global stiffness matrix.

2.2.6 Global Matrix Assembly and Dynamic Solution

Once the individual mass, stiffness and damping matrices are obtained for each element, they may be transformed to the global coordinate system and assembled into global matrices as shown in figure 2.6. The overlapping sections of the matrices are summed together, representing common DOFs at the elemental interfaces. The global matrix equations of motion are then

$$\mathbf{M}\ddot{\mathbf{x}} + \mathbf{C}\dot{\mathbf{x}} + \mathbf{K}\mathbf{x} = \mathbf{0} \tag{2.76}$$

where $\mathbf{x} = [x_1 \quad x_2 \quad \dots \quad x_n]^T$ is the displacement vector for the n global DOFs and $\mathbf{M}$, $\mathbf{C}$ and $\mathbf{K}$ are respectively the mass, damping and stiffness matrices. The general solution to this problem is found by using the state space representation

$$\mathbf{q} = \left\{ \begin{array}{c} \mathbf{x} \\ \dot{\mathbf{x}} \end{array} \right\}. \tag{2.77}$$

The matrices are rearranged to form

$$\mathbf{A}\dot{\mathbf{q}} + \mathbf{B}\mathbf{q} = \mathbf{0} \tag{2.78}$$

where

$$\mathbf{A} = \begin{bmatrix} \mathbf{C} & \mathbf{M} \\ \mathbf{I} & \mathbf{0} \end{bmatrix} \qquad \mathbf{B} = \begin{bmatrix} \mathbf{K} & \mathbf{0} \\ \mathbf{0} & -\mathbf{I} \end{bmatrix} \tag{2.79}$$

and $\mathbf{I}$ is the identity matrix. The solution is assumed to take the form

$$\mathbf{q} = \boldsymbol{\psi} e^{\lambda t} \tag{2.80}$$

where ψ describes the deflection shape of the structure as it oscillates. As with the single DOF example this is differentiated and substituted into eqn. (2.78) to give

$$(\lambda\mathbf{A} + \mathbf{B})\,\boldsymbol{\psi} = \mathbf{0}. \tag{2.81}$$

Eqn. (2.81) is a generalised eigenproblem, the solution to which can be obtained using any of a number of numerical procedures described by Golub and Van Loan [165]. First the eigenvalues are computed from the determinant of the eigenvalue problem

$$|\lambda \mathbf{A} + \mathbf{B}| = 0. \tag{2.82}$$

Substituting the eigenvalues into eqn. (2.81) allows the calculation of the eigenvectors, noting that the scaling of the eigenvectors is arbitrary and thus a further constraint must be imposed on the solution, such as setting the first element of the eigenvector to unity.

As with the single DOF frequency solution obtained before, the eigenvalues may be complex, where in this case the imaginary eigenvalue component represents the oscillatory frequency and the real component represents the rate of decay. The eigenvectors may also be complex, with the argument of each DOF describing the phase of its motion.

Once more, a variety of damping models exist, including the common Coulomb, viscous, and hysteretic models discussed in section 2.1. It is often reasonable to neglect damping, permitting a much simplified analysis; in this case the equation of motion is

$$\mathbf{M}\ddot{\mathbf{x}} + \mathbf{K}\mathbf{x} = \mathbf{0} \tag{2.83}$$

and the eigenproblem is simply

$$(\mathbf{K} - \lambda \mathbf{M})\,\boldsymbol{\psi} = \mathbf{0}. \tag{2.84}$$

The eigenvalue is now the square of the natural frequency, $\lambda = \omega_n^2$, and will be a positive real number. The eigenvectors will also be real, corresponding with the fact that the nodal displacements are all in phase or antiphase with one another in the absence of damping.

Where damping can not be neglected, one of two approaches can be taken: generalised damping or proportional damping. A popular practice is to assume that the damping matrix is a linear combination of the mass and stiffness matrices. This *proportional* damping affords great simplification, and has some physical basis as the source of material damping is often linked to the presence of mass and stiffness. Using this method the damping matrix becomes

$$\mathbf{C} = \alpha \mathbf{M} + \beta \mathbf{K}. \tag{2.85}$$

It can be shown that the eigenvectors for this system are the same as those for the undamped system and each natural frequency is related to the undamped natural frequency by

$$\omega_n = \omega_0 \sqrt{1 - \zeta^2} \tag{2.86}$$

where

$$\eta = \frac{1}{2}\left(\beta\omega_0 + \frac{\alpha}{\omega_0}\right). \tag{2.87}$$

The foregoing equations apply to proportional *viscous* damping; proportional *hysteretic* damping is described by

$$\mathbf{M}\ddot{\mathbf{x}} + (\mathbf{K} + i\mathbf{D})\mathbf{x} = \mathbf{0} \tag{2.88}$$

$$\mathbf{D} = \alpha\mathbf{M} + \beta\mathbf{K} \tag{2.89}$$

$$\omega_n^2 = \omega_0^2(1 + i\eta) \tag{2.90}$$

$$\eta = \beta + \frac{\alpha}{\omega_0^2}. \tag{2.91}$$

2.3 Modal Analysis

A notable facet of the foregoing discussion is that the eigenproblems in eqns. (2.81) and (2.84) yield not just one but many solutions. In contrast to the single degree of freedom (SDOF) systems considered in section 2.1, multiple degree of freedom (MDOF) systems have a number of resonant frequencies, equal to the number of DOFs. Each of these vibration modes has a corresponding damping ratio and a unique mode shape defined by the eigenvector. For the linear systems considered here, the principle of superposition dictates that the vibration of an MDOF structure can be described by a linear combination of these modes. The modes of a structure are thus assumed to form a complete description of its dynamics, and this premise forms the backbone for the field of modal analysis. Brown and Allemang provide an historical overview of the development of the field [166].

2.3.1 Orthogonality Conditions

Some important relationships in the derivation of modal results are examined here. The discussion will be limited to undamped systems but could equally be applied to proportionally damped systems. First, an eigenvector matrix is defined with each eigenvector forming a column of that matrix:

$$\mathbf{\Psi} = [\ \boldsymbol{\psi_1} \quad \boldsymbol{\psi_2} \quad \dots \quad \boldsymbol{\psi_n}\ ]. \tag{2.92}$$

The eigenvectors are orthogonal with respect to the mass and stiffness matrices, so pre- and post-multiplying by $\mathbf{\Psi}^T$ and $\mathbf{\Psi}$ diagonalises both matrices to give

$$\mathbf{\Psi}^T\mathbf{M}\mathbf{\Psi} = \begin{bmatrix} m_1 & 0 & \dots & 0 \\ 0 & m_2 & \dots & 0 \\ \vdots & \vdots & \ddots & \vdots \\ 0 & 0 & \dots & m_n \end{bmatrix} \quad \text{and} \quad \mathbf{\Psi}^T\mathbf{K}\mathbf{\Psi} = \begin{bmatrix} k_1 & 0 & \dots & 0 \\ 0 & k_2 & \dots & 0 \\ \vdots & \vdots & \ddots & \vdots \\ 0 & 0 & \dots & k_n \end{bmatrix}. \tag{2.93}$$

The diagonal elements of these matrices are the *modal masses* and *modal stiffnesses*, giving the natural frequencies as $\omega_i = \sqrt{k_i/m_i}$. It is common to normalise the eigenvectors with respect to the mass

matrix so that the i^{th} mass-normalised eigenvector is given by

$$\boldsymbol{\phi_i} = \frac{\boldsymbol{\psi_i}}{\sqrt{m_i}}. \tag{2.94}$$

Eqn. (2.84) can then be written

$$\mathbf{K\Phi} - \mathbf{M\Phi\Lambda} = \mathbf{0} \tag{2.95}$$

where the eigenvector matrix is now

$$\boldsymbol{\Phi} = [\ \boldsymbol{\phi_1} \quad \boldsymbol{\phi_2} \quad \ldots \quad \boldsymbol{\phi_n}\ ] \tag{2.96}$$

and the corresponding eigenvalue matrix is

$$\boldsymbol{\Lambda} = \begin{bmatrix} \lambda_1 & 0 & \ldots & 0 \\ 0 & \lambda_2 & \ldots & 0 \\ \vdots & \vdots & \ddots & \vdots \\ 0 & 0 & \ldots & \lambda_n \end{bmatrix}. \tag{2.97}$$

The mass-normalised eigenvectors give

$$\boldsymbol{\Phi}^T \boldsymbol{M\Phi} = \mathbf{I} \tag{2.98}$$

and pre-multiplying eqn. (2.95) by $\boldsymbol{\Phi}^T$ produces

$$\boldsymbol{\Phi}^T \boldsymbol{K\Phi} = \boldsymbol{\Lambda}. \tag{2.99}$$

These are the *orthogonality conditions*. The mass-normalised eigenvectors are orthonormal with respect to the mass matrix, defining an orthonormal basis in the modal, or *normal* coordinate system [167, 168].

2.3.2 MDOF Frequency Response Functions

The remainder of this section will examine how the modes contribute to the frequency response of the system. The matrix equation of motion for an undamped system subject to periodic excitation is

$$\mathbf{Kx} - \mathbf{M\ddot{x}} = \mathbf{f} \tag{2.100}$$

where $\mathbf{x}$ is the displacement vector and $\mathbf{f}$ is the forcing vector: $\mathbf{x} = \mathbf{X}e^{i\omega t}$ and $\mathbf{f} = \mathbf{F}e^{i\omega t}$. This equation has a solution of the form

$$(\mathbf{K} - \omega^2\mathbf{M})\boldsymbol{X} = \boldsymbol{F} \tag{2.101}$$

or

$$\boldsymbol{X} = (\mathbf{K} - \omega^2\mathbf{M})^{-1}\boldsymbol{F} \tag{2.102}$$

where the inverted matrix on the right is the FRF matrix

$$\mathbf{H}(\omega) = (\mathbf{K} - \omega^2\mathbf{M})^{-1}. \tag{2.103}$$

An element $H_{jk}(\omega)$ from this matrix gives the response at the j^{th} DOF produced by a unit excitation of frequency ω at the k^{th} DOF. A more useful formulation is produced by inverting eqn. (2.103), pre-multiplying by $\mathbf{\Phi}^T$, postmultiplying by $\mathbf{\Phi}$ and using the orthogonality conditions to get

$$\mathbf{\Phi}^T\mathbf{H}^{-1}\mathbf{\Phi} = \mathbf{\Lambda} - \omega^2\mathbf{I}. \tag{2.104}$$

Pre-multiplying and post-multiplying again, this time by $(\mathbf{\Phi}^T)^{-1}$ and $\mathbf{\Phi}^{-1}$, gives

$$\mathbf{H}^{-1} = (\mathbf{\Phi}^T)^{-1}(\mathbf{\Lambda} - \omega^2\mathbf{I})\mathbf{\Phi}^{-1} \tag{2.105}$$

so that

$$\mathbf{H}(\omega) = \mathbf{\Phi}(\mathbf{\Lambda} - \omega^2\mathbf{I})^{-1}\mathbf{\Phi}^T. \tag{2.106}$$

The response of DOF j to a unit excitation at DOF k is thus

$$H_{jk}(\omega) = \sum_{r=1}^{N} \frac{\phi_{jr}\phi_{kr}}{\omega_r^2 - \omega^2} = \sum_{r=1}^{N} \frac{{}_rA_{jk}}{\omega_r^2 - \omega^2} \tag{2.107}$$

and the numerator is referred to as the *modal constant*, or sometimes the *residue*. Evidently, the response goes to infinity at the natural frequencies for an undamped system; the damped equivalent of eqn. (2.107) does not suffer the same numerical problems, and is derived in the standard texts [162, 169] using the same approach to give

$$H_{jk}(\omega) = \sum_{r=1}^{N} \frac{{}_rA_{jk}}{\omega_r^2 - \omega^2 + i\eta_r\omega_r^2}. \tag{2.108}$$

From these expressions, the FRF is seen to be composed of a linear summation of SDOF response curves: one for each mode.

2.4 Dynamic Characteristics of Loaded Structures

It has long been established that stressing a structure induces changes in the natural frequencies. Stringed musical instruments have taken advantage of this for millennia, altering pitch by changing the tension of the strings [170]. It was apparently first exploited in an engineering context in 1936, when Stephens [171] explained how the natural frequencies of a structure can be used to determine the loads carried in its members. His derivation was later corrected by Lurie [172]. Many variations on this theme have since been reported; for example, Greening and Lieven [173] include axial loading effects in a model updating scheme for a redundant frame, and Tullini and Laudiero [174] cite further

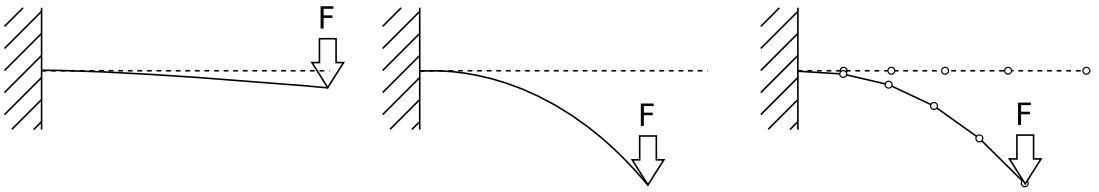

(a) Linear elastic response (b) Nonlinear elemental strain (c) Linear elemental strain with nonlinear elemental rotations

Figure 2.7: A cantilever beam subject to end load F. The linear elastic strain relations are compromised for larger forces.

examples in the context of their own scheme, which uses both frequency and mode shape data to identify axial loads and end fixity of a column. Greening's thesis [175] offers an extensive background on the topic.

2.4.1 Geometric Nonlinearity

The observed variations in dynamic response are caused by *geometric nonlinearities*. In a static context, the term encompasses any change resulting from spatial distortions of the structure. This includes follower forces, where the force vector is dictated by the structural alignment (for example, normal forces such as pressure can be sensitive to surface deflections), and the stiffness reconfigurations associated with changing geometries. The latter is characterised by large deformations of the structure, creating a qualitatively different topology. From an FE perspective, the deformations can be divided into two categories:

- Large elemental rotation
- Large elemental strain

As an illustration, consider the cantilever beam in figure 2.7. A linear beam element has no coupling between the axial and bending degrees of freedom (DOFs). Thus a vertical force on a horizontal cantilever will produce only vertical displacement at the end of the beam. For small forces and displacements this produces accurate results, as seen in figure 2.7(a). Larger forces, however, produce both transverse and axial displacements. In figure 2.7(b) the beam is still modelled as a single element, but with nonlinear strain relations. An alternative is to refine the element mesh, splitting the beam up into a series of smaller elements as in figure 2.7(c). In this case the elastic behaviour of each element is approximately linear and may be modelled as such, but each element is rotated to a new coordinate system. This can be accomplished fairly efficiently through linear matrix transforms, and avoids the need for computationally expensive nonlinear strain equations. In many situations, however, sufficient mesh refinement is impractical and engineering judgement must always be exercised as to whether to use large rotation, large strain, or a combination of the two.

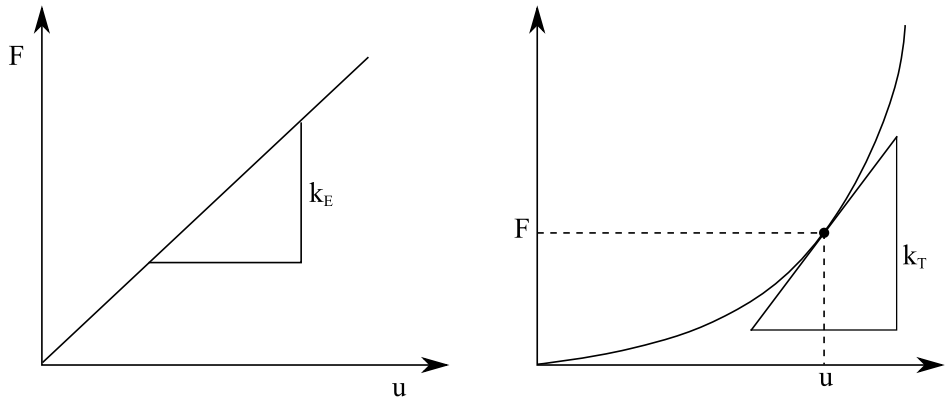

(a) Linear; the elastic stiffness is constant

(b) Nonlinear; the tangent stiffness varies with load

Figure 2.8: Two examples of static structural problems, with force plotted against displacement. The gradient of the graphs represents the stiffness at any given point.

A related effect is seen where slender beams or thin plates are subjected to axial or in-plane loading. In these cases, force coupling leads to effective transverse stiffness modifications. Compressive axial loads produce softening effects, while tensile loading results in apparent stiffening. Accordingly, the behaviour is known as *stress stiffening*. Of course, the stiffness of the member does not actually change; the effect is seen because, for small transverse deflections, the coupling between the axial and transverse forces is proportional to the displacement. Thus, the contribution of the axial load to the restorative force varies with the displacement, augmenting the restorative stiffness force in a manner consistent with an actual stiffness modification. Stress stiffening differs from the large deformation effects discussed above in that it can produce changes in the effective stiffness even when there is no significant structural displacement.

A simple example is shown in figure 2.8. Often it is useful and justifiable to make linear assumptions such that the displacements vary linearly with force. This is seen in figure 2.8(a). The gradient of the line on the force-displacement plot is the elastic stiffness, k_E, and this stays constant throughout the loading regime. In nonlinear systems the stiffness will vary with force or displacement as in figure 2.8(b). In this example the stiffness of the structure increases with loading, such that progressively greater force increments are required to produce uniform displacement intervals, and the force-displacement plot produces a curve instead of a line. The stiffness is still represented by the gradient of the curve but this now changes with load, and the stiffness at a given point is referred to as the *tangent stiffness*, k_T.

It is this tangent stiffness that is to be used in the dynamic analyses of this thesis. The dynamic loading is assumed to be small enough to satisfy linear stiffness approximations, with the geometric nonlinearities only being exhibited for the much higher static forces. The procedure is therefore firstly to determine the tangent stiffness from a nonlinear static solution, and then to employ that stiffness in a linear dynamic analysis. The first stage is usually tackled with iterative methods, discussed in

section 2.4.3. The dynamic solution follows the methods set out in section 2.2.6.

It is prudent to note that in static analyses, large deformation approaches are commonly employed without taking the stress stiffening into account. The displacement solutions obtained are still accurate, as the model will converge on a state where the forces are balanced, but the tangent stiffness will be incomplete. Where stress stiffening *is* included in the tangent stiffness, it serves to accelerate the solution convergence. In contrast, the dynamic solutions rely explicitly on the accuracy of the tangent stiffness, and *must* take stress stiffening into account. In fact, stress stiffening is expected to be the dominant effect in the work conducted here, where significant structural deformation is not anticipated. Ryu *et al.* [176] offer a criterion for quantifying the influence of stress stiffening on dynamic simulations.

2.4.2 Finite Element Formulation

A continuous two-dimensional beam model is presented in appendix A, where a general expression is derived to show the relationship between the static buckling load and the natural frequency under loading. In this section, finite element representations of beam elements under loading will be considered.

Mayo *et al.* [177] offer a review of the different formulations for geometric stiffening, covering the differing orders of approximation. Two derivations for the stress stiffening matrices will be examined here: The first uses energy methods, following a similar approach to that given in section 2.2 for a regular finite element. The second uses coordinate transformations; its advantage over the energy method is that it is more easily applied to gross deformations.

Energy Method

Adopting the approach of section 2.2, shear strains are neglected for the beam element, and only normal strains are accounted for. Thus,

$$\epsilon = \epsilon_x = \frac{\partial u}{\partial x}. \tag{2.109}$$

In eqn. (2.46) the axial displacement is related to the neutral axis displacement by

$$u = u_0 - \theta_0 y \tag{2.110}$$

so

$$\epsilon_x = \frac{\partial u_0}{\partial x} - \frac{\partial \theta_0}{\partial x} y. \tag{2.111}$$

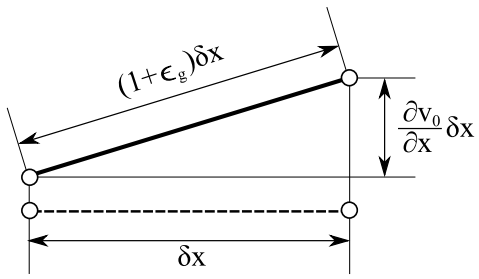

Figure 2.9: Illustration of nonlinear axial strain with transverse deflection.

The strain energy is given by

$$U_i = \frac{1}{2}E\int \epsilon_x^2\, dV \tag{2.112}$$

$$= \frac{1}{2}E\int \left(\frac{\partial u_0}{\partial x} - \frac{\partial \theta_0}{\partial x}y\right)^2 dV. \tag{2.113}$$

Multiplying out the brackets and integrating over the cross-section produces

$$U_i = \frac{EA}{2}\int_0^L \left(\frac{\partial u_0}{\partial x}\right)^2 dx + \frac{EI}{2}\int_0^L \left(\frac{\partial \theta_0}{\partial x}\right)^2 dx. \tag{2.114}$$

This expression is clearly analogous to eqn. (2.69). Evaluating it with the help of eqn. (2.58) gives

$$\begin{aligned} U_i =& \frac{EA}{2L}(u_1^2 - 2u_1u_2 + u_2^2) \\ &+ \frac{2EI}{L^3}(3v_1^2 + L^2\theta_1^2 + 3v_2^2 + L^2\theta_2^2 + 3Lv_1\theta_1 - 6v_1v_2 + 3Lv_1\theta_2 - 3L\theta_1v_2 + L^2v\theta_1\theta_2 - 3Lv_2\theta_2) \end{aligned} \tag{2.115}$$

and applying Castigliano's theorem gives

$$\mathbf{f} = \frac{EI}{L}\begin{bmatrix} \frac{A}{I} & 0 & 0 & \frac{-A}{I} & 0 & 0 \\ 0 & \frac{12}{L^2} & \frac{6}{L} & 0 & \frac{-12}{L^2} & \frac{6}{L} \\ 0 & \frac{6}{L} & 4 & 0 & \frac{-6}{L} & 2 \\ \frac{-A}{I} & 0 & 0 & \frac{A}{I} & 0 & 0 \\ 0 & \frac{-12}{L^2} & \frac{-6}{L} & 0 & \frac{12}{L^2} & \frac{-6}{L} \\ 0 & \frac{6}{L} & 2 & 0 & \frac{-6}{L} & 4 \end{bmatrix}\begin{Bmatrix} u_1 \\ v_1 \\ \theta_1 \\ u_2 \\ v_2 \\ \theta_2 \end{Bmatrix}. \tag{2.116}$$

The matrix produced here is identical to the stiffness matrix obtained in section 2.2.

For a nonlinear model, it is necessary to take account of the coupling between the axial and transverse displacements. This is illustrated for an infinitesimal beam segment in figure 2.9. If the length of the segment is δx then the geometric strain, ϵ_g, caused by the coupling can be calculated using Pythagoras' theorem with the triangle in figure 2.9:

$$\epsilon_g = \frac{\sqrt{\delta x^2 + \left(\frac{\partial v_0}{\partial x}\delta x\right)^2}}{\delta x} - 1 \tag{2.117}$$

$$= \sqrt{1 + \left(\frac{\partial v_0}{\partial x}\right)^2} - 1. \tag{2.118}$$

A Taylor series expansion leads to

$$\epsilon_g = \frac{1}{2}\left(\frac{\partial v_0}{\partial x}\right)^2 + O\left(\left(\frac{\partial v_0}{\partial x}\right)^4\right) \tag{2.119}$$

and the supplemented strain equation is

$$\begin{aligned}\epsilon &= \epsilon_x + \epsilon_g \\ &= \frac{\partial u_0}{\partial x} - \frac{\partial \theta_0}{\partial x}y + \frac{1}{2}\left(\frac{\partial v_0}{\partial x}\right)^2.\end{aligned} \tag{2.120}$$

Putting this new expression into eqn. (2.112) yields

$$U_i = \frac{1}{2}E\int\left(\frac{\partial u_0}{\partial x} - \frac{\partial \theta_0}{\partial x}y + \frac{1}{2}\left(\frac{\partial v_0}{\partial x}\right)^2\right)^2 dV. \tag{2.121}$$

Expanding, neglecting high order terms, and integrating over the cross sectional area while noting that integrals of the form $\int y\,dV$ vanish gives

$$U_i = \frac{EA}{2}\int_0^L\left(\frac{\partial u_0}{\partial x}\right)^2 dx + \frac{EI}{2}\int_0^L\left(\frac{\partial \theta}{\partial x}\right)^2 dx + \frac{EA}{2}\int_0^L \frac{\partial u_0}{\partial x}\left(\frac{\partial v_0}{\partial x}\right)^2 dx. \tag{2.122}$$

Contrasting this with eqn. (2.114) shows the only difference to be the final, nonlinear integral. From eqn. (2.58) the axial displacement derivative, $\partial u_0/\partial x$, is found to be independent of the position, x, so can be taken outside the integral. The axial load in the member can be approximated by

$$P = EA\frac{\partial u_0}{\partial x} \tag{2.123}$$

so that

$$U_i = \frac{EA}{2}\int_0^L\left(\frac{\partial u_0}{\partial x}\right)^2 dx + \frac{EI}{2}\int_0^L\left(\frac{\partial \theta}{\partial x}\right)^2 dx + \frac{P}{2}\int_0^L\left(\frac{\partial v_0}{\partial x}\right)^2 dx. \tag{2.124}$$

Evaluating the strain energy using eqn. (2.58) and applying Castigliano's theorem produces

$$\mathbf{f} = \left(\frac{EI}{L}\begin{bmatrix} \frac{A}{I} & 0 & 0 & \frac{-A}{I} & 0 & 0 \\ 0 & \frac{12}{L^2} & \frac{6}{L} & 0 & \frac{-12}{L^2} & \frac{6}{L} \\ 0 & \frac{6}{L} & 4 & 0 & \frac{-6}{L} & 2 \\ \frac{-A}{I} & 0 & 0 & \frac{A}{I} & 0 & 0 \\ 0 & \frac{-12}{L^2} & \frac{-6}{L} & 0 & \frac{12}{L^2} & \frac{-6}{L} \\ 0 & \frac{6}{L} & 2 & 0 & \frac{-6}{L} & 4 \end{bmatrix} + \frac{P}{L}\begin{bmatrix} 0 & 0 & 0 & 0 & 0 & 0 \\ 0 & \frac{6}{5} & \frac{L}{10} & 0 & \frac{-6}{5} & \frac{L}{10} \\ 0 & \frac{L}{10} & \frac{2L^2}{15} & 0 & \frac{-L}{10} & \frac{-L^2}{30} \\ 0 & 0 & 0 & 0 & 0 & 0 \\ 0 & \frac{-6}{5} & \frac{-L}{10} & 0 & \frac{6}{5} & \frac{-L}{10} \\ 0 & \frac{L}{10} & \frac{-L^2}{30} & 0 & \frac{-L}{10} & \frac{2L^2}{15} \end{bmatrix}\right)\begin{Bmatrix} u_1 \\ v_1 \\ \theta_1 \\ u_2 \\ v_2 \\ \theta_2 \end{Bmatrix} \tag{2.125}$$

The stiffness derived here can be seen to be comprised of two components: these are the elastic and

geometric stiffness matrices,

$$\mathbf{k} = \mathbf{k_e} + \mathbf{k_g} \tag{2.126}$$

where

$$\mathbf{k_e} = \frac{EI}{L}\begin{bmatrix} \frac{A}{I} & 0 & 0 & \frac{-A}{I} & 0 & 0 \\ 0 & \frac{12}{L^2} & \frac{6}{L} & 0 & \frac{-12}{L^2} & \frac{6}{L} \\ 0 & \frac{6}{L} & 4 & 0 & \frac{-6}{L} & 2 \\ \frac{-A}{I} & 0 & 0 & \frac{A}{I} & 0 & 0 \\ 0 & \frac{-12}{L^2} & \frac{-6}{L} & 0 & \frac{12}{L^2} & \frac{-6}{L} \\ 0 & \frac{6}{L} & 2 & 0 & \frac{-6}{L} & 4 \end{bmatrix} \quad \mathbf{k_g} = \frac{P}{L}\begin{bmatrix} 0 & 0 & 0 & 0 & 0 & 0 \\ 0 & \frac{6}{5} & \frac{L}{10} & 0 & \frac{-6}{5} & \frac{L}{10} \\ 0 & \frac{L}{10} & \frac{2L^2}{15} & 0 & \frac{-L}{10} & \frac{-L^2}{30} \\ 0 & 0 & 0 & 0 & 0 & 0 \\ 0 & \frac{-6}{5} & \frac{-L}{10} & 0 & \frac{6}{5} & \frac{-L}{10} \\ 0 & \frac{L}{10} & \frac{-L^2}{30} & 0 & \frac{-L}{10} & \frac{2L^2}{15} \end{bmatrix} \tag{2.127}$$

Coordinate Transformation Method

The problem with the energy method given above is that it exploits the assumption of small angular displacements, so that $\partial v_0/\partial x \approx \theta_0$. Where gross deformations occur, either at an elemental level or at a global level, this assumption is invalidated and another approach must be taken.

Jennings [178] uses coordinate transforms to break the problem down into discrete steps. He adopts three coordinate systems: the *joint displacements*, which correspond to the global DOF displacements; the *member intermediate displacements*, relating the displacements to the elemental coordinate system; and the *member basic displacements*, which describe the beam deformation in terms of its axial extension and the two end rotations. These coordinate systems are pictured in figure 2.10 and, adopting the notation of the original paper, the displacements are given by

$$\begin{aligned} \boldsymbol{X} &= \left\{ \begin{array}{cccccc} x_A & y_A & \theta_A & x_B & y_B & \theta_B \end{array} \right\}^T && \text{(joint displacements)} \\ \boldsymbol{U} &= \left\{ \begin{array}{cccc} u & v & \theta_{AB} & \theta_{BA} \end{array} \right\}^T && \text{(intermediate displacements)} \\ \boldsymbol{E} &= \left\{ \begin{array}{ccc} e & \phi_{AB} & \phi_{BA} \end{array} \right\}^T && \text{(basic displacements)} \end{aligned} \tag{2.128}$$

Transformations between these coordinate systems are defined so that

$$\boldsymbol{U} = \boldsymbol{T}\boldsymbol{X} \tag{2.129}$$

$$\boldsymbol{E} = \boldsymbol{A}\boldsymbol{U} \tag{2.130}$$

where

$$\boldsymbol{T} = \begin{bmatrix} -\cos\alpha & -\sin\alpha & 0 & \cos\alpha & \sin\alpha & 0 \\ \sin\alpha & -\cos\alpha & 0 & -\sin\alpha & \cos\alpha & 0 \\ 0 & 0 & 1 & 0 & 0 & 0 \\ 0 & 0 & 0 & 0 & 0 & 1 \end{bmatrix} \tag{2.131}$$

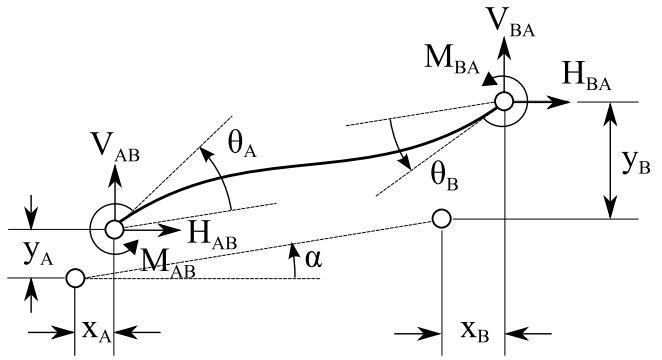

(a) Joint displacements and forces.

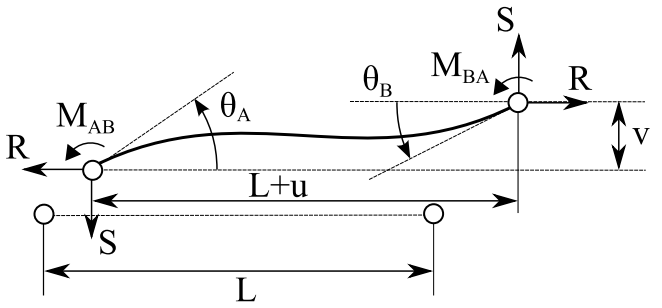

(b) Member intermediate displacements and forces.

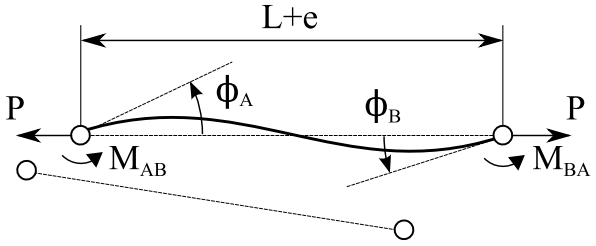

(c) Member basic displacements and forces.

Figure 2.10: Coordinate systems used in Jennings' nonlinear beam analysis.

and

$$\boldsymbol{A} = \begin{bmatrix} 1 & 0 & 0 & 0 \\ 0 & -1/L & 1 & 0 \\ 0 & -1/L & 0 & 1 \end{bmatrix} \tag{2.132}$$

The corresponding force vectors are given as

$$\begin{aligned} \boldsymbol{L} &= \left\{ \begin{array}{cccccc} H_{AB} & V_{AB} & M_{AB} & H_{BA} & V_{BA} & M_{BA} \end{array} \right\}^T && \text{(joint forces)} \\ \boldsymbol{R} &= \left\{ \begin{array}{cccc} R & S & M_{AB} & M_{BA} \end{array} \right\}^T && \text{(intermediate forces)} \\ \boldsymbol{P} &= \left\{ \begin{array}{ccc} P & M_{AB} & M_{BA} \end{array} \right\}^T && \text{(basic forces)} \end{aligned} \tag{2.133}$$

and these are related by the same transforms:

$$\boldsymbol{L} = \boldsymbol{T}^T \boldsymbol{R} \tag{2.134}$$

$$\boldsymbol{R} = \boldsymbol{A}^T \boldsymbol{P}. \tag{2.135}$$

Defining a linear elastic stiffness matrix for the member basic displacements,

$$\boldsymbol{k} = \begin{bmatrix} \frac{EA}{L} & 0 & 0 \\ 0 & \frac{4EI}{L} & \frac{2EI}{L} \\ 0 & \frac{2EI}{L} & \frac{4EI}{L} \end{bmatrix}. \tag{2.136}$$

and

$$\boldsymbol{P} = \boldsymbol{k}\boldsymbol{E}. \tag{2.137}$$

Combining eqns. (2.129), (2.130), (2.134), (2.135) and (2.137) yields

$$\boldsymbol{L} = \boldsymbol{T}^T \boldsymbol{A}^T \boldsymbol{k} \boldsymbol{A} \boldsymbol{T} \boldsymbol{X} \tag{2.138}$$

which implies a stiffness matrix of

$$\boldsymbol{K} = \boldsymbol{T}^T \boldsymbol{A}^T \boldsymbol{k} \boldsymbol{A} \boldsymbol{T}. \tag{2.139}$$

Evaluating the stiffness in this manner produces exactly the same result as the previous methods discussed. The flexibility of this method, however, and the reason it was selected for the analyses in this thesis, is the ease with which differing levels of nonlinearity may be accommodated. For example, if nonlinear elemental strains are important, the linear elastic relationship in eqn. (2.136) can be replaced with a full nonlinear elastic stiffness, and this is derived by Jennings. More commonly, it is sufficient to consider only nonlinear elemental rotations, and this is done by replacing the linear transform $\boldsymbol{A}$ with a nonlinear function $\boldsymbol{f_A(U)}$. Once again, Jennings derives an exact solution, but

here only a second order approximation will be discussed. This is defined by

$$\left.\begin{array}{rcl} e &=& u + \frac{v^2}{2L} \\ \phi_{AB} &=& \theta_{AB} - \frac{v}{L} \\ \phi_{BA} &=& \theta_{BA} - \frac{v}{L} \end{array}\right\} \qquad \boldsymbol{E} = \boldsymbol{f_A(U)} \tag{2.140}$$

and the joint forces (needed for iterative methods) are determined from

$$\boldsymbol{L} = \boldsymbol{T}^T \boldsymbol{A}^T \boldsymbol{k} \boldsymbol{f_A(TX)}. \tag{2.141}$$

Incremental displacements and forces are now considered so that

$$\begin{array}{rcll} \boldsymbol{x} &=& \left\{ \begin{array}{cccccc} \delta x_A & \delta y_A & \delta\theta_A & \delta x_B & \delta y_B & \delta\theta_B \end{array} \right\}^T & \text{(joint displacements)} \\ \boldsymbol{u} &=& \left\{ \begin{array}{cccc} \delta u & \delta v & \delta\theta_{AB} & \delta\theta_{BA} \end{array} \right\}^T & \text{(intermediate displacements)} \\ \boldsymbol{e} &=& \left\{ \begin{array}{ccc} \delta e & \delta\phi_{AB} & \delta\phi_{BA} \end{array} \right\}^T & \text{(basic displacements)} \\ \boldsymbol{\ell} &=& \left\{ \begin{array}{cccccc} \delta H_{AB} & \delta V_{AB} & \delta M_{AB} & \delta H_{BA} & \delta V_{BA} & \delta M_{BA} \end{array} \right\}^T & \text{(joint forces)} \\ \boldsymbol{r} &=& \left\{ \begin{array}{cccc} \delta R & \delta S & \delta M_{AB} & \delta M_{BA} \end{array} \right\}^T & \text{(intermediate forces)} \\ \boldsymbol{p} &=& \left\{ \begin{array}{ccc} \delta P & \delta M_{AB} & \delta M_{BA} \end{array} \right\}^T & \text{(basic forces)} \end{array} \tag{2.142}$$

The incremental intermediate displacements are related to the incremental basic displacements by differentiating eqns. (2.140) to give

$$\left\{ \begin{array}{c} \delta e \\ \delta\phi_{AB} \\ \delta\phi_{BA} \end{array} \right\} = \left[\begin{array}{cccc} 1 & v/L & 0 & 0 \\ 0 & -1/L & 1 & 0 \\ 0 & -1/L & 0 & 1 \end{array} \right] \left\{ \begin{array}{c} \delta u \\ \delta v \\ \delta\theta_{AB} \\ \delta\theta_{BA} \end{array} \right\} \tag{2.143}$$

or

$$\boldsymbol{e} = \overline{\boldsymbol{A}} \boldsymbol{u}. \tag{2.144}$$

Jennings uses the principle of virtual work to show that in this case,

$$\boldsymbol{R} = \overline{\boldsymbol{A}} \boldsymbol{L} \tag{2.145}$$

and taking the partial derivative with respect to first the forces then the displacements gives the incremental intermediate forces as

$$\boldsymbol{r} = \overline{\boldsymbol{A}}^T \boldsymbol{p} + \boldsymbol{D} \boldsymbol{u} \tag{2.146}$$

where

$$\boldsymbol{D} = \left[\begin{array}{cccc} 0 & 0 & 0 & 0 \\ 0 & P/L & 0 & 0 \\ 0 & 0 & 0 & 0 \\ 0 & 0 & 0 & 0 \end{array} \right]. \tag{2.147}$$

Applying the linear stiffness relationship, $\boldsymbol{p} = \boldsymbol{ke}$, the incremental joint forces are determined as

$$\boldsymbol{\ell} = \boldsymbol{T}^T(\overline{\boldsymbol{A}}^T\boldsymbol{k}\overline{\boldsymbol{A}} + \boldsymbol{D})\boldsymbol{T}\boldsymbol{x}. \tag{2.148}$$

From this equation the tangent stiffness is taken to be

$$\boldsymbol{K_T} = \boldsymbol{T}^T(\overline{\boldsymbol{A}}^T\boldsymbol{k}\overline{\boldsymbol{A}} + \boldsymbol{D})\boldsymbol{T}. \tag{2.149}$$

For comparison with the other techniques, the above equation is multiplied out assuming a nominal element rotation of $\alpha = 0$ and the force P is substituted with $u + \frac{v^2}{2L}$ (from eqn. (2.140)), giving

$$\boldsymbol{K_T} = \boldsymbol{K_E} + \boldsymbol{K_G} \tag{2.150}$$

where $\boldsymbol{K_E}$ is the standard linear elastic stiffness matrix derived in eqns. (2.70) and (2.116), and the stress stiffness matrix is

$$\boldsymbol{K_G} = \frac{EA}{L}\begin{bmatrix} 0 & \varepsilon_y & 0 & 0 & -\varepsilon_y & 0 \\ \varepsilon_y & \left(\varepsilon_x + \frac{3}{2}\varepsilon_y^2\right) & 0 & -\varepsilon_y & -\left(\varepsilon_x + \frac{3}{2}\varepsilon_y^2\right) & 0 \\ 0 & 0 & 0 & 0 & 0 & 0 \\ 0 & -\varepsilon_y & 0 & 0 & \varepsilon_y & 0 \\ -\varepsilon_y & -\left(\varepsilon_x + \frac{3}{2}\varepsilon_y^2\right) & 0 & \varepsilon_y & \left(\varepsilon_x + \frac{3}{2}\varepsilon_y^2\right) & 0 \\ 0 & 0 & 0 & 0 & 0 & 0 \end{bmatrix} \tag{2.151}$$

with

$$\varepsilon_x = \frac{x_B - x_A}{L} \qquad \text{and} \qquad \varepsilon_y = \frac{y_B - y_A}{L}. \tag{2.152}$$

This same result is derived by Cook [163] using energy methods with bar elements, and a similar derivation is provided by Murray and Wilson [179] for the case of plate elements.

2.4.3 Global Solution Procedures

Unlike the beam examples considered above, general nonlinear structural problems do not have closed form analytic solutions. Instead, numerical methods must be employed. NAFEMS provide guidance on the implementation of nonlinear FE simulations [180], and some of the methods are explored below. They can all be categorised as either single pass or iterative methods.

Single Pass Methods

A common approach is to make a single static loading pass to determine the load distribution throughout the structure. This loading is used to compute the stress stiffening, which can be used in a variety of applications. An example which has been discussed for a simple beam is Euler buckling prediction. Assuming the stress distribution remains constant, the structural stiffness can be written in matrix

form as

$$\mathbf{K_T} = \mathbf{K_E} + p\hat{\mathbf{K}}_\mathbf{G} \tag{2.153}$$

where $\mathbf{K_T}$ is the tangent stiffness matrix, $\mathbf{K_E}$ is the nominal elastic stiffness matrix, $\hat{\mathbf{K}}_\mathbf{G}$ is the unit stress stiffening matrix, and p is the magnitude of the applied force. A force perturbation vector, $\delta\mathbf{F}$, can then be written in terms of a displacement perturbation vector, $\delta\mathbf{u}$, as

$$\delta\mathbf{F} = \left(\mathbf{K_E} + p\hat{\mathbf{K}}_\mathbf{G}\right)\delta\mathbf{u}. \tag{2.154}$$

Buckling occurs at a point of neutral stability, where $\delta\mathbf{F} = 0$. The critical buckling loads are thus obtained from the eigenvalues, p, and the failure load is the lowest eigenvalue.

For some examples, in particular those involving pin-jointed trusses, loading below the first buckling load will produce no transverse deformations in thin or slender members. In these cases, the eigen-buckling solution is theoretically exact. Similarly, the exact dynamic behaviour of the structure at a range of loads can be determined from a single stress stiffening calculation, simply by scaling the geometric stiffness matrix appropriately for each new load. Many practical problems will approximate to this behaviour, and it can be a useful simplification.

More commonly, however, structures will deform steadily with loading, producing nonlinear stiffness variation (nonlinear nonlinearity, if you will). Even the real-world incarnations of the pinned trusses described above can never reproduce the ideal conditions of the theoretical models. Consequently, single pass solutions will generally overestimate buckling loads and underestimate geometric stiffening. A full iterative nonlinear analysis is required to obtain more accurate solutions.

Iterative Methods

Geometric nonlinearity is usually prescribed as a function of the displacements. Even where it is written in terms of the forces, these are elemental forces and are always computed from the elemental displacements. Given a displacement vector, it is thus a trivial matter to calculate the corresponding force vector from a nonlinear stiffness function:

$$\mathbf{P} = \mathbf{f_K}(\mathbf{u}). \tag{2.155}$$

The inverse problem, however, is considerably more difficult and does not generally permit a closed form solution.

The most common approach is to apply small load increments to the model using linear stiffness approximations, re-evaluating the tangent stiffness at each step. Such a procedure is detailed by Turner *et al.* [181]. Figure 2.11 shows an illustration of this technique. The zero-load tangent stiffness is the nominal elastic stiffness $\mathbf{K_E}$. At each step, the tangent stiffness is used in a linear solution to determine the displacements over the course of that load step, such that

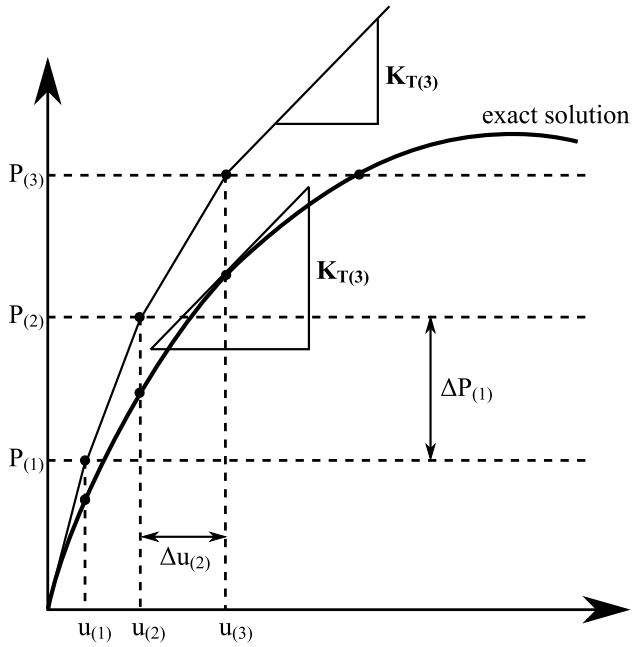

Figure 2.11: Incremental load steps in a non-linear static analysis.

$$\mathbf{\Delta u_{(n)}} = \mathbf{K_{T(n)}}^{-1}\mathbf{\Delta P_{(n)}} \tag{2.156}$$

where $\mathbf{\Delta u_{(n)}} = \mathbf{u_{(n+1)}} - \mathbf{u_{(n)}}$, $\mathbf{\Delta P_{(n)}} = \mathbf{P_{(n+1)}} - \mathbf{P_{(n)}}$, and the subscript (n) denotes the n^{th} load step. The global displacements are then converted to elemental displacements and used to compute the elemental stresses. These in turn lead to new stress stiffening matrices and a new global tangent stiffness, and the process is repeated for the next load step.

The disadvantage of this technique is that the incremental displacements obtained from eqn. (2.156) are not exact. Accordingly, the elemental stresses determined from these displacements are not compatible with the prescribed external loading and the tangent stiffness derived for the next load step will be inaccurate. For mild nonlinearity the discrepancies will generally be acceptably small, but even then it is necessary to use small load steps to avoid severe divergence of the solution such as that seen in figure 2.11.

One solution to this problem is to perform iterations at each load step to converge on the correct displacement for the applied load. A common choice is the Newton-Raphson scheme. Having computed an approximate displacement solution in the manner already described, the corresponding forces are determined from the nonlinear stiffness function:

$$\mathbf{\Delta u_{(n,i)}} = \mathbf{K_{T(n,i)}}^{-1}\mathbf{\Delta P_{(n,i)}} \tag{2.157}$$

$$\mathbf{P_{(n,i+1)}} = \mathbf{f_K}(\mathbf{u_{(n,i+1)}}). \tag{2.158}$$

where the subscript (n, i) denotes the i^{th} iteration at the n^{th} load step. This gives a new estimate of the force error for this load step, so instead of moving on to the next load step, another iteration is

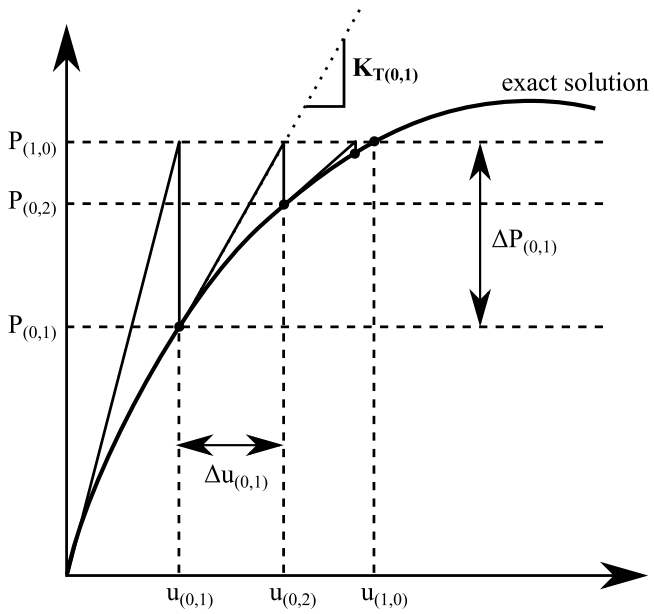

Figure 2.12: Newton-Raphson iterations over one load step in a non-linear static analysis.

performed at this load step using

$$\mathbf{\Delta P_{(n,i+1)}} = \mathbf{P_{(n+1,0)}} - \mathbf{P_{(n,i+1)}}. \tag{2.159}$$

Two versions of the technique can be used: the standard Newton-Raphson approach is to re-evaluate the tangent stiffness at each iteration. This method is seen in figure 2.12. Another option is to retain the same tangent stiffness over the course of one load step, referred to as the *modified* Newton-Raphson method, and illustrated in figure 2.13. The convergence of the solution is judged on the size of the residual displacements, $\mathbf{\Delta u}$, the residual forces, $\mathbf{\Delta P}$, or a combination of the two. One these are deemed small enough, the next load step is initiated by

$$\mathbf{u_{(n,0)}} = \mathbf{u_{(n-1,I)}} \tag{2.160}$$

$$\mathbf{\Delta P_{(n,0)}} = \mathbf{P_{(n+1,0)}} - \mathbf{P_{(n,0)}} \tag{2.161}$$

where I is the final iteration from the previous load step and the target force vectors $\mathbf{P_{(n,0)}}$ are predefined by the load steps.

At first glance the incremental method would seem the least demanding scheme, but in order to achieve accurate results it is necessary to perform many small load steps to get to the desired load. In contrast, the Newton-Raphson schemes can use much larger (and thus fewer) load steps but need to perform successive iterations at each step. Similarly, the modified Newton-Raphson method offers the benefit of fewer stiffness matrix assembly operations (including the demanding inversion process), but this comes at the cost of a greater number of iterations for a given load step increment. All of these factors need to be balanced to determine the most effective approach. Cook [163] considers all of the methods described here along with a few other variants, as well as touching on the problems of

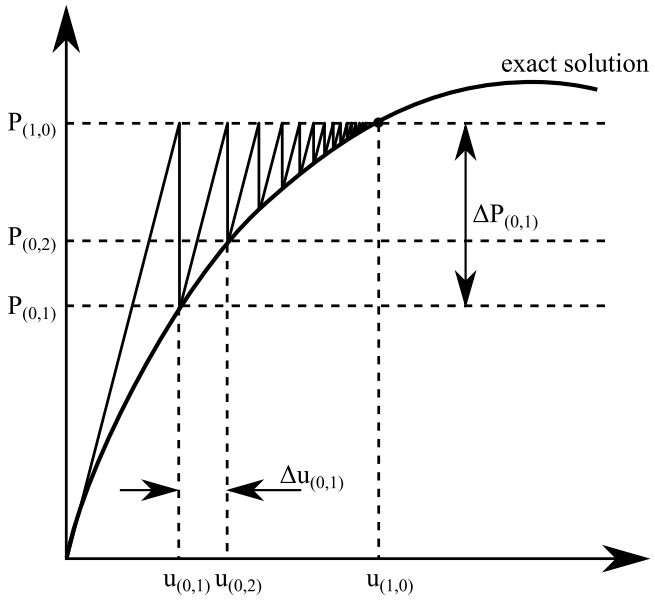

Figure 2.13: Modified Newton-Raphson iterations over one load step in a non-linear static analysis.

post-buckling behaviour and path dependancy.

Initial Perturbations

As mentioned already there are some structures, notably pinned trusses, which will theoretically show no transverse deflections in their members until the buckling load is reached. This behaviour is non-physical as imperfections, residual stresses, and misalignments of joints and loading will produce more gradual buckling characteristics, deforming the structure at forces below the Euler buckling load. When performing a full analytical nonlinear analysis, Zienkiewicz [182, p. 514] discusses the common practice of introducing small perturbations to beams and shells to initiate the deformations.

2.5 Modal Testing

This section will examine a variety of experimental approaches with a strong emphasis on modal parameter extraction. The hardware and general approach are described first, before detailing the mathematical postprocessing of the measured data.

2.5.1 Equipment and Methodology

All of the methods employed herein rely on some form of external excitation applied at one or more locations around the structure. One set of tests in this thesis uses hammer excitation. For the remainder of the tests the excitation is applied by means of a shaker. This electromechanical apparatus provides a uniaxial translational excitation prescribed by the supply from a power amplifier. This in

turn is controlled by a signal from a hardware signal generator or an analogue output from a digital computer. The shaker is connected to the test rig using a thin push rod called a *stinger*. At the attachment point, a force transducer is employed to measure the forces input to the structure. The stinger is designed to be stiff along its axis, allowing the transmission of loads from the shaker, but flexible in transverse directions, so as to minimise the effects from unmeasured external forcing. When using a hammer as excitation, the main consideration is the choice of tip. A force transducer is integrated into the hammer or connected between the hammer and the tip, and this can measure the excitation spectrum. The flexibility of the tip will influence the energies input to the structure at different frequencies and it is important that the frequency band of interest is covered by the excitation and that there are no 'dead spots'.

Measurements of the structural response can be made with a variety of equipment. Strain gauges are popular for their simplicity and low cost. In their most common form these are metal foils which must be bonded to a surface. The resistance of the gauge changes with the strain of the surface, making them suitable for measuring bending and axial or in-plane vibrations. Measurements of the resistance are usually made with a Wheatstone Bridge, and some common configurations are discussed in appendix B.

Another popular sensor is the accelerometer; these typically incorporate piezo-ceramic elements where the voltage across the crystals varies according to their compression. Small masses connected to the piezoelectric element cause compression and tension as the base undergoes acceleration. Piezo-ceramic force transducers operate in a similar manner. Accelerometers must be chosen according to the desired frequency measurement range as the masses and crystals are tuned to respond well within certain frequency bands. The output of an accelerometer can take one of four common forms:

- charge output
- IEPE output
- voltage output
- current output

Charge output accelerometers directly output the charge generated by the piezoelectric crystal. A charge amplifier is required to measure this output and the wiring connecting the sensor to the amplifier should be kept to a minimum due to the high output impedance.

Integrated Electronics Piezo Electric (IEPE) accelerometers, also known by the trade-name ICP, are a class of accelerometers that have built in electronics. Specifically, they use a two-wire system with a DC bias from which the electronics draw their power. The output is low-impedance and IEPE accelerometers are suited to uses where long cabling is required. Presently they are prevalent wherever high temperatures and low frequencies are not a concern. The DC bias must be filtered out of the signal, and this job is typically performed by the same hardware that supplies the power. Often this hardware also performs signal conditioning in the form of bandpass filtering and amplification.

Voltage and current output accelerometers also contain integrated electronics but these have separate power supply lines. It is common for current outputs to span a range of 4-20mA where 4mA is the zero reading; this serves as a safeguard against broken connections, which would produce a conspicuous lack of current. Current output sensors are commonly used in the process industry, where the 4-20mA output forms a standard interface.

The mounting of accelerometers should be given some attention, as the rigidity of the attachment affects the response of the accelerometer. While these sensors are designed to have a flat response within their operating range, their response inevitably drops off for low frequencies and reaches a resonance at high frequencies. A flexible mounting lowers the resonant frequency of the accelerometer and narrows its effective bandwidth. In particular, magnetic attachments allow a great deal of flexibility while threaded stud fittings provide the stiffest possible mounting.

Non-intrusive response measurements can also be made: laser doppler vibrometry provides velocity measurements and laser interferometry and stereoscopic imaging both provide displacement measurements. The latter captures high speed video frames from two separate cameras, the positions of which have been carefully calibrated. These images may be used to triangulate the position of recognisable features on a surface. Often the surface is sprayed with mottled colours to provide texture for the image processing algorithms to work with. There is no theoretical limit to the spatial discretisation of the measurements provided the points may be distinguished from the images. In contrast, the laser methods require that the lasers be directed at the point of measurement. Multiple measurements require multiple lasers or a scanning laser which can be programmed to target a set of measurement points in sequence. Continuous scanning methods are now also being developed where the laser measures a complete path rather than a set of points [183].

Nowadays the data processing is almost always performed on a digital computer. The analogue measurements are fed into an analogue-to-digital converter (ADC) and recorded in the computer. In these cases, it is critical that the pre-ADC amplification is adjusted correctly. Too much amplification will saturate the ADC and thus clip the measured response. Too little amplification results in unnecessary discretisation of the signal level. While this may seem insignificant on modern ADCs which often exceed 16 bits (65536 discrete points), figure 2.14 shows the dramatic effect of a fourfold decrase in the number of discretisation points on an FRF produced with an 8 bit ADC.

The purpose of testing is to identify the response of the test rig to a given excitation. Usually the desired result is the harmonic frequency response in a given range. Many different experimental approaches are available, characterised by their excitation patterns. They can be classified according to the processing methodology they demand as periodic, transient, or random. Countless variations on these are considered in the modal analysis textbooks [162, 169] but this thesis uses only three: hammer tests (transient), stepped sinusoidal (periodic) and broadband random excitation. Stepped sinusoidal excitation is the odd one out, in that it aims to excite a single frequency at a time, settling on steady response conditions before measuring the response. The other two both excite the full test frequency range at once, processing the response to give a frequency curve. In terms of processing,

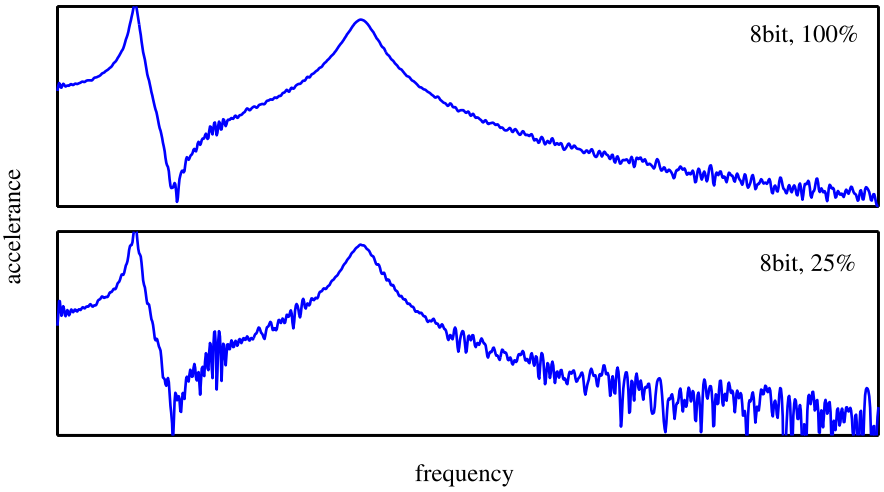

Figure 2.14: An FRF produced from an ideal impulse response for a system with two natural frequencies. The time domain signal has been discretised to 8 bits, and the figures show the increase in noise levels when only 25% of the 8 bit range is used compared to 100%.

however, the sinusoidal method is closely related to the transient hammer test, with the random excitation requiring special consideration.

If the ultimate purpose of the test is to estimate modal characteristics, they can be estimated either from the frequency response curves described above or from time domain data. Both methods are discussed in section 2.5.4.

2.5.2 Fourier Analysis

Fourier transforms are used to convert time-domain data to the frequency domain and vice versa. As such they are pervasive in vibration studies. The principle is outlined in many text books, for example refereces [162, 169, 184, 161], and is based on the premise that any periodic signal $x(t)$ may be split into an infinite series of harmonic components. It can then be represented as

$$x(t) = \sum_{n=-\infty}^{\infty} X_n e^{i\omega_n t} \tag{2.162}$$

where X_n are the complex Fourier coefficients given by

$$X_n = \frac{1}{T}\int_0^T x(t)e^{-i\omega_n t}dt \tag{2.163}$$

and ω_n are the frequencies of the harmonic components with common period T. The technique may be generalised to non-periodic signals provided the condition

$$\int_{-\infty}^{\infty} |x(t)|dt < \infty \tag{2.164}$$

is satisfied. The Fourier transform and its inverse can then be defined respectively as

$$x(t) = \int_{-\infty}^{\infty} X(\omega) e^{i\omega t} d\omega \tag{2.165}$$

and

$$X(\omega) = \frac{1}{2\pi} \int_{-\infty}^{\infty} x(t) e^{-i\omega t} dt. \tag{2.166}$$

The function pairings will be indicated with the shorthand notation

$$x(t) \Longleftrightarrow X(\omega). \tag{2.167}$$

One property of the transform will be examined here, partly as it is used later in this chapter, but maily because its derivation in many textbooks is either incomplete or entirely absent. To compound these problems, many of the Fourier integral tables encountered by the author misquote the formula. The property is that of scaling. If a function $f(t)$ is scaled time-wise by factor a, so that $g(t) = f(at)$, the Fourier transform is given by

$$G(\omega) = \frac{1}{2\pi} \int_{-\infty}^{\infty} f(at) e^{-i\omega t} dt. \tag{2.168}$$

Substituting $u = at$ for positive a yields

$$G(\omega) = \frac{1}{a} \frac{1}{2\pi} \int_{-\infty}^{\infty} f(u) e^{-i(\omega/a)u} \, du \tag{2.169}$$

$$= \frac{1}{a} F\left(\frac{\omega}{a}\right) \tag{2.170}$$

but, when $a < 0$, the sign of the limits on the integral are reversed so that

$$G(\omega) = \frac{-1}{a} F\left(\frac{\omega}{a}\right). \tag{2.171}$$

Thus it should be written

$$G(\omega) = \frac{1}{|a|} F\left(\frac{\omega}{a}\right) \tag{2.172}$$

and this means that

$$f(at) \Longleftrightarrow \frac{1}{|a|} F\left(\frac{\omega}{a}\right). \tag{2.173}$$

For experimentally aquired data it is often not possible to obtain a signal satisfying eqn. (2.164). Frequently the data will simply be a sample of fixed period from a continuous stream of data. In these circumstances the raw data will produce an effect known as *leakage* where the signal is clipped at either end. This leakage manifests itself as a distortion of the true frequency content of the signal. A common technique is to window the data before appling the Fourier transform, multiplying the signal

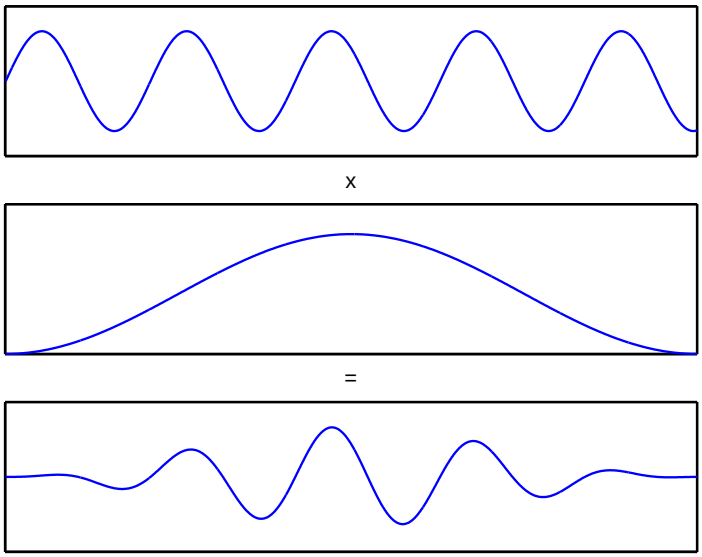

Figure 2.15: Example of a Hanning window applied to a sine signal to produce a signal with similar frequency content but that satisfies the conditions for the Fourier transform.

by a windowing function such as a Hanning window, shown in figure 2.15. The results from windowed data such as these are more representative of the true frequency content of the signal, particularly where the data are collected over short time periods. The results must, however, be rescaled to compensate for the windowing except where the frequency data is intended soley for comparison with another signal undergoing the same windowing, for example in the FRF computations described later.

Another form of conditioning which must be applied prior to the Fourier transform is filtering. The reason for this is an effect known as aliasing, where the computed response curve is comprised of the sum of the true curve and its reflection about the centre of the sampled frequency range. A low pass analogue filter applied before the sampling stage will remedy this artefact.

For more details on the Fourier transform and the appropriate signal conditioning, the reader is referred once again to texts such as Ewins [162], Maia *et al.* [169] and Lathi [184] for a fuller description. Noteworthy variations on the Fourier transform include the *discrete Fourier transform* (DFT), where the continuous functions above are adapted for use with discrete data samples, and the *fast Fourier transform* (FFT), which employs a more efficient algorithm for fast computation of the Fourier coefficients. The latter has an interesting history of discovery and re-discovery in various scientific fields [185–187]. The application of the FFT in conjuction with a windowing function is often referred to as the *short-time fast Fourier transform* (ST-FFT).

2.5.3 Signal Processing

Of the three test methods discussed, the stepped sinusoidal is the most intuitive. The structure is excited at a series of single harmonic frequencies in turn and the response allowed to settle to a steady state before measuring each response. At its simplest the analysis could proceed by measuring the

ratio of the peak amplitudes but a slightly more sophisticated approach is usually taken. Knowing the excitation period at each step, an integer number of periods are recorded for the excitation and response. The latter is also assumed to consist solely of a single frequency harmonic signal corresponding with a linear response to the excitation. A straightforward DFT may then be applied to both datasets without windowing, where only the complex coefficient of the Fourier series that corresponds with the excitation frequency need be derived (strictly this is a Fourier *series* expansion and not a Fourier *transform*). This coefficient conveys both the magnitude and phase of the frequency response. Each frequency is tested and processed in turn, providing the complete frequency response curve.

The test parameters that must be considered for a stepped sine test are the frequency range and the spectral resolution. The corresponding sinusoids are used as excitation signals. The test operator must also decide on the settling time to be allowed after each frequency step, the length of the samples (or the number of periods) to be captured, and an appropriate sampling frequency. When using Fourier transforms, the sampling frequency must be greater than the Nyquist frequency: twice the frequency of the signal to be measured. For a manual peak ratio comparison a much finer resolution will be necessary to identify the true magnitude of the signals.

Impact tests follow a similar procedure but with some important differences. Firstly, and fundamentally, the excitation of all frequencies of interest is performed simultaneously. The conversion from the time to frequency domains is made using the full DFT and in this case the Fourier transform dictates that the two signals should go to zero as $t \to \pm\infty$. This is more or less true for a transient hammer blow but often an exponentially decaying window is employed to reduce the sample time. Because of the variable nature of hammer impacts, particularly those administered by hand, it is good practice to average the frequency domain data over several runs. The operator should select an appropriate number of averages according to the test conditions; the coherence, discussed later, is a useful indicator of the quality of the results. Similarly, individual runs may be excluded from the average if they are inferior. This rejection could be based on a poor coherence or inadequate coverage of the frequency band of interest by the excitation signal. The latter can be determined by the input power spectral density, also discussed later.

Parameters that must be considered prior to a hammer test, in addition to the number of averages and the windowing function, are once again the frequency band and the spectral resolution. Generally speaking, the the highest measurable frequency will be half the sampling frequency. In practice, aliasing effects will corrupt the signal at the high end of this range due to the imperfect nature of the pre-transform filtering. The spectral resolution determines the sample length: the frequency interval will be inversely proportional to the sampling time.

The random excitation method is rendered more complicated as this type of excitation violates the requirements of the Fourier transform: the measured response is not due entirely to the measured excitation but also to that which has gone before. The redress to this obstacle is detailed in the data processing sections below, but despite the added computational complexity the method is the fastest

and most versatile of the three described. It is also well suited to automated testing as will prove useful in chapter 7. As with the hammer test, the sampling frequency and sample length must be chosen to match the frequency band and spectral resolution. Once again it is common to use the average of several runs but now there is also the option of allowing the sample sets to overlap, reducing the time taken and the data storage required.

With all of the above methods, the FRFs may be determined for various combinations of excitation and response points. Where mode shape data is needed, it is not merely possible: it is essential that a distribution of FRFs are available. Because of the symmetrical nature of the FRF matrix, it is equally viable to use a single excitation point with multiple measurement points or multiple excitation points with a single measurement point. The latter option is particularly useful where equipment is limited and a hammer test is to be performed.

Correlation Functions

Recognising that random excitation data can not be used directly in the Fourier transform, there is a need for signals with the same spectral content but which satisfy the conditions of the DFT. Such signals are found in the *correlation functions*. The *autocorrelation* gives the expected value of the product of the signal and one leading it by time τ:

$$R_{ff}(\tau) = E[f(t) \cdot f(t+\tau)] \tag{2.174}$$

where $f(t)$ is the excitation force signal and the subscript ff indicates the force autocorrelation. The corresponding equation for the displacement signal is

$$R_{xx}(\tau) = E[x(t) \cdot x(t+\tau)] \tag{2.175}$$

and the *cross correlations* can be defined

$$R_{xf}(\tau) = E[x(t) \cdot f(t+\tau)] \tag{2.176}$$

$$R_{fx}(\tau) = E[f(t) \cdot x(t+\tau)]. \tag{2.177}$$

If the signals and their associated processes are assumed to be ergodic then eqns. (2.174–2.177) can be written

$$R_{ff} = \lim_{T\to\infty} \frac{1}{T-\tau} \int_0^{T-\tau} f(t) \cdot f(t+\tau)\, dt \tag{2.178}$$

$$R_{xx} = \lim_{T\to\infty} \frac{1}{T-\tau} \int_0^{T-\tau} x(t) \cdot x(t+\tau)\, dt \tag{2.179}$$

$$R_{xf} = \lim_{T\to\infty} \frac{1}{T-\tau} \int_0^{T-\tau} x(t) \cdot f(t+\tau)\, dt \tag{2.180}$$

$$R_{fx} = \lim_{T\to\infty} \frac{1}{T-\tau} \int_0^{T-\tau} f(t) \cdot x(t+\tau)\, dt. \tag{2.181}$$

In practice only short time signals are available and as the sample time, T, is reduced from infinity the results obtained with the above equations become estimates of the correlations. As with the Fourier transform itself, windowing can improve the accuracy of the correlation functions on short samples. Most commonly, the windowing is applied to the output of the functions instead of the input, weighting the most accurate high-frequency information at the start of the data stream and discarding the less accurate low-frequency information towards the end. In either case, the importance is that the results can now be processed with the Fourier transform.

Power Spectral Densities

Taking the Fourier transform of the autocorrelation functions produces an indication of the spectral content of the original signals, much as the Fourier transform does on its own for periodic signals. The resultant function is called the auto-spectral density, or power-spectral density (PSD):

$$S_{xx}(\omega) = \frac{1}{2\pi}\int_{-\infty}^{\infty} R_{xx}(\tau)e^{-i\omega\tau}\,d\tau \tag{2.182}$$

$$S_{ff}(\omega) = \frac{1}{2\pi}\int_{-\infty}^{\infty} R_{ff}(\tau)e^{-i\omega\tau}\,d\tau. \tag{2.183}$$

Lathi [184] describes how an autocorrelation is equivalent to a convolution with one of the time sequences negated:

$$R_{xx}(\tau) = x(\tau) * x(-\tau) \tag{2.184}$$

where $*$ is the convolution operator. He shows that a convolution in the time domain corresponds with a multiplication in the frequency domain, and the scaling property gives $x(-t) \Longleftrightarrow X(-\omega)$ so that

$$S_{xx}(\omega) = X(\omega)\cdot X(-\omega) \tag{2.185}$$

$$= X(\omega)\cdot X^*(\omega) \tag{2.186}$$

$$= |X(\omega)|^2. \tag{2.187}$$

From this equation the nomenclature of the PSD is explained: it gives the spectral breakdown of the power in the signal. It is also conspicuous that the autocorrelation operation has removed the phase information from the original data. The texts by Inman [188], Meirovitch [161] and Maia et al. [169] express the displacement in terms of the convolution of the impulse response and the excitation force,

$$x(t) = h(t) * f(t) \tag{2.188}$$

so that

$$R_{xx}(\tau) = h(\tau) * f(\tau) * h(-\tau) * f(-\tau) \tag{2.189}$$

$$= h(\tau) * h(-\tau) * f(\tau) * f(-\tau). \tag{2.190}$$

Noting that the Fourier transform of the impulse response is the FRF, $h(t) \Longleftrightarrow H(\omega)$,

$$\begin{aligned} S_{xx}(\omega) &= H(\omega) \cdot H^*(\omega) \cdot S_{ff}(\omega) \\ &= |H(\omega)|^2 \cdot S_{ff}(\omega). \end{aligned} \tag{2.191}$$

Using this equation the magnitude of the response function can be reconstructed from the PSDs of the excitation and response signals. To determine the phase, further quantities are needed and these are provided in the form of the cross-spectral densities (CSDs):

$$S_{xf}(\omega) = \frac{1}{2\pi} \int_{-\infty}^{\infty} R_{xf}(\tau) e^{-i\omega\tau} \, d\tau \tag{2.192}$$

$$S_{fx}(\omega) = \frac{1}{2\pi} \int_{-\infty}^{\infty} R_{fx}(\tau) e^{-i\omega\tau} \, d\tau. \tag{2.193}$$

Following an analogous procedure to that of the auto-spectral densities above, it can be shown that

$$S_{fx}(\omega) = H(\omega) \cdot S_{ff}(\omega) \tag{2.194}$$

$$S_{xx}(\omega) = H(\omega) \cdot S_{xf}(\omega). \tag{2.195}$$

FRFs

From eqns. (2.191), (2.194) and (2.195) it is possible to produce two estimates of the receptance, referred to as H_1 and H_2. The first of these is the most widely adopted[1], given by

$$H_1(\omega) = \frac{S_{fx}(\omega)}{S_{ff}(\omega)}. \tag{2.196}$$

The second estimate is

$$H_2(\omega) = \frac{S_{xx}(\omega)}{S_{xf}(\omega)}. \tag{2.197}$$

Where the measurement signals are contaminated, the two estimates are affected in different manners: close to resonance the input forces are low and the force autocorrelation S_{ff} is susceptible to noise. Thus, H_1 estimates will be less accurate at resonance. In contrast, at antiresonance the displacements will be small and the displacement autocorrelation S_{xx} will suffer. Consequently, H_2 produces inferior estimates at antiresonance. In any case, the agreement between the two estimates provides a useful measure of their accuracy. Specifically, disagreement will provide a definitive indicator of inaccuracies in at least one of the estimates, while agreement serves to improve confidence in the results. The ratio of the two functions is called the coherence,

$$\gamma^2(\omega) = \frac{H_1(\omega)}{H_2(\omega)} \tag{2.198}$$

and values of unity are desirable. Values significantly below zero indicate one of two things: either there is noise on the measurement signals, or one or more of the assumptions made above is inadequate.

[1] Ewins [162] suggests the popularity of H_1 over H_2 is due to its marginal advantage with respect to computability.

The exception to this rule is at the poles and zeros of the system, where one or other of the estimates will always tend to exhibit inaccuracies, even with high fidelity data.

2.5.4 Modal Parameter Extraction

Many and varied techniques exist for estimating the modal properties of a system based on vibration test data. Some of these analyses are based in the frequency domain, using the FRFs derived in the previous section, while others use time domain data; this takes the form of the impulse response functions, obtained from the inverse Fourier transforms of the FRFs. In this section a few of the most intuitive methods, based on single degree of freedom (SDOF) assumptions, are reviewed before examining some more sophisticated multiple degree of freedom (MDOF) methods. Allemang and Brown present an analysis of the similarities and differences between many of the techniques [189].

SDOF methods

Single degree of freedom methods rely on the assumption that, at resonance, the behaviour of the structure is dominated by a single mode. Thus the properties of that mode may be estimated by neglecting the influence of the other modes and performing the analysis as per a single DOF system in that locality. The obvious drawback of this approach is its difficulty in processing data from systems with closely spaced modes. Two methods are described here: peak picking and circle fitting, both of which are based on frequency domain data.

Peak picking involves locating the resonant frequencies of the system using the peaks in the FRF magnitude. This step is often performed using the sum of a series of FRFs for response and excitation points located around a structure. For a given mode the peak magnitude, $|H_{jk}|_{max}$, is determined, locating the natural frequency ω_r. The *half-power points* are then established as the two points either side of the peak where the magnitude is $|H_{jk}|_{max}/\sqrt{2}$. Their separation gives an indication of the damping. If the frequencies at these points are denoted ω_a and ω_b, then the damping ratio is given by

$$\eta = \frac{\omega_b^2 - \omega_a^2}{2\omega_r} \tag{2.199}$$

$$\zeta = \frac{\eta}{2}. \tag{2.200}$$

Finally, the mode shapes are defined by the modal constants. From eqn. (2.108) these can be calculated for each FRF as

$${}_rA_{jk} = \omega_r^2 \eta |H_{jk}|_{max}. \tag{2.201}$$

The method assumes proportional damping and thus the computed mode shapes will always be real; this result is inevitable because the phase of the FRF is not used in the analysis. A further drawback is that there is no curve-fitting, so an accurate estimate of the natural frequency is dependent upon good spectral resolution in the frequency domain. More importantly, the measured peak amplitude

for lightly damped systems will be particularly sensitive to the spectral alignment.

The next method considered is a curve-fitting technique performed in the Nyquist, or complex, plane. As seen in figure 2.2(b), the FRF for a single DOF system forms a circle passing through the origin in the Nyquist plane. The first step in the process is to obtain the circular least squares fit for the measured data. Once this is found the path is characterised by the circle's diameter, the polar coordinates of its centre with respect to the origin, and the sweep rate $d\theta/d\omega$ which varies along the arc. The natural frequency is located as the point of maximum sweep rate. The modal damping ratio may be estimated from the maximum sweep rate but this can be inaccurate. A preferred method is to chose two points either side of the natural frequency and apply a generalised version of eqn. (2.199),

$$\eta = \frac{\omega_b^2 - \omega_a^2}{\omega_n^2 \left(\tan(\theta_a/2) + \tan(\theta_b/2)\right)} \tag{2.202}$$

where ω_a and ω_b are now any sensible choice of frequencies either side of the natural frequency, and θ_a and θ_b are the angles subtended in going from ω_a to ω_n and ω_n to ω_b respectively. Finally, the magnitude and argument of the complex modal constant can be identified from the diameter and orientation of the circle:

$$|A_{jk}| = D\omega_n^2\eta \tag{2.203}$$

$$\angle A_{jk} = \angle C_0 \tag{2.204}$$

where D is the diameter and C_0 is the centre of the circle. Evaluation of the modal constants for a range of FRFs allows the determination of the complex mode shapes. In practice, the circumference of the circle may be offset from the origin, indicating the influence of other modes. The above procedure may be adapted to account for this offset while broadly following the same steps.

A more in-depth explanation of these techniques is given in references [162, 169, 188], along with the derivations of the damping formulae stated above.

MDOF methods

Multiple degree of freedom methods attempt to account for the influence of all the modes simultaneously, producing estimates of each of their properties with a single (albeit sometimes protracted) computation. Methods in both the time and frequency domain are common.

For examples of frequency domain methods a reader could consult Ewins [162] about the non-linear least squares (NLLS) and rational fraction polynomial (RFP) methods [190], the latter of which formed something of a benchmark for MDOF methods, as well as what has become known as the Ewins-Gleeson method [191] for lightly damped structures. Maia *et al.* [169] build on this selection with the complex exponential frequency domain (CEFD) method [192] and a wide range of variations on these schemes. Peeters *et al.* discuss an extension of the CEFD method which has found recent

popularity, known as PolyMAX [193].

The above methods are referred to as single input single output (SISO) methods, as they can be applied to single FRFs. Where multiple FRFs are available, it is often desirable to incorporate them all into the analysis to average out any errors in the data. The resultant procedures are categorised as either single input multi output (SIMO), multi input single output (MISO) or multi input multi output (MIMO). Where modes are extremely closely spaced, or even coincident, it is impossible to determine the modal characteristics from SISO methods and one of the aforementioned categories must be employed; these are known collectively as *global* methods. The CEFD and RFP methods cited above may be extended to global methods in the form of the polyreference frequency domain (PRFD) and global rational fraction polynomial (GRFP) methods [194, 195].

Time domain techniques are equally numerous, and the modal analysis texts describe the Ibrahim time domain (ITD) method [196], the eigensystem realisation algorithm (ERA) [197], the complex exponential (CE) method [198] and its global extensions in the form of the least-squares complex exponential (LSCE) and polyreference complex exponential (PRCE) methods [199, 200]. Only one of these methods will be discussed here, as it is the one used for all of the modal identification in this thesis. It is the technique adopted by the proprietary LMS software, and it is the algorithm that has been incorporated into the author's own MATLAB code. It is the LSCE method, and its description here mirrors that found in the standard texts.

The explanation will begin with the simple CE method, as the extension to the LSCE is trivial. The first step in the process is to formulate the impulse response function (IRF) as the inverse Fourier transform (IFT) of the FRF. A fundamental premise behind modal analysis is that the principle of superposition holds true. As such, the impulse response may be expressed as a summation of the individual modal responses. Taking the IFT of eqn. (2.108) yields

$$h_{jk}(t) = \sum_{r=1}^{2N} {}_rA_{jk} e^{\lambda_r t}. \tag{2.205}$$

Substituting $t = \ell\Delta t$, $h_{jk}^{(\ell)} = h_{jk}(\ell\Delta t)$ and $V_r = e^{\lambda_r \Delta t}$ produces

$$\begin{aligned} h_{jk}^{(0)} &= \sum_{r=1}^{2N} {}_rA_{jk} \\ h_{jk}^{(1)} &= \sum_{r=1}^{2N} {}_rA_{jk} V_r \\ h_{jk}^{(2)} &= \sum_{r=1}^{2N} {}_rA_{jk} V_r^2 \\ &\vdots \quad \vdots \\ h_{jk}^{(L)} &= \sum_{r=1}^{2N} {}_rA_{jk} V_r^L. \end{aligned} \tag{2.206}$$

This set of equations can be solved using Prony's method [201]. First, a polnomial equation is defined

as

$$\beta_0 + \beta_1 V_r + \beta_2 V_r^2 + ... + \beta_L V_r^L = 0 \tag{2.207}$$

where it can be shown that constant real coefficients $\beta_0..\beta_L$ can be found to satisfy any V_r. Next, eqns. (2.206) are multiplied by the coefficients and summed to produce

$$\sum_{a=0}^{L} \beta_a h_{jk}^{(a)} = \sum_{a=0}^{L} \left(\beta_a \sum_{r=1}^{2N} {}_r A_{jk} V_r^a \right). \tag{2.208}$$

Rearranging gives

$$\sum_{a=0}^{L} \beta_a h_{jk}^{(a)} = \sum_{r=1}^{2N} {}_r A_{jk} \left(\sum_{a=0}^{L} \beta_a V_r^a \right) \tag{2.209}$$

and recognising that the rightmost sum is the polynomial from eqn. (2.207),

$$\sum_{a=0}^{L} \beta_a h_{jk}^{(a)} = 0. \tag{2.210}$$

Setting $L = 2N$ and using $(2N - 1)$ consecutive overlapping datasets from the IRF, a set of simultaneous equations are formulated from eqn. (2.210) and these can be expressed in matrix form as

$$\begin{bmatrix} h_{jk}^{(0)} & h_{jk}^{(1)} & h_{jk}^{(2)} & \dots & h_{jk}^{(2N)} \\ h_{jk}^{(1)} & h_{jk}^{(2)} & h_{jk}^{(3)} & \dots & h_{jk}^{(2N+1)} \\ h_{jk}^{(2)} & h_{jk}^{(3)} & h_{jk}^{(4)} & \dots & h_{jk}^{(2N+2)} \\ \vdots & \vdots & \vdots & \ddots & \vdots \\ h_{jk}^{(2N-1)} & h_{jk}^{(2N)} & h_{jk}^{(2N+1)} & \dots & h_{jk}^{(4N-1)} \end{bmatrix} \begin{Bmatrix} \beta_0 \\ \beta_1 \\ \beta_2 \\ \vdots \\ \beta_{2N} \end{Bmatrix} = \mathbf{0}. \tag{2.211}$$

Arbitrarily setting $\beta_{2N} = 1$ produces

$$\begin{bmatrix} h_{jk}^{(0)} & h_{jk}^{(1)} & h_{jk}^{(2)} & \dots & h_{jk}^{(2N-1)} \\ h_{jk}^{(1)} & h_{jk}^{(2)} & h_{jk}^{(3)} & \dots & h_{jk}^{(2N)} \\ h_{jk}^{(2)} & h_{jk}^{(3)} & h_{jk}^{(4)} & \dots & h_{jk}^{(2N+1)} \\ \vdots & \vdots & \vdots & \ddots & \vdots \\ h_{jk}^{(2N-1)} & h_{jk}^{(2N)} & h_{jk}^{(2N+1)} & \dots & h_{jk}^{(4N-2)} \end{bmatrix} \begin{Bmatrix} \beta_0 \\ \beta_1 \\ \beta_2 \\ \vdots \\ \beta_{2N-1} \end{Bmatrix} = - \begin{Bmatrix} h_{jk}^{(2N)} \\ h_{jk}^{(2N+1)} \\ h_{jk}^{(2N+2)} \\ \vdots \\ h_{jk}^{(4N-1)} \end{Bmatrix} \tag{2.212}$$

which can be solved for the coefficients β_a by inverting the IRF matrix:

$$\begin{Bmatrix} \beta_0 \\ \beta_1 \\ \beta_2 \\ \vdots \\ \beta_{2N-1} \end{Bmatrix} = - \begin{bmatrix} h_{jk}^{(0)} & h_{jk}^{(1)} & h_{jk}^{(2)} & \dots & h_{jk}^{(2N-1)} \\ h_{jk}^{(1)} & h_{jk}^{(2)} & h_{jk}^{(3)} & \dots & h_{jk}^{(2N)} \\ h_{jk}^{(2)} & h_{jk}^{(3)} & h_{jk}^{(4)} & \dots & h_{jk}^{(2N+1)} \\ \vdots & \vdots & \vdots & \ddots & \vdots \\ h_{jk}^{(2N-1)} & h_{jk}^{(2N)} & h_{jk}^{(2N+1)} & \dots & h_{jk}^{(4N-2)} \end{bmatrix}^{-1} \begin{Bmatrix} h_{jk}^{(2N)} \\ h_{jk}^{(2N+1)} \\ h_{jk}^{(2N+2)} \\ \vdots \\ h_{jk}^{(4N-1)} \end{Bmatrix}. \tag{2.213}$$

Once the coefficients are known, a polynomial solver may be used to obtain the values for V_r from eqn. (2.207) and hence λ_r. Note that the datasets need not necessarily overlap, and need not possess

any particular relationship with respect to one another. It is sufficient that each dataset shares a common time step. It is also not necessary to limit the number of datasets to $(2N-1)$; this number is simply the lower bound and in fact the inclusion of more data sets improves the results to some extent by averaging out noisy data. Furthermore, it is noted that every FRF from the system should share common poles, and thus common values for V_r and common coefficients β_a. Thus datasets from different IRFs may be combined in eqn. (2.213) to obtain the poles and modal damping ratios. The only change in methodology is that now instead of an ordinary matrix inversion as used in eqn (2.213), a pseudoinverse must be performed to fit the solution to the redundant data sets. This variation on the technique is what is referred to as the least squares complex exponential method, so called because the pseudo-inverse produces a least-squares approximation to the solution.

The real and imaginary parts of the complex values λ_r determine the damping ratios and natural frequencies of the modes respectively. With knowledge of the values V_r, the mode shapes may be computed as follows. Putting eqn. (2.206) in matrix form gives

$$\begin{bmatrix} 1 & 1 & 1 & \dots & 1 \\ V_1 & V_2 & V_3 & \dots & V_{2N} \\ V_1^2 & V_2^2 & V_3^2 & \dots & V_{2N}^2 \\ \vdots & \vdots & \vdots & \ddots & \vdots \\ V_1^{2N-1} & V_2^{2N-1} & V_3^{2N-1} & \dots & V_{2N}^{2N-1} \end{bmatrix} \begin{Bmatrix} {}_1A_{jk} \\ {}_2A_{jk} \\ {}_3A_{jk} \\ \vdots \\ {}_{2N}A_{jk} \end{Bmatrix} = \begin{Bmatrix} h_{jk}^{(0)} \\ h_{jk}^{(1)} \\ h_{jk}^{(2)} \\ \vdots \\ h_{jk}^{(2N-1)} \end{Bmatrix} \tag{2.214}$$

and inverting the problem gives the modal constants as

$$\begin{Bmatrix} {}_1A_{jk} \\ {}_2A_{jk} \\ {}_3A_{jk} \\ \vdots \\ {}_{2N}A_{jk} \end{Bmatrix} = \begin{bmatrix} 1 & 1 & 1 & \dots & 1 \\ V_1 & V_2 & V_3 & \dots & V_{2N} \\ V_1^2 & V_2^2 & V_3^2 & \dots & V_{2N}^2 \\ \vdots & \vdots & \vdots & \ddots & \vdots \\ V_1^{2N-1} & V_2^{2N-1} & V_3^{2N-1} & \dots & V_{2N}^{2N-1} \end{bmatrix}^{-1} \begin{Bmatrix} h_{jk}^{(0)} \\ h_{jk}^{(1)} \\ h_{jk}^{(2)} \\ \vdots \\ h_{jk}^{(2N-1)} \end{Bmatrix}. \tag{2.215}$$

Repeating the procedure with IRFs for different response or excitation points, j or k, allows determination of the mode shapes using eqn. (2.107). Another popular technique is, once the poles and damping loss factors are derived with the LSCE method, to apply a least squares frequency domain (LSFD) method to determine the modal constants. The LSFD method is cursorily described by Peeters *et al.* [193]. It is done by adapting eqn. (2.108) to matrix format for discrete frequency intervals $\Delta\omega$ so that

$$\begin{Bmatrix} H_{jk}(\Delta\omega) \\ H_{jk}(2\Delta\omega) \\ H_{jk}(3\Delta\omega) \\ \vdots \\ H_{jk}(n\Delta\omega) \end{Bmatrix} = \begin{bmatrix} {C_{1,1}}^{-1} & {C_{2,1}}^{-1} & \dots & {C_{2N,1}}^{-1} \\ {C_{1,2}}^{-1} & {C_{2,2}}^{-1} & \dots & {C_{2N,2}}^{-1} \\ {C_{1,3}}^{-1} & {C_{2,3}}^{-1} & \dots & {C_{2N,3}}^{-1} \\ \vdots & \vdots & \ddots & \vdots \\ {C_{1,n}}^{-1} & {C_{2,n}}^{-1} & \dots & {C_{2N,n}}^{-1} \end{bmatrix} \begin{Bmatrix} {}_1A_{jk} \\ {}_2A_{jk} \\ \vdots \\ {}_{2N}A_{jk} \end{Bmatrix}. \tag{2.216}$$

where the C is the characteristic polynomial

$$C_{r,n} = \omega_r^2 - (n\Delta\omega)^2 + i\eta_r\omega_r^2. \tag{2.217}$$

Using a pseudo inverse (denoted by $^+$) gives the least squares solution to the modal constants as

$$\begin{Bmatrix} {}_1A_{jk} \\ {}_2A_{jk} \\ \vdots \\ {}_{2N}A_{jk} \end{Bmatrix} = \begin{bmatrix} {C_{1,1}}^{-1} & {C_{2,1}}^{-1} & \dots & {C_{2N,1}}^{-1} \\ {C_{1,2}}^{-1} & {C_{2,2}}^{-1} & \dots & {C_{2N,2}}^{-1} \\ {C_{1,3}}^{-1} & {C_{2,3}}^{-1} & \dots & {C_{2N,3}}^{-1} \\ \vdots & \vdots & \ddots & \vdots \\ {C_{1,n}}^{-1} & {C_{2,n}}^{-1} & \dots & {C_{2N,n}}^{-1} \end{bmatrix}^+ \begin{Bmatrix} H(\Delta\omega) \\ H(2\Delta\omega) \\ H(3\Delta\omega) \\ \vdots \\ H(n\Delta\omega) \end{Bmatrix}. \tag{2.218}$$

The LSCE method is almost entirely automated, and only two aspects of the procedure may be tailored by the analyst:

- which data to use from the IRFs, and how much of it to include (typically the solution will be overdetermined by the measured data)
- how many modes the algorithm should attempt to fit to the data; in other words the order of analytic model that should be generated.

The first item is not usually critical to the solution, and while larger quantities of data help to compensate for noisy measurements, including all the data can produce an ill-conditioned inversion problem. The second item, on the other hand, is important. If too few modes are included then the results will be inaccurate, with some modes omitted from the solution and others distorted to compensate. Attempting to identify too many modes will produce non-existent computational modes which may confuse the results.

There are several possibilities for estimating the most appropriate model order. The first is to determine the rank of the IRF matrix in eqn. (2.213). This will directly give an indication of the model order. Another approach is to reconstruct the IRF from the computed modal properties and integrate the square of the error over the signal length. If this is repeated for increasing model orders then the error should be seen to drop off sharply as the correct order is reached.

Another method that has proved popular is to evaluate the modal properties using a range of model orders, and compare the positions of the poles on a *stabilisation diagram*. The physical modes should be identified at the same frequencies every time, provided the model order is high enough, but computational modes will tend to wander over the diagram. To give further confidence in the physical modes, the damping ratios and mode shapes are compared as well, and only when these stay within defined tolerances from one order to the next are they deemed to have stabilised. The operator may then identify the physical modes from the diagram, where high fidelity data should produce clear lines of stabilised modes, corresponding with the peaks in the overlaid FRF. An example of a stabilisation

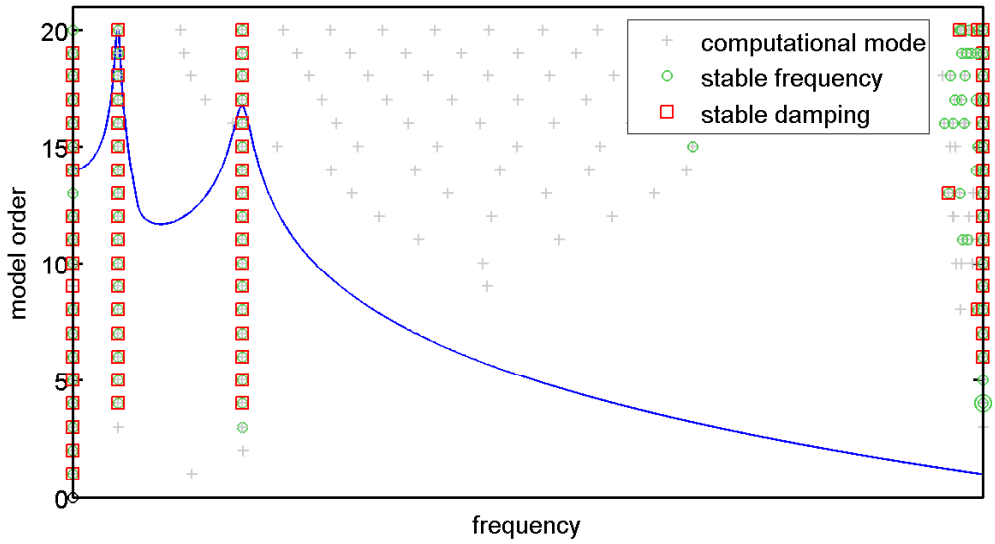

Figure 2.16: Stabilisation diagram for a simulated two DOF system.

diagram for a 2 mode system is seen in figure 2.16, produced using the author's own code. For this demonstration only a single FRF was processed so the stabilisation is based on the frequency and damping but not the mode shape vectors. Nonetheless, the identification of the modes from this simulated response data is unambiguous.

2.6 Data comparison and model validation

Once the analytical model has been computed and the experimental data processed, a means of comparing the two is needed. In fact, the techniques described below will prove useful not only in comparing numerical and physical results but also in comparing different sets of results from the same experiment or model. Three types of data are considered below: FRFs, natural frequencies, and mode shapes.

2.6.1 FRFs

The frequency response functions are perhaps the most obvious candidate for comparisons. Aside from the raw time history data, which is hard to replicate in an analytical model, the FRFs require the least processing of all the results presented above. In this regard, there is the least possibility of computational errors muddling the correlation. The trouble, however, lies in the damping. In analytical models of all but the simplest structures it is difficult to provide sound estimates of the damping. For this reason it is common practice to neglect damping in the creation of analytical models. The utility of an FRF computed without damping is highly questionable in these circumstances, not least because the curve would go to infinity at the resonances. For these reasons, this manuscript

will concern itself only with qualitative FRF comparisons, leaving the rigorous numerical validation of results to the modal data.

2.6.2 Natural Frequencies

The first port of call in results correlation is to compare the natural frequencies. On first inspection this is a trivial matter. Tabulating the results provides an easy comparison of the two mode sets. The two sets of frequencies may be plotted against one another, examples of which are seen in figure 3.9, and good correlation will produce points lying close to a line passing through the origin at 45°. Random deviations from the line are indicative of a poor model or inaccurate measured data. Systematic discrepancies may help to diagnose the problem: for example, if all the points lie on a line passing through the origin at an angle other than 45°, this may be indicative of a global density or Young's modulus error.

A difficulty with this approach is encountered in systems with closely spaced modes. In this case the order of the modes may vary in the two data sets. While the ordering may be easy to determine by inspection of the frequencies alone, it is more usual to correlate the two sets of modes using mode shape comparisons.

2.6.3 Mode Shapes

Realisation

The first thing to be considered in the analysis of experimental mode shapes is how to deal with their complexity. It has already been expalined that analytical models are, generally speaking, undamped. Even where damping is included, the prevalent model is that of proportional damping, producing real mode shapes. In reality all modes will exhibit some level of non-proportional damping and the elements of the experimental mode shape vectors will have differing phases, represented by imaginary components in the mode shapes. If these are to be compared to real analytic modes, they will need to be converted into their real equivalents. Several methods exist, none of which will be discussed in great depth here. This is because the structures considered in this manuscript possess very low and approximately uniform damping, so the phases of the mode shape components do not stray far from one another. The simplest method in this case is to retain only the magnitude and sign of each component and discard the phase information.

Model Expansion and Reduction

The next step in comparing analytic and experimental data is to correlate the DOFs. It is likely that the FE model will be comprised of a large number of DOFs. In contrast, practical considerations tend

to limit the number of DOFs that are measured on a physical specimen. In order to contrast the two result sets, it is necessary to adjust one or other so as to reflect the same information. This is done either by expanding the smaller set or reducing the larger set. Both techniques are based on the same principles.

Historically, model reduction was devised not as a means of comparing disparate data sets, but of distilling large analytic matrices to a more manageable size for eigensolution computation on the limited microprocessors of the time. The aim was to represent the stiffness and inertia characteristics of the structure with as few DOFs as possible. Guyan [202] proposed partitioning the eigenvectors into master and slave degrees of freedom denoted by the subscripts m and s, and partitioning the mass and stiffness matrices accordingly:

$$\boldsymbol{\phi}_i = \left\{ \begin{array}{c} \boldsymbol{\phi}_{mi} \\ \hdashline \boldsymbol{\phi}_{si} \end{array} \right\} \qquad \mathbf{M} = \left[\begin{array}{c:c} \mathbf{M_{mm}} & \mathbf{M_{ms}} \\ \hdashline \mathbf{M_{sm}} & \mathbf{M_{ss}} \end{array} \right] \qquad \mathbf{K} = \left[\begin{array}{c:c} \mathbf{K_{mm}} & \mathbf{K_{ms}} \\ \hdashline \mathbf{K_{sm}} & \mathbf{K_{ss}} \end{array} \right]. \tag{2.219}$$

Using these in eqn. (2.84) produces

$$-\lambda_i \left[\begin{array}{c:c} \mathbf{M_{mm}} & \mathbf{M_{ms}} \\ \hdashline \mathbf{M_{sm}} & \mathbf{M_{ss}} \end{array} \right] \left\{ \begin{array}{c} \boldsymbol{\phi}_{mi} \\ \hdashline \boldsymbol{\phi}_{si} \end{array} \right\} + \left[\begin{array}{c:c} \mathbf{K_{mm}} & \mathbf{K_{ms}} \\ \hdashline \mathbf{K_{sm}} & \mathbf{K_{ss}} \end{array} \right] \left\{ \begin{array}{c} \boldsymbol{\phi}_{mi} \\ \hdashline \boldsymbol{\phi}_{si} \end{array} \right\} = \mathbf{0} \tag{2.220}$$

and making the assumption that the inertial effects at the slave DOFs are negligible compared to the elastic forces, the bottom half of the matrix equation gives

$$\mathbf{K_{sm}}\boldsymbol{\phi}_{mi} + \mathbf{K_{ss}}\boldsymbol{\phi}_{si} = \mathbf{0} \tag{2.221}$$

so that

$$\boldsymbol{\phi}_{si} = -\mathbf{K_{ss}}^{-1}\mathbf{K_{sm}}\boldsymbol{\phi}_{mi}. \tag{2.222}$$

The full eigenvector is thus given by

$$\left\{ \begin{array}{c} \boldsymbol{\phi}_{mi} \\ \hdashline \boldsymbol{\phi}_{si} \end{array} \right\} = \left\{ \begin{array}{c} \mathbf{I} \\ \hdashline -\mathbf{K_{ss}}^{-1}\mathbf{K_{sm}} \end{array} \right\} \boldsymbol{\phi_{mi}} \tag{2.223}$$

or

$$\boldsymbol{\phi}_i = \mathbf{T}\boldsymbol{\phi}_{mi} \qquad \mathbf{T} = \left\{ \begin{array}{c} \mathbf{I} \\ \hdashline -\mathbf{K_{ss}}^{-1}\mathbf{K_{sm}} \end{array} \right\}. \tag{2.224}$$

Putting eqn. (2.224) into the orthogonality conditions gives

$$\boldsymbol{\phi}_{mi}^T\mathbf{T}^T\mathbf{M}\mathbf{T}\boldsymbol{\phi}_{mi} = \mathbf{I} \qquad \boldsymbol{\phi}_{mi}^T\mathbf{T}^T\mathbf{K}\mathbf{T}\boldsymbol{\phi}_{mi} = \boldsymbol{\Lambda} \tag{2.225}$$

so that the reduced mass and stiffness matrices are given by

$$\mathbf{M_R} = \mathbf{T}^T\mathbf{M}\mathbf{T} \qquad \mathbf{K_R} = \mathbf{T}^T\mathbf{K}\mathbf{T}. \tag{2.226}$$

The solution obtained with these matrices is exact only where $\omega = 0$ so that the technique is often referred to as *static reduction*. The approximation works well for low frequency modes where inertial effects are less significant, but the inaccuracies increase with the frequency. This problem is tackled in an extension to Guyan's method, called *dynamic reduction*, where instead of neglecting the inertial effects they are included for a single frequency, ω_{DR}. Eqn. (2.220) becomes

$$-\omega_{DR}^2 \left[\begin{array}{c|c} \mathbf{M_{mm}} & \mathbf{M_{ms}} \\ \hline \mathbf{M_{sm}} & \mathbf{M_{ss}} \end{array}\right] \left\{\begin{array}{c} \boldsymbol{\phi}_{mi} \\ \hline \boldsymbol{\phi}_{si} \end{array}\right\} + \left[\begin{array}{c|c} \mathbf{K_{mm}} & \mathbf{K_{ms}} \\ \hline \mathbf{K_{sm}} & \mathbf{K_{ss}} \end{array}\right] \left\{\begin{array}{c} \boldsymbol{\phi}_{mi} \\ \hline \boldsymbol{\phi}_{si} \end{array}\right\} = \mathbf{0} \tag{2.227}$$

and taking the bottom half of the equation again gives

$$(\mathbf{K_{sm}} - \omega_{DR}^2 \mathbf{M_{sm}})\boldsymbol{\phi}_{mi} + (\mathbf{K_{ss}} - \omega_{DR}^2 \mathbf{M_{ss}})\boldsymbol{\phi}_{si} = \mathbf{0} \tag{2.228}$$

and the slave degrees of freedom are related to the measured degrees of freedom using

$$\boldsymbol{\phi}_{si} = -\left(\mathbf{K_{ss}} - \omega_{DR}^2 \mathbf{M_{ss}}\right)^{-1} \left(\mathbf{K_{sm}} - \omega_{DR}^2 \mathbf{M_{sm}}\right) \boldsymbol{\phi}_{mi}. \tag{2.229}$$

In this case the transform for the matrix reduction is given by

$$\mathbf{T} = \left\{\begin{array}{c} \mathbf{I} \\ \hline -\left(\mathbf{K_{ss}} - \omega_{DR}^2 \mathbf{M_{ss}}\right)^{-1} \left(\mathbf{K_{sm}} - \omega_{DR}^2 \mathbf{M_{sm}}\right) \end{array}\right\}. \tag{2.230}$$

The reduced matrices give an exact solution at ω_{DR} but moving away from this frequency in either direction reduces the accuracy in the same way as with the static reduction. In fact, static reduction is simply a special case of dynamic reduction, with $\omega_{DR} = 0$.

Having derived the reduced matrices, the expansion and reduction of the eigenvectors is a trivial task. Reduction of the analytic eigenvectors is the simplest option; all that is needed is to omit the slave DOFs from the vector. Expansion of the experimental eigenvectors is known as Kidder's method [203] and involves reconstructing the slave DOFs from the measured (master) DOFs by putting $\omega_{DR}^2 = \lambda_i$ into eqn. (2.229) for each mode, i. The problem with this technique as a validation tool is that the expanded DOFs are based on the analytic mass and stiffness matrices. As such, they will exhibit a biased correlation with the numerical model. Used appropriately, however, they can provide improved visualisation and allow for further manipulation in advanced analyses.

Master DOFs

The model reduction techniques raise an interesting question: which DOFs provide the best representation of a structure? This is particularly important when selecting attachment points for measurement devices. Bearing in mind the premise behind Guyan reduction, that the inertia forces are negligible, the DOFs to be discarded should be those with low mass to stiffness ratios. A popular technique is to compare the diagonal mass and stiffness matrix entries and discard the DOFs with the lowest m_{ii}/k_{ii}

values. They should not be discarded all at once, but one at a time, computing the new reduced mass and stiffness matrices at each step.

Another approach is called the effective independence distribution vector method and relies on the computation of the full analytical eigenvectors. In a modal analysis context, the question of which DOFs are most important becomes one of determining which DOFs produce a linearly indepedent representation of all the modes being studied. If $\mathbf{\Phi}$ is taken to be the analytic eigenvector matrix containing only the modes of interest then the matrix

$$\mathbf{R} = \mathbf{\Phi}\mathbf{\Phi}^{+} = \mathbf{\Phi}(\mathbf{\Phi}^{T}\mathbf{\Phi})^{-1}\mathbf{\Phi}^{T} \tag{2.231}$$

will be full rank only while all the mode vectors are linearly independent [204]. Furthermore, the diagonal elements of $\mathbf{R}$ give the fractional contribution of each DOF to its rank, and thus the smaller values indicate the DOFs that should be eliminated. Once again, the DOFs should be removed one at a time, with the reduced matrices recomputed after each cull.

Mode Correlation

Once all of the modes are represented in a format suitable for comparison, there are a choice of methods. One method is to plot, for each mode, a graph of the mode vector elements, with the experimental values on one axis and the analytical values on the other. This is similar to the frequency comparison and good correlation will produce points lying on a straight line. This method is particularly useful for detecting systematic errors, but requires a lot of plots to represent the full modal model.

A better choice for assessing the correlation at a glance is the Modal Assurance Criterion (MAC),

$$\mathrm{MAC}_{jk} = \frac{\left(\boldsymbol{\psi}_j{}^{T}\boldsymbol{\psi}_k\right)^2}{\left(\boldsymbol{\psi}_j{}^{T}\boldsymbol{\psi}_j\right)\left(\boldsymbol{\psi}_k{}^{T}\boldsymbol{\psi}_k\right)} \tag{2.232}$$

The criterion produces, for any mode pair, a single value between zero and unity, where the former indicates no correlation and the latter attests an exact match. More precisely, the MAC is the inner product of the normalised eigenvectors. As such it affords a geometric interpretation: it is the square of the angle between the two vectors in the physical coordinate system defined by the eigenvector DOFs,

$$\mathrm{MAC}_{jk} = \cos^2\alpha_{jk}. \tag{2.233}$$

Usually, the MAC is evaluated for every pair within two sets of modes, and the results displayed in a table. It can be presented graphically by replacing the cells in the table with coloured squares, the size of which are proportional to the corresponding MAC entry. Examples are seen in figure 3.9, where in addition to the size variation, the colour of the squares ranges from dark blue (representing zero) through green to deep red (representing unity). This representation is consistent throughout the thesis. A perfect correlation between two sets is indicated by ones on the diagonal elements, with

the off-diagonal elements taking arbitrary values but usually close to zero.

Another common technique is to use a weighted MAC, referred to as a Normalised Cross Orthogonality (NCO). If the mass matrix is used as the weighting matrix then the NCO gives a measure of the angle, α, between the two eigenvectors in the *normal* coordinate system defined by the mass-normalised mode vectors[168]:

$$\mathrm{NCO}_{jk} = \cos^2\beta_{jk} = \frac{\left(\boldsymbol{\psi}_j{}^T \mathbf{M} \boldsymbol{\psi}_k\right)^2}{\left(\boldsymbol{\psi}_j{}^T \mathbf{M} \boldsymbol{\psi}_j\right)\left(\boldsymbol{\psi}_k{}^T \mathbf{M} \boldsymbol{\psi}_k\right)}. \tag{2.234}$$

The vectors should all be orthogonal in this coordinate system, so a perfect correlation will exhibit ones on the diagonals and zeros on the off-diagonals of the NCO matrix.

If the MAC is used to compare a mode set to itself then it is referred to as the autoMAC, and it is a useful measure of the linear independence of the eigenvectors. Applied to a reduced analytical mode set it will highlight a deficient DOF selection with large off-diagonal values.

Automated Mode Tracing

With the quantitative assessment provided by the MAC it is possible to automate the pairing of modes between two sets. This is useful in an array of situations; the two examples that will be explored in this thesis are parametric studies and model updating, as discussed below. Ideally, there will be a one-to-one correspondence between the two sets and the highest MAC value can be chosen for each row in turn. In practice this is rarely the case and the highest MACs for several rows may lie in the same column. The algorithm used in the code of this thesis is as follows: For any conflicts in the mode pairing, the pair with the highest MAC is kept, and the other rows must be re-evaluated without the contested column. This procedure is applied iteratively until all the modes are uniquely assigned.

2.7 Model Updating

Model updating is the process of adjusting parameters in a numerical model to bring the results in line with those of a physical test. Various approaches are reviewed by Mottershead and Friswell [205]. For the technique to be useful it is critical that the parameters are chosen wisely: given enough parameters it is a trivial matter to produce an analytic system which will match experimental data. The purpose of the task, however, is to produce a model which bears more physical resemblance to the real structure, such that identical alterations in the two systems produce corresponding changes in the dynamic response.

Choosing sensible parameters is a matter of engineering judgement. For example, solid structural members are generally well understood, whereas joints introduce uncertainties. The dynamic properties will be influenced by the tightness of bolts, friction in pinned connections, the strength or porosity of a weld, etcetera. The detail in intricate parts is often overlooked, lumping their composi-

tion into a few characteristic parameters which must be chosen carefully to reflect the behaviour of the component.

It is also important that the updating problem is well conditioned: the dynamic properties must be sensitive to the chosen parameters, and each parameter should affect the response in a different manner. This is represented by the conditioning of the sensitivity matrix described below, which should be comprised of linearly independent rows and columns.

2.7.1 Eigenstructure Sensitivities

The updating procedures employed in this thesis are concerned primarily with correcting the modal properties, characterised by the eigenstructure of the analytical problem. The approach focuses on a linearisation of the eigenstructure variation with respect to the parameters, reflected in the eigenvalue and eigenvector sensitivities.

Fox and Kapoor [206] derive the eigenvalue sensitivity to a parameter δ_j as

$$\frac{d\lambda_i}{d\delta_j} = \boldsymbol{\phi}_i^T \left(\frac{d\mathbf{K}}{d\delta_j} - \lambda_i \frac{d\mathbf{M}}{d\delta_j} \right) \boldsymbol{\phi}_i. \tag{2.235}$$

They derive the corresponding eigenvector sensitivity as a linear combination of the eigenvectors themselves (which, as an orthogonal set, can reproduce any vector within the eigenspace):

$$\frac{d\boldsymbol{\phi}_i}{d\delta_j} = -\frac{\boldsymbol{\phi}_i^T \frac{d\mathbf{M}}{d\delta_j} \boldsymbol{\phi}_i}{2} \boldsymbol{\phi}_i + \sum_{r \neq i} \frac{\boldsymbol{\phi}_r^T \left(\frac{d\mathbf{K}}{d\delta_j} - \lambda_i \frac{d\mathbf{M}}{d\delta_j} \right) \boldsymbol{\phi}_i}{\Delta\lambda_{ir}} \boldsymbol{\phi}_r. \tag{2.236}$$

where $\Delta\lambda_{ir} = \lambda_i - \lambda_r$. A drawback of using eqn. (2.236) to compute the eigenvector sensitivities is that knowledge of all the eigenvectors is needed for an accurate calculation. It is desireable to be able to compute the vector sensitivity from the modal properties of only the mode in question, and this can be accomplished using Nelson's method [207]. The procedure described by Friswell and Mottershead [204] starts by defining the i^{th} eigenvector sensitivity as the sum of the scaled i^{th} eigenvector and another vector representing the contribution of the remaining modes:

$$\frac{d\boldsymbol{\phi}_i}{d\delta_j} = c_i \boldsymbol{\phi}_i + \mathbf{d_i}. \tag{2.237}$$

The vector $\mathbf{d_i}$ is determined first, by differentiating eqn. (2.84), substituting eqn. (2.235) and putting $\frac{d\phi_i}{d\delta_j} = \mathbf{d_i}$ into the result so that

$$[\mathbf{K} - \lambda_i \mathbf{M}]\mathbf{d_i} = -\left[\frac{d\mathbf{K}}{d\delta_j} - \lambda_i \frac{d\mathbf{M}}{d\delta_j} - \boldsymbol{\phi}_i^T \left[\frac{d\mathbf{K}}{d\delta_j} - \lambda_i \frac{d\mathbf{M}}{d\delta_j} \right] \boldsymbol{\phi}_i \mathbf{M} \right] \boldsymbol{\phi}_i. \tag{2.238}$$

To tackle the problem of inverting $[\mathbf{K} - \lambda_i \mathbf{M}]$, which will be rank deficient, the k^{th} element of $\mathbf{d_i}$ is set to zero and the corresponding rows and columns are removed from eqn. (2.238). After solving for the remaining elements of $\mathbf{d_i}$, the zero is reinserted in the k^{th} position. Usually the index k is chosen

as the location of the maximum eigenvector element but the selection is not important provided the inversion procedure is well conditioned. Once $\mathbf{d_i}$ is determined, the mass orthogonality from eqn. (2.99) is differentiated and combined with eqn. (2.237) to produce

$$c_i = -\boldsymbol{\phi}_i^T \mathbf{M} \boldsymbol{d_i} - \frac{1}{2} \boldsymbol{\phi}_i^T \frac{d\mathbf{M}}{d\delta_j} \boldsymbol{\phi}_i. \tag{2.239}$$

To conclude, $\mathbf{d_i}$ and c_i are inserted into eqn. (2.237) to obtain the eigenvector sensitivity. Whilst awkward to explain, this scheme is computationally efficient, particularly where only one mode is being investigated.

2.7.2 Updating Schemes

Many different methods exist for model updating: Friswell and Mottershead [204] discuss direct methods using modal data, iterative methods using modal data and methods using frequency domain data.

The latter technique seeks to match the analytical FRFs to the measured FRFs, with no modal parameter extraction necessary. While this simplifies the measurement data processing, it introduces the question of how to model the damping, which can be difficult as discussed in section 2.6.1.

The direct methods involve a one step procedure which modifies the structural matrices directly to reproduce the experimentally determined modal properties. The results are matched exactly, but the adjustments to the structural matrices have little physical basis. In general the nodal connectivity of the updated model is not consistent with the initial model and does not correspond with the physical connectivity. Some studies [208, 209] have placed additional constraints on the solution to try to improve the physicality, but these still represent a compromise.

An interesting development is that of generic elements [210], where similar techniques are applied but to single elements. Once again, the changes may be constrained to allow preservation of the physical connectivity [211]. Generic elements have the advantage that they can be localised, permitting greater control of the structural modifications.

Friswell and Mottershead discuss several iterative methods. This thesis confines itself to the use of penalty function methods. Like the direct methods they attempt to match the numerical and experimental modal results. As the name implies, in this case the approach is iterative. At each step a linearisation of the modal sensitivities is used to estimate the parameter values which will minimise the errors in the updating variables. Convergence is assessed based on the change in parameter values; once the change falls below a given value the solution is deemed to have converged.

The data available as updating variables are the eigenvalues and the eigenvectors. The eigenvectors are widely thought to provide inferior updating variables when compared to the eigenvalues. The eigenvalues are generously overdetermined by the measurement data, and they are insensitive to

calibration errors on the measurement equipment. In contrast, the eigenvector elements each rely on a single measurement transducer and will be sensitive to both noise and calibration errors. It is generally preferred, therefore, to use only the eigenvalues in the updating process where feasible. Despite this preference, the eigenvectors sometimes contain unique information about the structure and chapter 6 discusses an alternative method to exploit this information without the need for the direct inclusion of the eigenvectors.

For every iteration, j, a sensitivity matrix is constructed with the elements of each row giving the sensitivity of the updating variables, z, to the parameters, δ:

$$\mathbf{S}_j = \begin{bmatrix} \frac{\partial z_1}{\partial \delta_1} & \frac{\partial z_1}{\partial \delta_2} & \cdots & \frac{\partial z_1}{\partial \delta_m} \\ \frac{\partial z_2}{\partial \delta_1} & \frac{\partial z_2}{\partial \delta_2} & \cdots & \frac{\partial z_2}{\partial \delta_m} \\ \cdots & \cdots & \ddots & \cdots \\ \frac{\partial z_n}{\partial \delta_1} & \frac{\partial z_n}{\partial \delta_2} & \cdots & \frac{\partial z_n}{\partial \delta_m} \end{bmatrix} \tag{2.240}$$

The estimated change, $\boldsymbol{\Delta z_j}$, in the analytic updating variables is then given in terms of the parameter change vector, $\boldsymbol{\Delta \delta_j}$, by

$$\boldsymbol{\Delta z_j} = \mathbf{S_j} \boldsymbol{\Delta \delta_j}. \tag{2.241}$$

An updating variable error vector is defined as the difference between the measured data, $\mathbf{z_m}$, and the data from the current iteration $\mathbf{z_j}$:

$$\boldsymbol{\varepsilon_j} = \mathbf{z_m} - \mathbf{z_j} \tag{2.242}$$

and the estimated error at the end of the iteration is given by

$$\begin{aligned} \tilde{\boldsymbol{\varepsilon}}_{\boldsymbol{j+1}} &= \boldsymbol{\varepsilon_j} - \boldsymbol{\Delta z_j} \\ &= \boldsymbol{\varepsilon_j} - \mathbf{S_j} \boldsymbol{\Delta \delta_j}. \end{aligned} \tag{2.243}$$

The objective is to minimise the estimated error at the end of the iteration and this is achieved in the least squares sense by minimising the penalty function

$$J(\boldsymbol{\Delta \delta_j}) = \tilde{\boldsymbol{\varepsilon}}_{\boldsymbol{j+1}}{}^T \tilde{\boldsymbol{\varepsilon}}_{\boldsymbol{j+1}}. \tag{2.244}$$

A weighting matrix is often included to attach differing importance to the updating variables. This is usually used where some measured data are considered more reliable than others. The penalty function then becomes

$$J(\boldsymbol{\Delta \delta_j}) = \tilde{\boldsymbol{\varepsilon}}_{\boldsymbol{j+1}}{}^T \mathbf{W}_{\varepsilon\varepsilon} \tilde{\boldsymbol{\varepsilon}}_{\boldsymbol{j+1}}. \tag{2.245}$$

It may also be desireable to attach a weighting matrix to the updating parameters; in addition to shaping the levels of variation applied to each parameter this serves as a regularisation method [212], with smaller values reducing the changes at each iteration. This is particularly useful if the scheme

exhibits convergence instablities. A new term is added to the penalty function to give

$$J(\boldsymbol{\Delta\delta_j}) = \boldsymbol{\tilde{\varepsilon}_{j+1}}^T \mathbf{W}_{\varepsilon\varepsilon} \boldsymbol{\tilde{\varepsilon}_{j+1}} + \boldsymbol{\Delta\delta_j}^T \mathbf{W}_{\delta\delta} \boldsymbol{\Delta\delta_j}. \tag{2.246}$$

Substituting eqn. (2.243) and differentiating with respect to $\boldsymbol{\Delta\delta_j}$, the minimum penalty function is given by

$$\boldsymbol{\Delta\delta_j} = [\mathbf{S_j}^T \mathbf{W}_{\varepsilon\varepsilon} \mathbf{S_j} + \mathbf{W}_{\delta\delta}]^{-1} \mathbf{S_j}^T \mathbf{W}_{\varepsilon\varepsilon} \boldsymbol{\varepsilon_j}. \tag{2.247}$$

This result gives the increment to the updating parameters based on the updating variable error. The model is then evaluated for the new parameter values and the next iteration begins. This procedure repeats until convergence is attained.

2.7.3 Model Updating with ANSYS

While the early chapters of this thesis rely on purpose-written code, and implement the updating schemes using exact sensitivity calculations, the later chapters rely on proprietary finite element code. The software package chosen is ANSYS [152], and the updating capabilities are provided by the *design optimisation* toolbox. These tools provide the facility to perturb the updating parameters sequentially, thus determining empirical sensitivities for the updating process. The design optimisation tools are not specifically intended for dynamic model updating; instead they seek to minimise whatever values the user specifies. For these purposes, an objective function is computed as the ℓ-2 norm of the eigenvalue errors. This value is passed to the design optimisation routine, allowing it to adjust the parameters to those which best match the dynamic properties of the experimental configuration. In order to use the optimisation tools it is necessary to provide a parametric ANSYS script which can build the model according to the design parameter values at each iteration, and run any necessary solutions to obtain the updating variables.

Another ANSYS feature which is employed in this thesis is the *gradient method*. This tool can be applied independently of a full optimisation run; it simply performs an empirical sensitivity analysis on the model, and by including a modal solution in the optimisation script the software can be configured to return the eigenvalue sensitivities to design parameters.

Chapter 3

Preliminary Stress Stiffening Investigations

3.1 Introduction

This chapter details several test configurations that were employed in performing experimental and numerical investigations of the effect of loading on structural dynamic behaviour. The primary objective at the outset was to verify theoretical predictions and determine the accuracy of the different approximations described in section 2.4. The simple configurations chosen for the tests also provided an opportunity to validate the generic finite element (FE) code developed by the author for the work in this thesis, and to identify aspects of the behaviour that could be exploited for beneficial modification of the dynamic response.

In the course of the experiments several peculiarities are explored, including the parameterisation of joints subject to loading and the effects of damping on the response functions in the presence of high modal overlap. Two configurations are used: one with pinned joints and one with welded joints. The former is used for FE code validation and joint studies while the latter is used to evaluate stress stiffening formulations, identify response suppression opportunities and investigate damping effects.

3.2 Validation Test Structure

A test structure was developed for the purposes of validating the theory and FE techniques presented in the foregoing chapters, and to establish the accuracy of the differing levels of approximation. The structure was designed to isolate the effects of loading from other effects, and so to minimise uncertainties. Following the example of Greening [175], a cross-braced rectangular framework was used, as illustrated in figure 3.1. To simplify the analysis a two-dimensional approximation was employed. An 8×30mm beam cross-section was chosen, with the smaller second moment of area corresponding to bending in the plane of the frame. This alignment produces high out-of-plane stiffness, and separates the in- and out-of-plane vibration modes. The centrelines of the beams were

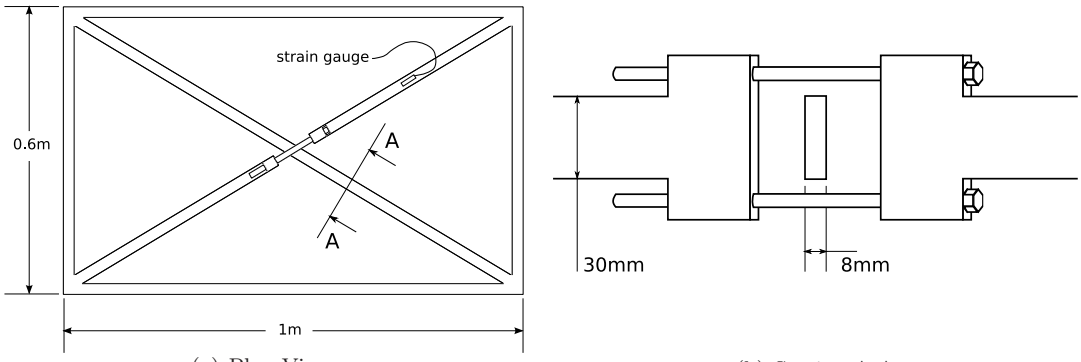

(a) Plan View

(b) Section A-A

Figure 3.1: The cross-braced rectangular frame exhibiting static redundancy, with two bolts forming a tensioning mechanism in one of the diagonals.

also arranged to lie in the same plane as each other, thus minimising the coupling between in- and out-of-plane modes.

The two diagonal cross-beams create a static redundancy so that shortening one member results in an internal load propagating around the structure. The tensioning mechanism is seen in figure 3.2 and is comprised of two bolts inserted in line with one of the cross-beams. The bolts thread through flanges in the beam segments and pass either side of the other diagonal member. This arrangement allows the two beams to cross without contacting each other, while ensuring the neutral axis reamins in-plane. Tightening the bolts shortens the member and induces the structural load. Two strain gauges are mounted on the top and bottom of the tensioning beam, mid-way between the tensioning mechanism and corner joint. The strain measurements allow calculation of the tension in the member, and balancing the two ensures that no bending moment is introduced.

Two variations were built: one with pinned corner joints, assembled as pictured in figure 3.3 to retain in-plane neutral axes, and the second with welded joints. The pin-jointed arrangement was intended to ensure the simplest static load case as the members would carry only axial loading, in contrast to the welded joints which would allow shear and moment transfer between members. In addition, the analytical buckling load for the pin-jointed truss has a closed form solution so the stressed structure could be compared to the exact buckling and stress stiffnening solutions, as outlined in appendix A. In practice, the pinned joints introduced more complications than had been anticipated and these are described in the next section.

The finite element model (FEM) was constructed using six two-dimensional Euler-Bernoulli beam elements for each member of the truss. The pinned corner joints were represented by another element for each of the interleaving, fingered sections. The tensioning mechanism was comprised of a further three elements representing the two flanges and the bolts. The arrangement of this region can be seen in figure 3.4. To simulate the tightening of the bolts, the bolts element is uncoupled from the flange element at one end. The free end of the flange is fully constrained, and the free end of the bolts element is constrained in the transverse and rotational DOFs. An axial load is applied to the free end of the bolts and the static analysis is performed. Once this analysis is complete, the loading and

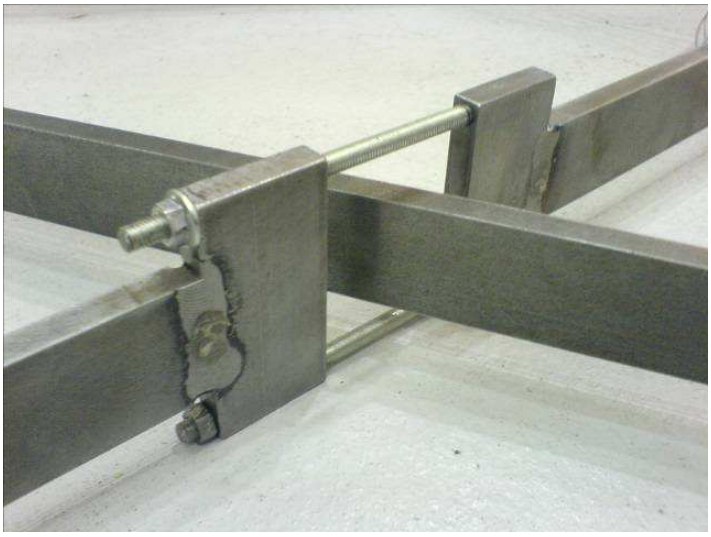

Figure 3.2: Photograph showing the tensioning mechanism in the redundant frame.

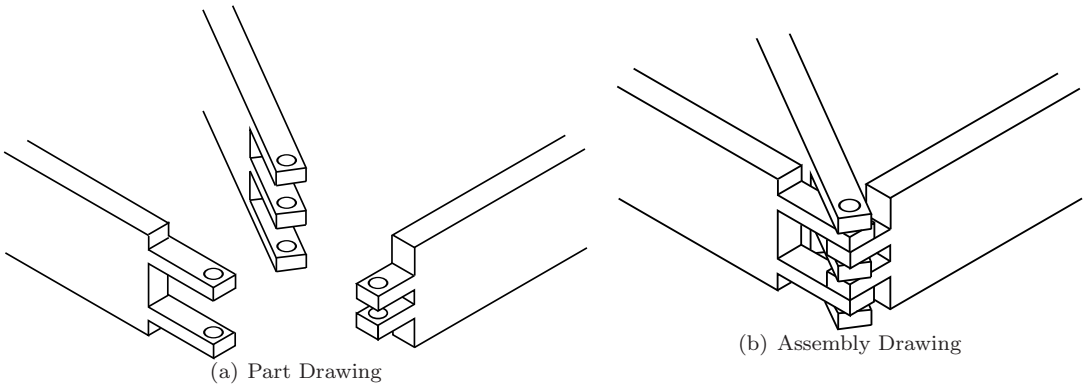

Figure 3.3: The pin-jointed members for the rectangular frame, shown separately and assembled.

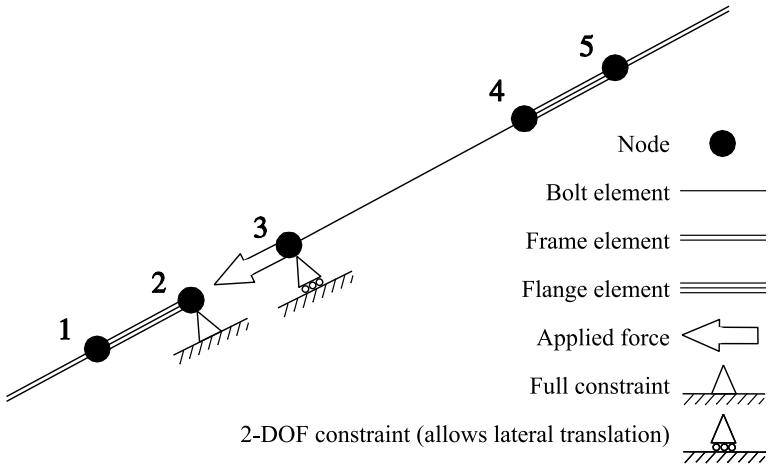

Figure 3.4: Finite element model of the tensioning mechanism. The figure is not to scale; in particular, nodes 2 and 3 are coincident in the unloaded FE model.

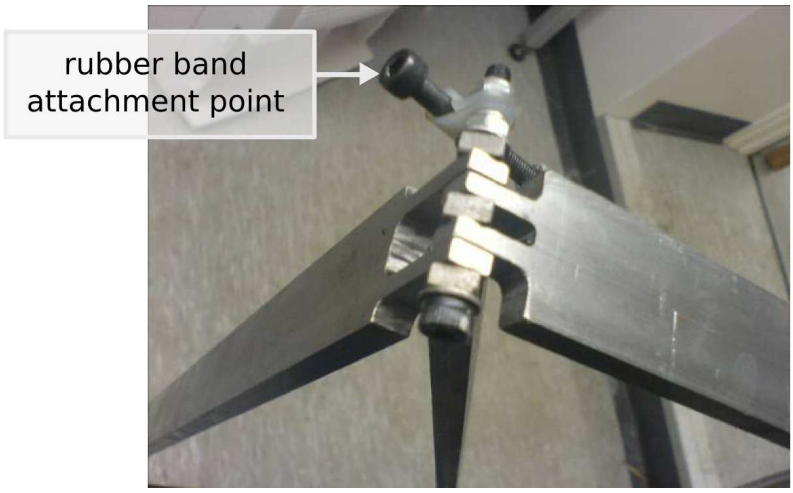

Figure 3.5: Corner joint arrangement in the pin-jointed frame.

contraints are removed and the free ends are coupled once more ready for the dynamic analysis. Small errors are introduced by the misalignment of the two free ends after loading but the displacement of the bolts was found to be relatively small and the effect on the mass and stiffness is negligible next to that of the stress stiffening itself; the approximation is justified by the simplification it affords.

3.3 Pin-Jointed Frame

3.3.1 Experimental Configuration

The pin-jointed frame was tested first. The corner joints are pictured in figure 3.5, with attachments for suspending the structure. It was suspended from rubber bands to approximate free vibration conditions as seen in figure 3.6. Two shakers were required to excite the structure; long flexible stingers were extended from these to the frame, where they were attached magnetically in line with force transducers (magnetic mounts are acceptable for the low frequencies being considered). Fourteen accelerometers were attached using wax, and the distribution of these is seen along with the shaker positioning in figure 3.7. The shakers were used to supply broadband excitation and force and acceleration measurements were recorded. Frequency response curves were computed and a least squares complex exponential method used to determine modal frequency and damping values, before estimating the mode shapes with the frequency domain least squares technique. These methods are outlined in section 2.5.

3.3.2 Preliminary Model Updating

In preparation for the load tests, the structure was first tested with the tensioning beam removed to validate the FE model. This arrangement is seen in figure 3.8 and eliminates the uncertainties associated with the tensioning mechanism. The results were expected to match the finite element

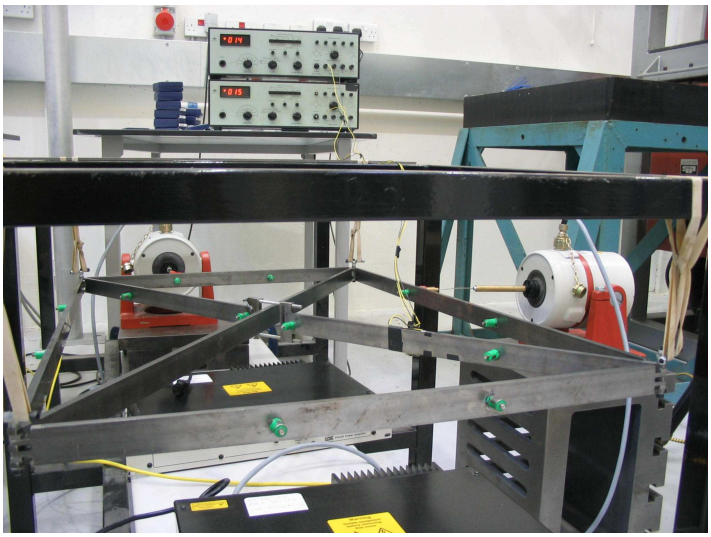

Figure 3.6: Experimental arrangement for the pinned frame.

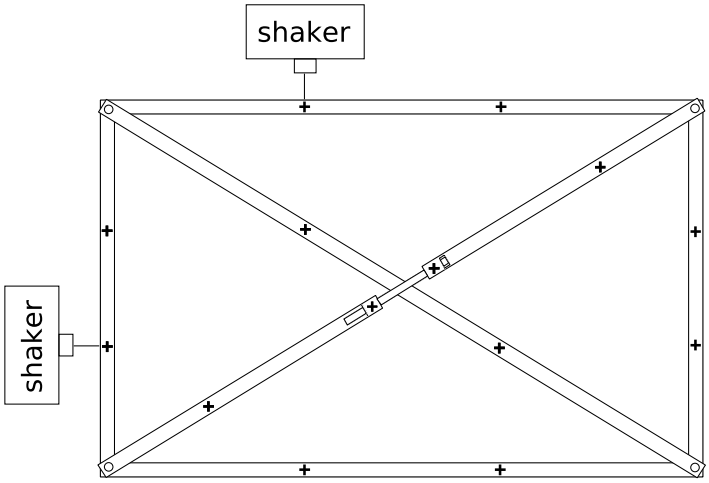

Figure 3.7: Experimental layout for the pin-jointed frame, showing the shaker attachment points and the accelerometer locations denoted by +.

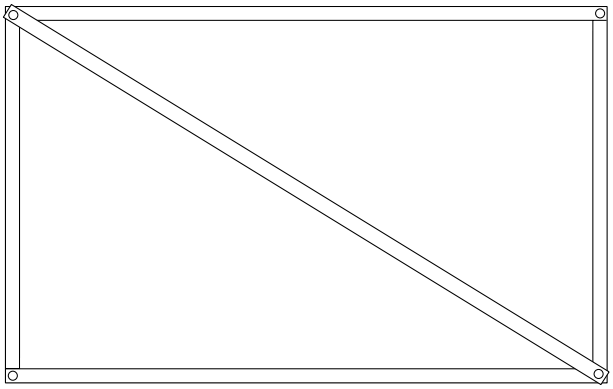

Figure 3.8: The pin-jointed frame with tensioning member removed.

prediction with a great degree of accuracy but this was not the case. The experimentally determined frequencies and mode shapes are compared with the finite element results in figure 3.9(a) using techniques from section 2.6. The most plausible source of error was in the pinned joints, where the stiffness and damping caused by friction had not been accounted for. Correcting for these omissions, small rotational springs were added to the model to couple the rotational DOFs at the ends of the beams. Three spring sets were introduced to model the stiffnesses at the three joint interfaces in each corner: between the long and short outside members, the diagonal and short members, and the diagonal and long members. These interfaces are highlighted in figure 3.10. An iterative sensitivity-based updating scheme was employed as described in section 2.7, using the first three experimental frequencies as updating variables in the penalty function. The model alteration thus determined was found to bring all of the FE results in line with the experimental data as revealed by figure 3.9(b). Several of the FE results that were not involved in the updating scheme, and that showed significant disagreement with the experimental results prior to updating, were found to correlate well using the updated parameters, instilling confidence in the updated model.

The convergence of the first three analytical frequencies on the experimentally obtained values is seen in figure 3.11(a) with the corresponding parameter values. The most striking feature of this plot is that one parameter converges on a much higher value than the other two. The parameters were re-evaluated using several different mode combinations as reference data in the updating scheme, and each time similar results were obtained. The high parameter value corresponds to the rotational stiffness between the diagonal and short outside members (the central and right-hand parts in figure 3.3(a)). Examining these parts, they were found to have an interference fit, restricting their relative motion. A file was taken to the mating faces until the parts moved more freely past each other. Reassembling the modified frame and testing it again verified that it was this interface that was responsible for the observed discrepancies. Comparing the new experimental results with those of the original FE model in figure 3.9(c) shows that the pinned assumption is more accurate for the modified structure. Updating the model once again using the first three experimental frequencies gives the near perfect correlation seen in figure 3.9(d). The strong stiffness between the diagonal and short members has been dramatically reduced, as seen in figure 3.11(b), while the estimates for the other two stiffnesses remain close to their original values.

With high confidence in the joint parameters, the tensioning member was reinserted in the structure. The experimental results for the complete structure compare favourably with the finite element results using both the pinned approximation (figure 3.12(a)) and the updated parameter values (figure 3.12(b)). The parameters were updated once more, this time using the first four frequencies, and they were found to have changed slightly with the additional member included (figure 3.13). This discovery is not altogether surprising as the parameter values obtained using the FE model are in fact averages of the real stiffnesses which will vary amongst the four corners. The two values which exhibit the greatest change are both associated with the diagonal members, as would be expected upon the inclusion of the second diagonal. The frequency convergence is seen to be less reliable than previously and this is attributed to the further uncertainties introduced by the tensioning mechanism. The dis-

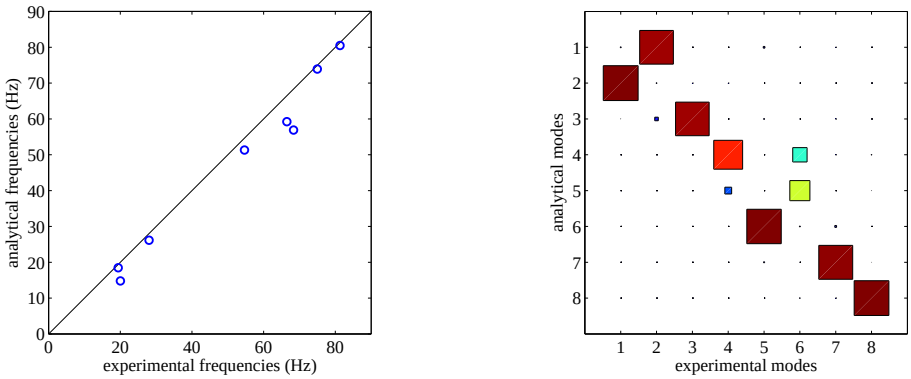

(a) Unmodified frame, ideal pinned configuration.

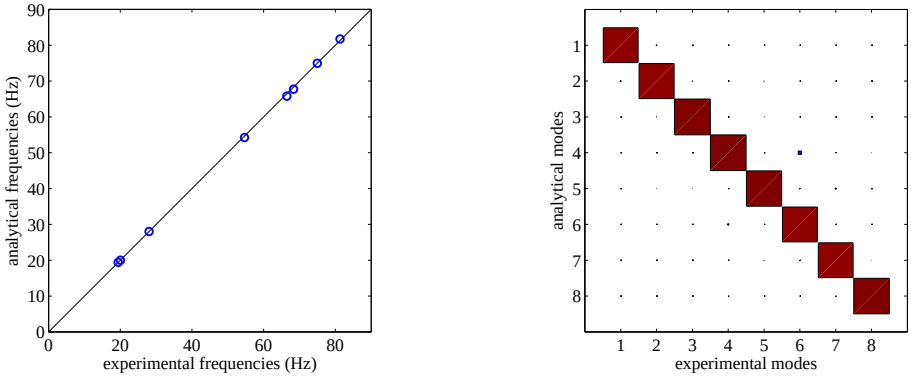

(b) Unmodified frame, updated spring parameters.

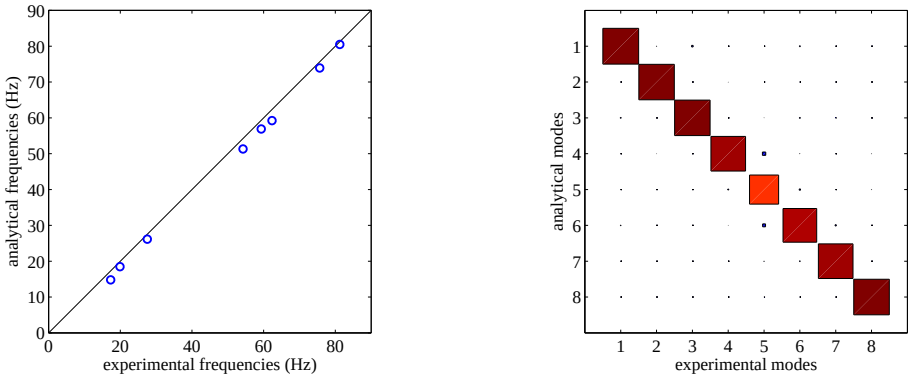

(c) Modified frame, ideal pinned configuration.

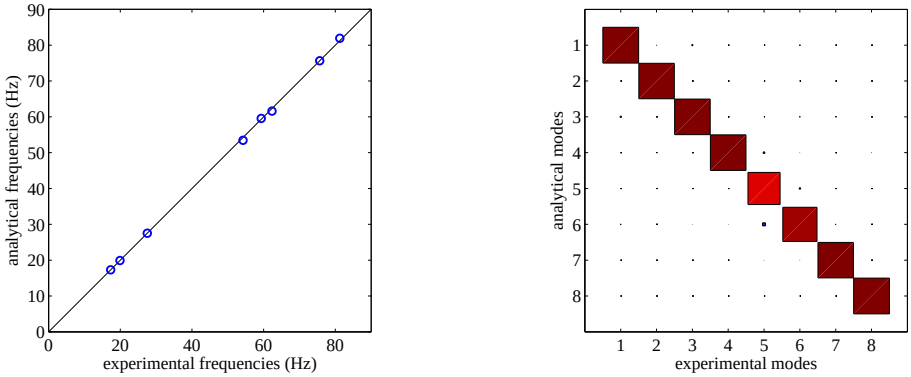

(d) Modified frame, updated spring parameters.

Figure 3.9: Comparison of the experimental and FE results for the frame with tensioning member removed, using frequency and Modal Assurance Criterion correlation techniques described in section 2.6.

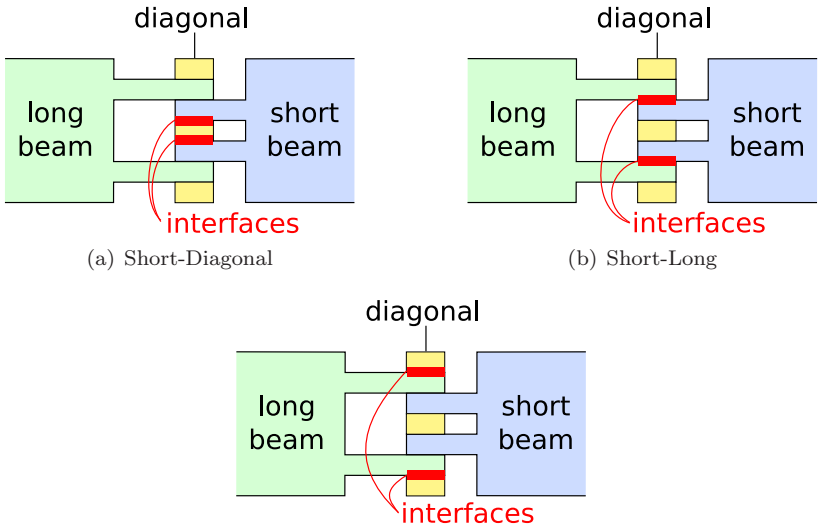

(a) Short-Diagonal (b) Short-Long

(c) Long-Diagonal

Figure 3.10: The three sets of joint interfaces in the interleaved corners of the pinned frame.

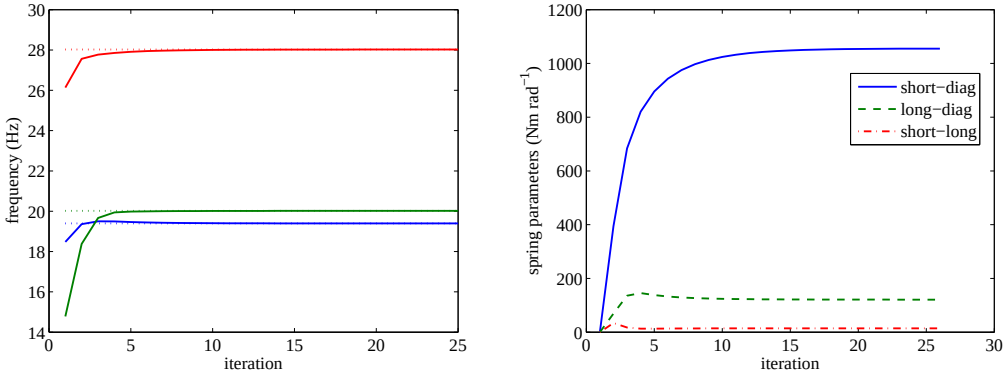

(a) Unmodified frame.

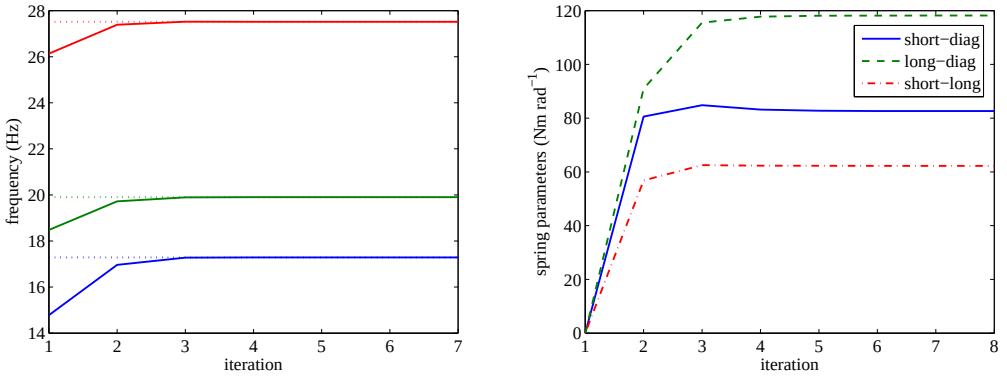

(b) Modified frame.

Figure 3.11: Convergence of the first three frequencies and the corresponding spring stiffness parameters as the model is updated, with the tensioning member removed.

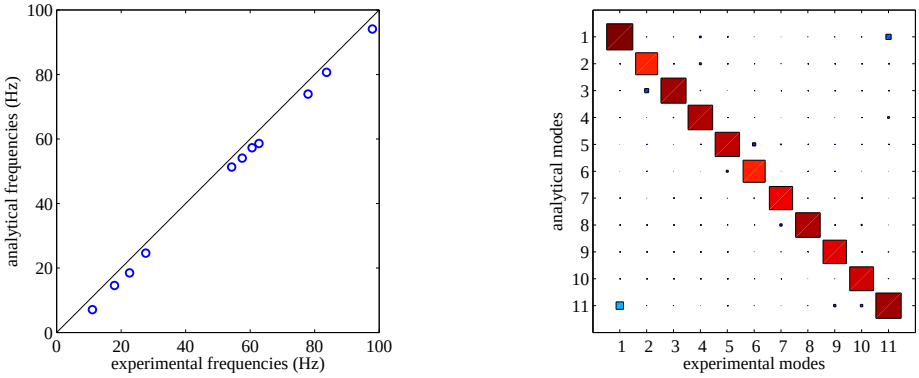

(a) Ideal pinned configuration.

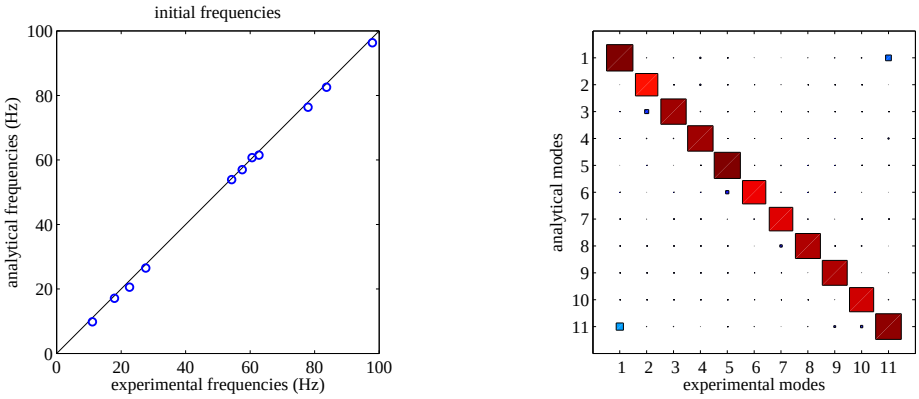

(b) Original spring parameters.

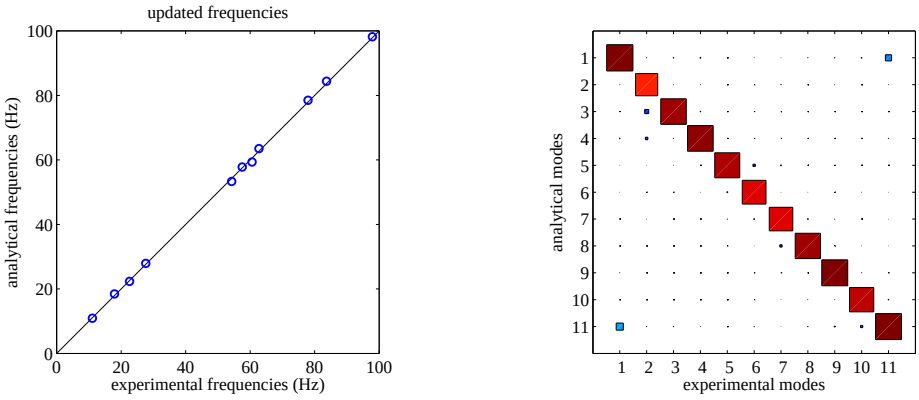

(c) Updated spring parameters.

Figure 3.12: Comparison of the experimental and FE results for the frame, complete with tensioning member.

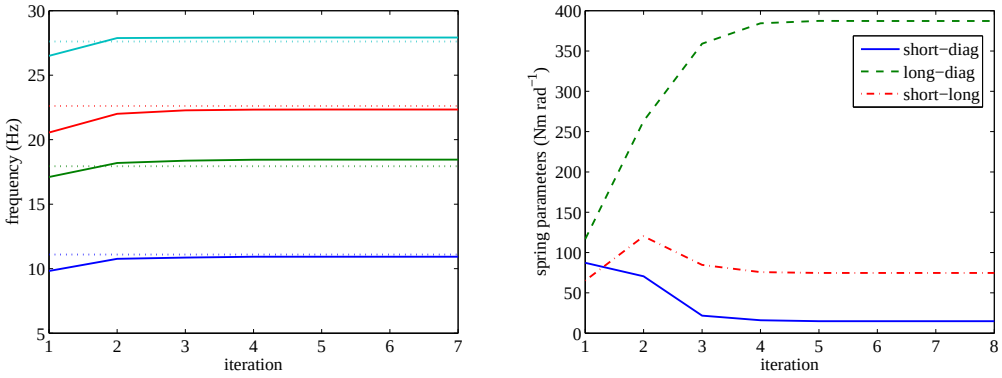

Figure 3.13: Convergence of the first four frequencies and the corresponding spring stiffness parameters as the model is updated, with the tensioning member included.

crepancies are not significant compared to those encountered in the earlier experiments, however, and the parameters are seen to converge on reasonable values. The FE results obtained using the final updated model compares well with the experimental data in figure 3.12(c).

3.3.3 Load testing

The structure was tensioned in approximately 300N steps until the buckling load was approached at 3800N, and mode shapes and natural frequencies were determined for each load case. The frequencies are plotted in figure 3.14(a). The FE model was evaluated at the same load steps, using Newton-Raphson iterations at each step, and compared to the experimental results. Several model configurations were investigated. As expected, the pinned joint assumption produced the relatively poor results seen in figure 3.14(b). Including the joint stiffness parameters gives much better results, illustrated in figure 3.14(c), but significant discrepancies still emerge at the higher loads. In an attempt to reconcile these differences, the parameters were re-evaluated at each load step. Using this approach produced the frequency curves in figure 3.14(d), matching the experimental results well. Parameter values for the two approaches are plotted against load in figures 3.15(a) and 3.15(b). Noting that all three parameters exhibit upward trends in the second model, it was postulated that as the loads on the joints increase, so do the friction forces responsible for the rotational coupling. The erratic meandering of the parameter values was attributed to stiction in the joints, causing spasmodic slipping as they were loaded. Adopting a linear model for the stiffness variation, a new updating scheme was implemented. This time six parameters were used; each of the three stiffnesses was defined in terms of a zero-load stiffness and a linear load-dependent component. The new scheme used data from all the load cases simultaneously, and the parameter values obtained are seen in figure 3.15(c). These parameters give an excellent reproduction of the experimental behaviour, as presented in figure 3.14(e).

These results demonstrate that the influence of friction on joint parameters demands the adaptation of parameters to the loading conditions. While many studies have been devoted to the effects of stress stiffening on dynamic response in slender beams and plates, there does not appear to be a

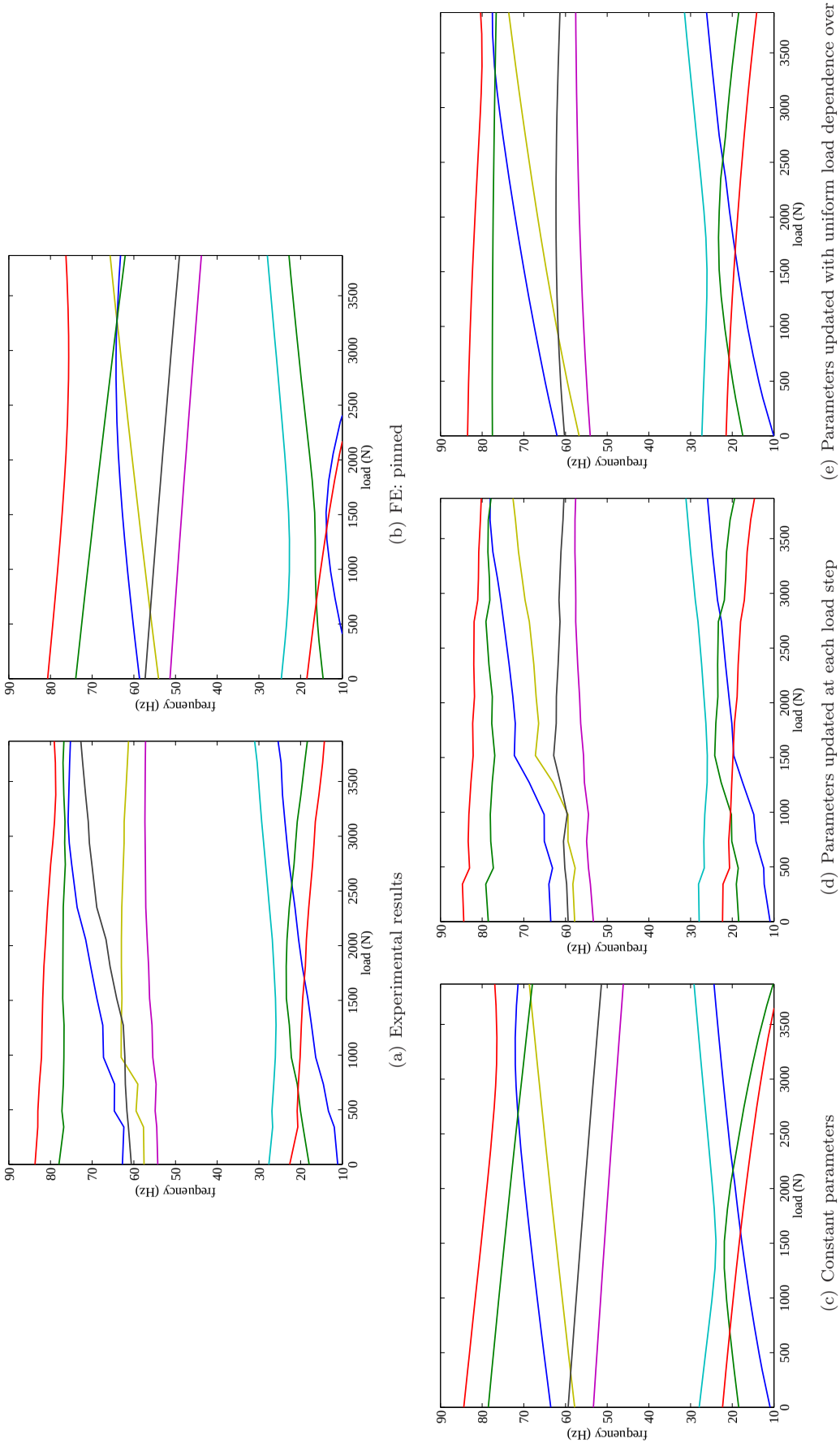

(a) Experimental results (b) FE: pinned (c) Constant parameters (d) Parameters updated at each load step (e) Parameters updated with uniform load dependence over all load steps

Figure 3.14: Variation of the natural frequencies with internal loading in the experimental rig and several FE configurations.

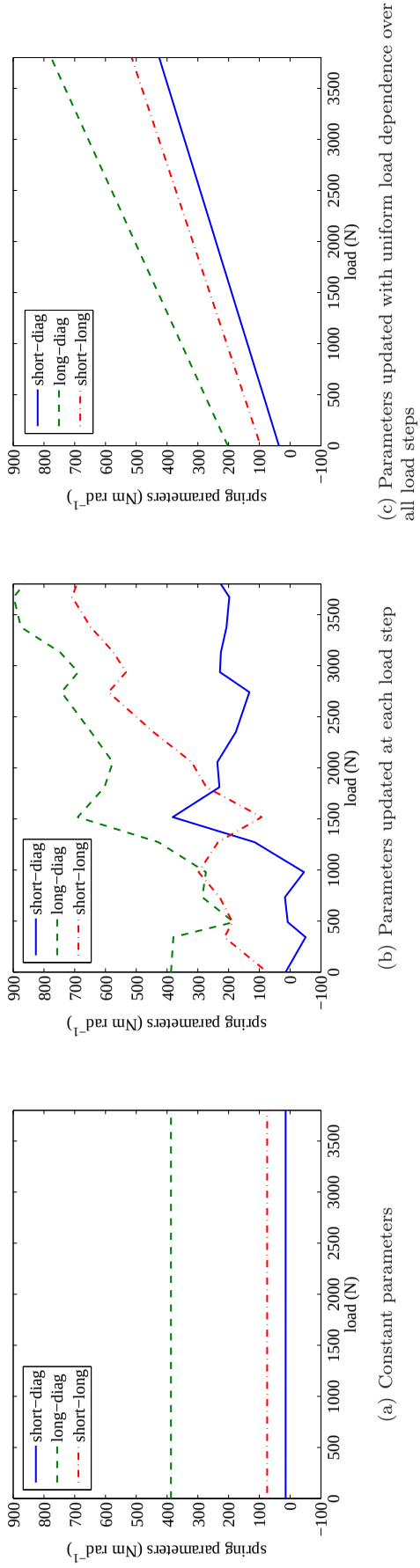

(a) Constant parameters

(b) Parameters updated at each load step

(c) Parameters updated with uniform load dependence over all load steps

Figure 3.15: Variation of the parameters with internal loading for several FE configurations.

standard approach in the literature for dealing with the effects of nonlinear static joint loading. Joint modelling in general has received much attention; for example, uncertainties in fastened joints are reviewed by Ibrahim and Petit [213]. The influence of loading has also been recognised: Bahra and Greening [214] discuss the difficulties of joint parameterisation in loaded frames, and recognise that boundary conditions are load-dependent variables. Folkman *et al.* [215] discuss the effects of gravitational loading on the damping ratios of pinned trusses and their findings are confirmed by the experimental results of Bingham and Folkman [216]. In a similar investigation Hsu *et al.* [217] include gravity effects in an analytic pinned joint model, but none of these studies propose a global analysis technique.

The work conducted here suggests that it would be beneficial to develop a set of common joint models which can respond in a continuous and realistic manner to loading. In fact, the results presented above show that without something of this nature it will be impossible to predict the dynamic behaviour of loaded structures accurately, even for simple configurations.

3.4 Welded Frame

3.4.1 Nonlinear Buckling

The welded frame differs from the pin-jointed frame in only one respect: the corner joints are welded as pictured in figure 3.16. The implications of this in terms of its behaviour under loading are concerned primarily with the shear and moment transfer between the members. In contrast to the pinned frame which exhibited abrupt, almost idealised buckling, the welded frame will be prone to a more gradual onset of buckling as the end moments contribute to the transverse beam deflections. The new frame does, however, possess greater stiffness and hence a higher buckling load. The welded joints are also expected to provide more reliable and predictable results than the pinned equivalents, free from the parametric uncertainties and damping of the previous model.

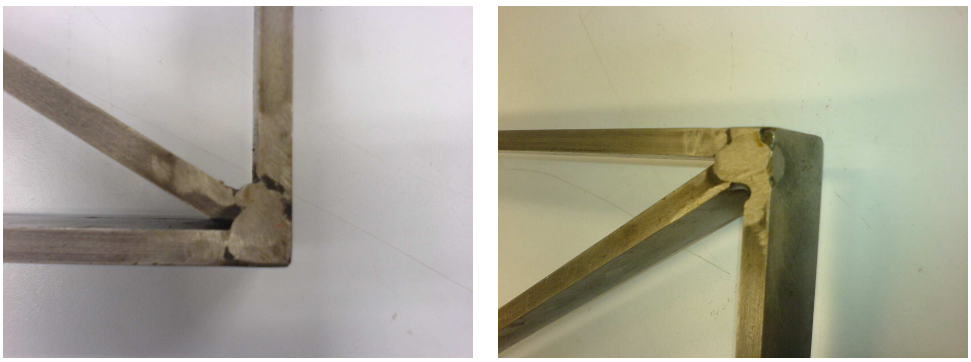

(a) (b)

Figure 3.16: Examples of the corner joints in the welded frame.

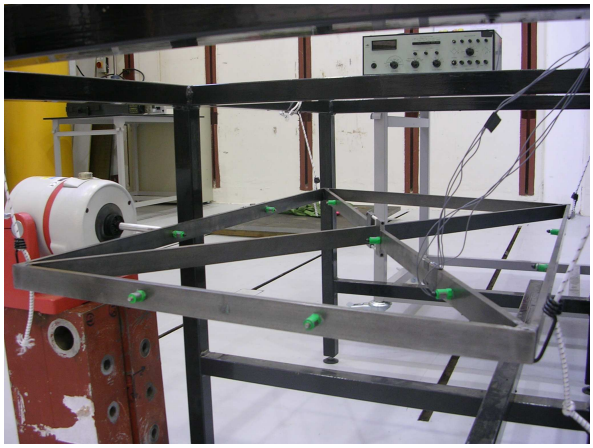

Figure 3.17: Experimental configuration for the welded frame tests.

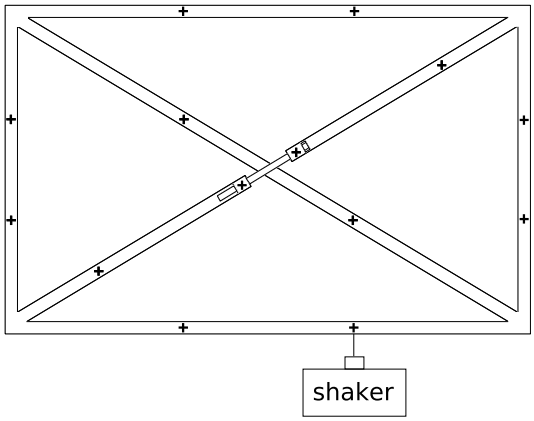

Figure 3.18: Arrangement of the shaker and accelerometers (denoted with +) for the welded frame experiment.

The expermental setup is pictured in figure 3.17. For this frame only one shaker is necessary as the welded joints couple the two translational DOFs. The position of the shaker is illustrated along with the accelerometer placements in figure 3.18. The frame was tensioned incrementally up to the buckling load at approximately 6800N and modal properties were determined as with the pinned frame, producing the frequency loci in figure 3.19(a).

The FE model was evaluated using 300N load steps with Newton-Raphson iterations, producing the frequencies in figure 3.19(b). It is seen that the two graphs, although similar, show some discrepancies at the higher loads, close to buckling. The deformation of the FE model, subject to loading below the buckling threshold, is seen in figure 3.20(a). The structure buckles abruptly at the critical load, in the mode illustrated in figure 3.20(b). This idealistic buckling behaviour is rarely seen outside of text books and computer simulations. As elaborated in section 2.4.3, small imperfections in beam and force alignments combined with material and assembly defects lead to a more gradual onset of buckling, usually at a lower load than the ideal case. Zienkiewicz [182] suggests the deliberate introduction of small imperfections to analytical models to simulate realistic buckling behaviour. Following this procedure, small perturbations in the beam alignment prior to loading were found to produce considerable changes in the buckling behaviour. Assuming an initial curvature of the long external members of the frame - caused perhaps by residual stresses from the welding process - the FE beams were endowed with a transverse displacement in the form of a half sine wave along their length. Varying the extent of this initial perturbation, it was found that an amplitude of 1.85mm (0.185% of the member length) produced frequencies that matched the experimental results, witnessed by figure 3.19(c) Figure 3.21 shows the load-displacement curves for the two cases at the point of application of the load (node 3 in figure 3.4). From these curves it is seen that the abrupt failure of the ideal structure is replaced with a gradual deformation in the imperfect model. The deformation takes approximately the same form as the eventual failure mode seen in figure 3.20(c). This behaviour conforms with the visual inspections of the experimental structure made as it reached the buckling load.

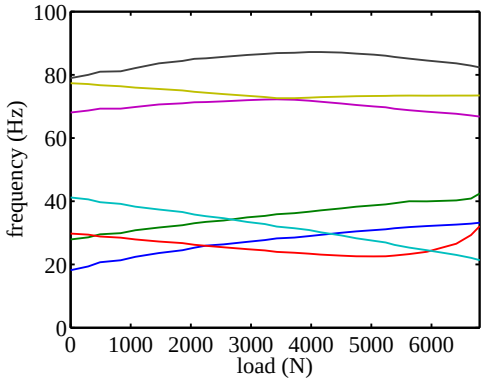

(a) Experimental data

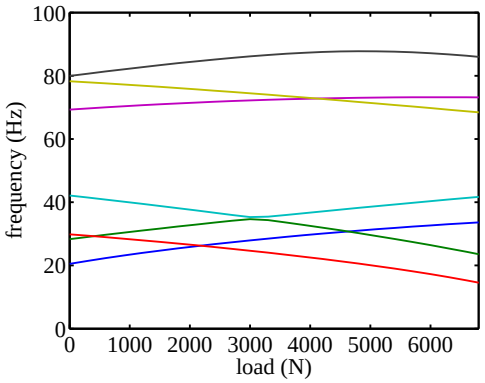

(b) Initial FE Results

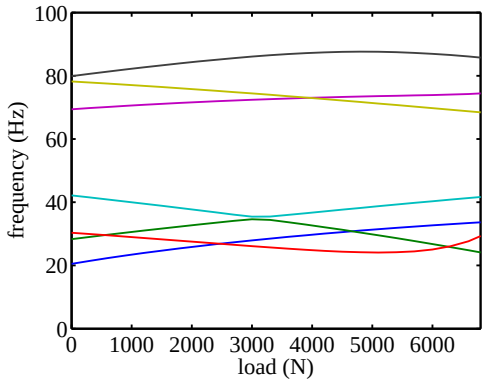

(c) Perturbed FE Results

Figure 3.19: Frequency loci in the welded frame under loading.

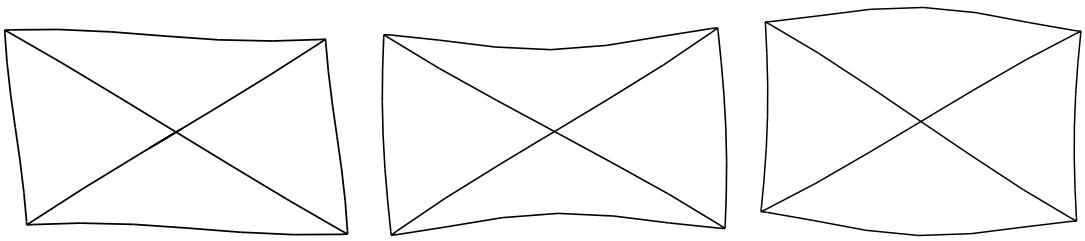

(a) Idealised, pre-buckling

(b) Idealised, post-buckling

(c) Perturbed, pre- and post-buckling

Figure 3.20: Deformation patterns and buckling modes for the welded frame with idealised conditions compared to those for a frame with initial curvature in the members.

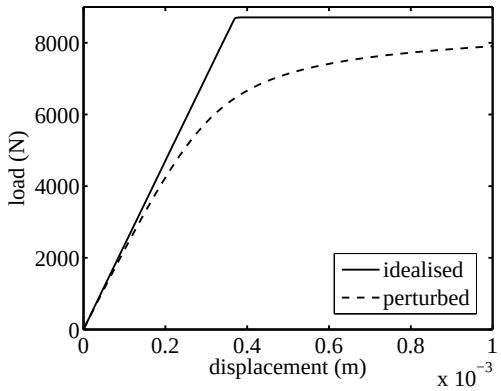

Figure 3.21: Load displacement curves comparing buckling in the idealised and perturbed FE models.

3.4.2 Investigation of Stress Stiffenening Approximations

Several levels of stress stiffening approximations are discussed in chapter 2. In this section the different techniques are applied to the welded frame structure to determine the limits of their applicability.

To recapitulate, the desired output from the nonlinear static solution is the tangent stiffness. This is computed using knowledge of the load distribution. The load distribution may be determined with a single computation, equivalent to a linear static analysis. Greater accuracy is introduced by applying the load incrementally and re-evaluating the tangent stiffness at each step. Still further accuracy is obtained by performing Newton-Raphson iterations (NRIs) at each load step to converge on a consistent load-displacement solution. These three cases will be examined below.

The effects of the different methods on the static solution are illustrated using a load-displacement plot for the free end of the tensioning mechanism in the FE model. Variation in the tangent stiffness manifests itself as changes in the gradient of the curve. In figure 3.22, five load steps take the model just shy of its buckling load. The linear solution uses a constant tangent stiffness and produces a linear load-displacement relationship. With the two iterative techniques, the discrepancies in the tangent stiffness become apparent at higher loads, where the incremental solution diverges from the more accurate Newton-Raphson result. The accuracy of the incremental solution may be increased by refining the load steps as shown in figure 3.23. In contrast, the Newton-Raphson method was found to produce identical results to seven significant figures, even when reduced to a single load step. (The latter required ten NRIs in contrast to the five-step case which required between four and eight NRIs for each load step.)

Noting that the linear displacement curve follows the iterative solutions reasonably well in the lower half of the loading spectrum, a linear tangent stiffness variation (corresponding to a constant load distribution) is used to produce the frequency loci in figure 3.24. They are found to closely resemble the Newton-Raphson results away from the buckling region. In figure 3.25 the differences in the two result sets are seen to increase as the nonlinear behaviour encroaches at higher loads. It is worth noting that the results for all but a select few modes remain within 0.5% of each other over the entire loading regime and the other results remain within 1.5% of each other for the lower half of the loading spectrum. This justifies the use of linear tangent stiffness variation in a range of modelling problems, and later chapters will take advantage of this simplifying assumption. For now, however, the iterative Newton-Raphson scheme is retained.

3.4.3 Frequency Response Analysis

Up to this point, only modal characteristics have been considered. In order to produce beneficial dynamic alterations, the magnitude of the response must be reduced. In this section the frequency response functions (FRFs) for the welded frame are examined. A slightly different experimental arrangement was used, primarily to investigate some curious behaviour observed in the FE results,

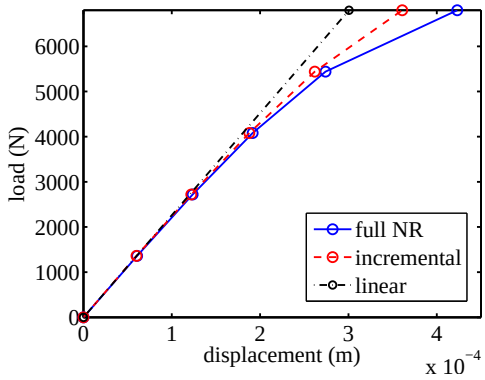

Figure 3.22: Load-displacement plot for the welded frame using linear, incremental, and full Newton-Raphson solution methods with large load step increments.

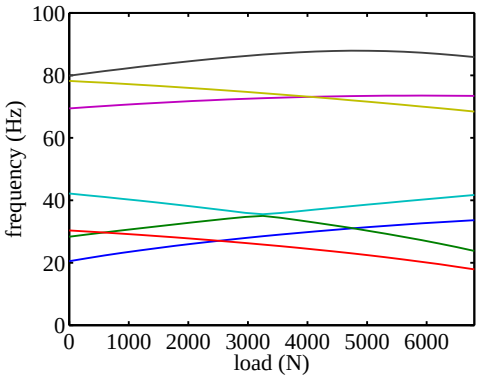

Figure 3.24: Frequency loci for the welded frame obtained using the linear stress stiffening approximation.

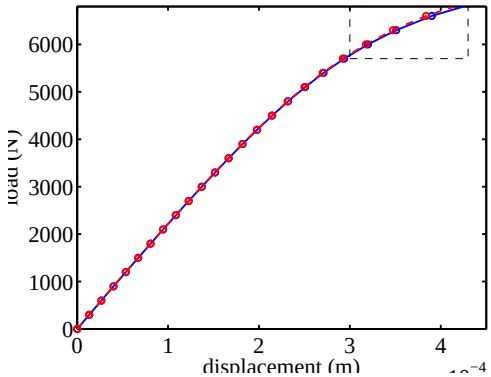

(a) Full scale; the boxed region is shown in (b).

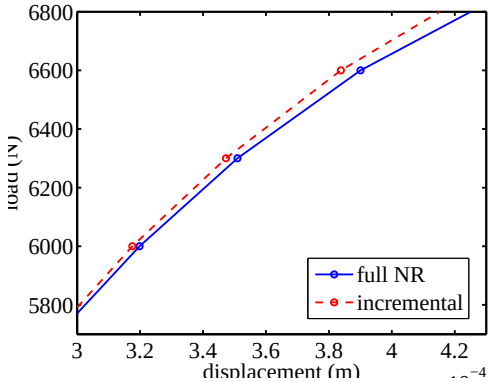

(b) Close up of the boxed region.

Figure 3.23: Load-displacement plot for the welded frame using incremental and full Newton-Raphson solution methods with small load step increments.

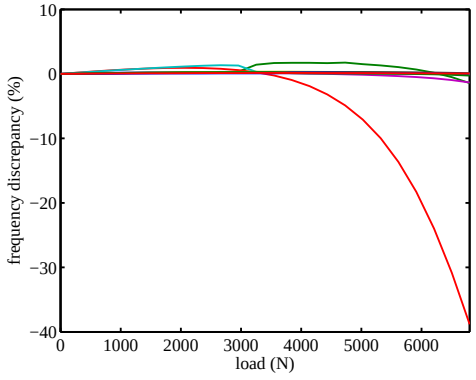

(a) All modes.

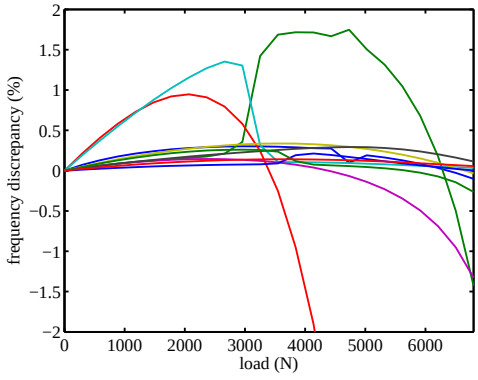

(b) Close examination of least affected modes.

Figure 3.25: Discrepancies in the natural frequency results obtained using full NR iterations and a linear stress stiffening approximation.

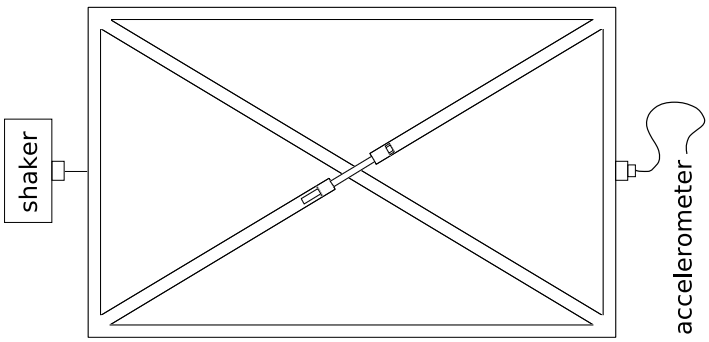

Figure 3.26: Arrangement of the response and excitation points for the FRF studies of the welded frame.

discussed later in this section. The setup is pictured in figure 3.26.

Using modal superposition and assuming a universal viscous damping ratio of 1.2×10^{-3} (the mean of the experimentally determined damping ratios), the frequency response function for the zero load case is plotted in figure 3.27 in terms of magnitude and phase. Similar FRFs are computed at 11.$\dot{3}$N intervals, their magnitudes producing the waterfall plot seen in figure 3.28(a) alongside the experimental results in figure 3.28(b). The two data sets compare well, with only small discrepancies: some noise is apparent in the experimental results and there are artefacts from small-amplitude modes which do not appear in the FE data. Examples are seen at approximately 40Hz and 95Hz. While these could be attributed to unmodelled complexities in the tensioning mechanism, they are more likely a contribution from out-of-plane modes, introduced through imperfect alignment of the beams, accelerometers and shaker. This hypothesis is supported by the fact that these anomalous modes vary to a much lesser degree with applied loading than the primary in-plane modes, as would be the case for bending about the much stiffer out-of-plane axis of the beams.

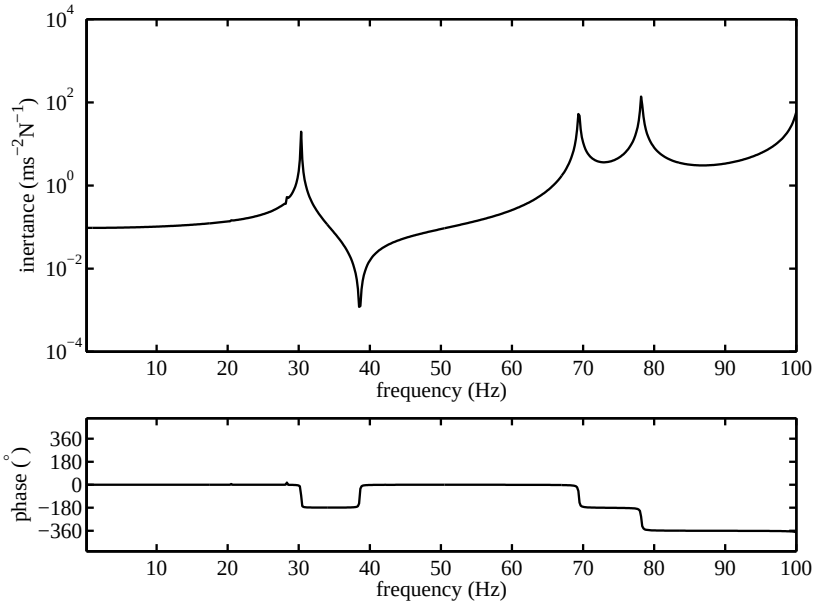

Figure 3.27: FRF of the welded frame measured on longitudinally opposite sides for the zero load case.

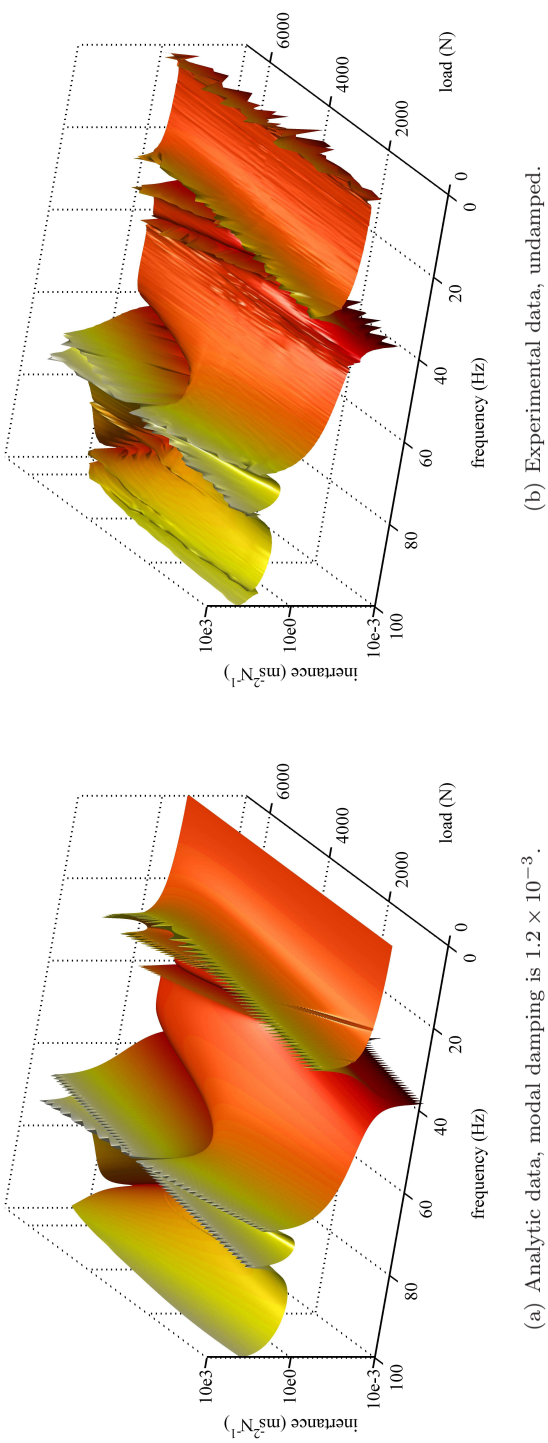

(a) Analytic data, modal damping is 1.2×10^{-3}.

(b) Experimental data, undamped.

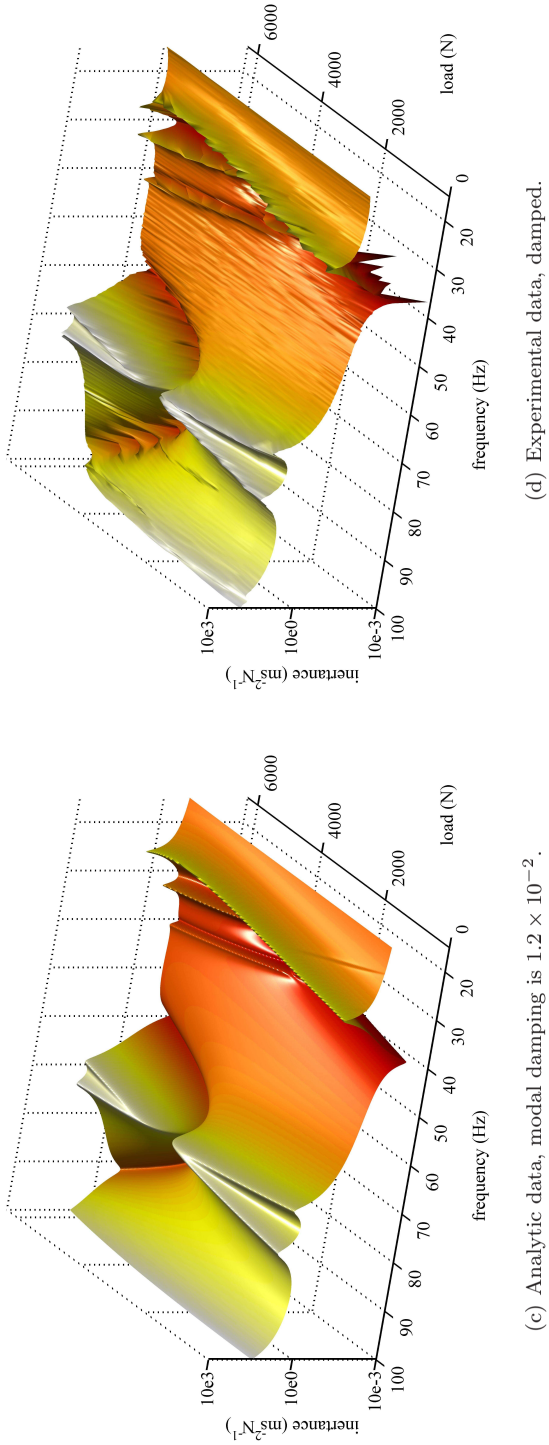

(c) Analytic data, modal damping is 1.2×10^{-2}.

(d) Experimental data, damped.

Figure 3.28: Waterfall plots showing the variation of FRFs for the welded frame with loading. Experimental and analytic data for two damping cases.

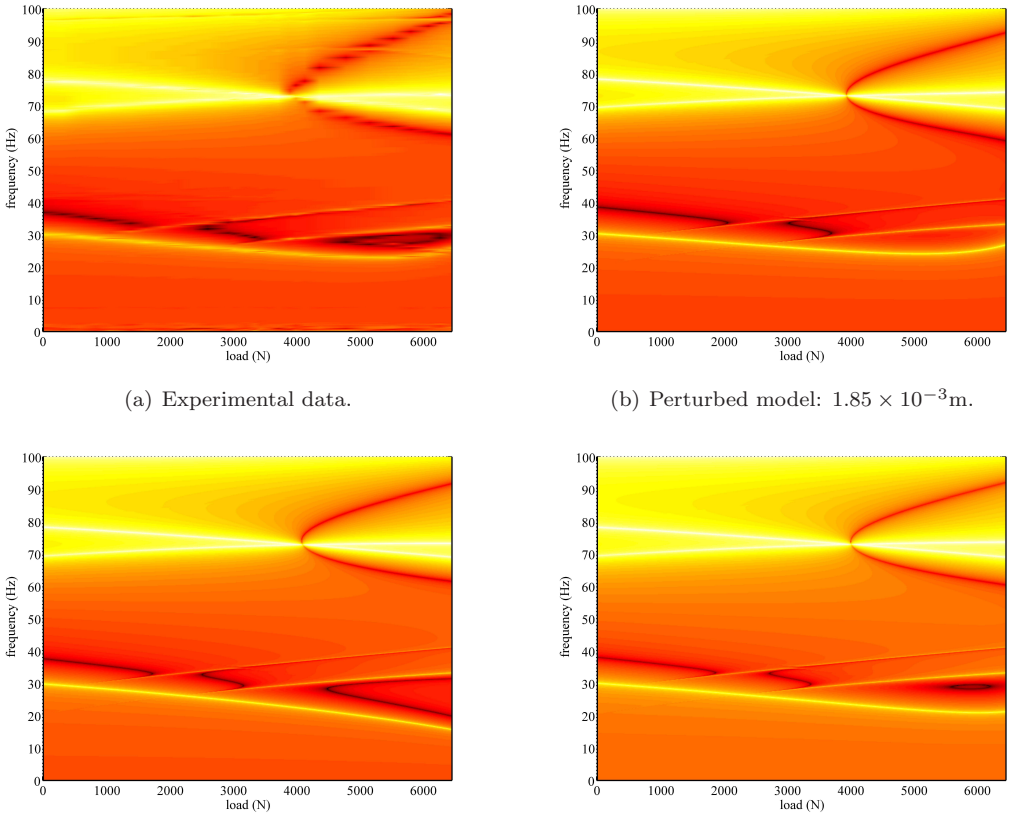

(a) Experimental data.

(b) Perturbed model: 1.85×10^{-3}m.

(c) Unperturbed model.

(d) Smaller perturbation: 1.2×10^{-3}m.

Figure 3.29: Contour plots comparing the FRFs over the loading regime, compared with the experimental FRF variations across the loading regime.

A clear overview of the behaviour of the FRFs under loading is afforded by viewing the waterfall plots from directly overhead, using colour to distinguish the amplitudes in a form of continuously varying contour plot. This approach will be adopted frequently throughout this thesis and several examples are seen in figure 3.29, comparing the effects of differing levels of initial beam perturbation on the response variations. From these charts it is apparent that, despite good modal parameter agreement, the FE model that has been developed still fails to describe exactly the behaviour of the welded frame. The differences manifest themselves most clearly in the antiresonances. In particular, the experimental results in figure 3.29(a) show an antiresonant 'ring' sandwiched between resonances in the bottom right corner of the plot, while the FE results in figure 3.29(b) show no antiresonances in this region. Reverting to the unperturbed model which was abandoned in section 3.4.1 reveals an antiresonant curve in fig.3.29(c), and adopting a smaller perturbation of 1.2×10^{-3}m produces a similar ring, seen in figure 3.29(d). An exact match cannot be obtained without introducing further parameters but this investigation illustrates the usefulness of the extra information in describing system behaviour. An updating scheme could, for example, make use of the antiresonances to increase the accuracy of the analytical model [218–220]. Care must be taken with such schemes, as antiresonance measurements will be strongly influenced by misplacement or misalignment of accelerometers, force transducers and other measurement apparatus.

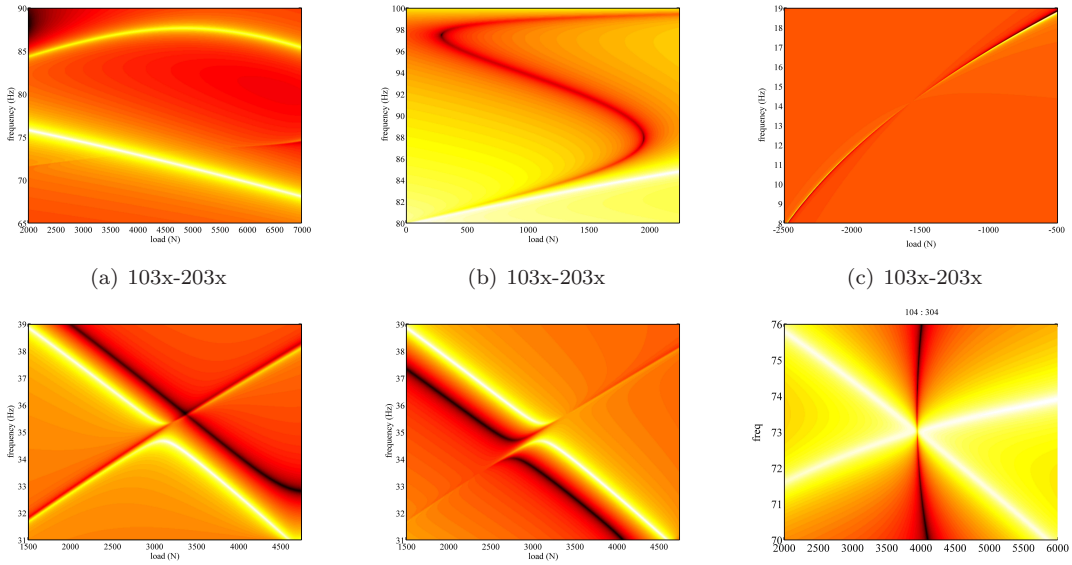

(a) 103x-203x (b) 103x-203x (c) 103x-203x

(d) 103x-503x (e) 103x-403y (f) 104x-304x

Figure 3.30: Examples of regions where the dynamic response can be manipulated to produce beneficial results. Labels refer to excitation and response nodes, as seen in figure 3.31.

Examining various analytical FRFs for the welded frame, several opportunities are identified for reducing response amplitudes. Examples are highlighted in figure 3.30, with locations referenced using the FE model node numbers from figure 3.31. The methods fall into two broad categories: manipulation of the natural frequencies, and manipulation of the antiresonances.

The former is the most obvious solution; if the natural frequencies are shifted away from the dominant excitation frequencies then a reduced response is achieved. This technique would provide flexibility in the design of structures with variable excitation conditions, as any natural frequencies within the excitation bandwidth could be actively controlled during operation to avoid coincidence with the excitation frequency. An example of natural frequencies that are sensitive to loading can be seen in figure 3.30(a).

Manipulation of antiresonances is performed in the same manner as with resonances, and the technique presents several opportunities for reducing response. By aligning antiresonances with excitation frequencies, the response at those frequencies is eliminated. A good example of antiresonance manipulation is seen in figure 3.30(b). Alternatively, antiresonances may be aligned with natural frequencies in order to cancel out the resonance. An example is given in figure 3.30(c). Essentially, by aligning an antiresonance with a resonance for a given FRF, the respective DOF becomes a node for the mode in question. The advantage of considering the problem in terms of antiresonances is that antiresonance sensitivities to parameter changes are easily calculated, thus simplifying the problem of determining appropriate parameter values. The drawback of these methods is that antiresonances vary from point to point around a structure so they can only influence local response levels and can not provide a system-wide solution.

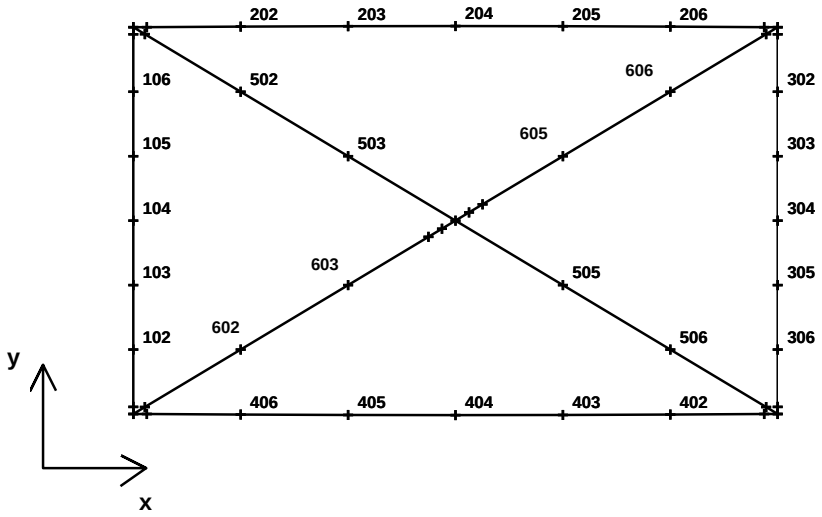

Figure 3.31: Locations and numbering of nodes in the FE model.

A third category of methods can also be considered, combining the methods discussed above to take advantage of some potentially useful side effects. These effects are observed where two frequency loci intersect; the interaction of the modes can sometimes lead to unusual results. In figure 3.30(d), the antiresonance associated with the rising frequency locus appears to punch a gap in the other mode's resonant ridgeline. Figure 3.30(e) shows a similar case, where one of the modes does not manifest itself strongly on the FRF but its interaction with the other mode creates a gap in the resonant band which may be exploited. These interactions are studied in detail in chapter 4. A different behaviour is seen in figure 3.30(f), as an antiresonance and two resonances coincide at the same point to cancel the response of both modes simultaneously. A numerical and experimental examination of this effect is undertaken in the next section. Because of the intrinsic involvement of antiresonances, it should be noted that these methods will once more produce differing effects around the structure.

3.4.4 Investigation of the Effect of Damping on Modal Interaction

The region identified in figure 3.30(f) is at the point where the fifth and sixth modes intersect, seen at around 70 Hz in figure 3.28. While the FE results predict a significant drop in the response where the two curves meet, the experimental data does not show the same level of reduction. The source of the discrepancy was thought to be the lack of resolution in the experimental data. The effect spans only a small parameter variation, and such a small range of influence is not only easy to overlook in an experiment but also has limited practical use. This section outlines experiments that were carried out in an effort to expand the parameter range spanned by the region of reduced response, with a view to verifying the FE predictions and investigating the potential for exploitation.

First the cause of the behaviour is examined, demonstrating how it is intrinsically linked to the interaction of the two proximate modes. The FRF in this region can be broken down into three parts: the individual contributions from modes five and six and the contribution from the rest of the modes,

where the contribution from the rest of the modes is close to zero for the range being considered. In figure 3.32 the real parts of the two significant contributions are plotted with the complete FRF overlaid. Using the principle of superposition afforded by linear dynamic approximations, the total FRF is given by summing the individual contributions. Where the contributions cancel each other out, regions of reduced response will result. Because the two modes being considered both exhibit similar peak response amplitude and damping, it is possible for this cancelation to nullify almost all of their contribution to the response. Three load cases are considered, resulting in three distinct classes of mode separation: well separated modes (figure 3.32(a)), proximate modes (figure 3.32(b)), and coincident modes (figure 3.32(c)). For the well-separated modes, the FRF roughly follows the peaks and troughs of the individual contributions. As the modes approach, the contibutions are summed to form a single peak with a high amplitude. Where the modes coincide, however, they all but eliminate the response.

For the modes to interact with one another favourably over a wider range of loading, they would need to cancel each other out even when their natural frequencies are non-coincident. To accomplish this, greater damping can be introduced. Damping has the effect of spreading the response peaks, allowing the modes to interact with greater separation between them. The analytical result can be seen in the FRFs in figure 3.33. The response for the coincident modes remains low, and the proximate modes now also see a reduced response. The trade-off is with the well-separated modes, which now experience a far greater bandwidth of high magnitude response.

In the experimental arrangement, the damping was provided at the frame supports. Instead of suspending the frame from bungee cords, it was supported by foam sponges as seen in figure 3.34. This was found to provide similar elastic boundary conditions to the bungee cords and similar results were obtained. The damping was introduced by soaking the sponges in oil. Whilst crude, this method served its purpose; all of the measured damping ratios were increased by approximately one order of magnitude. Accordingly, the FRFs were calculated for the FE model with an increased modal damping ratio of 1.2×10^{-2}. The experimental and analytical results are shown in figures 3.28(c) and 3.28(d). Similar behaviour is seen in each, from which it is clear that, as predicted, the parameter range covered by the region of reduced response is increased with greater damping at the expense of larger resonant bandwidths outside of this region.

If this behaviour were to be exploited, two adjacent modes would need similar response amplitudes at the spatial coordinate of interest, but 180° out of phase with each other (recognised by an even number of antiresonances between them). The fundamental principle is then to manipulate the modes such that their frequencies are coincident. It was noted in the course of these investigations that the two modes were never quite coincident in the laboratory tests; instead of crossing, the frequency loci veered away from one another as if repelled. A close examination of the intersection is seen in figure 4.4(c). This observation has significant consequences for the application of the ideas discussed here and was also found to be responsible for the behaviour seen in figs. 3.30(d) and 3.30(e). The next chapter will explore the intricacies of this frequency curve veering.

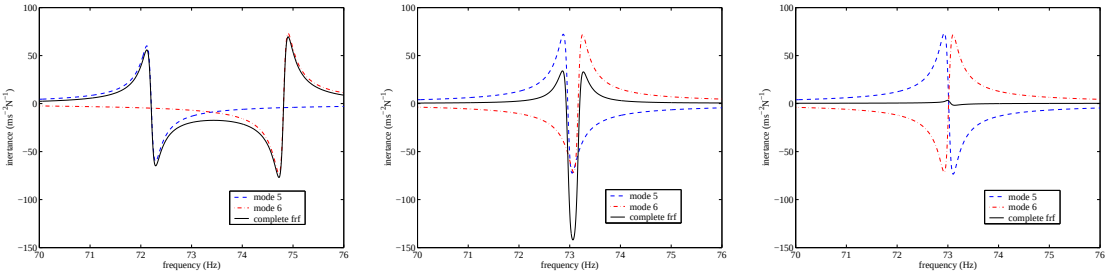

(a) 2720 N : separated (b) 3850 N : proximate (c) 3950 N : coincident

Figure 3.32: Real part of the FRF for the welded frame under loading (–); shown here with the two significant contributions, from modes 5 (- -) and 6 (-.). Modal damping is 1.2×10^{-3}.

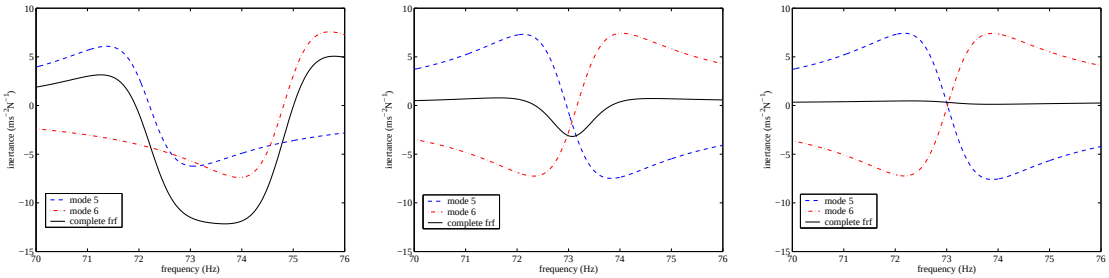

(a) 2720 N : separated (b) 3850 N : proximate (c) 3950 N : coincident

Figure 3.33: Real part of the FRF for the welded frame under loading (–); shown here with the two significant contributions, from modes 5 (- -) and 6 (-.). Modal damping is 1.2×10^{-2}.

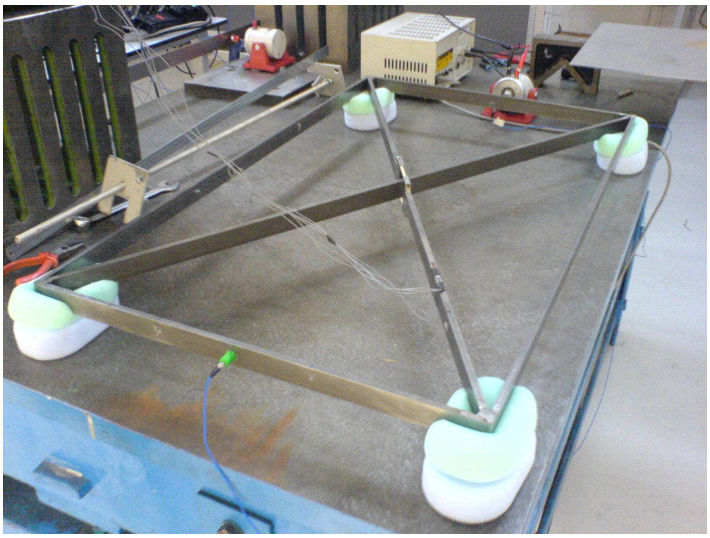

Figure 3.34: Experimental configuration for the damped welded frame.

3.5 Conclusions

From the investigations of the two frames it has been demonstrated that stress stiffening approximations can reproduce the dynamic behaviour of a structure under loading to a good degree of accuracy in terms of both modal properties and response functions. It was found that a full Newton-Raphson iterative scheme was generally the most suitable FE solution method, producing the most accurate results with the most effiecient use of computational effort. This is particularly true as structures approach their buckling load, and it was found that an accurate dynamic solution is obtained by following the same guidelines as used for nonlinear static solutions; this relates not only to the choice of solution method (linear, stress-stiffening, large rotation etc.) but also to considerations such as the introduction of small imperfections to induce nonlinear buckling. A convenient consequence of this finding is that wherever a linear static analysis may be applied, the load distribution may be considered constant thus providing a linear variation of the tangent stiffness with load. Using this assumption obviates the need for iterative schemes in the linear loading regime, which was found to extend to roughly half the buckling load in the examples studied here.

An important lesson learned from these experiments lies in the sensitivity of the FE solution to small parametric changes. Even for a simple structure the uncertainties can cause considerable discrepancies in the results. Significantly, it has been established that joint parameters updated for the zero-load case are unlikely to remain valid over the whole loading spectrum, especially where the parameters help describe friction effects within the joint. This was shown to be the case in the pin-jointed example despite good parametric consistency between different assembly configurations at zero load. A method of adapting joint parameters based on structural loading has been suggested, effectively implementing stress stiffening in the joints to complement that of the beam and shell elements.

Exploration of the FRFs from the analytical model reveals several opportunities for reducing response levels. These can be categorised either as natural frequency manipulations, antiresonance manipulations, or modal interactions. Natural frequency manipulations seek to avoid coincidence of natural frequencies and excitation frequencies. Antiresonance manipulations can be used to align antiresonances either with the excitation frequencies or with the natural frequencies. Modal interactions have been found to produce both interuption of resonant peaks through mode veering, and reduced response through modal superposition. Where modal interactions are to be exploited, it has been shown that increased damping may serve to broaden the region of influence of these effects.

Chapter 4

Eigenvalue Curve Veering

4.1 Introduction

In chapter 3, a phenomenon known as frequency curve veering was observed in the experimental results for the fifth and sixth modes. In contrast to the analytical results, where the two frequency loci cross at around 4 kN, the experimental loci follow intersecting trajectories but veer away from each other abruptly, each continuing on the path initially followed by the other. Early references to this type of behaviour in structural dynamics date back to the 1950s, and were the topic of much debate in the ensuing decades. Doubts were cast initially over the existence of veering outside of numerical models and, later, over its relevance to practical structures. More recent works have provided robust explanations for the phenomenon, and its manifestation has found practical application in some fields.

This chapter begins with a thorough investigation of the theory governing the behaviour, supported by experimental and numerical data. It is found to have bearing on a wide range of problems, yet, to date, no practicable method exists for quantifying its presence. The concluding sections of the chapter seek to reconcile this deficit by deriving new normalised criteria for measuring the intensity of effect. Section 4.2 reviews the historical and contemporary understanding, section 4.3 presents a numerical and experimental case study, and section 4.4 derives the new quantitative indices.

4.2 Overview

4.2.1 Historical Background

Early observations of eigenvalue curve veering in structural dynamics were highlighted by Claassen and Thorne [221]. Leissa [222] cited further examples [223–232] to draw attention to what he saw as fallacious artefacts in numerical models, and demonstrated that veering could be artificially induced through inadequate approximations. Later, Kuttler and Siglillito [233] used rigorous error bounds to

confirm the existence of curve veering in accurate mathematical models and Perkins and Mote [234] adapted Schajer's work [235] to present an exact mathematical solution exhibiting the behaviour. Further analytical examples can be found in references [236–241].

Principally, the description is applied to systems where two eigenvalue loci converge but veer suddenly away again, each one taking on the trajectory of the other. In this case all of the properties of the two modes are swapped, including damping ratios, sensitivities and eigenvectors (or eigenfunctions). The transition is always smooth, albeit abrupt, and will be shown to be an extreme manifestation of normal parametric variation. The effect is exploited by techniques for establishing the Poisson's ratio of orthotropic plates [242], plays a role in localisation [243–252] and can have a strong influence on dynamic response in systems with sensitive configurations [253]. It is also important in flutter prediction in rotating blade assemblies [254] and its use has been advocated for analytical model updating [255] and damage detection [256].

4.2.2 Contemporary Observations

A common theme amongst reported cases of veering is some form of symmetry in the structure being analysed. Modes in symmetric structures are always symmetric or antisymmetric with respect to that symmetry and many authors [234, 236–239] have noted that a symmetric mode's frequency locus will cross that of an antisymmetric mode while two symmetric or two antisymmetric modes will generally veer. An explanation for this behaviour is provided in section 4.2.3. Nair and Durvasula [241] observe that the introduction of small asymmetries to a symmetric system will change crossings to veerings (or to use their words, *quasi-degeneracies*). Consequently, as a result of imperfections, any practical symmetric structure will tend to exhibit some degree of veering.

Similar findings have been made in the related and better known field of localisation. Localisation is commonly encountered in systems with weakly coupled substructures and symmetric or periodic structures with some degree of disorder. Such structures are not exceptional; the occurence of this effect is well documented and there is much discussion of the relationship between veering and localisation in the literature, for example references [244–252]. More specifically, Natsiavas [257] notes that localisation is necessarily accompanied by veering but that veering may occur without localisation. The first explicit practical demonstration of localisation was given by Hodges and Woodhouse [243].

Some efforts have been made to predict and quantify veering. Pierre [246] explains how localisation and veering are related to two "couplings": the physical coupling between the component structures, and the modal coupling seen between mode shapes through parameter perturbations. Localisation and veering occur when the former is of the same order or smaller than the latter. Perkins and Mote [234] derive "coupling factors" to quantify the eigenfunction coupling. Only when the coupling factors are zero may the curves cross. If the coupling factors become large veering occurs gradually, losing much of its characteristic abruptness. Liu [249] suggests that a critical value could be defined for the derivative of the eigenvectors or for the second derivative of the eigenvalues, above which the

modes would be deemed to be veering.

A useful characterisation is to examine the eigenvector rotations of the two modes, responsible for their sometimes aesthetically bizarre transformations. Balmès [255] expressed system properties for a three degree of freedom lumped-mass system in terms of two eigenvalue perturbations and a rotation angle, and demonstrated that as two of the modes went through a veering region the eigenvectors both rotated in their plane by almost 90°. It will be shown that this result can be extrapolated to many veering systems.

A final consideration is the effect of damping on veering modes. Woodhouse [258] demonstrated how the effects of modal coupling can be offset by a large difference in modal damping factors. In this case, the eigenvectors may become significantly complex and the eigenvalue loci may cross instead of veering. Adhikari [259] showed how eigenvector sensitivities can differ from their undamped equivalents in veering regions, even when modal Q-factors are high (low damping). Intrinsic to both these examples, however, is a substantial level of non-proportional damping in the system, resulting in notable variation of the modal damping ratios as the loci approach. It is implicit that systems with uniform low damping may, as usual, be treated as undamped for analytical purposes.

4.2.3 Theoretical Basis

Perkins and Mote [234] use perturbation theory [260, 261] to derive expressions for the eigenvalues of two proximate modes in terms of a perturbation parameter, ε, as

$$\begin{aligned}\lambda_i(\varepsilon) =&\lambda_i^0 + [a_i]\,\varepsilon + \frac{1}{2}\left[D^2 a_i + D^2 d_i + \frac{D^2 x_{ij}}{\lambda_i^0 - \lambda_j^0}\right]\varepsilon^2 + O(\varepsilon^3)\\ \lambda_j(\varepsilon) =&\lambda_j^0 + [a_j]\,\varepsilon + \frac{1}{2}\left[D^2 a_j + D^2 d_j + \frac{D^2 x_{ji}}{\lambda_j^0 - \lambda_i^0}\right]\varepsilon^2 + O(\varepsilon^3).\end{aligned} \tag{4.1}$$

where λ_i is the i^{th} perturbed eigenvalue, λ_i^0 is the i^{th} unperturbed eigenvalue and a thorough definition of the other symbols may be found in Perkins and Mote's paper. For the present discussion only the curvature in the eigenvalue loci is of interest, given by the term in ε^2. As the loci converge and $|\lambda_i^0 - \lambda_j^0|$ approaches zero, the curvature expression is dominated by the third bracketed term. Perkins and Mote refer to $D^2 x_{ij}$ and $D^2 x_{ji}$ as the coupling factors, given by

$$\begin{aligned}D^2 x_{ij} = \frac{d^2}{d\theta^2}\big[&\big(< k[u_j^0], u_i^* >_\tau - \lambda_i^0 < m[u_j^0], u_i^* >_\tau\big)\\ &\times\big(< k[u_i^0], u_j^* >_\tau - \lambda_i^0 < m[u_i^0], u_j^* >_\tau\big)\big]\\ D^2 x_{ji} = \frac{d^2}{d\theta^2}\big[&\big(< k[u_i^0], u_j^* >_\tau - \lambda_j^0 < m[u_i^0], u_j^* >_\tau\big)\\ &\times\big(< k[u_j^0], u_i^* >_\tau - \lambda_j^0 < m[u_j^0], u_i^* >_\tau\big)\big]\end{aligned} \tag{4.2}$$

where u_i^0 is the i^{th} eigenfunction of the unperturbed eigenproblem, u_i^* is the corresponding eigenfunction of the adjoint eigenproblem, k and m are perturbation operators relating to a small perturbation

in the parameter θ, and $<,>_\tau$ represents an inner product over τ. These coupling factors determine the concavity of the loci as the modes converge: without coupling the loci are locally independent and free to cross; two positive factors will cause the curves to veer away from each other; two negative factors will cause them to veer towards each other (often associated with eigenvalue coalescence); and differing signs result in the loci veering with each other.

Perkins and Mote's coupling factors are written here for the case of self-adjoint system matrices:

$$\mathrm{CF}_{ij} = \frac{\mathrm{d}^2}{\mathrm{d}\theta^2} \left\{ \left[\phi_j^T \left(\mathbf{\Delta K} - \lambda_i \mathbf{\Delta M} \right) \phi_i \right]^2 \right\} \tag{4.3}$$

where $\mathbf{\Delta K}$ and $\mathbf{\Delta M}$ are changes in the mass and stiffness matrices with a change in parameter θ, and λ_r and ϕ_r are the r^{th} eigenvalue and eigenvector, respectively. Performing the differentiation about the point where $\mathbf{\Delta K} = \mathbf{\Delta M} = \mathbf{0}$ yields

$$\mathrm{CF}_{ij} = 2 \left[\phi_j^T \left(\frac{\mathrm{d}\mathbf{K}}{\mathrm{d}\theta} - \lambda_i \frac{\mathrm{d}\mathbf{M}}{\mathrm{d}\theta} \right) \phi_i \right]^2 . \tag{4.4}$$

This expression can only produce non-negative coupling factors; thus the eigenvalue loci of self-adjoint systems will either cross or veer away.

The coupling factors may be used to explain the observations of veering in symmetric structures. The system matrices for a symmetric structure can be arranged such that

$$\mathbf{M} = \begin{bmatrix} \mathbf{M}_d & \mathbf{M}_o \\ \mathbf{M}_o & \mathbf{M}_d \end{bmatrix} \qquad \mathbf{K} = \begin{bmatrix} \mathbf{K}_d & \mathbf{K}_o \\ \mathbf{K}_o & \mathbf{K}_d \end{bmatrix} \tag{4.5}$$

and

$$\mathbf{F} = \left(\frac{\mathrm{d}\mathbf{K}}{\mathrm{d}\theta} - \lambda_i \frac{\mathrm{d}\mathbf{M}}{\mathrm{d}\theta} \right) = \begin{bmatrix} \mathbf{F}_d & \mathbf{F}_o \\ \mathbf{F}_o & \mathbf{F}_d \end{bmatrix} . \tag{4.6}$$

The eigenvectors will then take the form

$$\phi_S = \begin{Bmatrix} \phi_s \\ \phi_s \end{Bmatrix} \qquad \text{or} \qquad \phi_A = \begin{Bmatrix} \phi_a \\ -\phi_a \end{Bmatrix} . \tag{4.7}$$

where ϕ_S is a symmetric eigenvector and ϕ_A is an antisymmetric eigenvector. Combining eqns. (4.4), (4.6) and (4.7) gives the coupling factor for a symmetric and an antisymmetric mode as

$$\mathrm{CF}_{SA} = 2 \left(\begin{Bmatrix} \phi_a \\ -\phi_a \end{Bmatrix}^T \begin{bmatrix} \mathbf{F}_d & \mathbf{F}_o \\ \mathbf{F}_o & \mathbf{F}_d \end{bmatrix} \begin{Bmatrix} \phi_s \\ \phi_s \end{Bmatrix} \right)^2 = 0. \tag{4.8}$$

The matrices multiply out such that the terms cancel and the coupling factor is always zero. Thus the eigenvalue loci are free to cross. With two symmetric or two antisymmetric eigenvectors the terms do not cancel in the same way and the coupling factors are generally non-zero. In these cases the modes will exhibit veering.

4.2.4 Analytical Methods

Balmès' approach [255] will be adopted in this chapter, studying the rotations of the eigenvectors as the modes veer. Analysis of the vector rotation requires the definition of a suitable set of basis vectors to act as reference; a reasonable choice is the eigenvectors of the two modes, experimental or analytical, anywhere in the vicinity of the veering, being careful to keep the phase consistent. Methods of eigenvector correlation are reviewed in section 2.6.3, and two are repeated here. The ubiquitous Modal Assurance Criterion (MAC) produces a measure of the angle, α, between the two eigenvectors in the *physical* coordinate system, defined by the eigenvector DOFs:

$$\mathrm{MAC}_{jk} = \cos^2\alpha_{jk} = \frac{\left(\boldsymbol{\psi}_j{}^T\boldsymbol{\psi}_k\right)^2}{\left(\boldsymbol{\psi}_j{}^T\boldsymbol{\psi}_j\right)\left(\boldsymbol{\psi}_k{}^T\boldsymbol{\psi}_k\right)} \tag{4.9}$$

where ψ_j is the j^{th} arbitrarily scaled eigenvector. If the mass matrix is used as the weighting matrix in a Normalised Cross Orthogonality (NCO) then it gives a measure of the angle, β, between the two eigenvectors in the *normal* coordinate system, defined by the mass-normalised eigenvectors:

$$\mathrm{NCO}_{jk} = \cos^2\beta_{jk} = \frac{\left(\boldsymbol{\psi}_j{}^T\mathbf{M}\boldsymbol{\psi}_k\right)^2}{\left(\boldsymbol{\psi}_j{}^T\mathbf{M}\boldsymbol{\psi}_j\right)\left(\boldsymbol{\psi}_k{}^T\mathbf{M}\boldsymbol{\psi}_k\right)} \tag{4.10}$$

If the mass matrix remains constant, as is the case in a stress-stiffened structure, then the normal coordinate system rotates but does not scale or skew, thus allowing comparison of vectors from different load cases. Analysis in the normal coordinate system has the advantage that the vectors both rotate by the same angle, as depicted in Figure 4.1. Note that any constant matrix which orthonormalises the vectors throughout veering may be used as the weighting matrix for this purpose.

In the experimental configuration, the subspace in which the vectors rotate is unlikely to be accurately represented by the measured degrees of freedom, so the experimental mode shapes are expanded using Kidder's method [203]. This approach permits the use of the analytical mass matrix as a weighting matrix. The bias introduced by the analytic data in these steps is unavoidable, but the mass matrix for this structure is known with some certainty and the distribution of measured response points on the structure prevents gross distortion of the low order mode shapes in the expansion.

4.3 Experimental Correlation

Mode veering in experimental results will often go undetected, for one of two reasons: firstly, where veering is rapid, occurring over a small parameter range with closely spaced frequencies, it is easily obfuscated by measurement discretisations. Conversely, where veering is more moderate the behaviour resembles ordinary parametric variation in most regards and may be deemed unremarkable. The former is particularly true of the parameter discretisation, as parametric refinement in experimental

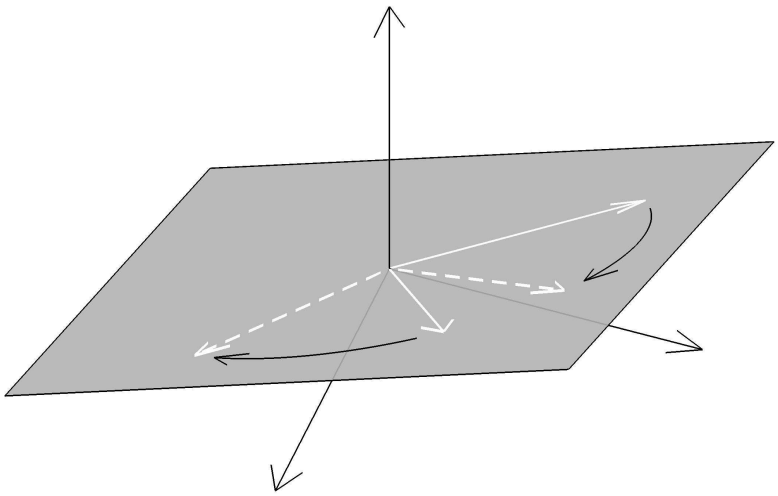

Figure 4.1: A representation of a plane or subspace in the normal coordinate system. The mass-normalised eigenvectors, shown in white, rotate in approximately the same plane throughout the veering region. After a 90° rotation the eigenvectors have swapped positions, with one eigenvector 180° out of phase with its pre-veering equivalent.

configurations can be laborious. Even where data *are* captured within a veering region the unfamiliar results will often be attributed to measurement or computational inaccuracies and dismissed as erroneous.

In recognition of the confusion caused by such results, Avitabile [262] documents the established observation that the mode shapes associated with repeated and pseudo-repeated frequencies in experimental data are often found to differ from those expected. He suggests that any orthogonal linear combinations of the mode shapes may be used to describe these modes and that experimentalists should interpret their data accordingly. This explanation is accurate for truly repeated modes, and provides valuable assistance in the interpretation of unexpected results. For pseudo-repeated modes, however, the mode shapes are not arbitrary, and the prescriptive nature of their variations can offer additional insight into the properties of the system. The significance of this insight will be investigated in later sections; this section will be concerned primarily with the identification of the mode shapes.

Despite widespread acceptance of veering theory, supporting experimental data are scarce, if not absent, in the literature. Such evidence is inferred in many cases: for example, the orthotropic plate experiments detailed by McIntyre and Woodhouse [242] rely on the manifestation of veering, and there is a wealth of data relating to rotor tuning in turbomachinery where mistuned blades and coupling between shaft and blade vibration modes lead to the related phenomena of localisation [263] and veering [264]. These do not provide categorical substantiation, however, and this section is intended to provide the first explict demonstration of the behaviour of two veering modes in a physical structure.

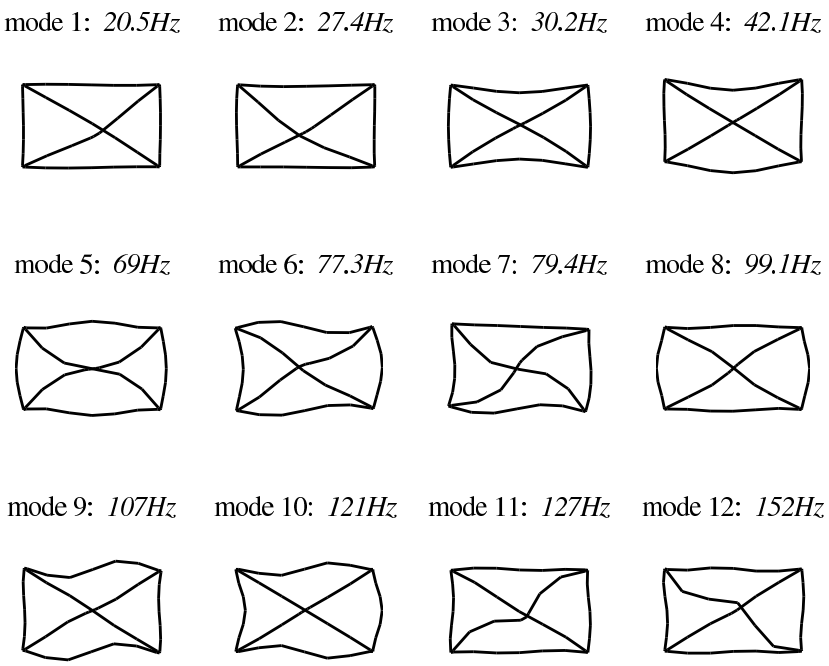

Figure 4.2: The first 12 modes of the welded frame for the zero load case.

4.3.1 Experimental and FE Configuration

The structure used for the demonstration is the welded frame described in chapter 3 and the experimental setup is not modified. In the course of the investigations of chapter 3, discrepancies were noted in the behaviour of the fifth and sixth modes of the experimental and FE data, and it is the intersection of these modes that will be investigated here.

Although the reflectional symmetry is broken by the tensioning mechanism, the structure does posses rotational symmetry. The first twelve mode shapes from the FE model are shown in figure 4.2 for zero applied load and, as expected, they are all symmetric or antisymmetric with respect to the 180° rotation. The fifth and sixth modes are displayed in figure 4.3, using a finer beam mesh for clarity, where mode 5 is seen to exhibit even symmetry and mode 6 exhibits odd symmetry. Thus, theory dictates that there will be no modal coupling between the two modes and they will cross instead of veering. The FE model upholds this prediction but the experimental data do not. This finding signifies a break in the symmetry of the practical structure.

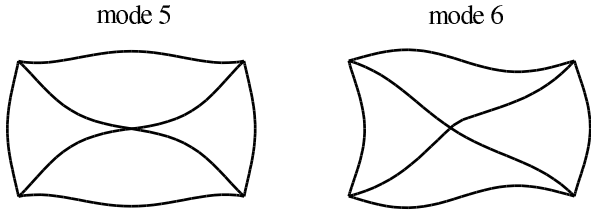

Figure 4.3: Modes 5 and 6 of the welded frame for the zero load case.

A source of significant uncertainty in the assembled structure is the welded corner joints. Referring to figure 3.16, it is possible to discern that because of accessibility problems the diagonal beams are only welded on one side, in some cases leaving a gap between the diagonal beam and the the long outside member. In addition, excessive power or a low feed rate in the welding process has caused erosion of the beam in places. These factors will create considerable variability in the stiffnesses at these joints. Accordingly, the symmetry of the FE model is broken by simulating a reduced stiffness at one end of a diagonal beam: specifically, the bottom right hand corner in the schematic of figure 3.1. This is achieved by reducing the width of the outermost element (spanning a length of 2.1 cm), affecting the second moment of area and the cross-sectional area of that element. The reduced width is chosen by trial and error; more rigorous methods are discussed in chapter 6. For the demonstration in hand, all that is needed is a qualitative reproduction of the experimental results and this was found to be given by reducing the width of the element by 70%.

4.3.2 Results

The eigenvalue loci for the symmetric model are shown crossing in figure 4.4(a). The loci for the asymmetric model can be seen veering in figure 4.4(b). These new FE results are compared with the experimental results in figure 4.4(c), where their resemblance supports the initial hypothesis: that the break in symmetry caused by weld variability is responsible for the observed veering of the modes. The experiment was performed on two separate occasions using different measurement equipment. The consistency between the two data sets in figure 4.4(c) demonstrates the repeatability of the effect.

A brief foray was made into a stochastic analysis of the eigenvalues using a method proposed by Doebling and Farrar [265]. The method is underpinned by estimates of the statistical FRF distributions based on the coherence functions. Once these are calculated a Monte Carlo simulation is performed to propagate the statistical properties to the modal parameters. The FRFs for the Monte Carlo simulations are constructed by superimposing Gaussian noise on the measured response functions according to the computed stochastic properties. Modal parameter extraction is then performed using the LSCE method detailed in section 2.5.4. It was hoped to automate the parameter extraction but after repeated efforts to implement a reliable scheme the author learned the hard way that producing an algorithm to perform this task is no mean feat, even where the expected results are known *a priori*. Thus the decision was made to abandon the endeavour, based in part on the assumption that the eigenvalues were measured to a higher degree of accuracy than the load parameter anyway, and that the time needed for manual parameter estimation would be time better spent elsewhere.

In the analysis that follows the welded frame is presumed to possess low damping throughout, with no substantial difference in damping between any of the modes or any two parts of the structure. This expectation is corroborated by the measured damping ratios in figure 4.5, where the observed variation is dominated by measurement noise, and justifies the use of real approximations for the eigenvectors. The mean modal damping ratios for modes 5 and 6 are found to be 1.14×10^{-3} and

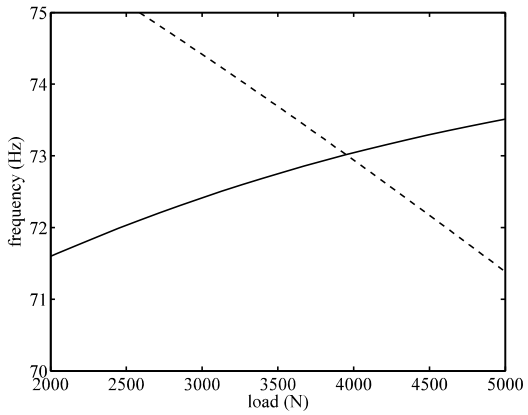

(a) Symmetric FE model.

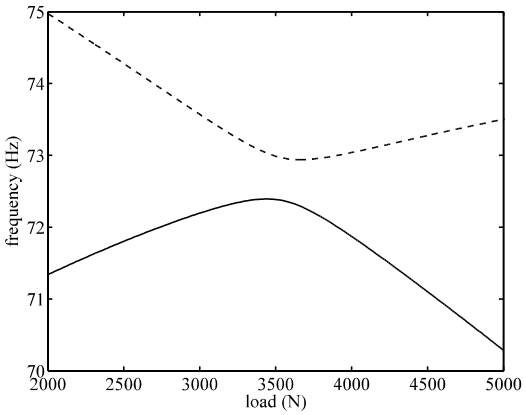

(b) Asymmetric FE model.

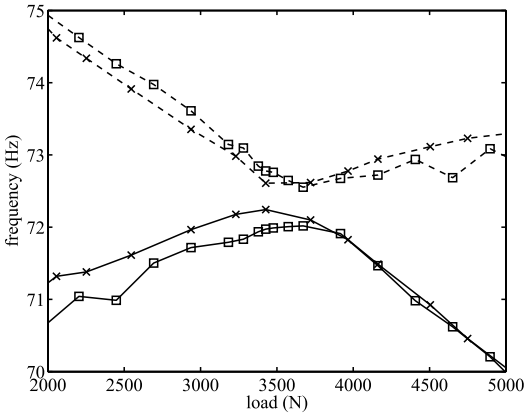

(c) Two sets of experimental data, × and □.

Figure 4.4: Close examination of the interaction between the fifth(–) and sixth(- -) modes. FE models use adaptive loadsteps, down to 2.25 N at maximum curvature.

1.20×10^{-3} respectively.

Mode tracing is facilitated by means of a MAC-based correlation, as discussed in section 2.6.3. The four elements of the MAC matrix for the veering modes are plotted in figure 4.6(a). Despite the coarse experimental load increments the MAC is seen to provide an unambiguous correlation: the diagonal elements of the MAC never drop below 0.79, while the off-diagonal terms never exceed 0.41. These values are in keeping with the FE model, for which a similar graph is plotted in figure 4.6(b).

While the MAC correlation given above is sufficiently conclusive for the demonstration in hand, it is clear that the veering modes will present difficulties to MAC-based mode tracing procedures. Bahra and Greening [266, 267] tackle the problem of mode tracing in the presence of changeable eigenvectors, and develop an augmented MAC to provide enhanced correlation. Implementing their technique of forward-casting the eigenvectors produces the improved analytic MAC results seen in figure 4.6(c). Unfortunately the technique requires knowledge of the eigenvector sensitivities, making it difficult to implement with experimental data. As such, mode tracing in experimental data remains dependent upon adequate parametric discretisation. In particular, care must be taken when correlating veering modes with modeshapes outside the veering region, or with those from a symmetric FE model.

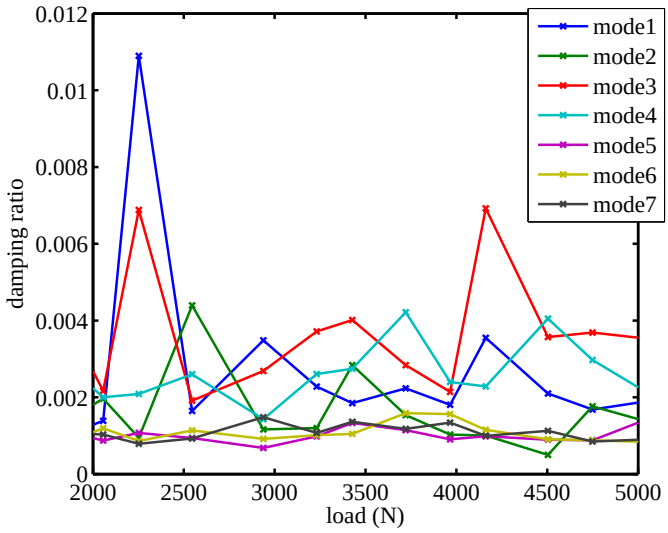

Figure 4.5: Measured damping ratios for the welded frame.

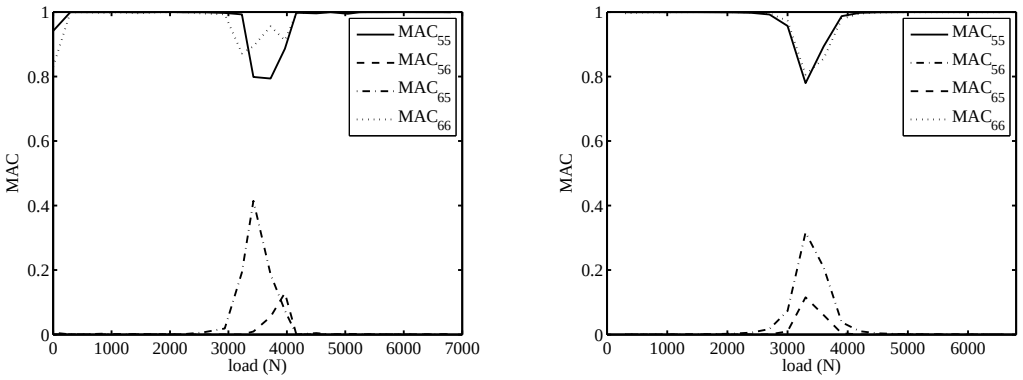

(a) Experimental data.

(b) Analytic data with 300 N loadsteps.

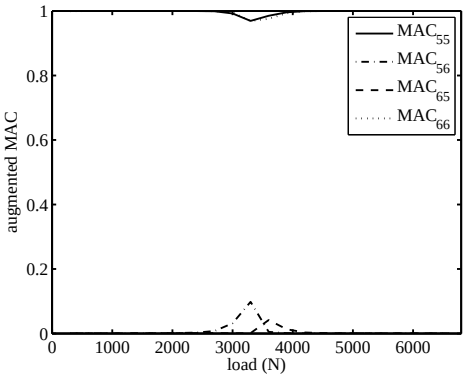

(c) Analytic data using Bahra and Greening's augmented MAC.

Figure 4.6: MAC correlation between consecutive load steps for modes 5 and 6.

The mode shapes determined from the experimental data are expanded and compared to the FE results in figure 4.7, where they are seen to correspond well. As expected, after the veering each mode takes on the form of the other through a continuous transformation. The results provide a clear and thorough substantiation of veering theory, complete with a demonstration of the mode shape mutations in the transition. In particular, the middle set of mode shapes appear quite unnatural, with undeflected members on opposite sides of each mode. It is transformations such as these that prompted Leissa to comment that veering mode shapes are, "figuratively speaking, a dragonfly one instant, a butterfly the next, and something indescribable in between." [222]

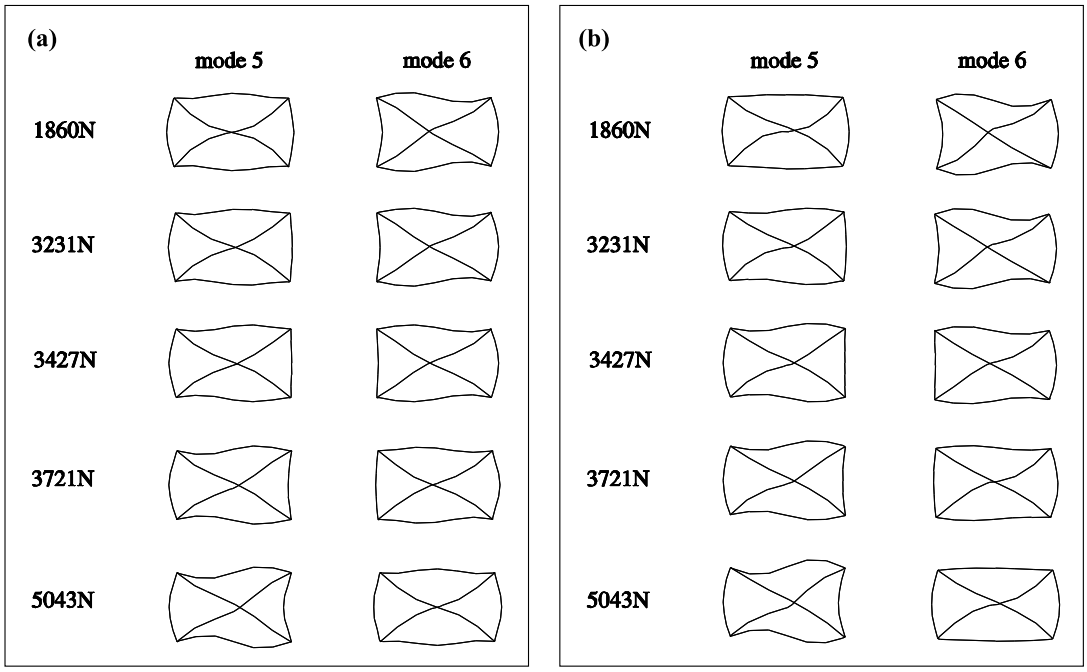

Figure 4.7: Mode shape variations as modes 5 and 6 veer: (a) FE Model. (b) Experimental Results.

4.3.3 Modal Cancellation

Attention will now be given to the frequency response at the intersection of the two modes. The response at this juncture was considered in section 3.4.4, and figure 3.28 depicts modes 5 and 6 exhibiting a reduced response where they intersect. This event occurs even in the symmetric model with no veering present, so it is interesting to explore how veering affects the behaviour.

In the lightly damped model, the response cancellation occurs only when the natural frequncies are coincident; when the modes are separated their phase difference inhibits their cancellation. As such, it was expected that the increased separation of the modes caused by veering would prevent the full cancellation and result in higher responses. In fact, this is not the case: figure 4.8 shows analytical response surfaces in the region of the intersection for the symmetric case and for the perturbed

symmetry case. Counter-intuitively, the asymmetric case shows a larger region of reduced response.

While the dip in response for the symmetric model is produced through modal superposition, the response variation in the asymmetric model is due to the eigenvector transformations. The vectors permute such that the residues of the two modal FRF contributions always sum to the same value. Accordingly, as they swap with one another, the response to each mode is similar to that of the combined response for intersecting modes. Greater modal coupling results in a slower transformation of the modes, having a similar effect on the response to that of the damping seen in fig. 3.28: an increase in the range of parameter values spanned by the region of reduced response.

Balmès [255] provides a rigorous mathematical confirmation that veering does not affect the total response of two modes within a frequency band, and Igusa [253] investigates the circumstances under which the response exhibits sensitive parameter dependence as found here.

4.3.4 FE Model Updating Repercussions

It has been shown that the eigenvector transformations in veering regions can cause difficulties for mode tracing algorithms. One technique that relies heavily on an ability to track modes from one step to the next is FE model updating. Here the experimental modes from which the reference data is taken must be correlated with the FE modes for the current iteration.

Bahra and Greening's method, used above, will offer significant improvements to correlation where the mode shapes change rapidly. It uses eigenvector derivatives to compare the eigenvectors to their *expected* form, instead of making a direct comparison between dissimilar vectors. In veering cases, however, not only the eigenvectors, but also the eigenvector *derivatives* will undergo significant changes, further frustrating mode tracing efforts.

Figure 4.9 illustrates the variation of the eigenvector derivatives for the veering case examined above, demonstrating how rapidly they can change. Over the same parameter range the eigenvalue sensitivities are also seen to swap with each other. Both of these changes will pose problems not only for the mode correlation, but also the stability of an updating scheme. Regularisation can help to slow the convergence and increase stability but even this may not be enough for abrupt variations. Thus careful consideration must be given to the implementation of updating schemes in the presence of this behaviour.

Balmès [255] offers a different perspective. He suggests that rather than creating an impediment, the mode shape transformations could be used to improve a model updating scheme. His idea is to use the orientation of the eigenvectors of two veering modes in the objective function of a penalty function method. The FE eigenvector rotations calculated with eqn. (4.10) are shown in figure 4.10(a), and these are broadly in agreement with the experimental results in figure 4.10(b). The differences

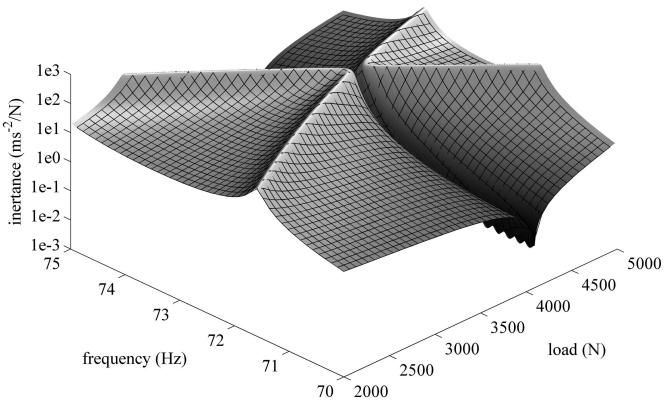

(a) Symmetric FE model.

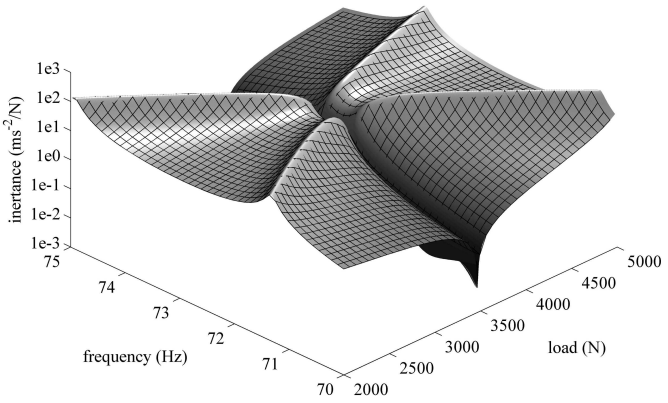

(b) Asymmetric FE model.

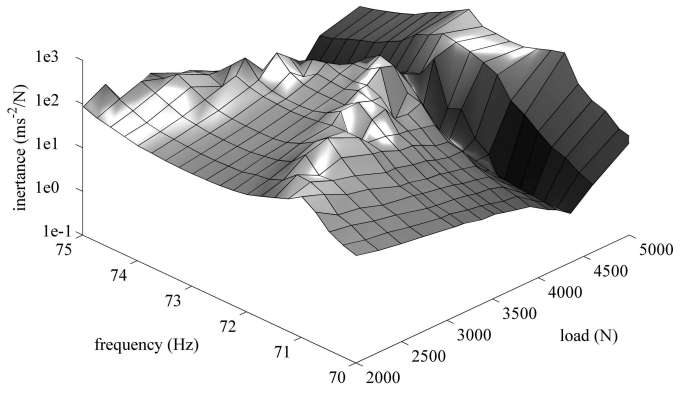

(c) Experimental data.

Figure 4.8: FRFs in the veering region. The analytical models both use uniform modal damping ratios of 1.2×10^{-3}.

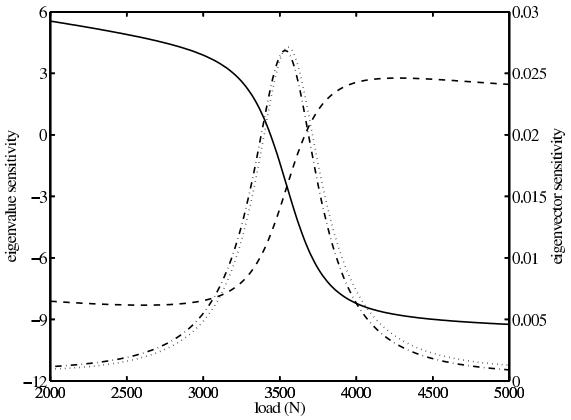

Figure 4.9: Modal parameter sensitivities to load variation: fifth(–) and sixth(- -) eigenvalue sensitivities, and ℓ^2-norms of the fifth(-.) and sixth(..) eigenvector sensitivities.

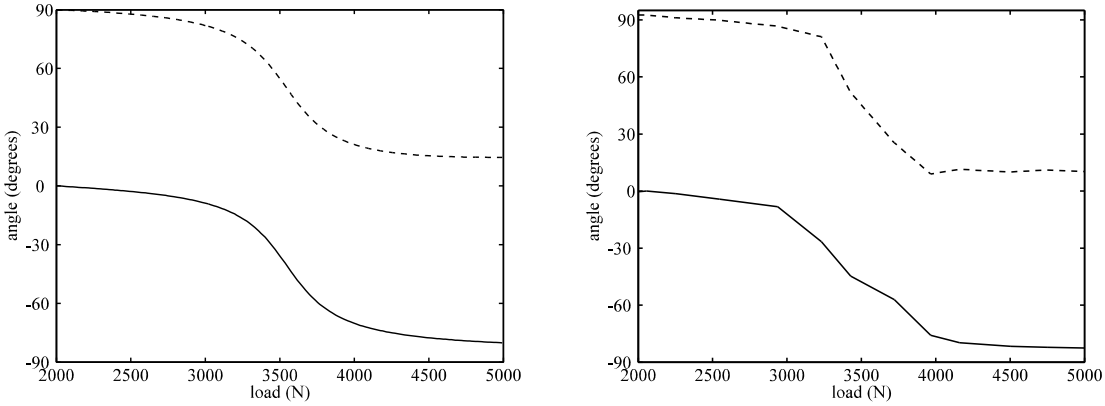

(a) FE model.

(b) Experimental data.

Figure 4.10: Eigenvector rotations of the fifth(–) and sixth(- -) modes in the normal coordinate system.

between the two experimental curves indicate a slight lack of orthogonality, which can be attributed both to errors in the measured eigenvectors and to the use of an estimated mass matrix, taken from the FE model.

Importantly, the vector rotations can be seen to provide a useful indication of the state of veering, and thus the parameter values associated with that state. The information provided by this value is related to that provided by the eigenvectors themselves, but by confining the measurement of the rotation to a particular subspace, much of the ambiguity associated with eigenvector-based updating schemes is removed. In this way the model adjustments can be tailored specifically to the coupling of the modes concerned; this may be desirable, for example, in systems where localisation is important.

As a final cautionary note, the experimental curves of fig. 4.10 are somewhat erratic compared to their analytical counterparts. Successful implementation of the method will be contingent on sufficiently high fidelity in these measurements, which may be found to suffer the same problems as measurements of the eigenvectors themselves. Chapter 6 considers an extended version of this scheme which circumvents the need for accurate eigenvector measurements. For now, the remainder of this chapter focuses on the detection and classification of veering.

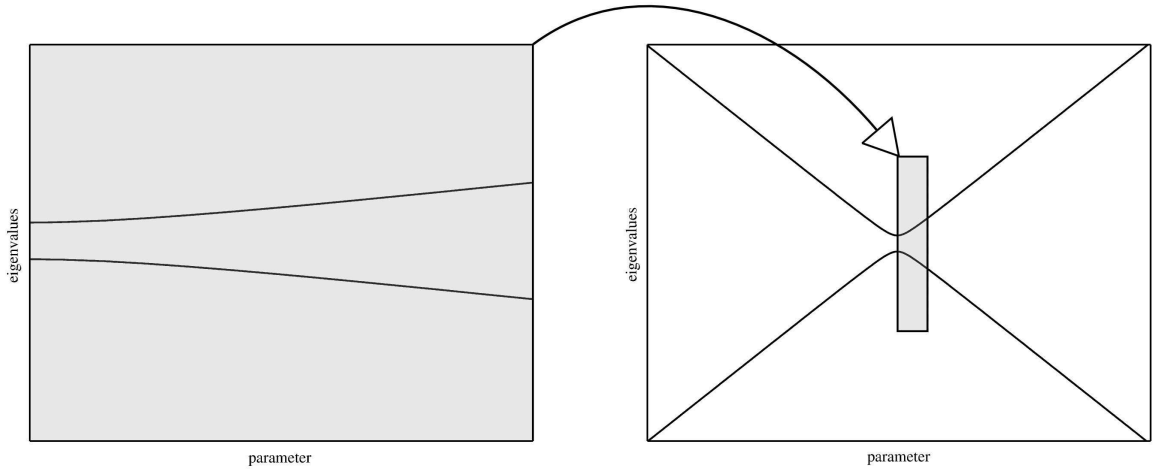

(a) Zoomed in (b) Zoomed out

Figure 4.11: A set of veering eigenvalues, plotted for different ranges.

4.4 Veering Index

The problem of quantifying veering is made difficult by the historically subjective nature of its identification. Its most tangible characteristic is the eigenvalue curvature or second derivative. Liu [249] suggests using critical values of this derivative, and of the eigenvector derivatives, to classify veering. The limitation of this approach is in differentiating between veering and other instances of high curvature, and Liu also concedes that the critical values would need to be determined on a case by case basis. Several authors refer to couplings between modes with respect to parameter variations, and Perkins and Mote's "coupling factors" are described in section 4.2.3. These factors provide great qualitative insight into the behaviour but once again, quantitative interpretation of the results can prove misleading.

In the remainder of this chapter, a non-dimensional approach is taken in order to allow universal identification of the behaviour. This approach will indicate the presence of veering even where limited range or atypical context may obfuscate it. This can lead to counter-intuitive results, for example the unexceptional data presented in figure 4.11(a) are recognisable as veering when plotted for different ranges in figure 4.11(b). The analysis that follows takes into consideration the distinguishing characteristics of veering to produce a physically meaningful method of quantification. Sections 4.4.1 and 4.4.2 examine some important characteristics of veering modes, which are applied in sections 4.4.3 and 4.4.4 to derive two descriptive quantities. Section 4.4.5 presents a discussion of these quantities and explains how they can be used to evaluate the behaviour, and section 4.4.6 gives a demonstration of their application.

4.4.1 Modal Coupling

Consider a self-adjoint, discrete, undamped structural dynamic eigenproblem. Fox and Kapoor [206] derive the eigenvalue sensitivity to a parameter δ_j as

$$\frac{d\lambda_i}{d\delta_j} = \phi_i^T \left(\frac{d\mathbf{K}}{d\delta_j} - \lambda_i \frac{d\mathbf{M}}{d\delta_j} \right) \phi_i \tag{4.11}$$

where λ_i and ϕ_i are the eigenvalue and mass normalised eigenvector of the i^{th} mode and $\mathbf{M}$ and $\mathbf{K}$ are the system mass and stiffness matrices. The corresponding eigenvector sensitivity is given as

$$\frac{d\phi_i}{d\delta_j} = -\frac{\phi_i^T \frac{d\mathbf{M}}{d\delta_j} \phi_i}{2} \phi_i + \sum_{r \neq i} \frac{\phi_r^T \left(\frac{d\mathbf{K}}{d\delta_j} - \lambda_i \frac{d\mathbf{M}}{d\delta_j} \right) \phi_i}{\Delta\lambda_{ir}} \phi_r \tag{4.12}$$

where $\Delta\lambda_{ir} = \lambda_i - \lambda_r$. Differentiating eqn. (4.11) with respect to δ_j and using eqn. (4.12) yields

$$\frac{d^2\lambda_i}{d\delta_j^2} = \phi_i^T \left(\frac{d^2\mathbf{K}}{d\delta_j^2} - \lambda_i \frac{d^2\mathbf{M}}{d\delta_j^2} - 2\frac{d\lambda_i}{d\delta_j} \frac{d\mathbf{M}}{d\delta_j} \right) \phi_i + 2 \sum_{r \neq i} \frac{\left[\phi_r^T \left(\frac{d\mathbf{K}}{d\delta_j} - \lambda_i \frac{d\mathbf{M}}{d\delta_j} \right) \phi_i \right]^2}{\Delta\lambda_{ir}} \tag{4.13}$$

where $\frac{d^2\lambda_i}{d\delta_j^2}$ is the second derivative, or curvature, of the eigenvalue. If the i^{th} and k^{th} eigenvalues become close such that $\Delta\lambda_{ik}$ is very small then the expression for curvature is dominated by the corresponding term in the summation where $r = k$, and it is this term that is responsible for the veering of the eigenvalue loci. The numerator of the term is $2\left[\phi_k^T \left(\frac{d\mathbf{K}}{d\delta_j} - \lambda_i \frac{d\mathbf{M}}{d\delta_j} \right) \phi_i \right]^2$, which is analogous to Perkins and Mote's "coupling factor". For the purposes of this thesis the "modal coupling" shall be defined slightly differently as

$$\kappa_{ijk} = \phi_k^T \left(\frac{d\mathbf{K}}{d\delta_j} - \lambda_i \frac{d\mathbf{M}}{d\delta_j} \right) \phi_i. \tag{4.14}$$

Expanding this to the full set of modes, a sensitivity matrix can be defined:

$$\mathbf{\Sigma}_j = \mathbf{\Phi}^T \frac{d\mathbf{K}}{d\delta_j} \mathbf{\Phi} - \mathbf{\Phi}^T \frac{d\mathbf{M}}{d\delta_j} \mathbf{\Phi} \mathbf{\Lambda} \tag{4.15}$$

where $\mathbf{\Phi}$ is the complete matrix of eigenvectors, $[\phi_1, \phi_2 ... \phi_N]$, and $\mathbf{\Lambda}$ is a diagonal matrix of eigenvalues. The diagonal terms in $\mathbf{\Sigma}_j$ are the eigenvalue sensitivities and the off-diagonal terms are the modal coupling, which can be interpreted as cross-sensitivities representing the contribution of each mode to the derivatives of the other modes' properties.

4.4.2 Eigenvector Rotation

For proximate modes i and k, if $\Delta\lambda_{ik} << \Delta\lambda_{ir}$ for all $r \neq i, k$ then eqn. (4.12) can be represented by

$$\frac{d\phi_i}{d\delta_j} \approx -\left(\frac{1}{2} \phi_i^T \frac{d\mathbf{M}}{d\delta_j} \phi_i \right) \phi_i + \left(\frac{\kappa_{ijk}}{\Delta\lambda_{ik}} \right) \phi_k. \tag{4.16}$$

From this equation (and the equivalent expression for $\frac{d\phi_k}{d\delta_j}$) it is seen that the two vectors throughout veering can always be represented by a linear combination of a single pair of vectors; as they transform, they always remain in the same plane or subspace. Furthermore, the validity of this assumption can be quantified for each mode by comparing the ℓ^2-norms of eqns. (4.16) and (4.12) within the normal basis:

$$Q_{ijk} = \sqrt{\frac{-\left(\frac{1}{2}\phi_i^T \frac{d\mathbf{M}}{d\delta_j}\phi_i\right)^2 + \left(\frac{\kappa_{ijk}}{\Delta\lambda_{ik}}\right)^2}{-\left(\frac{1}{2}\phi_i^T \frac{d\mathbf{M}}{d\delta_j}\phi_i\right)^2 + \sum_{r\neq i}\left(\frac{\kappa_{ijr}}{\Delta\lambda_{ir}}\right)^2}} \tag{4.17}$$

and noting that the summed term in the denominator is easily computed using a single column of the sensitivity matrix in eqn. (4.15).

Suppose that a constant matrix, $\mathbf{A}$, can be found such that $\mathbf{\Psi}_{ik}^T \mathbf{A} \mathbf{\Psi}_{ik} = \mathbf{I}$ for all values of δ_j, where $\mathbf{I}$ is an identity matrix and $\mathbf{\Psi}_{ik}$ is the $N \times 2$ matrix of $\mathbf{A}$-normalised eigenvectors, $[\psi_i, \psi_k]$. In this case, the two eigenvectors will always form an orthonormal basis with respect to $\mathbf{A}$, and their magnitude and orientation within the subspace can be defined relative to a set of reference vectors by a single angle. This is illustrated in figure 4.12, and can be expressed

$$\mathbf{\Psi}'_{ik}(\mathbf{\Psi}_{ik}, \alpha) = \mathbf{\Psi}_{ik}\mathbf{T}, \qquad \mathbf{T} = \begin{bmatrix} \cos\alpha & -\sin\alpha \\ \sin\alpha & \cos\alpha \end{bmatrix}. \tag{4.18}$$

where the prime ($'$) denotes the property set for an arbitrary parameter value, ${\delta_j}'$, distinct from the property set for parameter value δ_j. Eqn. 4.18 is a generalisation of the system described by Balmés [255] and demonstrates that his observations may be extrapolated to any veering system, contingent on the existence of an appropriate orthonormalising matrix and satisfactory agreement with eqn. (4.16). The former is achieved most readily by keeping either the mass or stiffness matrix constant and these two scenarios will be considered in the analysis that follows.

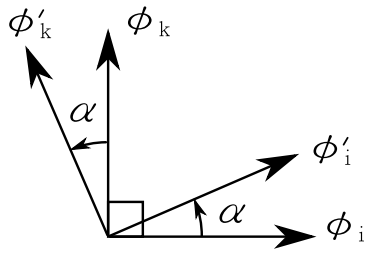

Figure 4.12: Orthogonal mode shape vectors, for jth and kth modes, transforming into new modes within their subspace.

4.4.3 Cross-Sensitivity Quotient

In this section the variation of the modal coupling throughout veering is investigated. A reduced sensitivity matrix for modes i and k shall be defined as

$$\mathbf{\Sigma}_{ijk} = \mathbf{\Phi}_{ik}^T \frac{d\mathbf{K}}{d\delta_j} \mathbf{\Phi}_{ik} - \mathbf{\Phi}_{ik}^T \frac{d\mathbf{M}}{d\delta_j} \mathbf{\Phi}_{ik} \mathbf{\Lambda}_{ik} = \begin{bmatrix} \sigma_{iji} & \kappa_{ijk} \\ \kappa_{kji} & \sigma_{kjk} \end{bmatrix} \tag{4.19}$$

where σ_{iji} is equivalent to the eigenvalue sensitivity, $d\lambda_i/d\delta_j$. Considering a linear variation in the stiffness matrix, represented by δ_K, the mass matrix remains constant and serves as an orthonormalising matrix, allowing the substitution of eqn. (4.18) in eqn. (4.19) using $\mathbf{\Psi}_{ik} = \mathbf{\Phi}_{ik}$. Noting that $\frac{d\mathbf{M}}{d\delta_K} = 0$ and $\frac{d^2\mathbf{K}}{d\delta_K^2} = 0$ so $\frac{d\mathbf{K}}{d\delta_K} = \frac{d\mathbf{K}}{d\delta_K}'$, this substitution produces

$$\mathbf{\Sigma}'_{iKk} = \mathbf{\Phi}'^T_{ik} \frac{d\mathbf{K}}{d\delta_K}' \mathbf{\Phi}'_{ik} = \mathbf{T}^T \mathbf{\Phi}_{ik}^T \frac{d\mathbf{K}}{d\delta_K} \mathbf{\Phi}_{ik} \mathbf{T} = \mathbf{T}^T \mathbf{\Sigma}_{iKk} \mathbf{T} \tag{4.20}$$

where $\mathbf{\Sigma}'_{iKk}$ and $\frac{d\mathbf{K}}{d\delta_K}'$ are the sensitivity and stiffness matrices corresponding to the eigenvectors $\mathbf{\Phi}'_{ik}$. $\mathbf{\Sigma}'_{iKk}$ is a symmetric 2×2 matrix in which the off-diagonal elements are equal:

$$\begin{aligned} \kappa'_{iKk} = \kappa'_{kKi} &= \kappa_{iKk}(\cos^2\alpha - \sin^2\alpha) + (\sigma_{kKk} - \sigma_{iKi})\cos\,\alpha\,\sin\,\alpha \\ &= \overline{\kappa}_{iKk}\cos\,\,(2\alpha - 2\beta) \end{aligned} \tag{4.21}$$

where

$$\tan\,(2\beta) = \Delta\sigma_{kKi}/2\kappa_{iKk} \tag{4.22}$$

$$\overline{\kappa}^2_{iKk} = {\kappa_{iKk}}^2 + \left(\Delta\sigma_{kKi}/2\right)^2 \tag{4.23}$$

and $\Delta\sigma_{kKi} = \sigma_{kKk} - \sigma_{iKi}$. The modal coupling is seen to vary harmonically with the orientation of the vectors. The maximum coupling is given by eqn. (4.23) and this is used to define a corresponding set of reference vectors, $\overline{\mathbf{\Phi}}_{ik}$. Setting $\mathbf{\Phi}'_{ik} = \overline{\mathbf{\Phi}}_{ik}$ gives $\kappa'_{iKk} = \overline{\kappa}_{iKk}$ and hence from eqn. (4.21) $\alpha = \beta$, so that eqn. (4.22) describes the angle between $\mathbf{\Phi}_{ik}$ and $\overline{\mathbf{\Phi}}_{ik}$. Setting $\mathbf{\Phi}'_{ik} = \mathbf{\Phi}_{ik}$ gives $\kappa'_{iKk} = \kappa_{iKk}$ and $\alpha = 0$, so that eqn. (4.21) produces

$$\kappa_{iKk} = \overline{\kappa}_{iKk}\cos\,\,(2\beta) \tag{4.24}$$

From eqn. (4.22) the angle β is zero when $\Delta\sigma_{kKi} = 0$ and the sensitivities of the two modes are equal: effectively the point where the eigenvalue loci swap trajectories. This corresponds to the point where the eigenvalues are closest, and since eqns. (4.13) and (4.16) can be written $\frac{d^2\lambda_i}{d\delta_K^2} \approx 2(\kappa^2_{iKk}/\Delta\lambda_{ik})$ and $\frac{d\phi_i}{d\delta_K} \approx (\kappa_{iKk}/\Delta\lambda_{ik})\phi_k$ for this case (as $\frac{d\mathbf{M}}{d\delta_K} = \frac{d^2\mathbf{M}}{d\delta_K^2} = \frac{d^2\mathbf{K}}{d\delta_K^2} = \mathbf{0}$) it is also the point where the eigenvalue curvature and eigenvector sensitivity are greatest. These reference vectors form a veering datum set where the modal coupling, or cross-sensitivity, is greatest. The cross-sensitivity thus provides a useful measure of the intensity of veering, its square being proportional to the eigenvalue curvature. The

maximum cross-sensitivity over a range of δ_K is easily computed from the modal properties for any single value of δ_K, and it is convenient to define a cross-sensitivity quotient as $\mathrm{CSQ}_{iKk} = \left(\kappa_{iKk}/\overline{\kappa}_{iKk}\right)^2$. Using eqns. (4.23-4.24),

$$\mathrm{CSQ}_{iKk} = \cos^2(2\beta) = \frac{\kappa_{iKk}^2}{\kappa_{iKk}^2 + \left(\Delta\sigma_{kKi}/2\right)^2}. \tag{4.25}$$

A more general definition is afforded by examining the eigenvector rotations. As $\beta \to \pm\frac{\pi}{4}$, the modal coupling goes to zero so from eqn. (4.16) the vector rotation also halts. Thus for an idealised veering case (without interaction from other modes), the datum vectors are oriented exactly half way between their asymptotic limits. This definition is used to derive a CSQ for the case of mass matrix variation as follows.

Consider a linear variation in the mass matrix, represented by δ_M, with constant stiffness matrix. The stiffness matrix may be used as the orthonormalising matrix such that

$$\boldsymbol{\Psi}_{ik}^T \mathbf{K} \boldsymbol{\Psi}_{ik} = \mathbf{I}, \qquad \boldsymbol{\Psi}_{ik} = \boldsymbol{\Phi}_{ik} \boldsymbol{\Lambda}_{ik}^{-\frac{1}{2}} \tag{4.26}$$

where $\boldsymbol{\Lambda}$ is a diagonal matrix so the inverse square root needs no further clarification. Combining eqns. (4.19) and (4.26) while noting $\frac{d\mathbf{K}}{d\delta_M} = 0$ yields

$$\boldsymbol{\Sigma}_{iMk} = -\boldsymbol{\Lambda}_{ik}^{\frac{1}{2}} \boldsymbol{\Psi}_{ik}^T \frac{d\mathbf{M}}{d\delta_M} \boldsymbol{\Psi}_{ik} \boldsymbol{\Lambda}_{ik}^{\frac{3}{2}} \tag{4.27}$$

This matrix is not symmetric, and maximum values for κ_{iMk} and κ_{kMi} will not necessarily coincide. In order to define a cross-sensitivity quotient for the two modes in the same manner as before, a symmetric matrix is defined in the form of an adapted sensitivity matrix:

$$\boldsymbol{\Sigma}_{iMk}^* = \boldsymbol{\Lambda}_{ik}^{-\frac{1}{2}} \boldsymbol{\Sigma}_{iMk} \boldsymbol{\Lambda}_{ik}^{-\frac{3}{2}} = -\boldsymbol{\Psi}_{ik}^T \frac{d\mathbf{M}}{d\delta_M} \boldsymbol{\Psi}_{ik}. \tag{4.28}$$

Substituting eqn. (4.18) and remembering $\frac{d\mathbf{M}}{d\delta_M} = \frac{d\mathbf{M}}{d\delta_M}'$,

$$\boldsymbol{\Sigma}_{iMk}^*{}' = -\boldsymbol{\Psi}_{ik}'^T \frac{d\mathbf{M}}{d\delta_M}' \boldsymbol{\Psi}_{ik}' = -\mathbf{T}^T \boldsymbol{\Psi}_{ik}^T \frac{d\mathbf{M}}{d\delta_M} \boldsymbol{\Psi}_{ik} \mathbf{T} = \mathbf{T}^T \boldsymbol{\Sigma}_{iMk}^* \mathbf{T}. \tag{4.29}$$

This is equivalent to eqn. (4.20) and, by analogy,

$$\mathrm{CSQ}_{iMk}^* = \frac{\kappa_{iMk}^*{}^2}{\kappa_{iMk}^*{}^2 + \left(\Delta\sigma_{kKi}^*/2\right)^2} = \frac{\frac{\kappa_{iMk}^2}{\lambda_i \lambda_k^3}}{\left(\frac{\kappa_{iMk}^2}{\lambda_i \lambda_k^3} + \frac{1}{4}\left(\frac{\sigma_k}{\lambda_k^2} - \frac{\sigma_i}{\lambda_i^2}\right)^2\right)}. \tag{4.30}$$

Note that the eigenvalues are generally close at veering, and if $\lambda_i \approx \lambda_k$ then $\kappa^* \approx \kappa$ and $\mathrm{CSQ}^* \approx \mathrm{CSQ}$. Eqns. (4.25) and (4.30) are valid for any symmetric, undamped structural eigenproblem with linear variation of the mass or stiffness matrices.

4.4.4 Modal Dependence Factor

Veering is distinguished from other forms of parametric variation by the swapping of modal properties from one mode to another. This is effected by a transformation of the eigenvectors within a fixed subspace. If the vectors stray significantly outside their subspace, it is an indication that they are interacting with other modes. On this premise, a modal dependence factor (MDF) is derived below to quantify the contribution of the interaction between two modes to their total variation.

Eqn. (4.17) gives an exact measure of the conformity of the mass-normalised eigenvectors to their subspace. As before, considering a change in parameter δ_K causing a variation of the stiffness matrix such that $\frac{d\mathbf{M}}{d\delta_K} = 0$, eqn. (4.17) can be written

$$\mathrm{MDF}_{iKk} = \mathrm{Q}^2_{iKk} = \frac{\left(\kappa_{iKk}/\Delta\lambda_{ik}\right)^2}{\sum_{r\neq i}\left(\kappa_{iKr}/\Delta\lambda_{ir}\right)^2} \tag{4.31}$$

This equation requires knowledge of the modal parameters for all the modes, but it is desirable that the modal dependence factor, as with the cross-sensitivity quotient, may be computed using only modal parameters for the two modes concerned. The eigenvector derivative, $\frac{d\phi_i}{d\delta_K}$ can be obtained in a computationally efficient manner using only modal properties for the i^{th} mode with Nelson's method [207]. Transposing eqn. (4.12), post-multiplying by $\mathbf{M}\phi_k$ and noting the orthogonality properties gives

$$\frac{d\phi_i}{d\delta_K}^T \mathbf{M}\phi_k = \kappa_{iKk}/\Delta\lambda_{ik}. \tag{4.32}$$

Post-multiplying eqn. (4.12) again, this time by $\mathbf{M}\frac{d\phi_i}{d\delta_K}$, and remembering $\dfrac{d\mathbf{M}}{d\delta_K} = 0$ gives

$$\frac{d\phi_i}{d\delta_K}^T \mathbf{M}\frac{d\phi_{i,K}}{d\delta_K} = \sum_{r\neq i}\left(\frac{\kappa_{iKr}}{\Delta\lambda_{ir}}\right)^2. \tag{4.33}$$

Combining eqns. (4.31-4.33) yields

$$\mathrm{MDF}_{iKk} = \frac{\left(\frac{d\phi_i}{d\delta_K}^T \mathbf{M}\phi_k\right)^2}{\frac{d\phi_i}{d\delta_K}^T \mathbf{M}\frac{d\phi_i}{d\delta_K}}, \tag{4.34}$$

giving the contribution of the k^{th} mode to the derivative of the i^{th} eigenvector. From vector algebra and inner products, this is seen to be equivalent to the cosine of the angle between the eigenvector derivative and the plane $\mathbf{\Phi}_{ik}$ in the normal coordinate system. The same approach may be taken for mass matrix variation with $\frac{d\mathbf{K}}{d\delta_M} = 0$, to produce

$$\mathrm{MDF}^*_{iMk} = \frac{\left(\frac{d\psi_i}{d\delta_M}^T \mathbf{K}\psi_k\right)^2}{\frac{d\psi_i}{d\delta_M}^T \mathbf{K}\frac{d\psi_i}{d\delta_M}}. \tag{4.35}$$

where ψ_i is once more the stiffness-normalised i^{th} eigenvector, and careful attention must be given to

the correct normalisation of $\frac{d\psi_i}{d\delta_j}$ when using Nelson's scheme. In the case of several modes veering simultaneously, the MDFs may also be summed to quantify the confinement of the vector within the larger subspace.

4.4.5 Veering Index

Veering has been shown to occur in the presence of strong modal coupling and proximate modes. Contrarily, subjective observations of the behaviour are most often made in systems with weak modal coupling outside of the veering regions. In these circumstances the eigenvalues must be closer to induce veering, producing more rapid and hence more discernible instances of the effect.

The difficulty in quantifying the behaviour lies in determining what values constitute strong modal coupling and close eigenvalues. A better definition is afforded by considering the modal interactions in the context of the complete system: to produce veering the two modes must be close *with respect to their coupling*, and they must be isolated from the influence of other modes. These two requirements are quantified with the CSQ and the MDF, respectively. It is necessary and sufficient that they are both close to unity to produce veering.

A geometric interpretation is given in Figure 4.13. From this the MDFs are seen to describe the extent to which the eigenvector derivatives deviate from their subspace, while the CSQ describes their orientation relative to the veering datum within that subspace. Thus the MDFs determine whether the modes *will* veer, and on this presumption the CSQ determines whether they *are* veering.

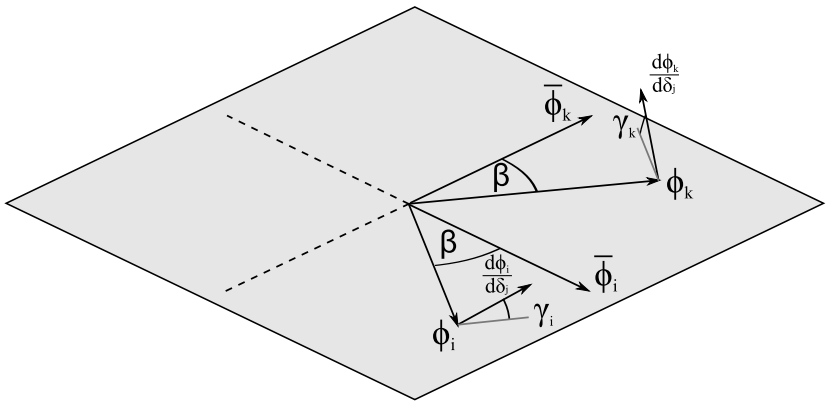

Figure 4.13: A geometric interpretation of the cross-sensitivity quotient and modal dependence factors described by $\mathrm{CSQ}_{ijk} = \cos^2(2\beta)$, $\mathrm{MDF}_{ijk} = \cos(\gamma_i)$ and $\mathrm{MDF}_{kji} = \cos(\gamma_k)$. Depicted is a plane or subspace in the normal coordinate system containing two eigenvectors ϕ_i and ϕ_k. These vectors are separated from the veering datum vectors for that subspace, $\overline{\phi}_i$ and $\overline{\phi}_k$, by angle β. The corresponding eigenvector derivatives are pictured forming angles γ_i and γ_k with the subspace.

A veering index is proposed as the product of the CSQ and the two MDFs:

$$\mathrm{VI}_{iKk} = \mathrm{MDF}_{iKk} \times \mathrm{CSQ}_{iKk} \times \mathrm{MDF}_{kKi} \tag{4.36}$$

$$\mathrm{VI}^*_{iMk} = \mathrm{MDF}^*_{iMk} \times \mathrm{CSQ}^*_{iMk} \times \mathrm{MDF}^*_{kMi} \tag{4.37}$$

This index provides an unambiguous measure of the extent to which two modes are swapping properties with each other. It is a definitive indicator for the presence of veering between two modes, based not upon subjective observations but on physically relevant manifestations.

4.4.6 Examples

Two examples are presented here: the first is a simple 2 degree of freedom (DOF) system which will demonstrate the principles of the veering quotient. The second example has been chosen to demonstrate some of the more surprising results obtained with the veering index.

Figure 4.14 shows the 2 DOF system, consisting of two grounded spring-mass arrangements and a light coupling spring between them. In this example $k_1 = k_2 >> s$. Away from veering, each mass dominates the motion for its respective vibration mode. As m_2 varies, the natural frequencies of the two modes converge and veer, forming two symmetrical mode shapes where $m_2 = m_1$. The eigenvalue loci are plotted in figure 4.15(a). Because there are only two modes in this system, the modal dependency factors MDF_{1m2} and MDF_{2m1} will always be unity. In this case, the cross-sensitivity quotient and the veering index are identical and are plotted in figure 4.15(b) using eqn. (4.30). They provide a clear indication of the intensity of veering. The "half-SCQ parameter bandwidth" has also been marked, denoting the region within which the SCQ exceeds 0.5. The effect of veering on the eigenvalue loci is most pronounced in this range.

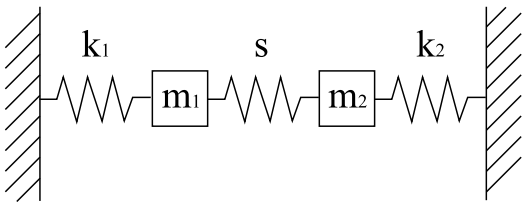

Figure 4.14: Two degree of freedom spring mass system with light spring coupling, s, between the two masses.

The second example is illustrated in figure 4.16. It consists of two pairs of lightly coupled spring-mass systems as used in the first example, with an even lighter spring coupling the two systems together. The masses are all equal in this example and the parameter change δ_j corresponds to a linear increase in the stiffnesses of k_1 and k_2. The initial spring stiffnesses, k_{1-4}, are chosen such that prior to veering modes 1-4 are dominated by the motion of DOFs 1-4 respectively and the coupling springs, s_{1-3}, introduce light modal coupling where $s_1 = s_2 >> s_3$. With this arrangement it is expected that mode 1 will be closely coupled to mode 3 and that mode 2 will be closely coupled to mode 4. Modes 1 and 4 may be lightly coupled while modes 2 and 3 should experience the least coupling. The eigenvalues are plotted in figure 4.17(a), where on first inspection modes 2 and 3 appear to veer away from each

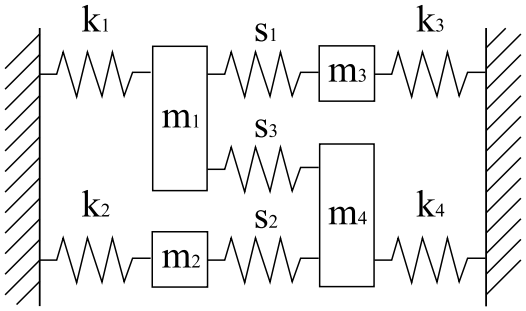

Figure 4.16: Four degree of freedom spring mass system with light spring couplings s_{1-3} between the masses.

other. In fact the observed veering is caused by concurrent interaction of mode pairs 1-3 and 2-4, and this is clearly indicated by the veering indices in figure 4.17(b). The only curves to rise substantially above zero in this plot are those corresponding to VI_{1j3} and VI_{2j4}. Examining the cross-sensitivity quotients in figure 4.17(c) shows that as the two mode pairs veer the vectors swing close to the veering datums for other mode pair combinations; the sharp peaks at $\delta_j \approx 77$ correspond to pairs 2-3 and 1-4. Consultation of the modal dependency factors in figure 4.17(d), however, confirms that while the factors for the veering mode pairs stay close to unity, those for the spurious mode combinations remain small, ensuring a true representation of the modal transformations in the veering index.

Increasing the coupling between the two spring-mass systems so that s_3=s_2=s_1 produces similar eigenvalue loci, presented in figure 4.17(a). Referring to the veering indices in figure 4.17(b), the observed curvature is now seen to be attributable to interaction between several modes, in three distinct phases. First modes 1 and 3 begin to veer. As mode 3 takes on the properties of mode 1 its coupling to mode 2 increases. At the same time the 2nd and 3rd eigenvalues get closer and the combination of these effects causes those two modes to veer, taking the dominant role in the variation. As these modes diverge again the 2nd mode starts to veer with the 4th and the corresponding veering index peaks. At no stage are any two modes interacting solely with one another and this is witnessed by the veering indices which are always significantly below unity.

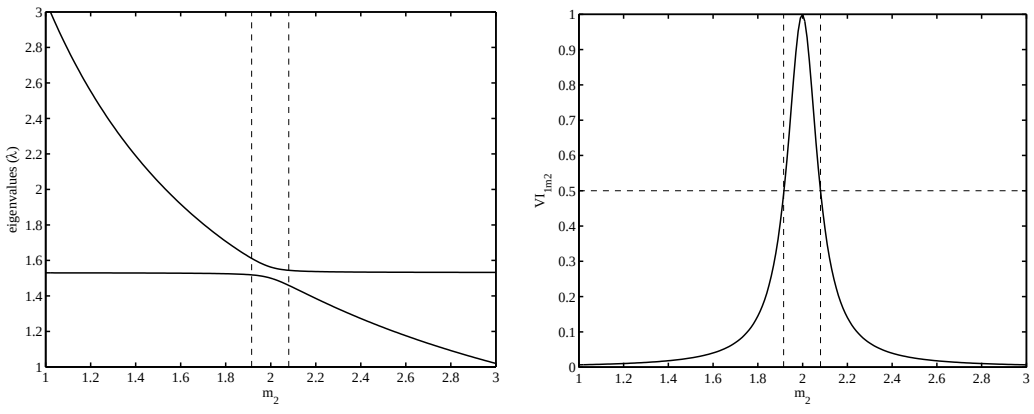

(a) eigenvalues (b) veering index

Figure 4.15: 2 DOF system plotted for $k_1 = k_2 = 3$, $m_1 = 2$, $s = 0.0625$ and $m_2 = 1...3$. Dotted lines indicate the half-SCQ parameter bandwidth.

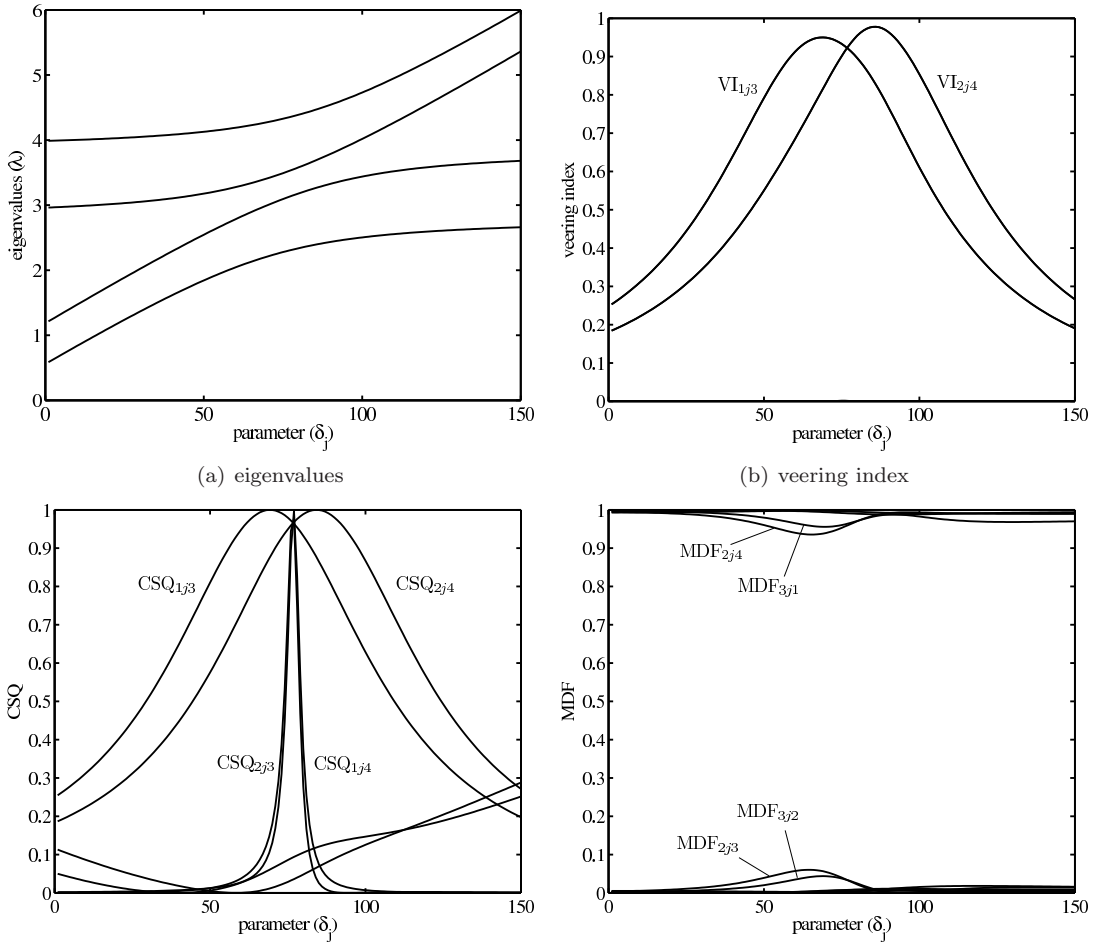

(a) eigenvalues

(b) veering index

(c) veering quotient

(d) veering participation factor

Figure 4.17: 4 DOF system plotted for $m_1 = m_2 = m_3 = m_4 = 1$, $s_1 = s_2 = 0.6$, $s_3 = 0.05$, $k_1 = 0.1 + 0.03\delta_j$, $k_2 = 0.75 + 0.03\delta_j$, $k_3 = 2.2$, $k_4 = 3.2$ and $\delta_j = 1...150$.

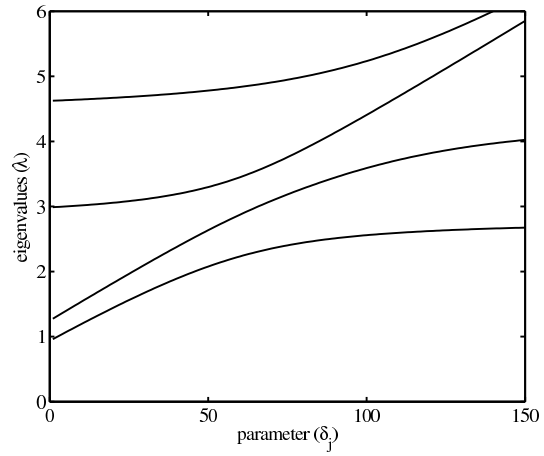

(a) eigenvalues

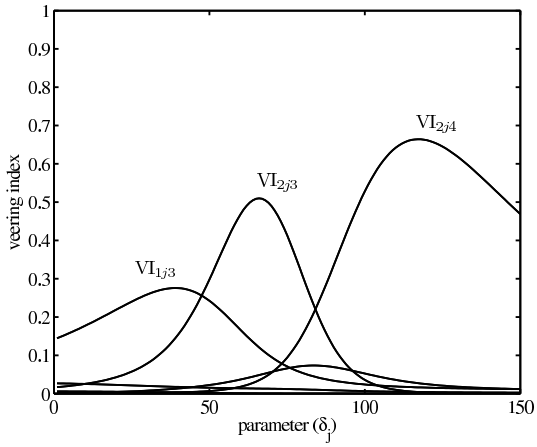

(b) veering indices

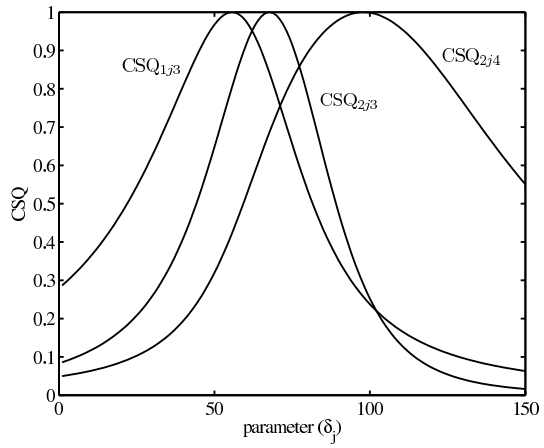

(c) cross sensitivity quotients

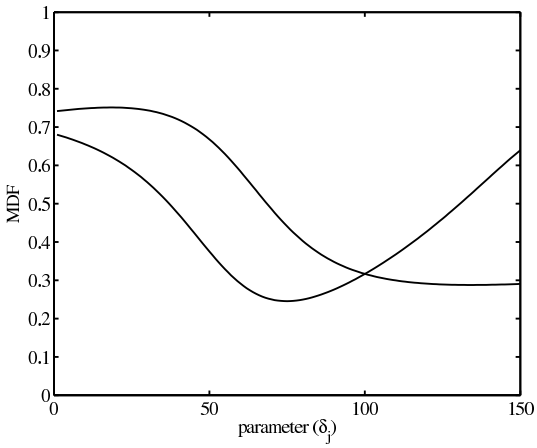

(d) MDF_{1j3} and MDF_{3j1}

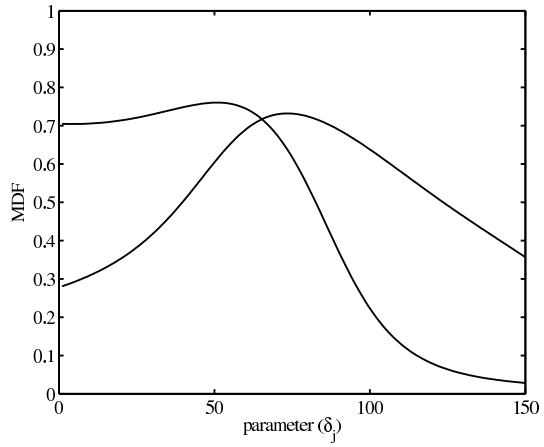

(e) MDF_{2j3} and MDF_{3j2}

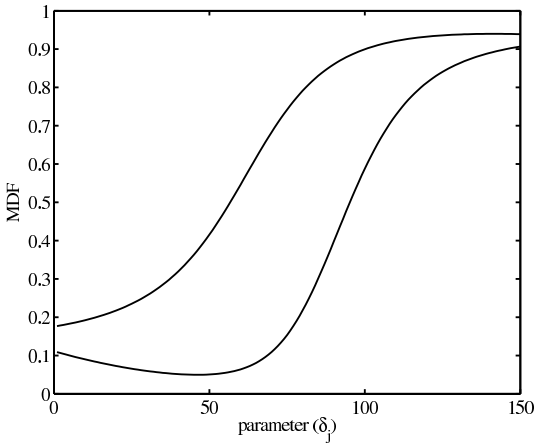

(f) MDF_{2j4} and MDF_{4j2}

Figure 4.18: The 4 DOF system plotted for $s_1 = s_2 = s_3 = 0.6$.

4.5 Conclusions

Possibly the first explicit experimental demonstration of eigenvalue curve veering has been given, along with the associated mode shape transformations. The results correspond well with those from a finite element model. These findings are important with regard to the interpretation of experimentally determined modal parameters. The abrupt and counterintuitive variations may also cause problems for model updating and general modal correlation techniques; in particular, idealised models of symmetric or periodic structures may overlook the behaviour entirely. Properly accounted for, however, the eigenvector rotations within a subspace are found to offer sensitive information about structural parameters and could provide an important contribution to updating schemes.

The investigations have highlighted a hitherto unsatisfied need for a meaningful method of quantitative identification of veering. The new techniques presented here allow analysis of the mechanisms through which veering is manifested, notably the migration of properties from one mode to another. Three normalised criteria are proposed: The *cross-sensitivity quotient* describes the state of veering of two modes within their subspace, the *modal dependence factor* identifies the conformity of the modes to that subspace, and the *veering index* combines the two to give a definitive quantification of mode veering. An important feature of the technique is that it requires only knowledge of the modal properties for the two modes concerned at a single parameter value, anywhere in the vicinity of veering. The method offers insight when used in isolation but its principal application is expected to be in the interpretation and extrapolation of less esoteric quantities, as described in the following chapters.

Chapter 5

Application of Veering Indices

5.1 Introduction

The preceding chapter has developed tools for the identification and quantification of eigenvalue curve veering. The results they produce are insightful but the normalised appraisal they provide is not suited to dimensionalised assessments. In this chapter the tool kit is extended to facilitate the evaluation of more physical quantities.

In sections 5.2–5.5, expressions are derived for the datum values of various modal properties. These are formulated in terms of the modal properties for an arbitrary eigensolution in the vicinity of veering, and offer a consistent dimensionalised representation of the coupling between the modes regardless of the transient parameter variations. They are derived first for stiffness matrix variations, and the results are extrapolated to mass matrix variations in section 5.6. Their application is demonstrated with regard to two simple lumped mass systems in section 5.7.

To conclude, section 5.8 assesses all of the methods of both this chapter and the last, with reference to a full FE model. The evaluation includes comparisons with recently proffered veering metrics from the literature.

5.2 Veering Parameter Datum

The equations of motion for an undamped dynamic system are given by

$$\mathbf{K\Phi} - \mathbf{M\Phi\Lambda} = \mathbf{0} \tag{5.1}$$

Considering a linear variation of the stiffness matrix,

$$\mathbf{K}' = \mathbf{K} + \frac{d\mathbf{K}}{d\delta_K}\Delta\delta_K, \tag{5.2}$$

where $\Delta\delta_K = \delta'_K - \delta_K$ is the change in the parameter δ_K and the prime ($'$) is once again used to differentiate the properties for the arbitrary parameter value ${\delta_j}'$ from those for δ_j. The equation of motion for the modified system can then be written

$$\left(\mathbf{K} + \frac{d\mathbf{K}}{d\delta_K}\Delta\delta_K\right)\boldsymbol{\Phi}' - \mathbf{M}'\boldsymbol{\Phi}'\boldsymbol{\Lambda}' = \mathbf{0}. \tag{5.3}$$

Once again a constant mass matrix is assumed so that the transformation of the mass-normalised eigenvectors takes the form of a rotation, α, in the orthonormal basis thus defined. Limiting the eigenvector matrices to include only the two veering modes, premultiplying by ${\boldsymbol{\Phi}'_{ik}}^T$ and using eqn. (4.18) gives

$$\mathbf{T}^T\boldsymbol{\Phi}_{ik}^T\left(\mathbf{K} + \frac{d\mathbf{K}}{d\delta_K}\Delta\delta_K\right)\boldsymbol{\Phi}_{ik}\mathbf{T} - {\boldsymbol{\Phi}'_{ik}}^T\mathbf{M}'\boldsymbol{\Phi}'_{ik}\boldsymbol{\Lambda}'_{ik} = \mathbf{0}. \tag{5.4}$$

Applying orthogonal relationships to eqn. 5.4 and using eqn. (4.19) with $\frac{d\mathbf{M}}{d\delta_K} = 0$, the modified eigenvalues can be expressed in terms of the initial modal properties so that

$$\boldsymbol{\Lambda}'_{ik} = \mathbf{T}^T\boldsymbol{\Lambda}\mathbf{T} + \mathbf{T}^T\boldsymbol{\Sigma}_{iKk}\mathbf{T}\Delta\delta_K \tag{5.5}$$

where the diagonal elements of the matrix equation give

$$\begin{aligned}\lambda'_i =& \lambda_i\cos^2(\alpha) + \lambda_k\sin^2(\alpha)\\ &+ \left(\sigma_{iKi}\cos^2(\alpha) + 2\kappa_{iKk}\cos(\alpha)\sin(\alpha) + \sigma_{kKk}\sin^2(\alpha)\right)\Delta\delta_K \qquad (5.6)\\ \lambda'_k =& \lambda_i\sin^2(\alpha) + \lambda_k\cos^2(\alpha)\\ &+ \left(\sigma_{iKi}\sin^2(\alpha) - 2\kappa_{iKk}\cos(\alpha)\sin(\alpha) + \sigma_{kKk}\cos^2(\alpha)\right)\Delta\delta_K, \qquad (5.7)\end{aligned}$$

and the off-diagonal elements identically prescribe

$$\Delta\lambda_{ki}\cos(\alpha)\sin(\alpha) + \left(\Delta\sigma_{kKi}\cos(\alpha)\sin(\alpha) + \kappa_{iKk}(\cos^2(\alpha) - \sin^2(\alpha))\right)\Delta\delta_K = 0. \tag{5.8}$$

Rearranging the latter allows the determination of the parameter variation required to produce a given vector rotation,

$$\Delta\delta_K = -\frac{\Delta\lambda_{ki}\sin(2\alpha)}{\Delta\sigma_{kKi}\sin(2\alpha) + 2\kappa_{iKk}\cos(2\alpha)}. \tag{5.9}$$

Dividing numerator and denominator by $\cos(2\alpha)$ gives

$$\Delta\delta_K = -\frac{\Delta\lambda_{ki}\tan(2\alpha)}{\Delta\sigma_{kKi}\tan(2\alpha) + 2\kappa_{iKk}}, \tag{5.10}$$

and setting $\alpha = \beta$ so that $\Delta\delta_K = \overline{\delta}_K - \delta_K$, substitution of eqn. (4.22) produces

$$\overline{\delta}_K = \delta_K - \frac{(\Delta\lambda_{ki}/2)(\Delta\sigma_{kKi}/2)}{(\Delta\sigma_{kKi}/2)^2 + \kappa_{iKk}^2} \tag{5.11}$$

where $\overline{\delta}_K$ is the veering parameter datum: the parameter value required to align the eigenvectors with the veering datum set. This parameter value locates the point where the eigenvector sensitivities are

greatest, the eigenvalues are closest, and their loci effectively swap trajectories. Using eqns. (4.23) and (4.25) gives the alternative expressions

$$\overline{\delta}_K = \delta_K - \frac{\Delta\lambda_{ki}\Delta\sigma_{kKi}}{4\overline{\kappa}^2_{iKk}} \tag{5.12}$$

and

$$\overline{\delta}_K = \delta_K - \frac{\Delta\lambda_{ki}\Delta\sigma_{kKi}}{4\kappa^2_{iKk}}\mathrm{CSQ}_{iKk}. \tag{5.13}$$

5.3 Eigenvalue Determination

It is now possible to determine the eigenvalues at the veering datum. Rearranging eqns. (5.6) and (5.7), and setting $\alpha = \beta$ so that $\lambda'_i = \overline{\lambda}_i$, $\lambda'_k = \overline{\lambda}_k$, and $\Delta\delta_K = \overline{\delta}_K - \delta_K$ gives

$$\begin{aligned}\overline{\lambda}_i =& \frac{\lambda_i + \lambda_k}{2} - \frac{\Delta\lambda_{ki}}{2}\cos(2\beta) \\ &+ \left(\frac{\sigma_{iKi} + \sigma_{kKk}}{2} - \frac{\Delta\sigma_{kKi}}{2}\cos(2\beta) + \kappa_{iKk}\sin(2\beta)\right)\left(\overline{\delta}_K - \delta_K\right) \qquad (5.14)\\ \overline{\lambda}_k =& \frac{\lambda_i + \lambda_k}{2} + \frac{\Delta\lambda_{ki}}{2}\cos(2\beta) \\ &+ \left(\frac{\sigma_{iKi} + \sigma_{kKk}}{2} + \frac{\Delta\sigma_{kKi}}{2}\cos(2\beta) - \kappa_{iKk}\sin(2\beta)\right)\left(\overline{\delta}_K - \delta_K\right). \qquad (5.15)\end{aligned}$$

From eqns. (4.22) and (4.24),

$$\sin(2\beta) = \frac{\Delta\sigma_{kKi}}{2\overline{\kappa}_{iKk}} \tag{5.16}$$

$$\cos(2\beta) = \frac{\kappa_{iKk}}{\overline{\kappa}_{iKk}} \tag{5.17}$$

so

$$\overline{\lambda}_i = \frac{\lambda_i + \lambda_k}{2} - \frac{\Delta\lambda_{ki}}{2}\frac{\kappa_{iKk}}{\overline{\kappa}_{iKk}} + \left(\frac{\sigma_{iKi} + \sigma_{kKk}}{2}\right)\left(\overline{\delta}_K - \delta_K\right) \tag{5.18}$$

$$\overline{\lambda}_k = \frac{\lambda_i + \lambda_k}{2} + \frac{\Delta\lambda_{ki}}{2}\frac{\kappa_{iKk}}{\overline{\kappa}_{iKk}} + \left(\frac{\sigma_{iKi} + \sigma_{kKk}}{2}\right)\left(\overline{\delta}_K - \delta_K\right). \tag{5.19}$$

Substituting eqn. (5.12),

$$\overline{\lambda}_i = \frac{\lambda_i + \lambda_k}{2} - \frac{(\sigma_{iKi} + \sigma_{kKk})\Delta\lambda_{ki}\Delta\sigma_{kKi}}{8\overline{\kappa}^2_{iKk}} - \frac{\Delta\lambda_{ki}\kappa_{iKk}}{2\overline{\kappa}_{iKk}} \tag{5.20}$$

$$\overline{\lambda}_k = \frac{\lambda_i + \lambda_k}{2} - \frac{(\sigma_{iKi} + \sigma_{kKk})\Delta\lambda_{ki}\Delta\sigma_{kKi}}{8\overline{\kappa}^2_{iKk}} + \frac{\Delta\lambda_{ki}\kappa_{iKk}}{2\overline{\kappa}_{iKk}}. \tag{5.21}$$

5.4 Eigenvalue Separation

A useful quantity is the separation of the eigenvalues at their closest point, the veering datum. It is trivial to determine this value from the difference of eqns. (5.6) and (5.7), but the expression may also

be derived without the intermediate rumination of the parameter datum. From eqns. (5.6) and (5.7),

$$\begin{aligned}\Delta\lambda'_{ki} &= \lambda'_k - \lambda'_i \\ &= \Delta\lambda_{ki}\left(\cos^2(\alpha) - \sin^2(\alpha)\right) \\ &\quad + \left(\Delta\sigma_{ki}(\cos^2(\alpha) - \sin^2(\alpha)) - 4\kappa_{iKk}\cos(\alpha)\sin(\alpha)\right)\Delta\delta_K \\ &= \Delta\lambda_{ki}\cos(2\alpha) + \left(\Delta\sigma_{ki}\cos(2\alpha) - 2\kappa_{iKk}\sin(2\alpha)\right)\Delta\delta_K \end{aligned} \tag{5.22}$$

Once more setting $\alpha = \beta$ so that $\Delta\lambda'_{ki} = \Delta\overline{\lambda}_{ki}$ and applying eqns. (5.17) and (5.16), the term in $\Delta\delta_K$ vanishes so that

$$\frac{\Delta\lambda_{ki}}{\Delta\overline{\lambda}_{ki}} = \frac{\overline{\kappa}_{iKk}}{\kappa_{iKk}}. \tag{5.23}$$

This simple result provides a powerful means of determining the minimum eigenvalue separation of two veering modes. Employing eqns. (4.23) and (4.25), the minimum separation can be expressed in terms of the properties for an arbitrary parameter value:

$$\Delta\overline{\lambda}_{ki} = \frac{\Delta\lambda_{ki}|\kappa_{iKk}|}{\sqrt{{\kappa_{iKk}}^2 + \left(\Delta\sigma_{kKi}/2\right)^2}} = \Delta\lambda_{ki}\sqrt{\mathrm{CSQ}_{iKk}}. \tag{5.24}$$

5.5 Eigenvalue Curvature

It has been shown that the eigenvectors and eigenvalues of a system at the veering datum are easily computed; in addition, the system matrices may be determined in a straightforward manner using knowledge of the veering parameter datum from eqn. (5.11) in a linear expression such as

$$\overline{\mathbf{K}} = \mathbf{K} + \frac{d\mathbf{K}}{d\delta_K}(\overline{\delta}_K - \delta_K). \tag{5.25}$$

Equipped with this knowledge, any other properties may be derived. One more quantity will be considered here: the curvatures, or second derivatives, of the eigenvalue loci are not only a useful quantity in their own right, but along with the eigenvalue separation they provide a dimensionalised means of comparing the intensity of different veering cases.

Eqn. (4.13) gives an expression for the eigenvalue curvature, and the accompanying discussion explains that the contribution of the k^{th} mode to the i^{th} second derivative is

$$\left.\frac{d^2\lambda_i}{d\delta_j^2}\right|_k = -\frac{2\left[\phi_k^T\left(\frac{d\mathbf{K}}{d\delta_j} - \lambda_i\frac{d\mathbf{M}}{d\delta_j}\right)\phi_i\right]^2}{\Delta\lambda_{ki}} = -\frac{2\kappa_{ijk}^2}{\Delta\lambda_{ki}}. \tag{5.26}$$

At the veering datum this term is likely to dominate the curvature, and under this assumption it is expressed as

$$\overline{\frac{d^2\lambda_i}{d\delta_j^2}} = -\frac{2\overline{\kappa}_{ijk}^2}{\Delta\overline{\lambda}_{ki}}. \tag{5.27}$$

Using eqn. (5.23), it can be written

$$\overline{\frac{d^2\lambda_i}{d\delta_j^2}} = -\frac{2\overline{\kappa}_{ijk}^3}{\kappa_{ijk}\Delta\lambda_{ki}}, \tag{5.28}$$

or, once more substituting eqn. (4.23),

$$\overline{\frac{d^2\lambda_i}{d\delta_j^2}} = -\frac{2\left[\kappa_{ijk}^2 + (\Delta\sigma_{kKi}/2)^2\right]^{3/2}}{\kappa_{ijk}\Delta\lambda_{ki}}. \tag{5.29}$$

5.6 Mass Matrix Variation

Now considering a linear mass matrix variation with constant stiffness matrix, the eigenvectors are normalised with respect to the stiffness matrix as in eqn. (4.26), and eqn. (5.2) becomes

$$\mathbf{K}'\mathbf{\Psi}' - \left(\mathbf{M} + \frac{d\mathbf{M}'}{d\delta_M}\Delta\delta_M\right)\mathbf{\Psi}'\mathbf{\Lambda}' = \mathbf{0}. \tag{5.30}$$

Using only modes i and k, premultiplying by ${\mathbf{\Psi}'_{ik}}^T$, postmultiplying by ${\mathbf{\Lambda}'_{ik}}^{-1}$ and introducing eqn. (4.18) produces

$${\mathbf{\Psi}'_{ik}}^T\mathbf{K}'\mathbf{\Psi}'_{ik}{\mathbf{\Lambda}'_{ik}}^{-1} - \mathbf{T}^T\mathbf{\Psi}_{ik}^T(\mathbf{M} + \frac{d\mathbf{M}'}{d\delta_M}\Delta\delta_M)\mathbf{\Psi}_{ik}\mathbf{T} = \mathbf{0}. \tag{5.31}$$

Rearranging and appling eqn. (4.28) in conjunction with the orthogonality conditions,

$${\mathbf{\Lambda}'_{ik}}^{-1} = \mathbf{T}^T\mathbf{\Lambda}_{ik}^{-1}\mathbf{T} - \mathbf{T}^T\mathbf{\Sigma}^*_{iMk}\mathbf{T}\Delta\delta_M. \tag{5.32}$$

This is analogous to eqn. (5.5) so that

$$\overline{\delta}_M = \delta_M + \frac{\Delta\lambda^*_{ki}\Delta\sigma^*_{kMi}}{{\overline{\kappa}^*_{iMk}}^2}, \tag{5.33}$$

$$\overline{\lambda^*}_i = \frac{\lambda^*_i + \lambda^*_k}{2} - \frac{(\sigma^*_{iKi} + \sigma^*_{kKk})\Delta\lambda^*_{ki}\Delta\sigma^*_{kKi}}{8{\overline{\kappa^*}}^2_{iKk}} - \frac{\Delta\lambda^*_{ki}\kappa^*_{iKk}}{2\overline{\kappa^*}_{iKk}}, \tag{5.34}$$

$$\overline{\lambda^*}_k = \frac{\lambda^*_i + \lambda^*_k}{2} - \frac{(\sigma^*_{iKi} + \sigma^*_{kKk})\Delta\lambda^*_{ki}\Delta\sigma^*_{kKi}}{8{\overline{\kappa^*}}^2_{iKk}} + \frac{\Delta\lambda^*_{ki}\kappa^*_{iKk}}{2\overline{\kappa^*}_{iKk}}, \tag{5.35}$$

$$\Delta\overline{\lambda}^*_{ki} = \frac{\Delta\lambda^*_{ki}|\kappa^*_{iMk}|}{\sqrt{{\kappa^*_{iMk}}^2 + (\Delta\sigma^*_{kMi}/2)^2}} = \Delta\lambda^*_{ki}\sqrt{\mathrm{CSQ}^*_{iKk}}, \tag{5.36}$$

and

$$\frac{\Delta\lambda^*_{ki}}{\Delta\overline{\lambda}^*_{ki}} = \frac{\overline{\kappa}^*_{iMk}}{\kappa^*_{iMk}} \tag{5.37}$$

where $\mathbf{\Lambda}^* = \mathbf{\Lambda}^{-1}$. The relationship between modal coupling and eigenvalue separation is not as elegant for mass matrix variation as it is for stiffness matrix variation, and can not be determined directly from eqn. (5.37). To determine the datum eigenvalue separation it is necessary to compute

the eigenvalues individually using eqns. (5.34) and (5.35), and to calculate the difference. This value is no longer the minimum eigenvalue, however, as the minimum is not exactly coincident with the datum.

Similarly, the determination of the eigenvalue curvature at the datum is protracted for mass variation. Following the methods of section 5.5 yields

$$\overline{\frac{d^2\lambda_i}{d\delta_j^2}} = 2\overline{\kappa}_{ijk}^2 \overline{\kappa}_{ijk}^* / \Delta\lambda_{ki}^* \kappa_{ijk}^* \overline{\lambda}_i \overline{\lambda}_k \tag{5.38}$$

or

$$\overline{\frac{d^2\lambda_i}{d\delta_j^2}} = 2\overline{\kappa}_{ijk}^* {}^3\overline{\lambda}_i / \Delta\lambda_{ki}^* \kappa_{ijk}^*. \tag{5.39}$$

This solution once again requires the prior evaluation of eqn. (5.35) to obtain $\overline{\lambda}_i$.

5.7 Examples

The application of these ideas will be demonstrated with reference to the two examples used in section 4.4.6. The first of these is the 2 DOF system seen in figure 4.14, where the parameter being varied is the mass m_2. The stiffness matrix remains constant so using eqn. 5.37, the quantity $\Delta\lambda_{ki}^*$ can be plotted on the same axes as its predicted minimum value, $\Delta\overline{\lambda^*}_{ki}$. These results are seen in figure 5.1(a), where the minimum separation is seen to be predicted exactly for all values of m_2. Of note is the well-behaved, symmetric appearance of the curves afforded by the transformation of $\Delta\lambda$ to $\Delta\lambda^*$. Unfortunately, $\Delta\lambda^*$ can not be used directly to obtain the eigenvalue separation; instead, using eqns. (5.34) and (5.34) produces the datum eigenvalue predictions seen in figure 5.1(b) along with the actual eigenvalues. Once again, the predictions are exact for this 2 DOF system. The separation of the eigenvalues is then simple to determine, as shown in figure 5.1(c). The symmetry of figure 5.1(a) is not present in the new figure, helping to explain the need for a more intensive computation. As expected, however, the minimum value is located almost exactly at the veering datum.

The second example of section 4.4.6 is the 4 DOF system presented in figure 4.16. The parameter variation in this example is manifested as a linear change in the stiffness matrix. This parameter allows the use of eqn. (5.23) to directly determine the eigenvalue separation at veering, without the more involved computations required for mass matrix variation. Two cases are presented: in the first, the coupling between DOFs 1 and 4 is much lower than that between the DOF pairs 1-3 and 2-4. As a result, veering is observed between those two mode pairs, but not for any other modes. Figure 5.2(a) shows the predicted eigenvalue separations for the two mode pairs compared to the actual eigenvalue separations. The predictions are almost constant over the parameter range and acurately forecast the minimum separation. Nearly indistinguishable, small discrepancies arise in the predictions due to the interference of other modes with the idealised veering behaviour. The eigenvalue separation predictions for the remaining mode pairs are seen in figures 5.2(c) and 5.2(b), but these are not valid because the

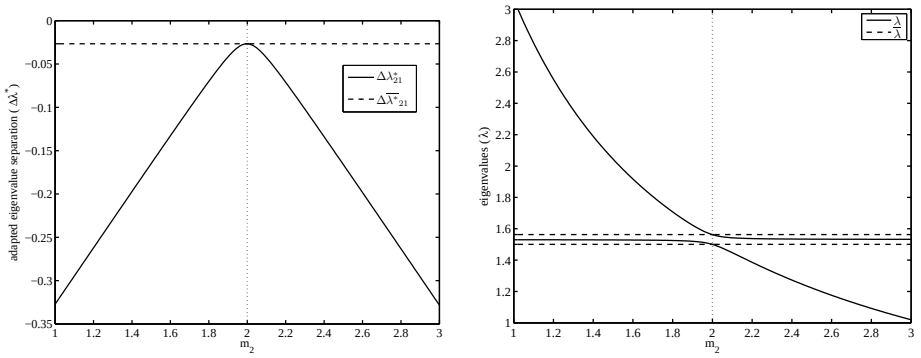

(a) adapted eigenvalue separation

(b) eigenvalues

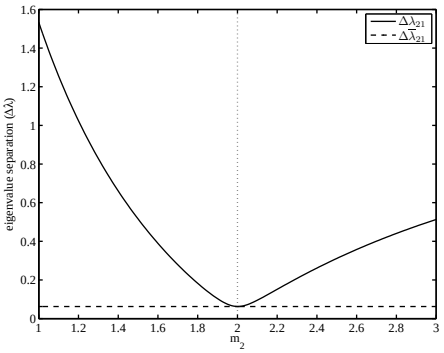

(c) eigenvalue separation

Figure 5.1: Modal properties of the 2-DOF system plotted with veering peak estimates for varying values of parameter m_2. The vertical dotted line denotes the veering datum.

modes in question are not veering. Accordingly, they are seen to meander over the parameter range and provide no meaningful information. A good indication of the validity of the estimates is provided by the MDF, with values close to unity assuring an accurate result. It is interesting to note that, necessarily, the estimates match the actual values wherever the CSQ is unity, regardless of the MDFs. This is exhibited in figure 5.2(b).

The second case presented for the 4 DOF system is with equal coupling between DOF pairs 1-3, 2-4 and 1-4. The corresponding modes are all observed to veer but never in isolation. This behaviour is accompanied by lower MDFs for mode pairs 1-3 and 2-4, but increased MDFs for pairs 2-3 and 1-4. As such, the estimates for pairs 1-3 and 2-4 plotted in figure 5.3(a) are seen to be less reliable than before, while figure 5.3(b) shows that those for pairs 2-3 and 1-4 to have improved. As with the first case, the predictions for the non-veering modes in figure 5.3(c) give no useful information. None of the predictions are particularly good, and this second case study highlights the importance of the MDF in ascertaining the accuracy of the eigenvalue separation predictions.

5.8 Practical Exposition

Chapter 4 demonstrated the presence of veering phenomena in experimental data. Having now developed tools for the analysis of the behaviour, they are applied to the original structure in fig. 3.1

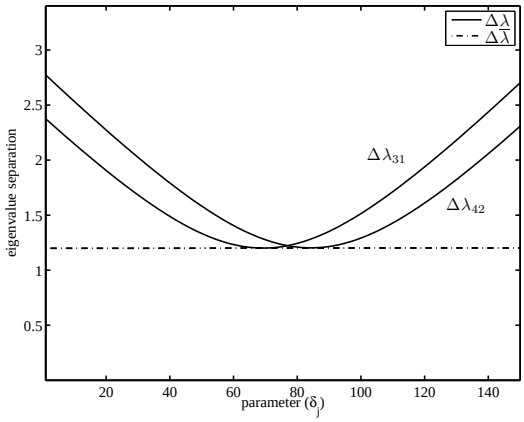

(a) Mode pairs 1-3 and 2-4.

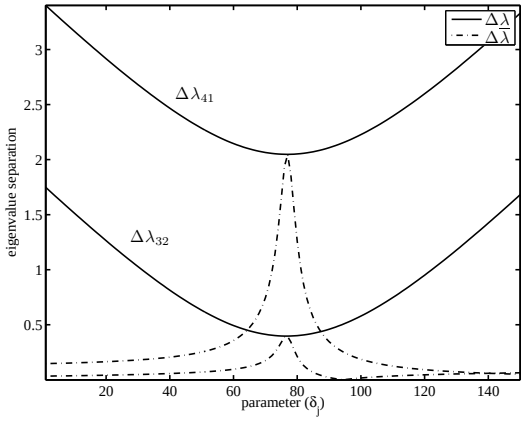

(b) Mode pairs 2-3 and 1-4.

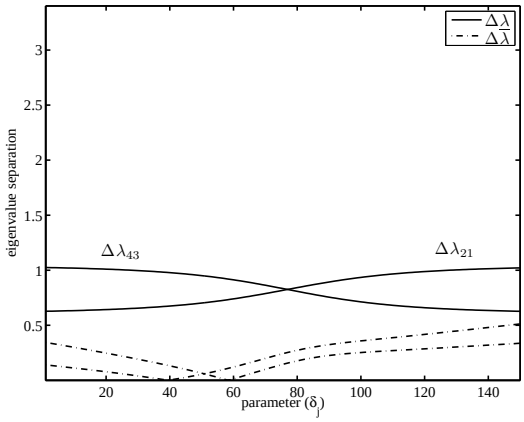

(c) Mode pairs 1-2 and 3-4.

Figure 5.2: Eigenvalue separation (–) in the 4-DOF system compared to the estimated minimum (datum) separation (-.-) for variation of parameter δ_j, using $s_1 = s_2 = 0.6$ and $s_3 = 0.05$.

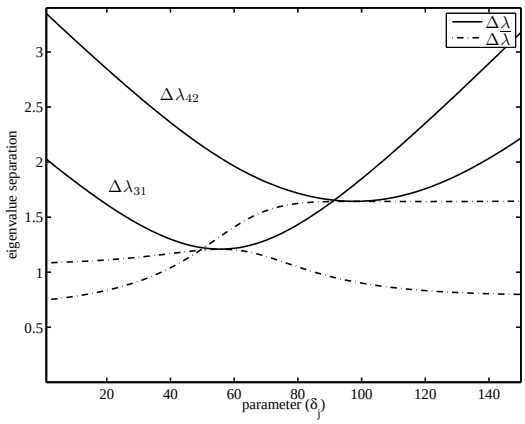

(a) Mode pairs 1-3 and 2-4.

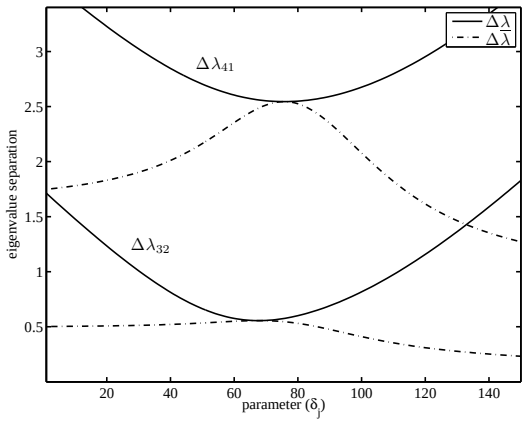

(b) Mode pairs 2-3 and 1-4.

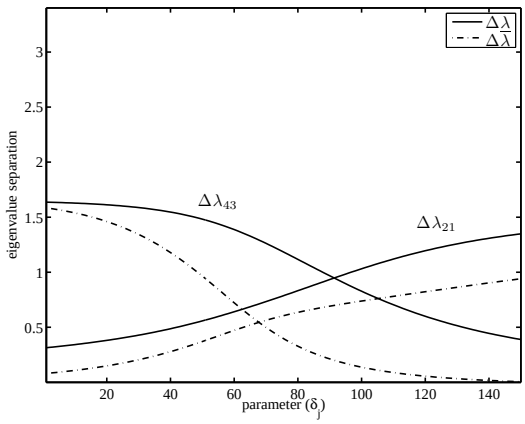

(c) Mode pairs 1-2 and 3-4.

Figure 5.3: Eigenvalue separation (–) in the 4-DOF system compared to the estimated minimum (datum) separation (-.-) for variation of parameter δ_j, using $s_1 = s_2 = s_3 = 0.6$.

to demonstrate their utility. Comparisons are then drawn with existing methods to highlight the advantages of the new techniques.

5.8.1 Veering Analysis of a Real Structure

The stressed structure described in section 3.4 has many intersecting eigenvalue loci. Modes 2 and 4 are seen to intersect at around 3000N (with mode numbers referenced from the zero load case; modes 2 and 3 cross at 555N). These modes will be examined in detail below.

While the modes are seen to veer in both figure 3.19(b) and figure 3.19(c), the coarse load steps used to produce the graph do not disclose the precise behaviour at the intersection. Refining the load steps in this region to 6.5 N produces the frequency loci seen in figure 5.4. These curves are indisputably veering, and this interpretation is supported by the veering index seen in figure 5.5. The corresponding CSQ and MDFs are seen in figure 5.6. An interesting feature of this plot is the sharp rise in both CSQ_{2P4} and MDF_{4P2} at around 4650 N, seeming to "bounce" back from zero. These upturns are not an indication of veering, and MDF_{2P4} remains low so that the veering index is representative of this fact. This example epitomises the manner in which the two MDFs window the CSQ to form the veering index, restricting it to the region for which it provides a valid measure of veering. This window must be inferred when interpreting other results as well. For example the eigenvalue separation is shown in figure 5.7 along with the estimated minimum, which is seen to be accurate within the window but again shows significant deviation at around 4650N.

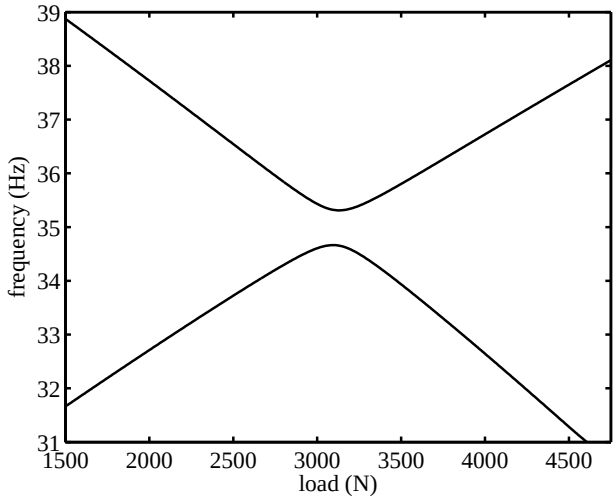

Figure 5.4: Close examination of the veering frequency loci for the 2nd and 4th modes.

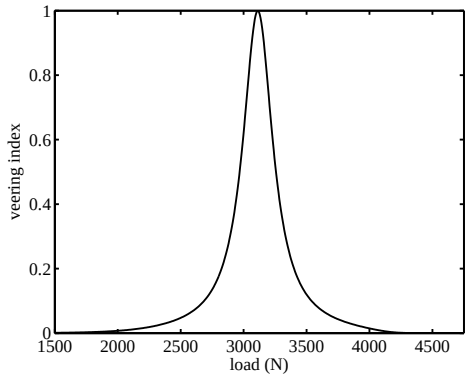

Figure 5.5: Veering index for modes 2 and 4 in the welded frame.

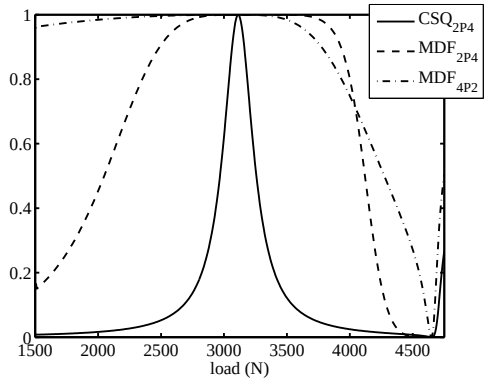

Figure 5.6: Cross-sensitivity quotient and modal dependence factors for modes 2 and 4 in the welded frame.

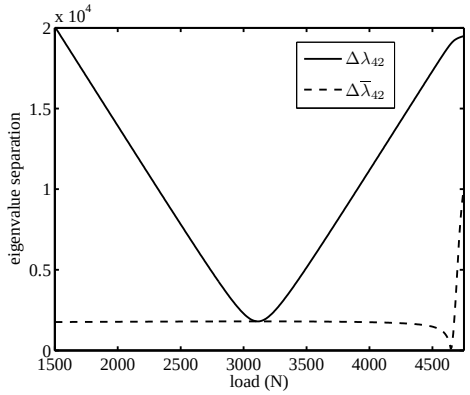

Figure 5.7: Eigenvalue separation of the 2nd and 4th modes in the welded frame, along with the value estimated using veering approximations.

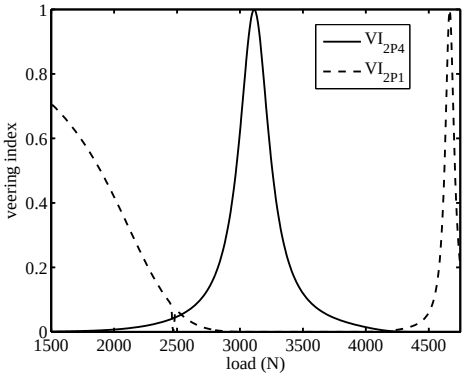

Figure 5.8: Veering indices for mode 2 with respect to modes 1-10. The prominent indices are labelled in the legend, while the other indices are close to zero and indistinguishable at the bottom of the plot.

Figure 5.8 shows all of the veering indices of mode 2 with respect to modes 1-10. Besides VI_{2P4}, only one other index stands out. This index is VI_{2P1}, corresponding to veering between modes 2 and 1. Figure 5.9 shows the first four frequency loci, where mode 1 is seen to rise gradually, crossing mode 3 before veering with mode 2. (Note that modes 2 and 3 have already crossed below the load range of this figure.) Where the modes veer at the right of the plot, a sharp peak is seen in VI_{2P1}, explaining the anomalies at around 4650N noted previously. The gentler slope to the left of the plot indicates a much more gradual veering, spanning the loading range to the extent that it is difficult to observe at the scale of figure 5.9. In fact, the behaviour is first interrupted by the veering of modes 2 and 4 (whereupon the gentler veering is transferred from mode 2 to mode 4), and then curtailed by the onset of buckling in the structure. In this instance it would be nearly impossible to recognise the occurence of veering without using the veering index. The significance of veering in these circumstances is that once it has been recognised, all of the tools presented in this chapter and the last become available for the analysis of the modes concerned.

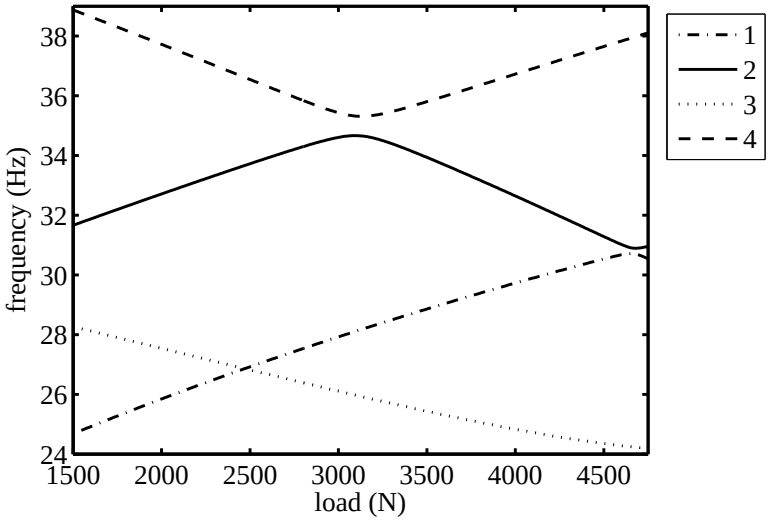

Figure 5.9: The first four frequency loci for the welded frame.

5.8.2 Comparison of Veering Quantifiers

Having explored the traits of the cross-sensitivity quotient, modal dependency factors and veering index, the new quantities will now be contrasted with existing metrics. For the purposes of identifying and quantifying veering, the primary candidates are the modal coupling, or coupling factors, suggested by Perkins and Mote [234] and the derivatives and second derivatives of the eigenvectors and eigenvalues as suggested by Liu [249].

The "modal coupling" and "coupling factors" convey the same information for a self-adjoint system, the coupling factor being proportional to the square of the modal coupling. Figure 5.10 shows the coupling factors for mode 2 with respect to the other modes. While the two rapid instances of veering stand out with high peaks, the gradual instance of veering between modes 2 and 1 in the lower loading spectrum shows unremarkable modal coupling values. In fact, figure 5.10(b) shows that another coupling factor involving mode 6 is greater than that for mode 1, yet modes 6 and 2 are not veering. A similar artefact is observed at the high end of the loading range, where the coupling factor for mode 6 rises substantially, once again without any of the other traits associated with veering. Thus, despite conveying important information about a system, the modal coupling factors are not a reliable indicator of the presence or extent of veering.

The eigenvector sensitivities and eigenvalue second derivatives are both dominated by similar terms to each other in veering regions, as discussed in section 4.4.1. Accordingly, the plots in figure 5.11 and 5.12 both show similar trends. Once more the most abrupt occurrences of veering are identified but the gentler veering of modes 2 and 1 is not evident. In contrast to the veering index, the two criteria have substantial non-zero values for non-veering modes, which mask the significance of the veering modes' curvature. Addressing a technical point, two spurious impulses are seen in each graph

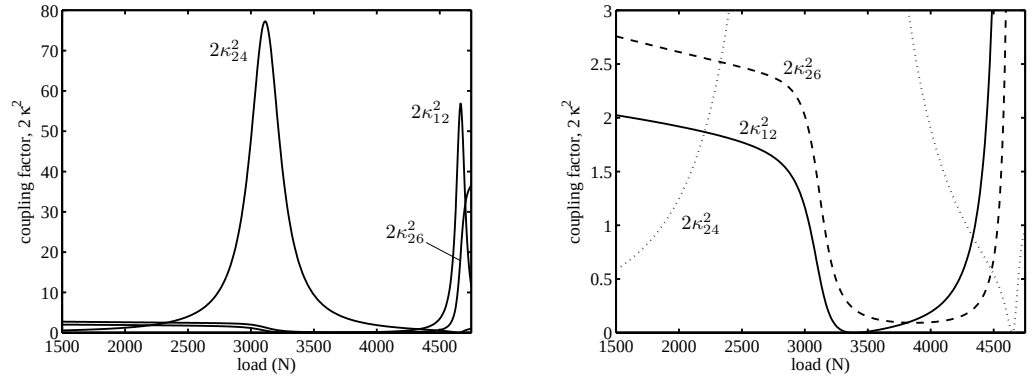

(a) Full scope. (b) Lower range.

Figure 5.10: Modal coupling factors for mode 2 with respect to modes 1 and 3-7 in the welded frame.

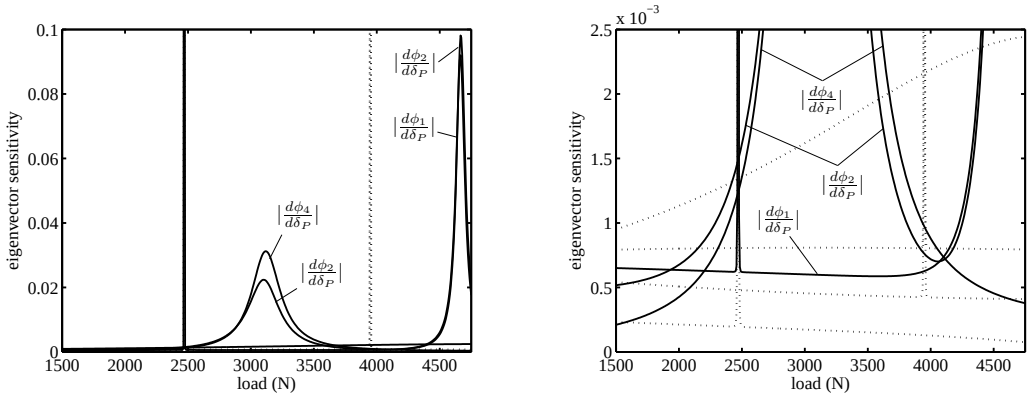

(a) Full scope. (b) Lower range.

Figure 5.11: The ℓ^2 norm of the eigenvector sensitivities for the first seven modes of the welded frame.

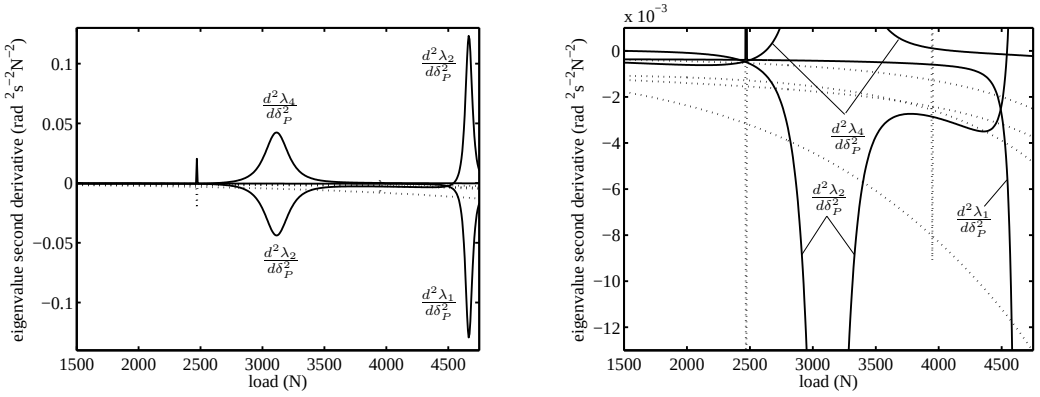

(a) Full scope. (b) Lower range.

Figure 5.12: The eigenvalue sensitivities for the first seven modes of the welded frame.

at 2500 N and 4000 N, where frequency loci cross. These are numerical artefacts caused by the erroneous calculation of small but finite modal coupling where there should be none, combined with the appearance of $\Delta\lambda_{ki}$ (which goes to zero as the modes cross) on the denominator of the respective expressions. As with the modal coupling, the eigenproperty derivatives are found to be inadequate for the identification of veering, endorsing the choice of the newly-derived veering index for these purposes.

5.9 Conclusions

The concepts of a veering datum and modal coupling, taken from chapter 4, have been used to determine expressions for the extremums of various system properties throughout a veering region. Once again these can be determined from a single eigensolution anywhere in the vicinity of veering. While the equations given are strictly only valid for linear systems, problems involving such systems are common: in particular, stress stiffening formulations may often be treated as such. Furthermore, linear approximations can form a basis for iterative nonlinear solutions.

The extremum properties are useful in dimensionalised comparisons, describing the influence of modal couplings on the system dynamics over the parameter space. This characterisation could be useful in correlation exercises such as model updating, or in fact anywhere where modal interactions are significant. Notable examples are localisation and stability studies of bladed disk assemblies.

The new tools have been shown to offer significant advantages over existing techniques for quantifying veering, and their application has been successfully demonstrated with respect to a practical structure.

Chapter 6

Modal Coupling in Model Updating

6.1 Introduction

Finite element model updating is a technique that receives much attention within the modal analysis community; however, all but the simplest of structures continue to frustrate attempts to replicate the intricacies of their dynamic response by numerical means. An important part of the evolution of this discipline is the development of new tools to locate and quantify the discrepancies between actual structures and their digital counterparts.

Section 4.3 considered the possibility of using eigenvector transformations within a subspace to aid with parametric identification. Two difficulties compromise the operation of such a scheme. Firstly, eigenvectors are infamously difficult to determine experimentally. Measuring the orientation of the eigenvectors within a subspace offers some level of abstraction from the eigenvectors themselves, but the results of section 4.3.2 suggest that this quantity is still not reliable enough to be useful.

The second difficulty lies in the sensitivity of the vector rotations to other parameters in these regions. For example, in the welded frame the behaviour of modes 5 and 6 in the vicinity of their intersection was seen to depend strongly on the weld stiffnesses. Without accurate knowledge of these parameters the utility of the vector rotations as updating variables is diminished.

This chapter develops and implements a new approach for a model updating scheme, based upon eigenvector rotations with respect to two or more parameters. All but one of the parameters are those to be determined by the scheme, while the remaining parameter is deliberately varied to produce multiple results sets. The concept of using parametric variations to enrich the available dataset is not a new one. Chen *et al.* [268] and Lammens *et al.* [269] discuss perturbed boundary condition testing, where the structure is adapted by means of mass and stiffness elements, and the extended result sets offer better conditioning to the updating problem. Where perturbed boundary condition tests tend to employ discrete structural modifications, the method presented here uses continuous variations (albeit sampled at discrete intervals). This approach permits the novel introduction of modal coupling

properties, which contribute qualitatively different information to the updating scheme. In particular, they will be shown to offer unique insights into uncertainties in symmetric structures.

First the proposed technique is set out, and the theory developed for extracting the veering properties from experimental data. A discussion of the properties and their application to an updating scheme follows, before a numerical and experimental example is demonstrated with regard to the welded frame.

6.2 Theory

The principle behind the proposed technique is to collect sets of response data for a system while deliberately varying one parameter. This will be referred to as the "control parameter". These data are used to evaluate the veering characteristics, or veering properties, of two modes with respect to the control parameter and in turn to update the dependent parameters of the FE model. The assumption of "ideal veering" is made in this analysis, corresponding to mode pairs with both MDFs close to unity.

The control parameter in the example that follows will take the form of structural loading, but for the development of the technique the parameter may be considered to be any linear modification of the stiffness matrix, δ_K. An analogous method can be derived for mass matrix variation. The direction of rotation of the eigenvectors throughout veering plays an important role, so to measure this it is first necessary to establish a set of reference vectors. These may be from the analytical or experimental results and may correspond to any parameter values, but a convenient choice is the veering datum vectors. The datum vectors may be established easily from the analytical model using the tools of chapters 4 and 5. Most modal analysists will be familiar with the idea that the sign of an eigenvector is arbitrary, but it is critical throughout the process described here that the sign of the reference vectors is kept constant. Without a constant reference it is not possible to establish a direction for the eigenvector rotation, which conveys important information about the parameter variations in symmetric structures.

Once the reference vectors are established, the veering properties may be extracted from the test data, and these are then used to update the FE model.

6.2.1 Veering Property Extraction

Veering property extraction is the process of determining the veering characteristics from experimental data. It consists of two stages: eigenvalue curve fitting and eigenvector sensitivity analysis. Most of the veering characteristics are established in the first step but arguably the most important piece of information, the eigenvector rotation direction, is obtained in the eigenvector analysis.

The curve fitting is itself broken down into two steps. The first determines the mean eigenvalue trajectory while the second identifies the separation of the two loci. The mean eigenvalue locus traces a straight line under linear stiffness variation. The least squares solution is

$$\left\{ \begin{array}{c} p_1 \\ p_2 \end{array} \right\} = \left[\begin{array}{cc} \delta_K^{(1)} & 1 \\ \delta_K^{(2)} & 1 \\ \vdots & \vdots \\ \delta_K^{(n)} & 1 \end{array} \right]^+ \left\{ \begin{array}{c} \mu_\lambda^{(1)} \\ \mu_\lambda^{(2)} \\ \vdots \\ \mu_\lambda^{(n)} \end{array} \right\} \tag{6.1}$$

where $\mu_\lambda^{(n)} = (\lambda_i^{(n)} + \lambda_k^{(n)})/2$, bracketed superscripts denote the experimental data point, and $+$ denotes the pseudo-inverse such that

$$\mathbf{A}^+ = (\mathbf{A}^T\mathbf{A})^{-1}\mathbf{A}^T. \tag{6.2}$$

The locus is then defined by the gradient of the line and the mean eigenvalue at the veering datum, given by

$$\frac{\mathrm{d}\mu_\lambda}{\mathrm{d}\delta_K} = p_1 \qquad \text{and} \qquad \mu_{\overline{\lambda}} = \overline{\delta}_K p_1 + p_2. \tag{6.3}$$

The second curve fitting step is performed using the eigenvalue separation, $\Delta\lambda_{ki}$, computed directly as the difference of the measured eigenvalues. From eqns. (4.23), (5.12) and (5.23),

$$\Delta\lambda_{ki}^2 = (4\overline{\kappa}_{iKk}^2)\delta_K^2 - (8\overline{\kappa}_{iKk}^2\overline{\delta}_K)\delta_K + (4\overline{\kappa}_{iKk}^2\overline{\delta}_K^2 + \Delta\overline{\lambda}_{ki}^2). \tag{6.4}$$

Thus in the vicinity of the veering, where the MDFs are close to unity, $\Delta\lambda_{ki}^2$ is described by a quadratic in the controlled parameter δ_K. The least squares curve fit is obtained from

$$\mathbf{p} = \left[\begin{array}{ccc} {\delta_K^{(1)}}^2 & \delta_K^{(1)} & 1 \\ {\delta_K^{(2)}}^2 & \delta_K^{(2)} & 1 \\ \vdots & \vdots & \vdots \\ {\delta_K^{(n)}}^2 & \delta_K^{(n)} & 1 \end{array} \right]^+ \left\{ \begin{array}{c} {\Delta\lambda_{ki}^{(1)}}^2 \\ {\Delta\lambda_{ki}^{(2)}}^2 \\ \vdots \\ {\Delta\lambda_{ki}^{(n)}}^2 \end{array} \right\} \tag{6.5}$$

where

$$\mathbf{p} = \left\{ \begin{array}{c} 4\overline{\kappa}_{iKk}^2 \\ -8\overline{\kappa}_{iKk}^2\overline{\delta}_K \\ 4\overline{\kappa}_{iKk}^2\overline{\delta}_K^2 + \Delta\overline{\lambda}_{ki}^2 \end{array} \right\}. \tag{6.6}$$

From eqn. (6.6) the veering properties $\overline{\kappa}_{iKk}$, $\overline{\delta}_K$ and $\Delta\overline{\lambda}_{ki}$ may be established in turn, and all that remains is to determine the the sign of $\overline{\kappa}_{iKk}$. This is not possible from consideration of the eigenvalues alone, and the eigenvectors must be consulted.

There are several methods available for establishing the sign of $\overline{\kappa}_{iKk}$, the simplest being inspection of the eigenvector rotations. Having established a set of reference vectors, the eigenvector orientations can be determined as in section 4.3.4. This permits their rotation to be plotted against the controlled

parameter as in figure 4.10. From eqn. (4.22), a positive eigenvector rotation direction corresponds with negative modal coupling[1] so the sign is easily ascertained from such a plot. This distinction allows the determination of parameters which would otherwise be insoluble due to symmetry.

6.2.2 Choice of Updating Variables

The eigenvalue curves in the vicinity of the veering can be completely described with five variables: four of these variables define the straight lines of the two uncoupled modes, upon which the eigenvalues converge asymptotically away from veering, and the remaining variable describes the coupling. The properties derived in the preceding section are a linear permutation of these five variables. In this section the physical relevance of each of the veering properties is discussed, and their suitability as updating variables is assessed.

Of the five properties derived, two describe the location of the veering datum: $\overline{\delta}_K$ and $\mu_{\overline{\lambda}}$. A third describes the orientation of the mean eigenvalue locus, $\frac{\mathrm{d}\mu_\lambda}{\mathrm{d}\delta_K}$, leaving the remaining two to describe the relationship between the two loci.

The maximum modal coupling, $\overline{\kappa}_{iKk}$, seems an obvious choice for describing the coupling between the modes. Significantly, it conveys the direction of rotation of the eigenvectors. In practice, however, the modal coupling at the datum will often show little variation over a wide range of configurations. Remembering that, in the limit, the modal coupling goes to zero away from veering, eqn. (4.23) (or inspection of eqn. (6.4)) reveals the maximum modal coupling to be a measure of the difference in gradients of the two asymptotic eigenvalue loci. Apart from the special case of uncoupled modes (where the modal coupling at the intersection is undefined), the maximum value of the modal coupling does not provide any real measure of the actual coupling between the modes.

The minimum eigenvalue separation is then the only property which holistically conveys the magnitude of the coupling between the two modes. Its shortcoming as an independent quantifier of the coupling is that it can only be positive or zero; the eigenvector rotation direction is not represented. Other eigenvalue-based quantifiers such as the eigenvalue curvature suffer from the same inadequacy.

In the search for a suitable property to represent the coupling, the most promising candidate is the rate of eigenvector rotation within the subspace, $\frac{\mathrm{d}\beta}{\mathrm{d}\delta_K}$. It is related to, but not entirely equivalent to, the eigenvector sensitivities. Importantly, the maximum rotation rate $\overline{\frac{\mathrm{d}\beta}{\mathrm{d}\delta_K}}$ occurs at the veering datum and conveys both the magnitude and sign of the coupling. Rearranging eqn. (5.12) and differentiating yields

$$\frac{\mathrm{d}\delta_K}{\mathrm{d}\beta} = \frac{\Delta\sigma_{ki}}{4\overline{\kappa}_{iKk}^2}\frac{\mathrm{d}\Delta\lambda_{ki}}{\mathrm{d}\beta} + \frac{\Delta\lambda_{ki}}{4\overline{\kappa}_{iKk}^2}\frac{\mathrm{d}\Delta\sigma_{ki}}{\mathrm{d}\beta}. \tag{6.7}$$

[1] Remembering that β is the angle a vector set must rotate through to coincide with the veering datum, a positive rotation of the eigenvectors results in a positive β prior to veering and a negative β after veering. Conversely, $\Delta\sigma_{ki}$ will always be negative prior to veering as the eigenvalues converge, and positive after veering as they diverge again. Thus a positive eigenvector rotation produces a negative modal coupling and vice versa.

Eqns. (5.16), (5.17) and (5.23) produce

$$\Delta\sigma_{ki} = 2\overline{\kappa}_{iKk}\sin(2\beta) \qquad \text{and} \qquad \Delta\lambda_{ki} = \frac{\Delta\overline{\lambda}_{ki}}{\cos(2\beta)} \tag{6.8}$$

so that differentiating gives

$$\frac{\mathrm{d}\Delta\sigma_{ki}}{\mathrm{d}\beta} = 4\overline{\kappa}_{iKk}\cos(2\beta) \qquad \text{and} \qquad \frac{\mathrm{d}\Delta\lambda_{ki}}{\mathrm{d}\beta} = 2\frac{\Delta\overline{\lambda}_{ki}}{\cos^2(2\beta)}\sin(2\beta). \tag{6.9}$$

Substituting eqns. (5.16), (5.17) and (5.23) again,

$$\frac{\mathrm{d}\Delta\sigma_{ki}}{\mathrm{d}\beta} = 4\kappa_{iKk} \qquad \text{and} \qquad \frac{\mathrm{d}\Delta\lambda_{ki}}{\mathrm{d}\beta} = \frac{\Delta\sigma_{ki}\Delta\lambda_{ki}}{\kappa_{iKk}}. \tag{6.10}$$

Combining eqns. (6.10) and (6.7) and rearranging yields

$$\frac{\mathrm{d}\delta_K}{\mathrm{d}\beta} = \frac{\Delta\lambda_{ki}}{\overline{\kappa}^2_{iKk}}\left(\frac{(\Delta\sigma_{ki}/2)^2 + \kappa^2_{iKk}}{\kappa_{iKk}}\right), \tag{6.11}$$

and using eqn. (4.23) this becomes

$$\frac{\mathrm{d}\delta_K}{\mathrm{d}\beta} = \frac{\Delta\lambda_{ki}}{\kappa_{iKk}}. \tag{6.12}$$

The eigenvector rotation rate is then given by

$$\frac{\mathrm{d}\beta}{\mathrm{d}\delta_K} = \left(\frac{\mathrm{d}\delta_K}{\mathrm{d}\beta}\right)^{-1} = \frac{\kappa_{iKk}}{\Delta\lambda_{ki}} \tag{6.13}$$

and the *maximum* rotation rate by

$$\overline{\frac{\mathrm{d}\beta}{\mathrm{d}\delta_K}} = \frac{\overline{\kappa}_{iKk}}{\Delta\overline{\lambda}_{ki}}. \tag{6.14}$$

Although this function is the most physically recognisable, it is discontinuous across $\Delta\overline{\lambda}_{ki} = 0$, making its inverse, $\overline{\frac{\mathrm{d}\beta}{\mathrm{d}\delta_K}}^{-1}$, more suitable for updating schemes.

6.2.3 Updating Scheme

Having ascertained the veering properties from the experimental data, it remains to derive the equivalent properties and their derivatives from the FE data for the purposes of implementing a sensitivity based updating scheme. A key advantage of the method proposed is that these values can be derived from a single eigensolution, without the need to obtain multiple eigensolutions over a range of δ_K.

This study will focus on three properties, ignoring the gradients of the eigenvalue loci and describing the curves only in terms of the vector rotation rate and the datum position on both axes. The computation of the datum position in terms of $\overline{\delta}_K$ and $\mu_{\overline{\lambda}}$ is documented in chapter 5. The vector rotation rate is defined above in terms of $\overline{\kappa}_{iKk}$ and $\Delta\overline{\lambda}_{ki}$, whose derivation are in turn described by chapters 4 and 5.

The sensitivities of these properties with respect to the dependent parameters are now derived below.

The first step is to obtain the derivative of the eigenvalue sensitivities and modal coupling, contained within the sensitivity matrix. Differentiating eqn. (4.19) with respect to an arbitrary parameter δ_p produces

$$\frac{d\mathbf{\Sigma}_{iKk}}{d\delta_p} = \begin{bmatrix} \frac{d\sigma_{iKi}}{d\delta_p} & \frac{d\kappa_{iKk}}{d\delta_p} \\ \frac{d\kappa_{kKi}}{d\delta_p} & \frac{d\sigma_{kKk}}{d\delta_p} \end{bmatrix} = \frac{d\mathbf{\Phi}_{ik}}{d\delta_p}^T \frac{d\mathbf{K}}{d\delta_K}\mathbf{\Phi}_{ik} + \mathbf{\Phi}_{ik}^T \frac{d\mathbf{K}}{d\delta_K}\frac{d\mathbf{\Phi}_{ik}}{d\delta_p}, \tag{6.15}$$

where the parameters δ_K and δ_p are assumed to be independent so that $\frac{d^2\mathbf{K}}{d\delta_K d\delta_p} = 0$ and δ_K affects only the stiffness so that $\frac{d\mathbf{M}}{d\delta_K} = 0$. The eigenvalue derivative $\frac{d\mathbf{\Phi}_{ik}}{d\delta_p}$ is best obtained with Nelson's method [207]. The eigenvalue derivatives are obtained with eqn. (4.11), and the following relationships are noted:

$$\frac{d\Delta\lambda_{ki}}{d\delta_p} = \frac{d\lambda_k}{d\delta_p} - \frac{d\lambda_i}{d\delta_p} \tag{6.16}$$

$$\frac{d\Delta\sigma_{ki}}{d\delta_p} = \frac{d\sigma_k}{d\delta_p} - \frac{d\sigma_i}{d\delta_p}. \tag{6.17}$$

The sensitivity of the maximum modal coupling is determined by differentiating eqn. (4.23) to produce

$$\frac{d}{d\delta_p}\overline{\kappa}_{iKk}^2 = 2\kappa_{iKk}\frac{d\kappa_{iKk}}{d\delta_p} + \frac{\Delta\sigma_{ki}}{2}\frac{d\Delta\sigma_{ki}}{d\delta_p} \tag{6.18}$$

and hence

$$\frac{d}{d\delta_p}\overline{\kappa}_{iKk} = \frac{\kappa_{iKk}}{\overline{\kappa}_{iKk}}\frac{d\kappa_{iKk}}{d\delta_p} + \frac{\Delta\sigma_{ki}}{4\overline{\kappa}_{iKk}}\frac{d\Delta\sigma_{ki}}{d\delta_p}. \tag{6.19}$$

The sensitivity of the minimum eigenvalue separation is found by differentiating eqn. (5.23), yielding

$$\frac{d\Delta\overline{\lambda}_{ki}}{d\delta_p} = \frac{\kappa_{iKk}}{\overline{\kappa}_{iKk}}\frac{d\Delta\lambda_{ki}}{d\delta_p} + \frac{\Delta\lambda_{ki}}{\overline{\kappa}_{iKk}}\frac{d\kappa_{iKk}}{d\delta_p} - \frac{\Delta\lambda_{ki}\kappa_{iKk}}{\overline{\kappa}_{iKk}^2}\frac{d\overline{\kappa}_{iKk}}{d\delta_p}. \tag{6.20}$$

It is now possible to determine the derivative of the maximum vector rotation rate, or more specifically its inverse, from eqn. (6.14):

$$\frac{\partial}{\partial\delta_p}\left(\frac{d\beta}{d\delta_K}^{-1}\right) = \frac{1}{\overline{\kappa}_{iKk}}\frac{d\Delta\overline{\lambda}_{ki}}{d\delta_p} - \frac{\Delta\overline{\lambda}_{ki}}{\overline{\kappa}_{iKk}^2}\frac{d\overline{\kappa}_{iKk}}{d\delta_p}. \tag{6.21}$$

Similarly the derivative of the datum parameter value is found by rearranging and differentiating eqn. (5.12) to give

$$\frac{d\overline{\delta}_K}{d\delta_p} = \frac{\Delta\sigma_{ki}\Delta\lambda_{ki}}{4\overline{\kappa}_{iKk}^4}\frac{\partial}{\partial\delta_p}\overline{\kappa}_{iKk}^2 - \frac{\Delta\sigma_{ki}}{4\overline{\kappa}_{iKk}^2}\frac{d\Delta\lambda_{ki}}{d\delta_p} - \frac{\Delta\lambda_{ki}}{4\overline{\kappa}_{iKk}^2}\frac{d\Delta\sigma_{ki}}{d\delta_p}. \tag{6.22}$$

Finally, the mean eigenvalue at the veering datum is found from eqns. (5.20) and (5.21),

$$\mu_{\overline{\lambda}} = \frac{\overline{\lambda}_i + \overline{\lambda}_k}{2} = \frac{\lambda_i + \lambda_k}{2} - \frac{(\sigma_{iKi} + \sigma_{kKk})\Delta\lambda_{ki}\Delta\sigma_{kKi}}{8\overline{\kappa}_{iKk}^2}, \tag{6.23}$$

and differentiated to give

$$\begin{aligned}\frac{d\mu_{\overline{\lambda}}}{d\delta_p} =& \frac{\frac{d\lambda_i}{d\delta_p} + \frac{d\lambda_k}{d\delta_p}}{2} - \frac{\Delta\lambda_{ki}\Delta\sigma_{ki}}{8\overline{\kappa}^2_{iKk}}\left(\frac{d\sigma_i}{d\delta_p} + \frac{d\sigma_k}{d\delta_p}\right) \\ & - \frac{(\sigma_i+\sigma_k)\Delta\sigma_{ki}}{8\overline{\kappa}^2_{iKk}}\frac{d\Delta\lambda_{ki}}{d\delta_p} - \frac{(\sigma_i+\sigma_k)\Delta\lambda_{ki}}{8\overline{\kappa}^2_{iKk}}\frac{d\Delta\sigma_{ki}}{d\delta_p} \\ & + \frac{(\sigma_i+\sigma_k)\Delta\lambda_{ki}\Delta\sigma_{ki}}{8\overline{\kappa}^4_{iKk}}\frac{d}{d\delta_p}\overline{\kappa}^2_{iKk}. \end{aligned} \tag{6.24}$$

Eqns. (5.12), (6.14) and (6.21–6.24) are incorporated into the sensitivity-based updating routine described in section 2.7.

6.3 Welded Frame Example

It is anticipated that model updates based on the veering properties will produce the best results when these properties are used in conjunction with more commonplace updating variables, notably the eigenvalues. For this example, however, the veering properties will be used in isolation to demonstrate their utility. To this end, the method developed above will now be applied to the welded frame described in section 3.4 to produce an informed estimate of the weld stiffnesses at the corners.

6.3.1 Tangent Stiffness Derivative

To perform the updating computations as detailed above, the tangent stiffness derivative $\frac{d\mathbf{K}}{d\delta_K}$ must be known. It was shown in section 3.4 that under the majority of practicable conditions the structural stiffness experiences approximately linear variation with loading. Making this assumption greatly simplifies the study of veering modes, allowing direct application of the expressions in chapters 4 and 5 and simplifying any updating scheme based upon these principles. The stiffness matrix derivative required for the calculations can be determined from a single linear static solution. The solution is performed for unit load, and the stress stiffening matrix is determined as in section 2.4.2. The linear approximation then gives

$$\mathbf{K} = \mathbf{K_T} = \mathbf{K_E} + \hat{\mathbf{K}}_\mathbf{G}\delta_K \tag{6.25}$$

where δ_K is the applied load and $\hat{\mathbf{K}}_\mathbf{G}$ is the stress stiffening matrix for unit load. From this,

$$\frac{d\mathbf{K}}{d\delta_K} = \hat{\mathbf{K}}_\mathbf{G}. \tag{6.26}$$

Where appropriate, this approximation greatly reduces the computational effort. In the following example, however, it was found that significant nonlinearities were present over the load range studied, so instead a numerical finite difference technique was used. This technique provides greater accuracy at the expense of doubling the number of eigensolutions, by using two load steps and calculating the

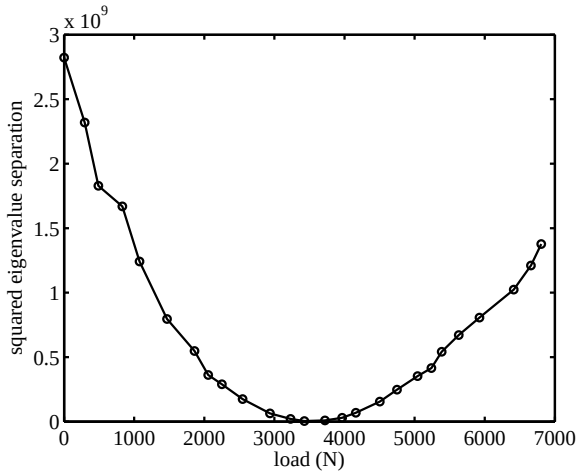

Figure 6.1: Experimentally determined eigenvalue separation of modes 5 and 6 in the welded frame, squared to give $\Delta\lambda^2$.

stiffness derivative as

$$\frac{d\mathbf{K}}{d\delta_K} = \frac{\mathbf{K}^{(n+1)} - \mathbf{K}^{(n)}}{\delta_K^{(n+1)} - \delta_K^{(n)}} \tag{6.27}$$

where the bracketed superscripts refer to the load step.

6.3.2 Veering Property Extraction

The update in this example is based upon the veering of modes 5 and 6, whose eigenvalue loci are presented in figure 4.4(c). The first set of results is used and the squared eigenvalue separation is plotted in figure 6.1. The curve shows significant deviation from a smooth path; the disturbances are attributed primarily to the load measurements which were only accurate to within ±50 N. The quadratic trend is clear, but the mild nonlinearity of the structural loading causes a shift over the course of the loading range. For this reason the data points used in the curve fitting should be limited to the vicinity of the veering. In contrast, it is desirable to include sufficient points so as to produce a reliable estimate of the true curve. Where possible, plentiful data should be collected over the range of the veering but if this is not practical then a sensible compromise must be reached.

The approach taken here is to evaluate the veering property estimates obtained using varying load ranges, centered approximately about the veering datum, and assess the quality of the curve fit as the range increases. Figure 6.2 shows the results of the two extremes; in figures 6.2(a) and 6.2(b) the curve is fitted to only the three central points and in figures 6.2(c) and 6.2(d) all of the available data is used. Neither case produces a satisfactory model of the behaviour in the vicinity of the veering so a reasonable middle ground is sought. Figure 6.3 shows the variation of the modal properties as the load range is expanded to encompass more data points. It is found that between the 1 kN and 3 kN ranges the estimates settle to reasonable values before diverging to the invalid global least squares fit. Accordingly modal property values are chosen based on the estimates from this range, as indicated by the dashed lines. These values produce the quadratic curves in figures 6.4(a) and 6.4(b),

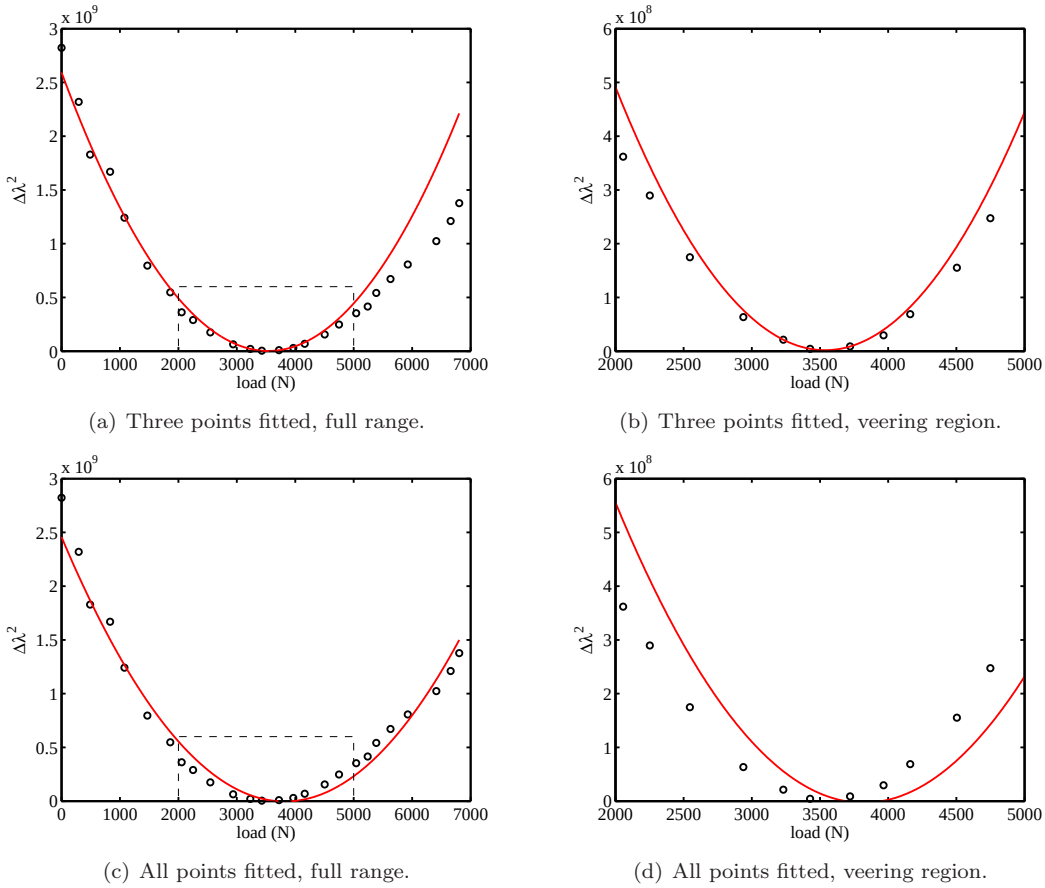

(a) Three points fitted, full range.

(b) Three points fitted, veering region.

(c) All points fitted, full range.

(d) All points fitted, veering region.

Figure 6.2: Curve fitting the experimental eigenvalue separation using differing numbers of data points, and viewed at different scales.

corresponding with the eigenvalue loci in figures 6.4(c) and 6.4(d). They exhibit a good approximation, with significant differences emerging only at the outermost extents of the loading spectrum.

6.3.3 Model Updating

Using the FE model described in chapter 3, the weld stiffnesses connecting the diagonal members to the rest of the frame are parameterised once more using the cross-sectional width of the short beam elements at the ends of each member. This time all four corners are considered. Using traditional eigenvalue-based techniques the symmetry of the structure prevents the determination of a unique solution to the update. Inclusion of the vector rotation rate resolves this difficulty, as the sign of the rotation rate differentiates the effects of two symmetrical parameters.

In section 4.3 it was recognised that the welds do not form perfectly rigid joints, so here the four parameters are initialised to 70% of the full stiffness. Despite the additional information given by the vector rotation rate, the structure exhibits reflectional symmetry about two planes, as well as rotational symmetry, so it is still not posssible to update all four parameters simultaneously without the solution diverging. This information deficiency would likely be resolved by incorporting the veering properties for further modes, but this example will simply consider the two parameter pairs separately.

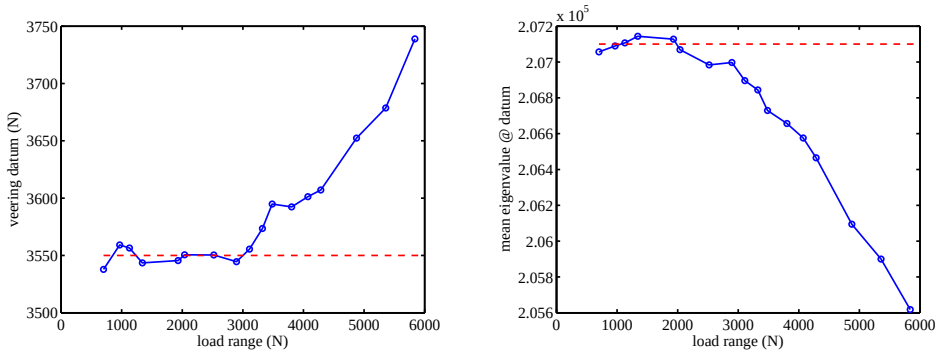

(a) Veering Parameter Datum

(b) Mean Eigenvalue at Veering Datum

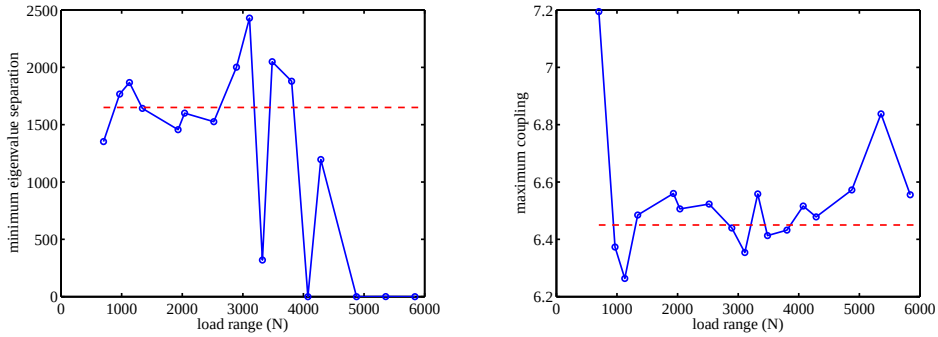

(c) Minimum Eigenvalue Separation

(d) Maximum Modal Coupling

Figure 6.3: Veering properties extracted from the experimental data using data points from varying load ranges, centered approximately about the veering datum (–o–), and chosen values (- -).

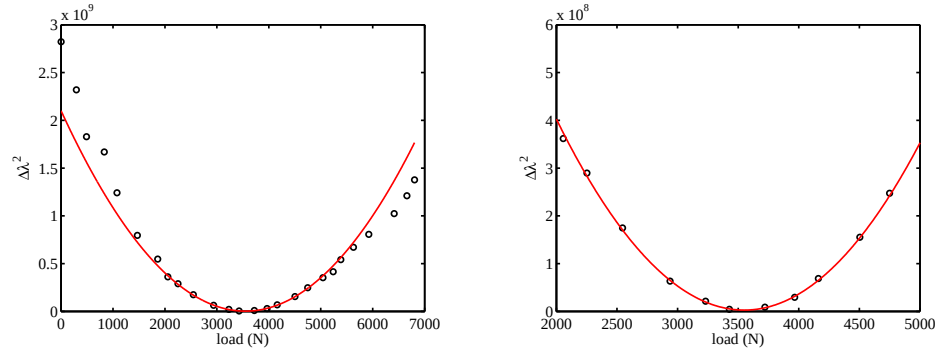

(a) Quadratic curve, full range

(b) Eigenvalue loci, veering region

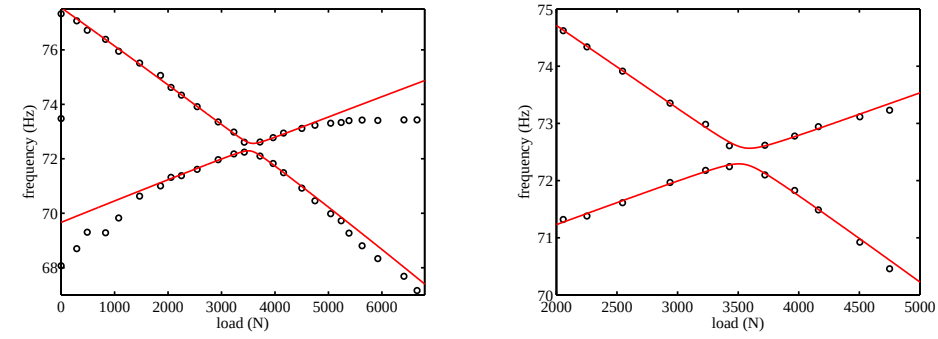

(c) Quadratic curve, full range

(d) Eigenvalue loci, veering region

Figure 6.4: Quadratic curves and eigenvalue loci produced by the mathematical veering model (–), and the experimental data (o).

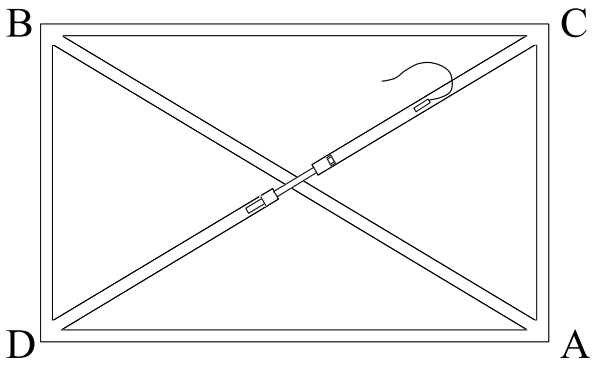

Figure 6.5: Schematic of the welded frame with labels denoting the weld stiffness parameters in each corner.

Taking this approach also obviates the need for determining other properties besides the veering characteristics.

To update two parameters at least two measured quantities must be used. The first of these must be the maximum vector rotation rate. For the second, two quantities will be considered here in turn: the veering parameter datum and the mean eigenvalue at veering. The sensitivity is thus selected as a 2×2 submatrix of

$$\mathbf{S} = \begin{bmatrix} \frac{\partial}{\partial \delta_A}\left(\overline{\frac{d\beta}{d\delta_K}}\right)^{-1} & \frac{\partial}{\partial \delta_B}\left(\overline{\frac{d\beta}{d\delta_K}}\right)^{-1} & \frac{\partial}{\partial \delta_C}\left(\overline{\frac{d\beta}{d\delta_K}}\right)^{-1} & \frac{\partial}{\partial \delta_D}\left(\overline{\frac{d\beta}{d\delta_K}}\right)^{-1} \\ \frac{\partial}{\partial \delta_A}\overline{\delta}_K & \frac{\partial}{\partial \delta_B}\overline{\delta}_K & \frac{\partial}{\partial \delta_C}\overline{\delta}_K & \frac{\partial}{\partial \delta_D}\overline{\delta}_K \\ \frac{\partial}{\partial \delta_A}\mu_{\overline{\lambda}} & \frac{\partial}{\partial \delta_B}\mu_{\overline{\lambda}} & \frac{\partial}{\partial \delta_C}\mu_{\overline{\lambda}} & \frac{\partial}{\partial \delta_D}\mu_{\overline{\lambda}} \end{bmatrix} \tag{6.28}$$

where the subscripts A-D refer to the welds at locations A-D in figure 6.5.

The full sensitivity matrix for the first iteration is

$$\mathbf{S} = \begin{bmatrix} -473.7 & 473.7 & -420.9 & 420.9 \\ 358.0 & 358.0 & 260.5 & 260.5 \\ 2061 & 2061 & 1670 & 1670 \end{bmatrix}. \tag{6.29}$$

From this it is clear that the vector rotation rate is the only variable differentiating the symmetric parameters from one another (A from B and C from D). In addition it is seen that the two sets of symmetric parameters have similar sensitivities, confirming the need for more independent data if all the parameters are to be updated simultaneously. Accordingly, only the first two parameters will be considered in this example, corresponding to the weld stiffnesses at each end of the non-tensioned member (that is, the member which does not contain the tensioning mechanism).

The parameters are first updated using rows 1 and 2 of $\mathbf{S}$, corresponding to the vector rotation rate, $\left(\overline{\frac{d\beta}{d\delta_K}}\right)^{-1}$, and the veering parameter datum, $\overline{\delta}_K$. Figure 6.6 shows the parameter values and the updating variables' convergence history. As expected for equal numbers of parameters and variables, the variables converge exactly. The updated parameter values suggest that the weld stiffness is greater in the top left corner than the bottom right. Visual examination of the two welds in figure 6.7 does

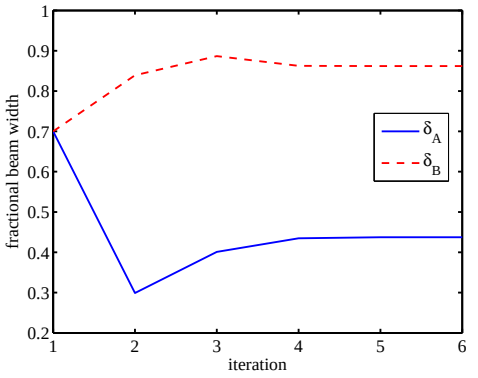

(a) Parameter values.

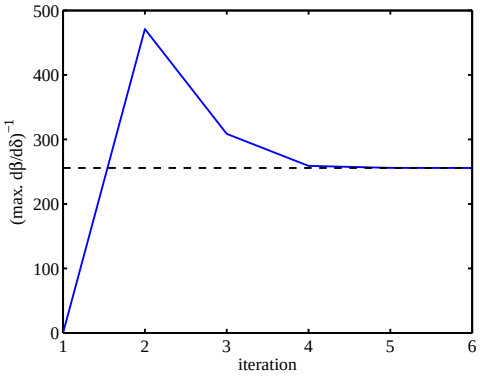

(b) Maximum vector rotation rate.

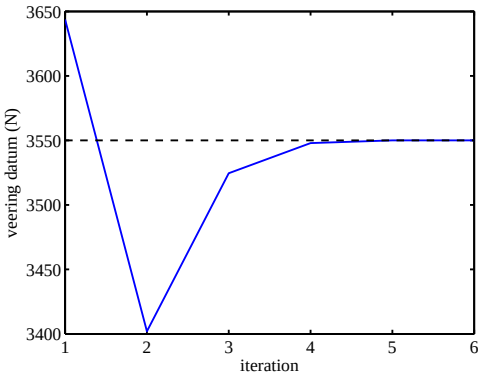

(c) Datum control parameter value.

Figure 6.6: Parameter values and convergence history for the welded frame, updated using the eigenvector rotation rate, $\left(\overline{\frac{d\beta}{d\delta_K}}\right)^{-1}$, and the veering parameter datum, $\overline{\delta}_K$. Dotted lines indicate experimentally obtained values.

(a) Bottom right (A).

(b) Top left (B).

Figure 6.7: Welded joints in the corners; these weld stiffnesses are used as parameters in the model update.

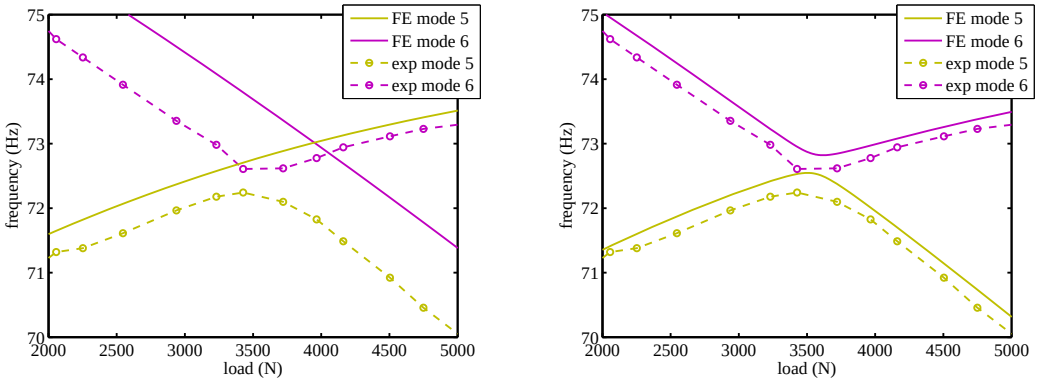

(a) Initial symmetric parameters.

(b) Updated joint parameters.

Figure 6.8: The eigenvalues of the updated FE model compared to those of the experimental data, before and after updating. This update was based on the eigenvector rotation rate and the veering parameter datum.

not provide a rigorous confirmation of this result, although the weld bead does appear thicker in the top left corner and the base metal errosion greater in the lower left corner. The updated FE model is then loaded incrementally to produce the eigenvalue loci in figure 6.8. These are seen to reproduce the experimental trends well, although the eigenvalues are higher than those obtained in the experimental data.

The update is performed again, this time with respect to the mean eigenvalue at veering, $\mu_{\overline{\lambda}}$, instead of the veering parameter datum, $\overline{\delta}_K$. The new results in figure 6.9 show similar trends, with the top left corner stiffer than the bottom right, but now both weld stiffness parameters are seen to be lower. This is to be expected, as this time the update procedure seeks to compensate for the high eigenvalues obtained in the first example. The new eigenvalue loci are seen in figure 6.10. The datum eigenvalues have been brought in line but the compromise is that the veering parameter datum now does not match that of the experiment.

A trivial explanation for the discrepancies in the updated model could be that the load cell calibration was incorrect; the load measurements have already been identified as a likely source of errors, and offsetting the values would bring the veering parameter datum in the second example into line. A more likely explanation, however, lies in the remaining unknown parameters which must still be accounted for. For example, a total of twelve weld stiffness parameters could be included, representing the different joints between all the members (three joints in each of four corners). The tensioning mechanism also introduces uncertainty, and the list continues.

Comparisons can be drawn with the updating scheme used in section 3.3 with the pin-jointed frame. In that experiment, the symmetry of the structure prevented distinction of the parameters at individual corners and each corner was assumed to be identical to the others. Using the technique presented here with sufficient mode pairs, it should be possible to overcome this limitation and update all the joint parameters independently.

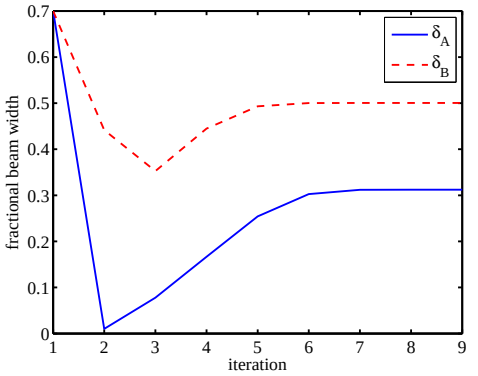

(a) Parameter values.

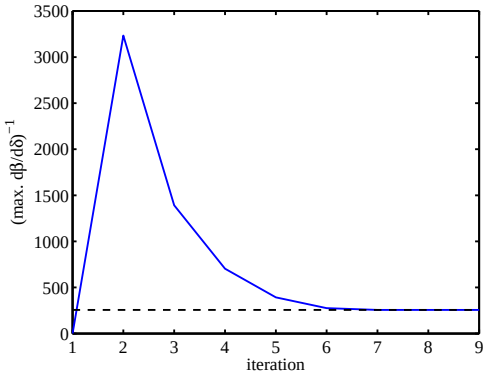

(b) Maximum vector rotation rate.

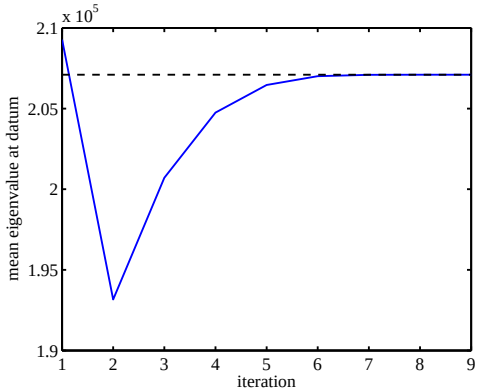

(c) Datum control parameter value.

Figure 6.9: Parameter values and convergence history for the welded frame, updated using the eigenvector rotation rate, $\left(\overline{\frac{d\beta}{d\delta_K}}\right)^{-1}$, and the mean eigenvalue at the veering datum, $\mu_{\overline{\lambda}}$. Dotted lines indicate experimentally obtained values.

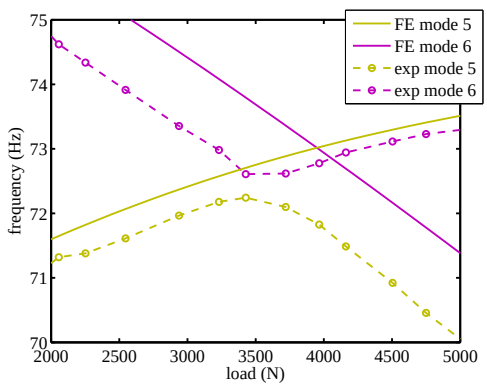

(a) Initial symmetric parameters.

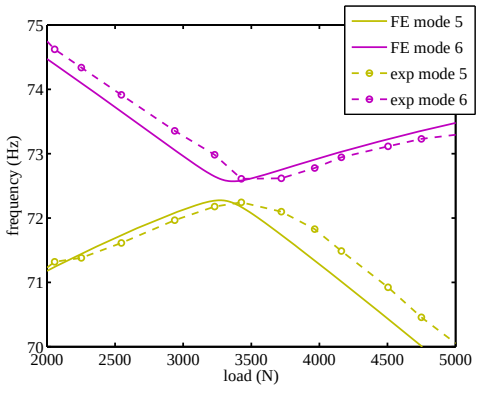

(b) Updated joint parameters.

Figure 6.10: The eigenvalues of the updated FE model compared to those of the experimental data, before and after updating. This update was based on the eigenvector rotation rate and the mean eigenvalue at veering.

6.4 Conclusions

This chapter has presented a new selection of properties to be used in model updating schemes. They are based upon the characteristics of veering modes, and permit the inclusion of valuable information which can not be determined from eigenvalues alone. In particular, the maximum eigenvector rotation rate throughout a veering region has been shown to be an invaluable tool in characterising veering and distinguishing between otherwise evasive symmetric parameter adjustments. Each veering instance has the potential to resolve one plane of symmetry, or one degree of periodicity, as well as providing better conditioning than can generally be achieved in symmetric updating problems.

A novel experimental technique has been developed for extracting the veering properties, taking advantage of the quantitative accuracy of the eigenvalues and the important qualitative information from the eigenvectors. This vector information can be gathered reliably with only two carefully selected measurement locations: far fewer than would be needed for an eigenvector-based updating scheme. Large amounts of experimental data are required by the method, but the repetition of the test for varying parameter values is generally a simple task compared to the initial setup of an experimental rig.

A practical demonstration has shown the methods to work well, providing a unique solution to a hitherto ambiguous updating problem, although it has also highlighted the dangers of introducing further uncertainties through the new control parameter. Future development of this work could focus on demonstrating the techniques with respect to a multiply symmetric updating problem using veering properties from a range of mode pairs. It would also be instructive to compare the techniques directly with results from other updating variable candidates such as the eigenvectors themselves.

Chapter 7

Automated Response Suppression Example

7.1 Introduction

The foregoing chapters describe investigations into the effects of structural loading on dynamic response. In particular, section 3.4.3 identifies several behaviours which could be exploited for reducing vibration amplitudes. Of these, the simplest methods involve direct manipulation of the natural frequencies and antiresonances. This capability will prove useful wherever variable operating conditions may bring excitation frequencies in line with structural resonances. Such variation could be caused by either an alteration in the structural configuration or a change in the excitation conditions.

This chapter describes a proof-of-concept study into the use of quasi-static structural loading in an adaptive system for response suppression. The structure used to demonstrate the concept is a three-dimensional space frame. An actuator is embedded in the structure and a fully automated control system is developed to respond to a range of varying narrow band excitation conditions by varying the internal loading.

Two systems are tested: the first is ambitious in its scope, attempting not only to avoid the excitation of structural resonances but also to optimise the response further at key locations using continuous load adjustments. This approach inevitably leads to compromises in the performance and the results also highlight inadequacies in the generality of the demonstration. A second study addresses these shortcomings, using a simpler binary actuation scheme to improve on the performance while at the same time demonstrating a more versatile functionality.

To begin, sections 7.2 and 7.3 define the test structure and develop an FE model to assist the analyses. Sections 7.4 and 7.5 explain the actuation and frequency estimation strategies, before section 7.6 reports the outcome of the initial tests. The approach to generalising the demonstration is described in section 7.7, leading to the final tests in section 7.8. The results of the tests indicate the frequency estimation to be the weakest component in the implementation so section 7.8.2 offers further analysis of this aspect of the system ahead of the conclusions in section 7.10.

7.2 Baseline Test Structure & FE Model

The structure chosen for the implementation of the system is an adaptation of the Meroform® space frame used by Mottershead *et al.* in assessing various updating techniques [270]. The advantages of this structure are that updating parameters have already been established and tested and that it is easily adapted or extended, being comprised of modular components. The beams of the Meroform® M12 set are available as hollow tubes in a selection of lengths as multiples of $\sqrt{2}$, allowing a range of geometric configurations based around isosceles right triangles. Figure 7.1 shows the nodes and beam end connectors used. The configuration adopted by Mottershead *et al.* is seen in figure 7.2 and this arrangement is used as the baseline configuration here.

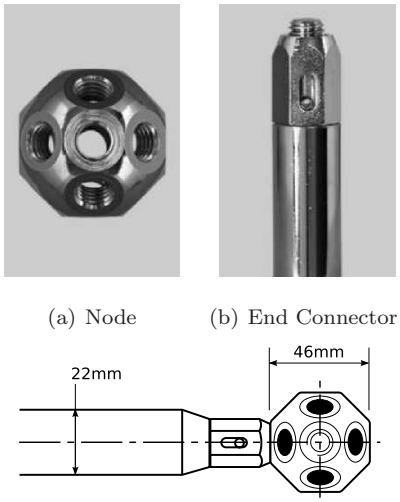

(a) Node (b) End Connector

(c) Node attached to end connector

Figure 7.1: The Meroform M12 components.

For initial tests and FE model correlation the structure is fitted with 31 accelerometers, one in the x- and one in the y-direction at each of the 16 nodes labelled in figure 7.3, with the exception of node 1 which was fitted with only one accelerometer in the y-direction. The remaining data acquisition channel was used for a hammer force transducer. Hammer tests were performed and the modal properties extracted using the methods described in section 2.5, with 5 averages of 1024 spectral lines in the range 0Hz to 256Hz. The first nine modes are shown in figure 7.4.

The FE model is assembled in ANSYS® [152]. Each member is divided into 5 beam elements, and following the procedure of Mottershead *et al.* a further rigid section is modelled at each end to represent the stiffer connectors. Extra masses and moments of inertia are included to account for the end connectors, nodes and accelerometers.

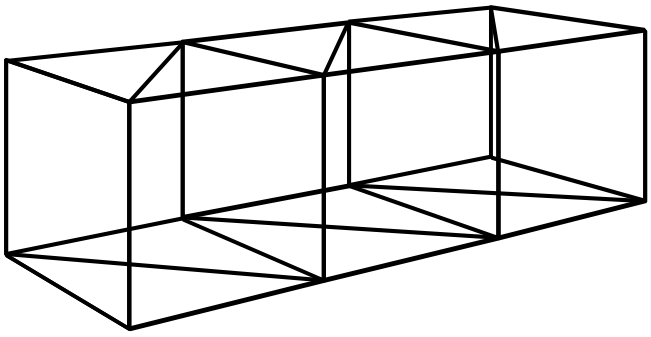

Figure 7.2: Baseline space frame configuration.

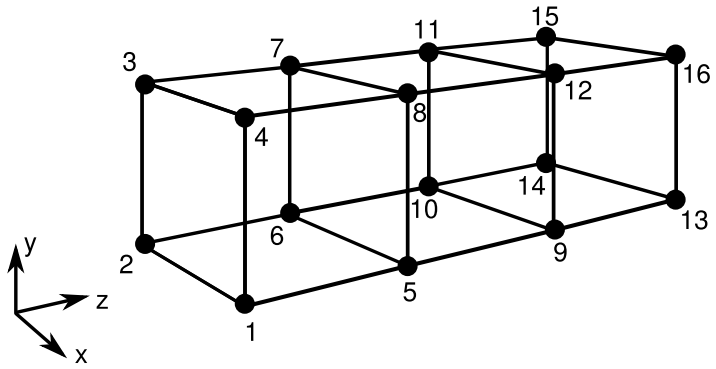

Figure 7.3: The sixteen structural nodes of the space frame; accelerometers for the first set of tests are attached in the x- and y-directions.

The baseline configuration is updated using the design optimisation tools of ANSYS, discussed in section 2.7.3. The three updating parameters are the wall thickness of the tubes (which cannot be directly measured without destroying one of the members), the offset of each end connector centre of mass from the node, and the length of the rigid sections used to model the end connectors. The objective function to be minimised is the sum of the squares of the frequencies for modes 1 and 4-8. Modes 2 and 3 are omitted for simplicity due to their proximity and the likelihood of the mode numbers being reversed.

The natural frequencies from the FE model before and after the updating process are compared with those from the experiment in figure 7.5, and the MACs are seen to be largely unchanged in figure 7.6. The figures indicate excellent correlation for both cases, marginally improved in the updated model. It is apparent from the MACs that modes 2 and 3 are reversed in the two result sets. This is not of significant concern as the frequencies of the modes are close. In fact, accounting for this artefact in the frequency comparison improves the frequency correlation for mode 2, as seen in figure 7.5(c).

The trade-off in swapping modes 2 and 3 is a reduced correlation for mode 3. This mode also exhibits poor MAC correlation. Examining the third analytic mode shape in figure 7.7 reveals that it is dominated by motion in the z-direction, with negligible displacements in the measured x- and y-DOFs. Thus poor MACs are to be expected for this mode, and the natural frequency will be difficult to determine with confidence. Similarly, FE mode 9 primarily involves bending of the individual beams with little translational motion at the measured DOFs. This explains the discrepancy in the frequencies, and the high cross-correlations in the MACs for modes 8 and 9.

With the justifiable exception of modes 3 and 9, the FE model provides an accurate representation of the dynamics of the baseline configuration.

7.3 Introducing Redundancy

The baseline structure does not contain sufficient members to carry axial loading in a pin-jointed statically determinate manner. As a result, internal loading will be carried primarily by the bending

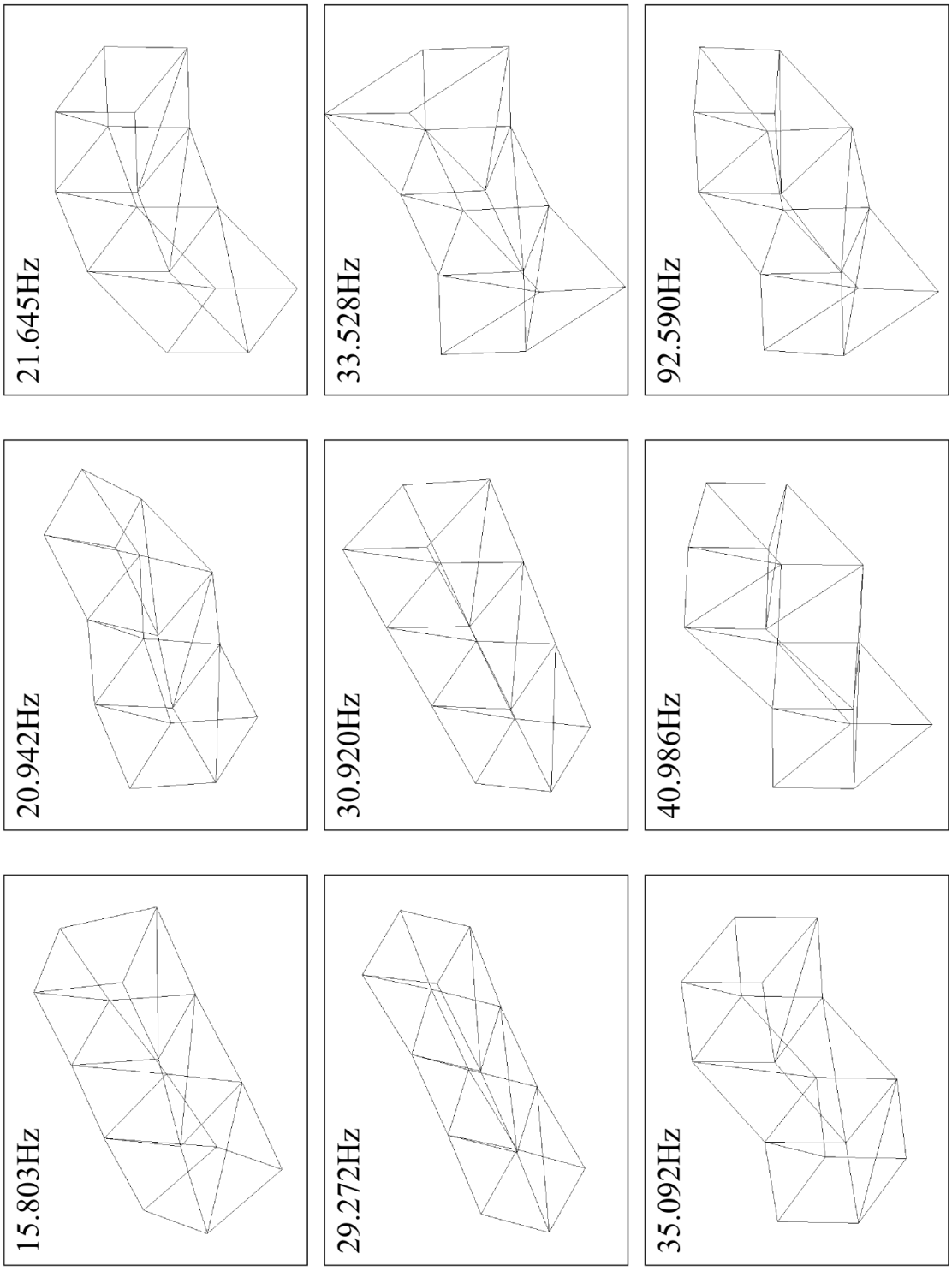

Figure 7.4: Experimental modal results from the baseline space frame configuration.

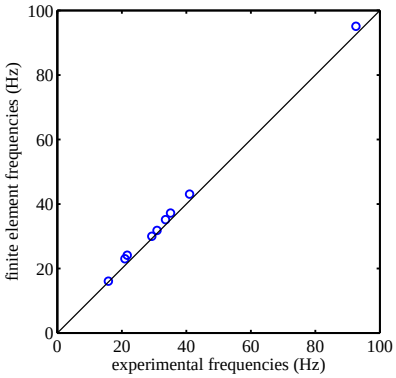

(a) Prior to updating.

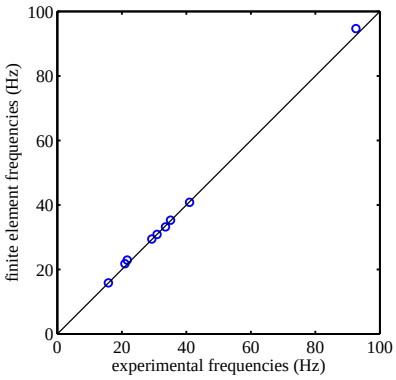

(b) After updating.

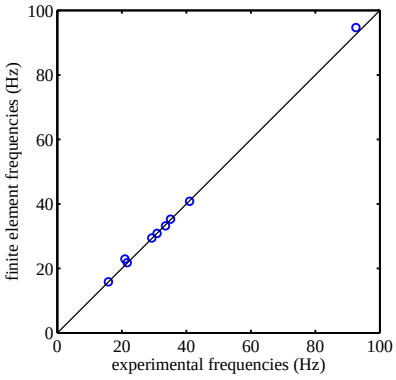

(c) Experimental modes 2 and 3 swapped.

Figure 7.5: Frequency correlation between the analytical and measured test data in the baseline configuration, before and after model updating.

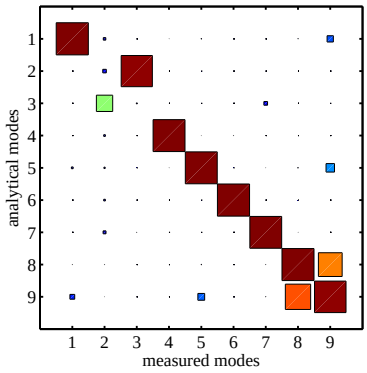

(a) Prior to updating.

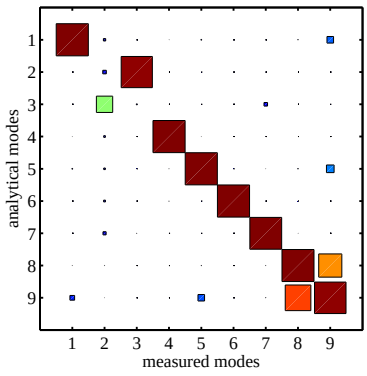

(b) After updating.

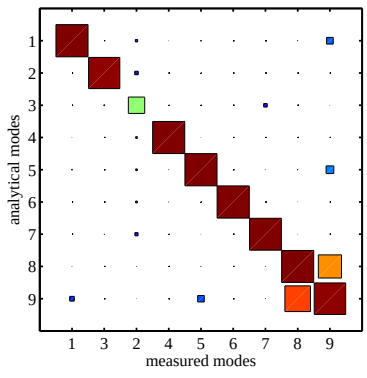

(c) Experimental modes 2 and 3 swapped.

Figure 7.6: MAC correlation between the analytical and measured test data in the baseline configuration, before and after model updating.

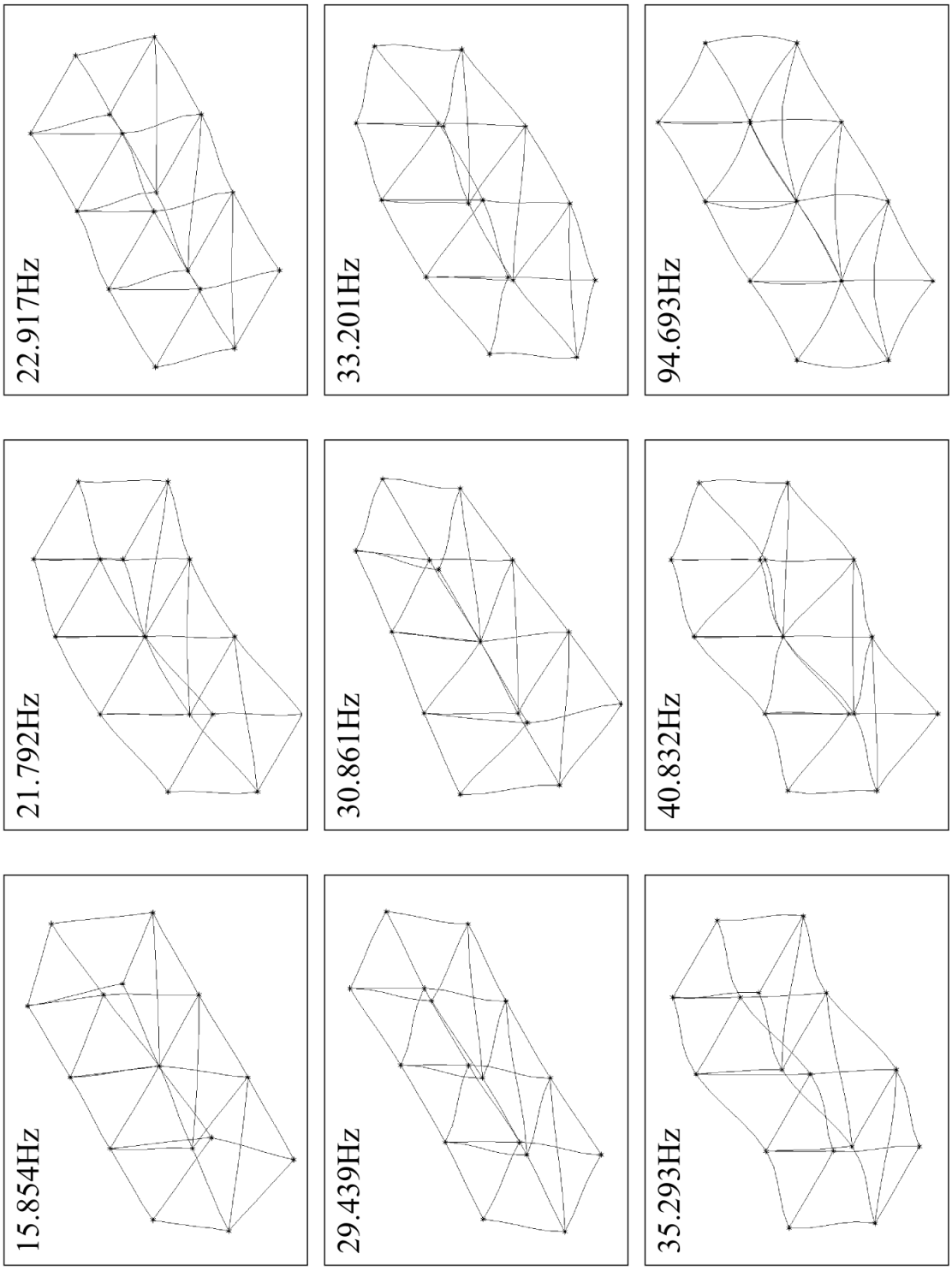

Figure 7.7: FE mode shapes and natural frequencies for the baseline configuration after updating.

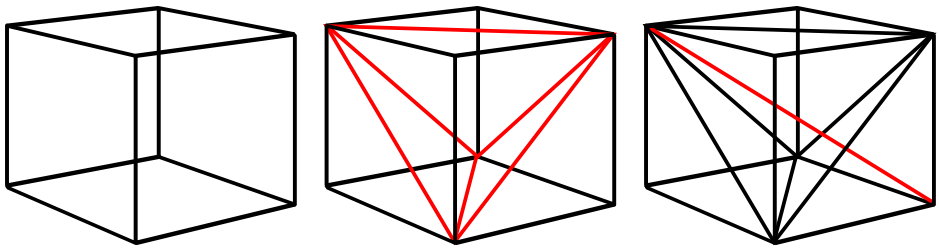

(a) Simple cube. (b) Statically determinate. (c) Statically redundant.

Figure 7.8: A cube built up from a simple configuration with only edge members, through a statically determinate case with square diagonals, to a redundant structure with a cubic diagonal.

stiffness of the members, transferred through the node connectors. Such an arrangement will result in large deflections of the structure before any significant axial loading is induced. While this will undoubtedly produce a change in the dynamic properties, it is neither desirable nor feasible in an airframe and so will not be the subject of this demonstration.

To encourage axial stress propagation, the structure must be reinforced with additional members to form a redundant load path. An actuator may then be incorporated into one of these members such that shortening the member propagates the loads. The central cube is pictured in figure 7.8(a) with no diagonal members. A statically determinate cube is presented in figure 7.8(b). To produce the necessary redundancy a further member is required and this takes the form of the cubic diagonal shown in figure 7.8(c). The standard Meroform components do not accommodate cubic diagonal members so two nodes are adapted and a custom beam connector is created to compensate for the new angle and the restricted space, as seen in figure 7.9. The redundant cube is substituted for the central cube in the original configuration, leaving the outboard cubes as they are, and the complete arrangement is seen in figure 7.10.

Unlike the other aluminium beams, the cubic diagonal is made of steel, and introduces further uncertainties to the FE model because of the different joint connectors employed at the beam ends. To compensate for these uncertainties another parameter is introduced: another rigid length section, as used before but this one unique to the cubic diagonal member. The configuration of the FE model at the ends of the member is clarified in figure 7.11. The tube length is known from measurements, so the distribution of the remaining length between the bolts and the rigid elements is decided by the rigid

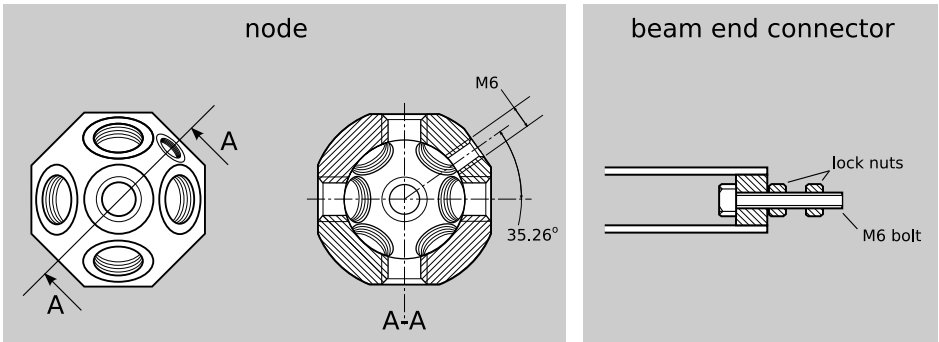

Figure 7.9: The node and end connectors adapted for the cubic diagonal.

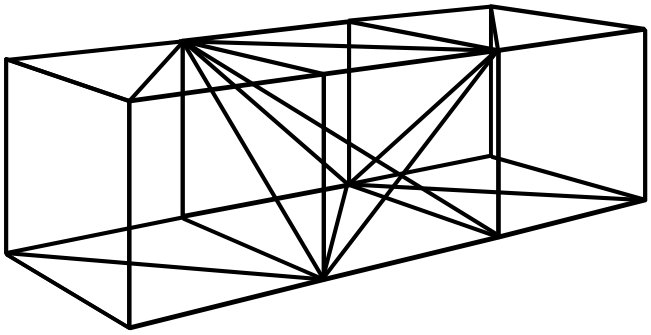

Figure 7.10: The redundant space frame configuration, with reinforcing members in the central section.

length parameter. This approximation is considered to be sufficient for determining the fundamental bending behaviour of the structural members. To provide for better modal correlation, it was found helpful to add two accelerometers to the centre of the cubic diagonal member, perpendicular to the beam alignment and each other, with one accelerometer lying in the horizontal plane. Measurement channel limitations necessitate the removal of two other accelerometers, arbitrarily taken from node 5 in the x-direction and node 10 in the y-direction (where mode numbers and orientations refer to those in figure 7.3).

Prior to updating, the new cubic diagonal rigid length parameter is initialised to the same value as used for the other, standard members. The FE results from this model are compared to the experimental data. Figure 7.12(a) shows reasonable correlation for the frequencies, with small discrepancies in modes 5 to 8. The MACs plotted in figure 7.13 are encouraging, but only the first two modes show good correlation. Modes 3 and 4 show significant cross-correlation, but it is noted that their frequencies are close; following chapter 4's discussion of mode shape transformations for proximate modes in symmetric and periodic structures, this cross-correlation is unsurprising. Importantly, the subspace occupied by the two modes is in good agreement. This is approximately assessed by summing the MAC values for the two modes: if an analytical mode lies in the subspace defined by two measured mode shapes, and these are assumed to be orthogonal, then the two MAC values will sum to unity. The same subspace arguments apply to modes 5 and 6, although the correlation is not quite as good for this pair. The worst agreement is seen for modes 7–9. Consulting the analytical mode shapes in figure 7.14, it is seen that these modes primarily involve bending motion of the individual members,

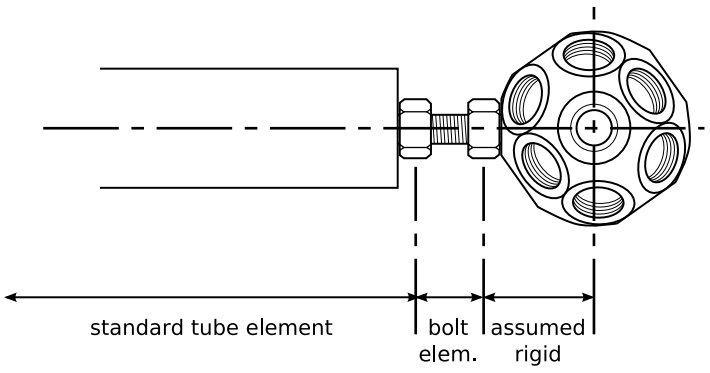

Figure 7.11: The cubic diagonal end connector broken into sections for the purposes of FE modelling.

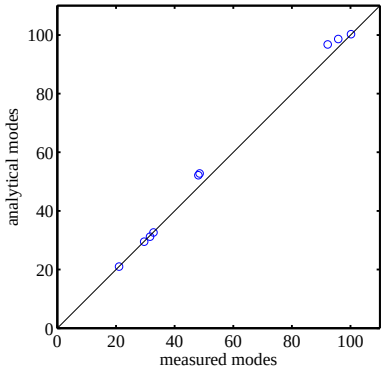

(a) Prior to updating.

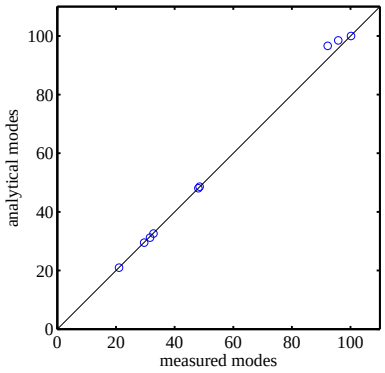

(b) After updating.

Figure 7.12: Frequency correlation between the analytical and measured test data in the redundant structure, before and after the cubic diagonal connector stiffness is updated.

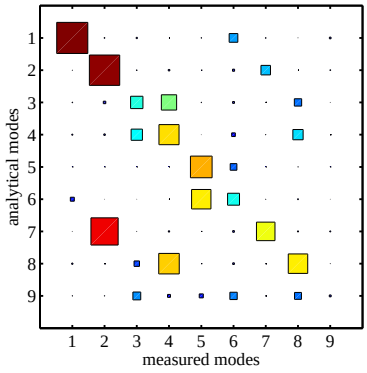

(a) Prior to updating.

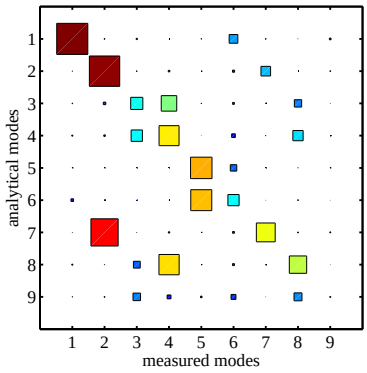

(b) After updating.

Figure 7.13: Mode shape correlation between the analytical and measured test data in the redundant structure, before and after the cubic diagonal connector stiffness is updated.

with little translational movement at the Meroform nodes. As before, the measured DOFs represent these modes poorly, explaining the lower MACs for modes 7 and 8 and the abysmal correlation for mode 9.

In light of this measurement ambiguity, it is prudent to mention a procedural improvement that could have produced more satisfactory results. The choice of measured DOFs for this experiment was made intuitively, guided heavily by the configuration of previous tests and the convenience of attaching accelerometers at structural nodes. A better approach would be to compute the locations in the FE model that are most representative of the modes being considered. Methods of performing this computation are discussed in section 2.6.

For the case in hand, the eigenvalues upon which to base the FE updating scheme must be chosen carefully. The most reliable and distinct modes, assessed from the MACs, are considered to be 1, 2, 7, and 8. Modes 5 and 6, being dominated by the motion of the cubic diagonal member, will also have a strong influence on the stiffness parameter being updated so these are included as well. The updated frequencies are compared with the experimental results in figure 7.12(b). Modes 5 and 6 now show good agreement, while the other modes are largely unaffected. Negligible changes are observed in the analytical mode shapes and the MAC values. The final properties adopted for the FE model are thus

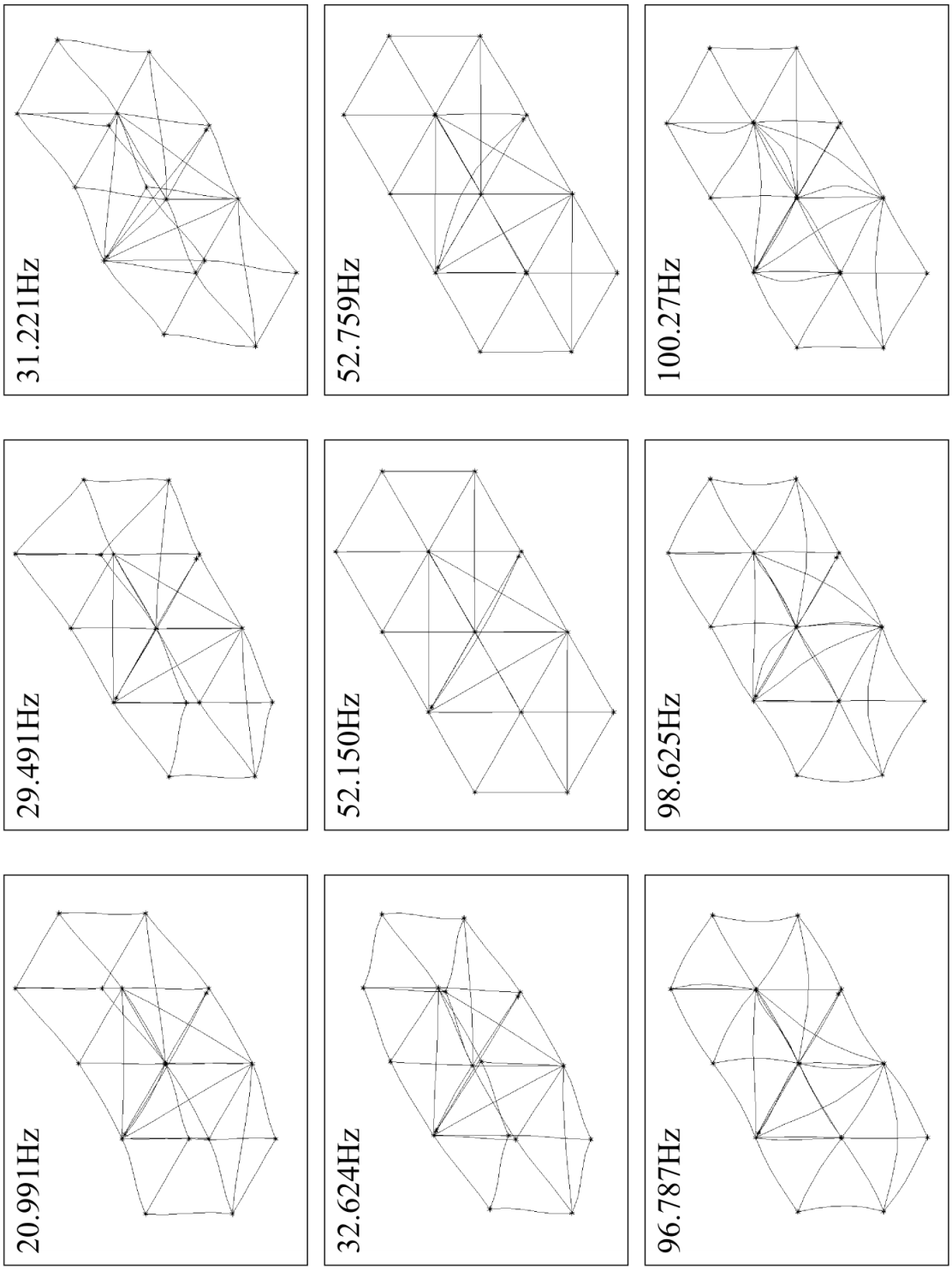

Figure 7.14: The mode shapes for the FE model with the redundant configuration prior to updating. The fifth mode is unclear from the angle presented, but is dominated by motion of the cubic diagonal member in the plane perpendicular to the viewing plane.

Property	Value	
ρ_{Al}	2710	kg m^{-3}
ρ_{steel}	7860	kg m^{-3}
E_{Al}	71	GPa
E_{steel}	210	GPa
node mass	78.000	g
node mass moment of inertia	2.08×10^{-5}	kgm^2
(calculated as shell, radius 20mm)		
accelerometer mass (includes attachments)	23.000	g
accelerometer mass moment of inertia	1.217×10^{-5}	kgm^2
end connector mass (standard members)	56.997	g
end connector mass (cubic diagonal member)	34.629	g
cubic diagonal connecting bolt length	37.5	mm
cubic diagonal connecting bolt diameter	6.00	mm
outer tube radius	11.000	mm
inner tube radius*	10.086	mm (10.015 mm)
end connector CoM offset from node*	30.006	mm (30 mm)
rigid length (standard connectors)*	17.839	mm (20 mm)
rigid length (cubic diagonal connectors)*	1.000	mm (17.839 mm)

Table 7.1: Properties used in the FE model of the Meroform space frame, including the updated properties denoted by *. (Starting values for the updated properties are indicated in brackets.)

listed in table 7.1. It is noted that after the updating process the rigid lengths at the ends of the cubic diagonal are reduced to 1 mm, which is an unrealisitic value that corresponds to the minimum bound specified in the optimisation routine. In making this adjustment, the updating routine has reduced the stiffness of the joint as far as possible, suggesting that it is compensating for unmodelled flexibility in the newly introduced joint interfaces. Although the solution is not entirely satisfactory, the value obtained produces good correlation in the frequency results. This agreement gives some degree of confidence in the buckling and stress stiffening results as well: like the natural frequencies, these results will essentially be dependent on the overall bending stiffnesses of the constituent members.

7.4 Actuation

The choice of actuator location for the current configuration is simplified by noting that the structure exhibits only one degree of redundancy. That is, only one linearly independent load distribution exists (neglecting the small influence of moment and shear transfer at the nodes). The significance of this observation is elaborated in section 8.2; essentially the choice of actuator location within the central cube is arbitrary as every location will result in the same axial load distribution. For these tests it is placed in line with the diagonal member in the top face of the cube between nodes 7 and 12, as indicated in figure 7.15.

A critical prerequisite for the actuator implementation is a knowledge of the failure load of the structure. To this end, an eigenbuckling solution is obtained from the FE model as described in section 2.4.3. Following the same procedure used in section 3.2, one end of the actuated beam is uncoupled from

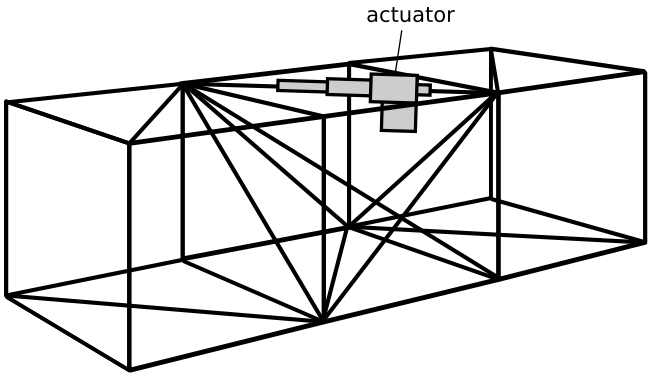

Figure 7.15: Location chosen for integration of the actuator in the space frame.

the Meroform node. The Meroform node is fully constrained and the end of the beam is constained in all but the axial DOF. An axial load is then applied. The buckling load obtained from this solution is 2810.7 N but it is noted that the true buckling load is usually slightly lower than the eigensolution. A full nonlinear analysis is run and the displacement curve shown in figure 7.16 is produced. From this graph the 2811N estimate seems reasonable, but it is acknowledged that this value is still likely to be artificially high due to the perfect alignments in the analytic structure.

The chosen loading range is 0-2250N, leaving a reserve factor of 1.25 with respect to the buckling load obtained from the FE model. In an adaptive system there are no stringent requirements for the actuator bandwidth, and the displacements seen in figure 7.16 are small (approximately 7.5mm immediately pre-buckling) so a linear ball screw actuator is selected to the appropriate load specification. The actuator is driven by a 24V, 6A DC motor, powered from a direct drive amplifier.

For accurate load control the actuator is fitted in line with a load cell. The load cell is tailored to be sensitive to forces in the 0-2250N range by waisting a steel bar to a $39mm^2$ cross-section. The design is seen in figure 7.17, with one end fashioned to accommodate the actuator lug and the other fitted to the internal diameter of a Meroform tube, where it is glued and pinned in place. Strain gauges are attached either side of the waisted section and these are included in opposite sides of a Wheatstone bridge, as described in section 2.5.1. The actuator-loadcell arrangement is pictured in figure 7.18.

The local feedback loop is completed with a proportional-integral-derivative (PID) controller, implemented in a dSpace® rapid control prototyping (RCP) board. The RCP board incorporates analogue to digital and digital to analogue converters (ADC/DAC), an onboard processor, and a computer interface for data logging. The code for the processor is compiled using the real-time workshop facility in Simulink® [150] and uploaded to the board.

The full load control system is seen in figure 7.19. Values for the amplifier gain and PID controller are chosen to produce a compromise between fast response and short settling time. Examples of the response are shown in figure 7.20. On the rising edge the overshoot is limited by the amplifier saturation, hence the flat region. The falling edge demonstrates a more typical response. The rise time is indicated as 1.25s while the equivalent time for the falling step response is 0.6s.

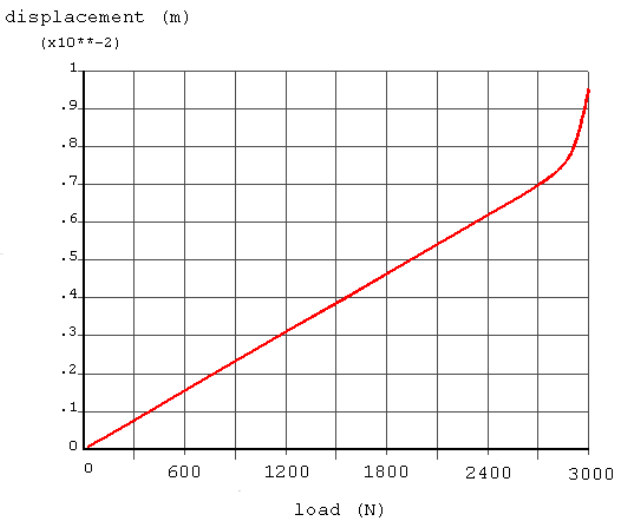

Figure 7.16: The load-displacement curve for the redundant structure indicates the onset of buckling at around 2850N, where the actuator displacement is roughly 7.5mm.

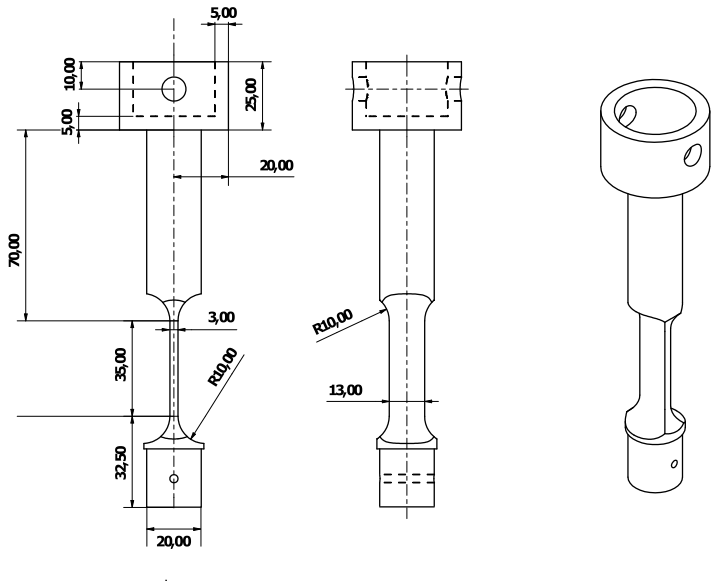

Figure 7.17: The waisted beam section used to build the loadcell.

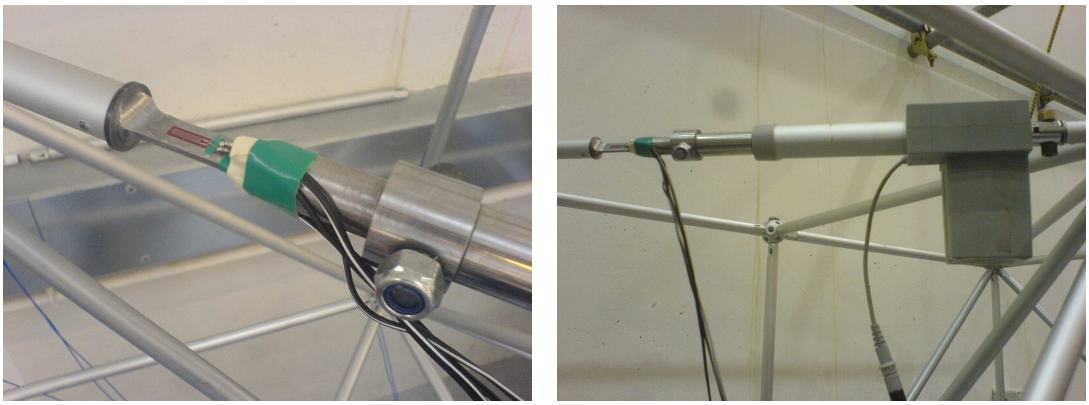

(a) Load cell.

(b) Actuator-loadcell arrangement.

Figure 7.18: The actuator and loadcell installed in the space frame.

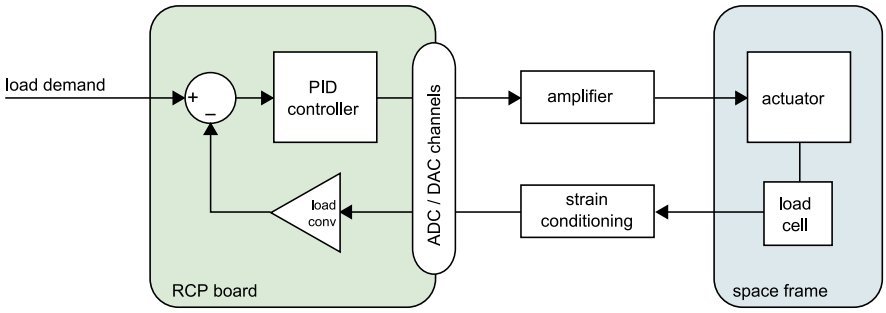

Figure 7.19: Closed-loop load control.

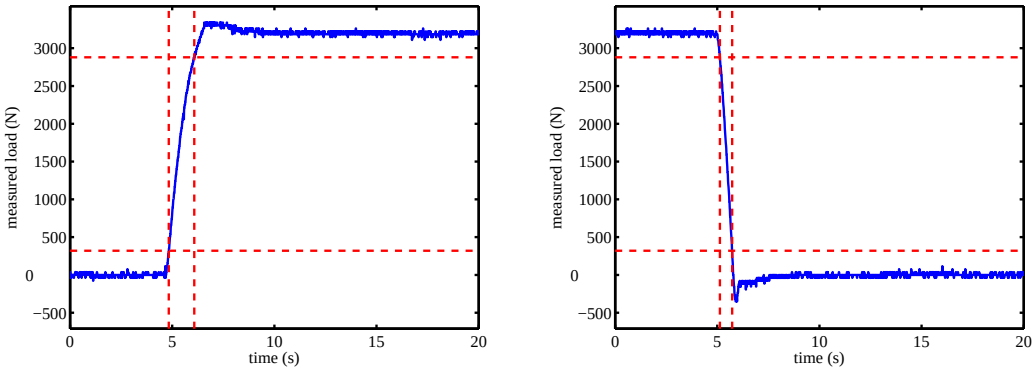

(a) 0→3200 N (b) 3200→0 N

Figure 7.20: Step response for the actuator, load cell and PID controller. Dashed lines indicate rise/fall times.

Property	Value	
Mass	2.749	kg
CoM_x	118.0	mm
CoM_y	34.0	mm
CoM_z	13.7	mm
I_{xx}	0.023	kg m^2
I_{yy}	0.025	kg m^2
I_{zz}	0.029	kg m^2

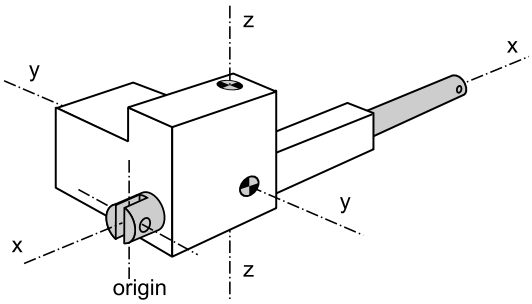

Table 7.2: Actuator inertial properties and coordinate system definition.

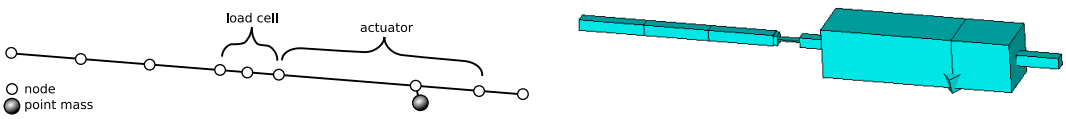

(a) Connectivity. (b) Solid beam representation.

Figure 7.21: The FE model of the actuator and load cell incorporated into the Meroform beam.

To incorporate the actuator in the FE model, its mass and inertia properties are determined as described in appendix C, and these are listed in table 7.2. The actuator is assumed to be rigid in comparison to the beams of the space frame, and is modelled as three light, rigid beam elements and a point mass with inertia. Two further beam elements represent the solid bar and waisted section of the load cell. The FE implementation can be seen in figure 7.21.

7.5 Frequency Estimation

The objective of the adaptive system is to reduce the response to variable narrow-band excitation. As such, the controller relies on real time estimates of the drive frequency.

The input for the frequency estimation is provided by a single accelerometer, attached close to the source of the excitation. This is connected to the RCP board via an IEPE filter and amplifier as described in section 2.5.1. The spectral content of the vibration signal is determined using a short-time fast Fourier transform (ST-FFT), described in section 2.5.2. The Simulink ST-FFT block is used; in addition to the standard windowing and FFT steps, the block contains a digital filter which serves the purpose of averaging the results over several data frames, and a normalising stage to compensate for the scaling introduced by the windowing.

To determine the main excitation frequency, a simple peak picking method is applied to the Fourier decomposition. This approach is not expected to be particularly robust, but should provide adequate performace for the proof-of-concept tests.

A Simulink diagram showing the full frequency estimation process can be found in figure 7.22. First the input is converted to a discretised signal with the zero-order hold, then buffered to create data frames. The data frames form the input for the ST-FFT block. The spectral response output from the ST-FFT is filtered through a 'maximum' block, which gives the index of the maximum value in the spectral response, and this index is then adjusted using an offset and a gain to produce the frequency as an output. The algorithm uses a sampling frequency of 1000 Hz and an FFT buffer of 512 samples with with 128 sample overlaps.

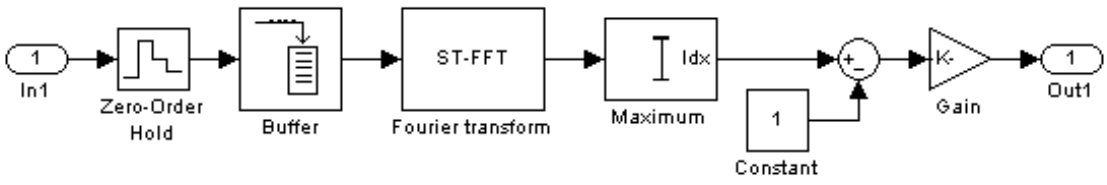

Figure 7.22: Simulink implementation of the frequency estimation algorithm.

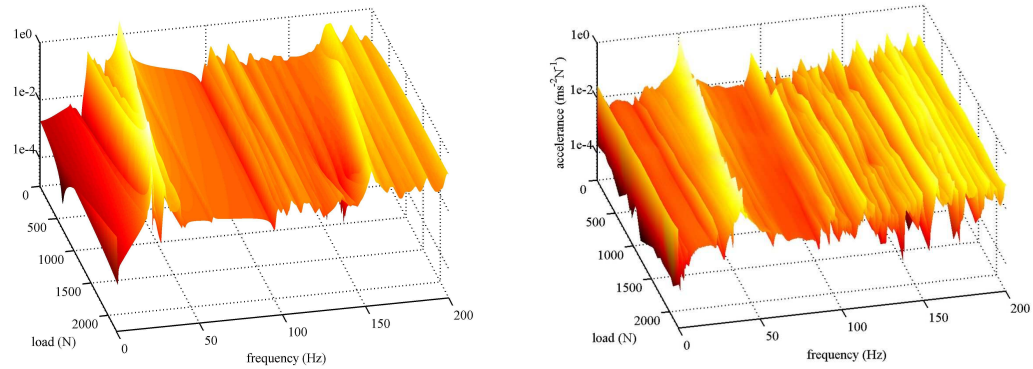

(a) FE data.

(b) Experimental data.

Figure 7.23: Frequency response at the centre of the cubic diagonal member.

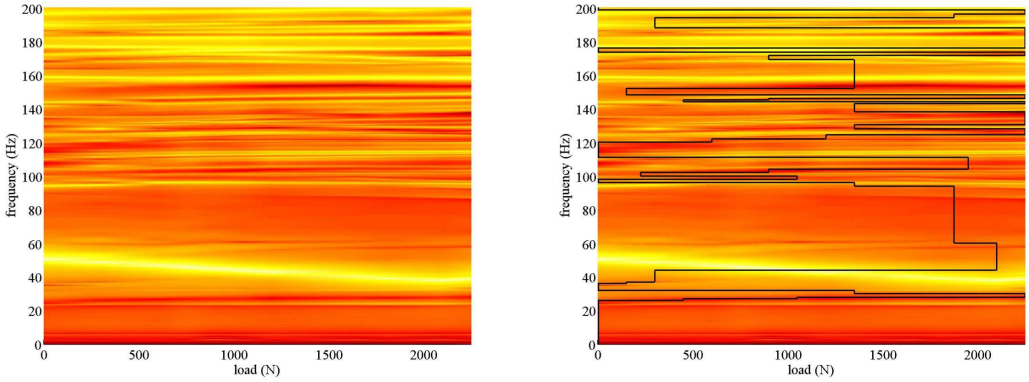

(a) FRF

(b) FRF with optimised actuator load path overlaid in black.

Figure 7.24: Experimental response contour plots: light regions represent high response and dark regions represent low response.

7.6 Preliminary Experimental Evaluation

7.6.1 Control Strategy

To complete the control loop a lookup table is implemented, stipulating the optimum actuation force for a given drive frequency. These optimum values are determined below, using experimental FRFs, measured at discrete intervals over the loading range.

Before conducting the experimental identification, a variety of waterfall plots are produced by the FE model to determine how the response is expected to vary at different locations around the structure. Of particular interest is the response at the centre of the cubic diagonal member, seen in figure 7.23(a). The dominant feature of the plot is the resonant ridge at around 50 Hz, dwarfing the other response modes. This mode is seen to be affected by the loading, with the natural frequency dropping by more than 10 Hz over the loading spectrum. This provides an ideal opportunity for demonstrating the principles of the adaptive response tuning.

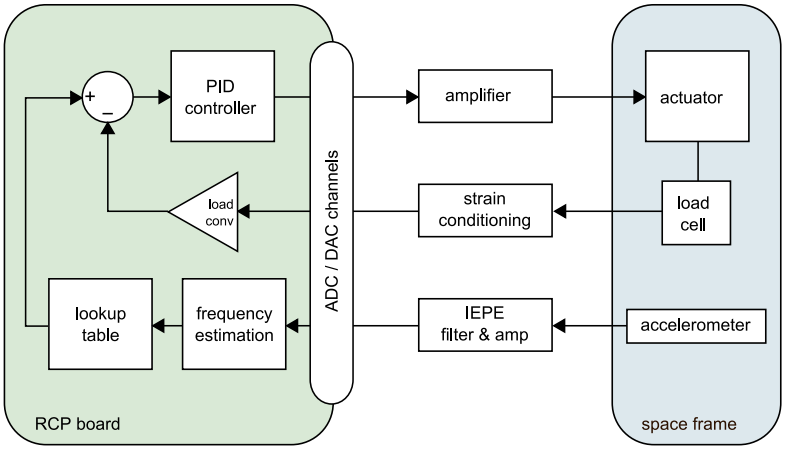

Figure 7.25: Full adaptive vibration control system.

Hammer tests are performed to obtain the experimental FRFs and confirm the analytical results. The response data is averaged over three runs for each load, in steps of 150 N from 0 N to 2250 N. Figure 7.23(b) shows the FRFs for the response point located on the cubic diagonal member. The same dominant mode for this point is recognised at around 50 Hz, decreasing in frequency as the load is increased. Thus, a preliminary demonstration is conducted with the primary objective of avoiding excitation of the dominant 50Hz mode. Two secondary objectives are also considered: firstly, for every frequency in the range 0Hz to 200Hz to avoid coincidence of the drive frequency with resonant frequencies; and secondly, to align the drive frequency with an antiresonance wherever possible. This plan is to be accomplished by controlling the actuation load to manipulate the FRFs: Figure 7.24 illustrates a path through the response surface which attempts to fulfil these requirements and this is used to create the lookup table for the control system. The lookup table takes the output of the frequency estimation as its input and the load demand from its output is fed to the actuator controller, forming the complete controller illustrated in figure 7.25.

7.6.2 Testing

The structure is pictured in figure 7.26 with the actuator embedded. A shaker is attached via a flexible push-rod to node 1 in the z-direction (as labelled in figure 7.3) and a stepped sinusoidal input is applied. Each frequency is held constant for ten seconds at intervals of 2 Hz and the vibration data from the accelerometers are logged to record a full time history. This test is carried out twice: first with the control system activated, and then with it deactivated. The resulting time histories for the cubic diagonal response are shown in figure 7.27(a). A clearer picture of

Figure 7.26: Space frame suspended by bungee cords, with the actuator mounted at the top.

the results is obtained from the root mean square (RMS), plotted in figure 7.27(b) using averages over 0.5 s. These graphs are plotted on a linear scale; figure 7.28 shows a more familiar logarithmic plot.

The most striking feature of these curves is the marked reduction in response in the region of the 50 Hz mode. In fact, the true extent of the improvement is greater than can be seen, as the measurement from the accelerometer in the non-adaptive experiment was inadvertently clipped at 1 ms^{-2} by the ADC. The adaptive system successfully avoids the peak of the resonance in this region. The only time it falters is in a brief adjustment period, seen as the tall spike in the adaptive results. This is an important result: it demonstrates that without any damping, and without the use of fully active control systems, the driving frequency can traverse a region containing a resonant mode of vibration without exciting that mode. This could be useful, for example, in helicopter rotor spin-up. Furthermore, the force required from the actuator to achieve this goal is unrelated to the level of force generated by the excitation signal, so that a well-designed system based on this principle will use far less power than an active system directly countering the dynamic loads.

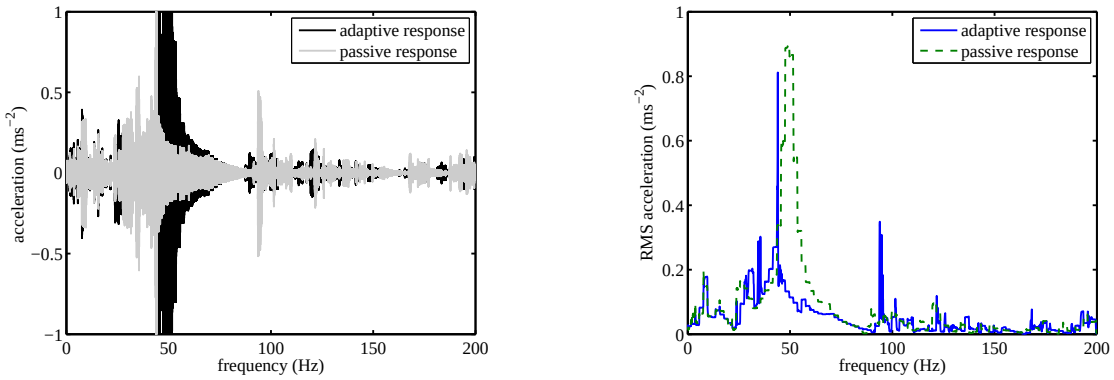

(a) response time history

(b) RMS response time history

Figure 7.27: Time histories of the response measured on the cubic diagonal. The horizontal axis labels indicate the excitation frequency (found by dividing the time in seconds by 5).

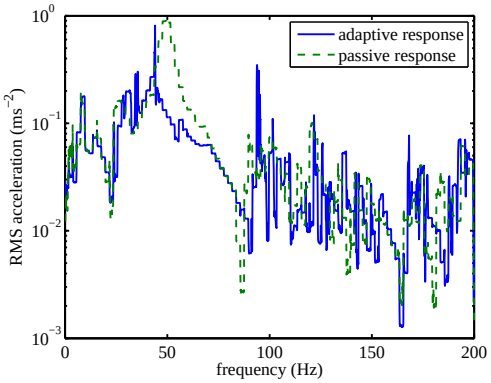

Figure 7.28: The response of the adaptive structure compared to that of the passive structure on a logarithmic scale.

Outside of the 40-70 Hz region, and particularly in regions of high modal density, the actuation is less effective and response levels are sometimes even higher with the control system enabled. This can be attributed largely to the accuracy of the two feedback measurements. In this setup the strain gauge measurements do not compensate for temperature changes or other ambient conditions and as such the readings will wander with time, affecting performance. Despite this deficiency, however, the relatively low sensitivity of the natural frequencies to loading means that this is less of a concern than the accuracy of the drive frequency estimation.

The shortcomings of the frequency estimation algorithm were recognised at its conception and as a result it suffers from two problems: these will be referred to as "misidentification" of the excitation frequency and "inaccurate" assessment of the frequency. The former produces an entirely incorrect identification of the drive frequency, often alternating between two very different values, and is thought to be responsible for rapid oscillations in the actuation that were observed during the test. Not only is this inefficient for power consumption but it can produce higher levels of structural response, with two examples seen as a series of spikes in the response at around 35Hz and 95Hz. "Inaccurate" frequency assessment refers to estimates that are in the vicinity of the actual drive frequency but fail to identify the true peak exactly. These errors are thought to be less significant but hamper the ability of the device to function amongst closely spaced modes.

Further analysis of these shortcomings can not be undertaken here as the necessary data were not recorded during the study. This omission was due to the prohibitively large quantity of data. In the following sections the development and implementation of a new study is described, for which comprehensive data were recorded, permitting a full interrogation.

7.7 Generalising the Demonstration

The prime success of the first demonstration was in manipulating the dominant 50Hz mode such as to avoid exciting this mode. Examining the frequency loci from the FE model in figure 7.29, the resonance is in fact seen to be composed of two closely spaced modes, numbers 7 and 8 from the zero-load case. (The question of which modes veer and which cross is not tackled here; some clearly veer while others are more ambiguous.) Examining the mode shapes from the FE model in figure 7.30 it is seen that they involve little motion other than that of the cubic diagonal member. Located in the central cube, this member lies directly in the load path for the actuation forces. As such, the demonstration constitutes a relatively trivial example of frequency manipulation in a single axially stressed beam. The study described below is intended to provide a more general illustration of the potential of the technique.

In most load-bearing structures there exists some degree of redundancy. Because of this redundancy, it is inevitable that the influence of actuator forces will be diminished in parts of the structure away from the actuator attachment points. So far it has been demonstrated that the response of the structure

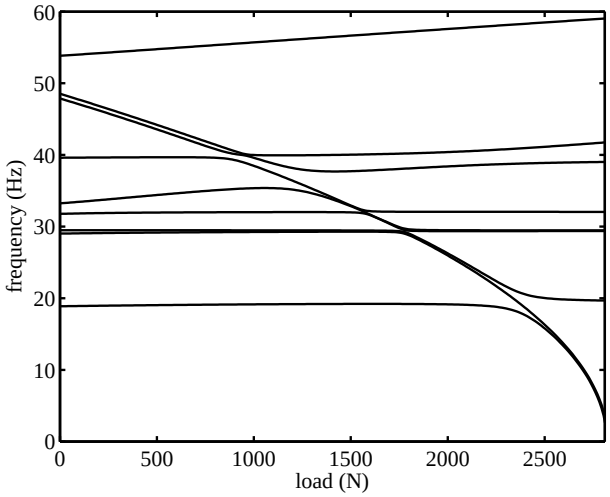

Figure 7.29: Frequency loci from the FE model for the redundant frame.

in the locality of the the actuator can be reduced. What remains to be demonstrated is the reduction of the response at a point outside the primary load path of the actuator.

The sensitivity of a mode to structural forces is a function of the mode shape and the force distribution. This is discussed in greater detail in section 8.2; for now it is simply stated that to influence the natural frequencies the two must overlap spatially. In other words, the static axial loading must coincide with dynamic transverse bending. The load distribution for the current redundant configuration is shown in figure 7.31(a). It is apparent that the load is confined mostly to the central cube. Therefore, to manipulate the response outside of this cube, the mode shapes must simultaneously involve motion of both the central and outboard cube sections.

To facilitate this modal uniformity, adequate coupling must exist between the different cubes. To achieve the coupling in the 50 Hz mode, the attachment points of the cubic diagonal member are stiffened. From figure 7.9 the joint is seen to contain a narrow section of threaded bar which is significantly more flexible than the rest of the structure. This is believed to be responsible for the localisation of modes 7 and 8 in figure 7.30. Accordingly, the joint is replaced with that in figure 7.32, similar to the standard joints used throughout the rest of the structure. In addition, the outboard cubes are reinforced with further diagonal members to bring their stiffnesses in line with that of the central section. Three new configurations were investigated: one with all three cubic diagonals in place, one with the leftmost cubic diagonal removed, and one with the rightmost cubic diagonal removed. These configurations are pictured in figure 7.33.

Assuming the new end connectors to have the same stiffness as the standard connectors, the new actuator load distribution is computed and shown in figure 7.31(b). The stress is still found to be concentrated in the central cube, albeit with small loads now carried in the outboard cubes as well. An eigenbuckling analysis of the FE model estimates the buckling load for the stiffer structure as 8542 N, allowing a greater load range of 0 N to 3200 N to be adopted in the new study, detailed below.

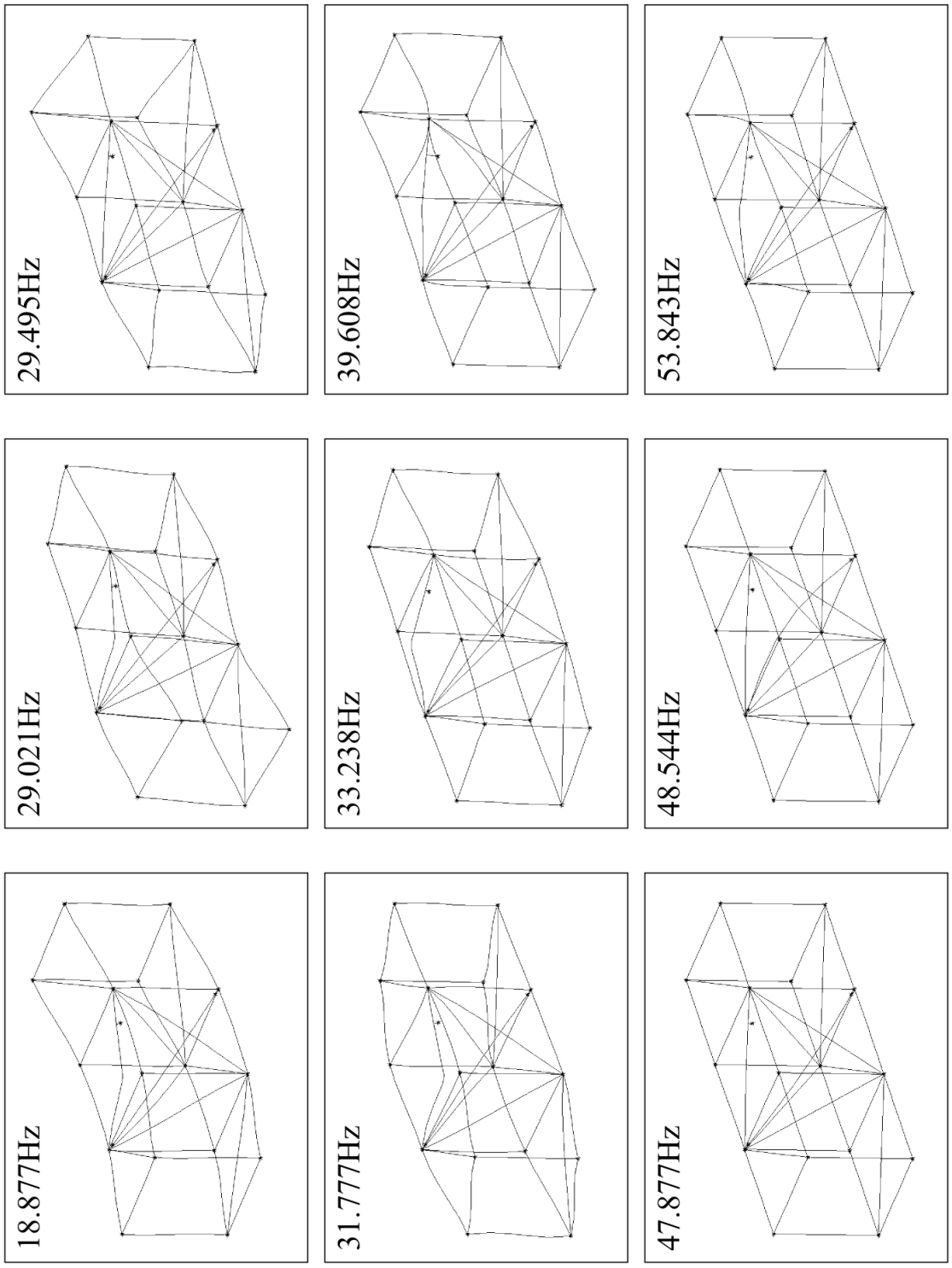

Figure 7.30: Mode shapes from the FE model of the redundant structure with the actuator included.

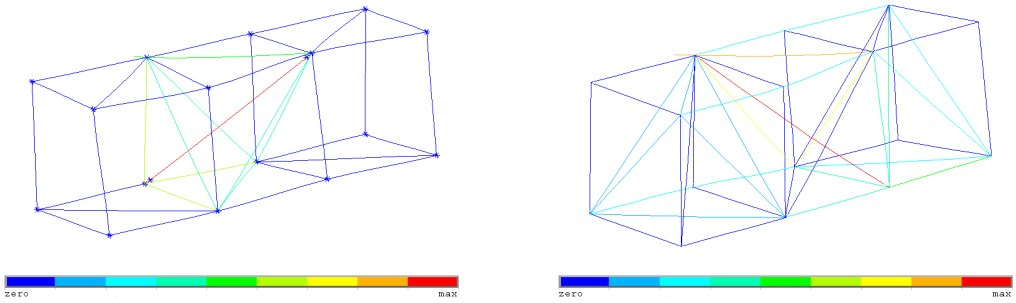

(a) Original configuration.

(b) Fully redundant configuration.

Figure 7.31: The axial load distribution in the space frame under actuation.

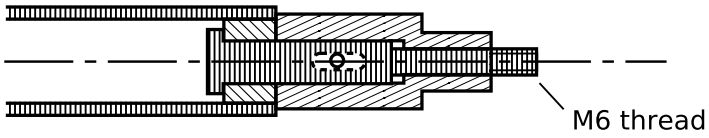

Figure 7.32: The new stiffer end connector for the cubic diagonal member: similar to the standard connector but with a small diameter at the contact surface due to space limitations.

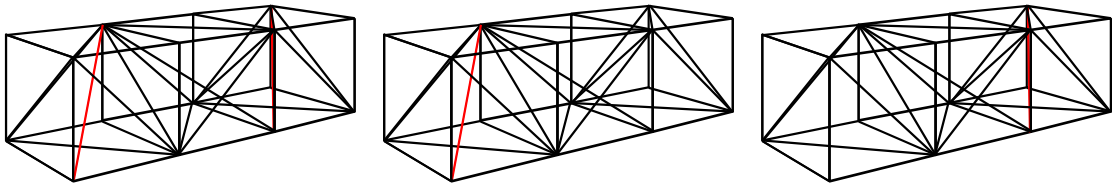

(a) Fully redundant configuration

(b) Right-hand cubic diagonal removed.

(c) Left-hand cubic diagonal removed.

Figure 7.33: The space frame configurations used in the follow-up study.

Figure 7.34: Fully redundant space frame, with the shaker attachment seen in the bottom left corner.

7.8 Follow-Up Experimental Evaluation

7.8.1 Control Strategy

For the second study, the preparatory tests use a finer measurement resolution in both the load and frequency domains to investigate the possibility of weaving through the densely spaced modes. To facilitate the large number of tests required for the detailed spectral waterfall plots, a new test procedure is developed. While the first study employed dedicated LMS® [151] modal testing hardware and software to determine the frequency response, the second takes advantage of the RCP hardware to automate the aquisition and processing of the data while simultaneously controlling the actuator and shaker signals.

The experimental setup is shown in figure 7.34. The shaker is attached as before, powered by an amplifier supplied with random broadband excitation from the RCP. The load demand for the actuator is determined by a timer, stepping down from 3200 N to 0 N in steps of 40 N, using the controller in figure 7.35. Prior to ADC conversion, the transducer signals are all conditioned through an IEPE filter and a further amplification stage. Force and acceleration data are collected for 10 minutes at each load step to permit high quality estimates of the FRFs and the sampling rate is reduced to 500 Hz to cover the 0 Hz to 200 Hz range while minimising the data storage. The resultant FRF curves have a spectral resolution of 0.2216 Hz.

Frequency response contour plots are presented in figure 7.36 for the first of the new configurations. Due to the large number of load steps, the high spectral resolution and the large number of averages, the tests took a total of 13 hours to complete. Over the course of this time, significant changes in the dynamics of the structure were observed. While the resonant ridgelines are mostly smooth and follow reasonable paths, the more sensitive antiresonances are seen to meander as the load is varied. There also appear to be several abrupt events affecting all of the FRFs, creating sharp transitions in the contour plots. Two of these are seen to have partially, then fully dislodged an accelerometer at 3000 N and 1500 N in the third plot. Interestingly, the channel still registers a weak but correlated signal after the accelerometer is detached, attributed to crosstalk in the signal leads.

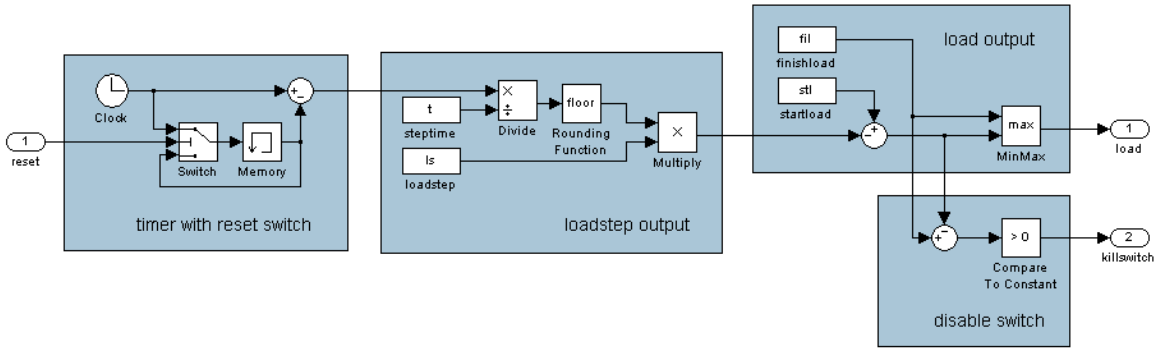

Figure 7.35: The timing system for the load demand output, including a disable switch which is triggered at the end of the test to turn off the test equipment.

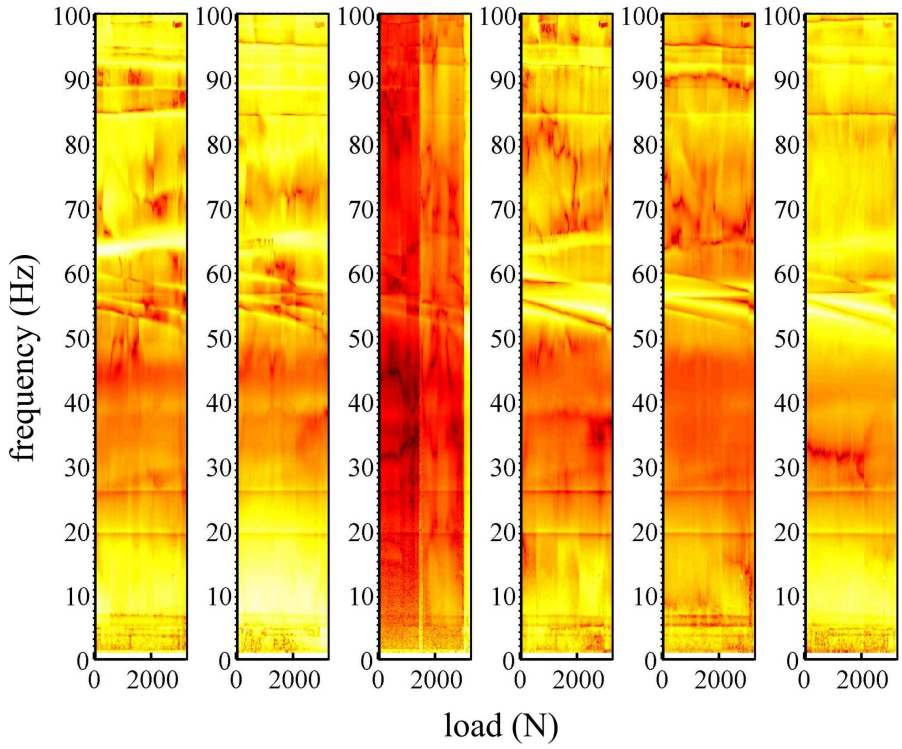

Figure 7.36: Spectral response of the space frame at response points on the left, central and right cubic diagonal members as viewed in figure 7.33. Accelerometers are located in the vertical and horizontal planes, and the plots from left to right represent: left, vertical; left, horizontal; central, vertical; central, horizontal; right, vertical; right, horizontal.

The cause of the abrupt changes is unknown; it is possible that they can all be attributed to changes in the accelerometer attachment conditions. The accelerometers in the centres of the beams are mounted using wax and thirteen hours of vibration could loosen these connections. The vibrations could also have an effect on the joints at the node connectors, and both of these circumstances would help to explain the meandering antiresonances. Another explanation that was tendered was that temperature variation could affect both the wax stiffness and the structural response itself. Monitoring the laboratory temperature over the course of the tests proved inconclusive, however: the range covered was seen to remain within the measurement device's specified tolerance of $\pm 1°C$.

The outboard diagonals are removed in turn and the new results are seen in figures 7.37(a) and 7.37(b). Once again an accelerometer is seen to fall from the structure in the 4th plot of figure 7.37(a). The fallen accelerometer once more registers low-level results from the crosstalk in the wires and this was mimicked by the spare accelerometers, which were left attached to a stationary desk. The spectral patterns are similar for each of the three cases, with the latest two configurations showing greater promise for resonance avoidance. This is because the quasi-periodicity of the structure creates several resonances in close proximity, all responding in the same manner to the actuator loading. The distribution of the natural frequencies spans a similar range to the *change* in natural frequencies afforded by actuation, thus compromising the ability to skip over all of the resonant peaks as before: adjusting the load to avoid one resonance will simply bring another one in line. Removing one of

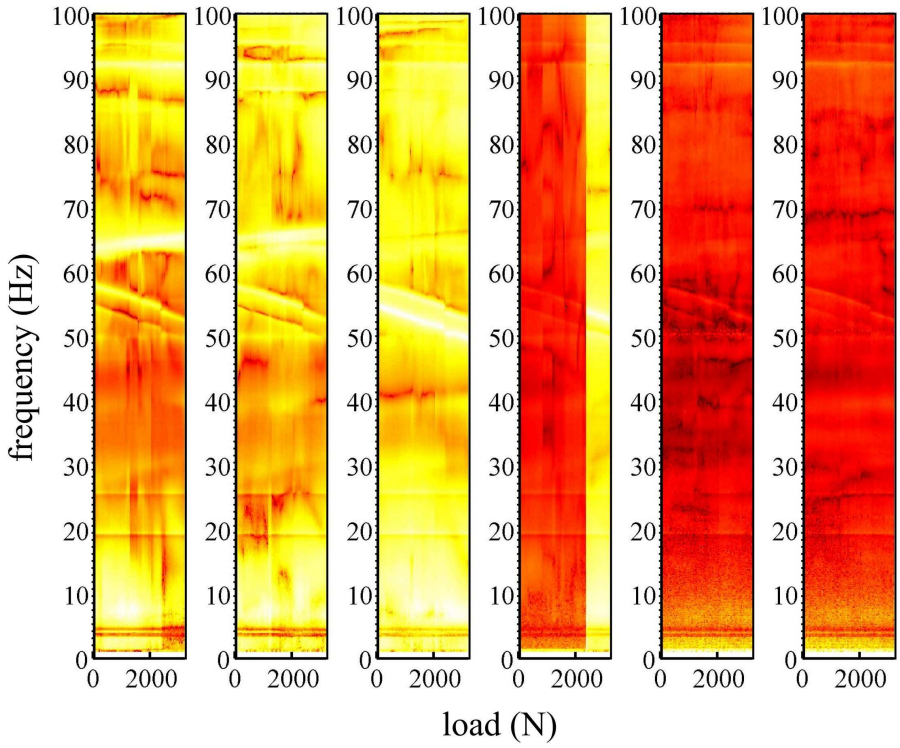

(a) Right cubic diagonal removed.

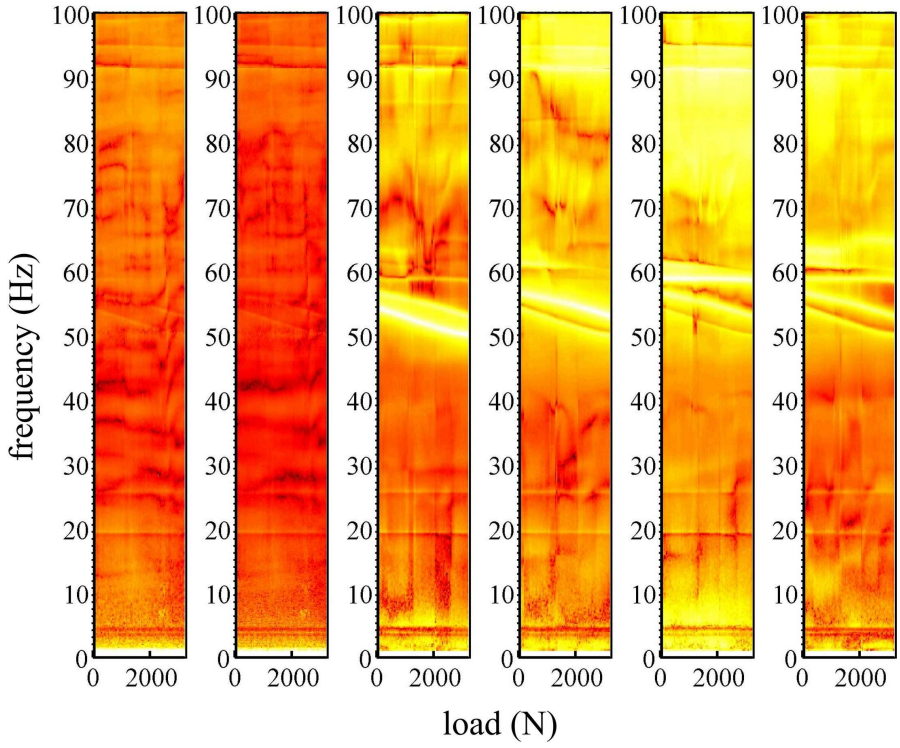

(b) Left cubic diagonal removed.

Figure 7.37: Spectral response of the space frame for the final two configurations. Charts represent response points on the left, central and right cubic diagonal members as viewed in figure 7.33. Accelerometers are located in the vertical and horizontal planes, and the plots from left to right represent: left, vertical; left, horizontal; central, vertical; central, horizontal; right, vertical; right, horizontal.

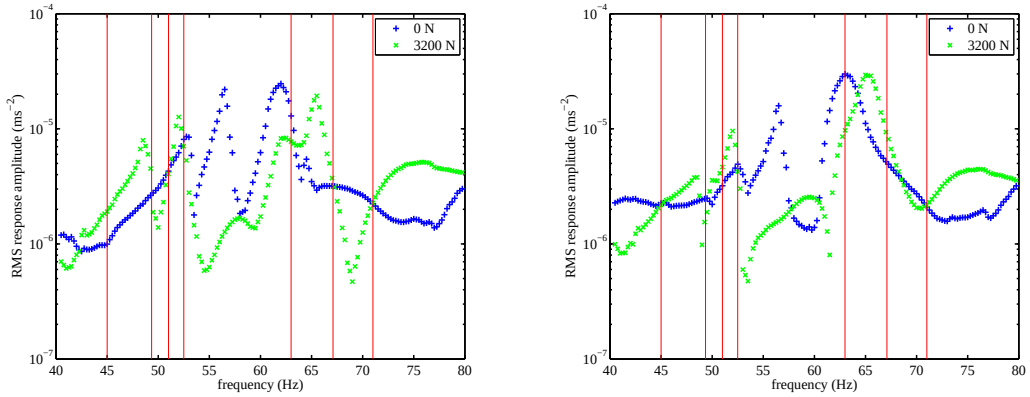

(a) Horizontal plane

(b) Vertical plane

Figure 7.38: Passive RMS response measurements for the binary actuation study on the space frame, measured at the centre of the outboard cubic diagonal member, perpendicular to the beam in the horizontal and vertical planes. Vertical lines indicate the chosen actuation change points.

the three diagonals reduces the multiplicity and provides a more amenable structure. Thus, the right hand cubic diagonal is removed for the remainder of the tests.

The shortcomings acknowledged in the accuracy of the frequency estimates from the first study suggest that with the current test setup it is futile trying to weave through regions of high modal density. In addition, the unpredictable antiresonances seen in the latest tests indicate that aligning drive frequencies with antiresonances will be unreliable. Consequently, the continuous adjustment of the actuator load is abandonned in favour of a binary mode of operation, using only a 0N or 3200N load at any given time, with the sole aim of avoiding excitation of resonant frequencies.

The binary actuation method not only provides a simplified implementation, but also provides a simplified method of planning. Instead of determining the full response surface across the load-frequency plane, it is instead possible to perform two tests, one at each load, and simply choose the load which provides the lowest response for each drive frequency. Essentially, wherever the two response curves cross, the actuation should change.

The stepped sine excitation is supplied via the shaker, adapting the timed system used for the stepped load control in figure 7.35 to the purpose. Ignoring the regions of high modal density and restricting the demonstration to the 40Hz to 80Hz range, the sinusoid is stepped in intervals of 0.5Hz holding for 10 seconds at each frequency. This is performed for the two static loading cases, sequentially, and the results are plotted in figure 7.38. These results are the RMS averaged response, with averages taken over 5s and overlapping by 2.5s. The actuation change points are chosen as indicated in the figure, intended to optimise the response of the horizontal DOF measurements.

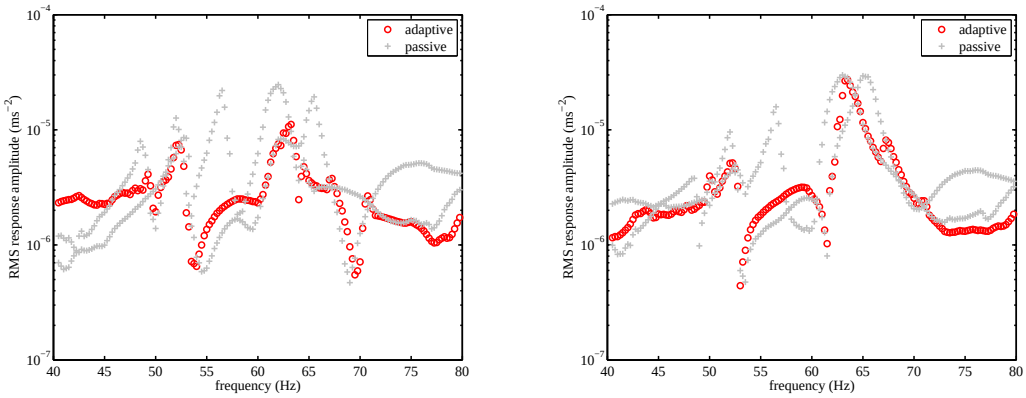

(a) Horizontal plane

(b) Vertical plane

Figure 7.39: RMS response measurements for the binary actuation study on the space frame. Results with the adaptive control enabled are compared to the passive responses, measured at the centre of the outboard cubic diagonal member, perpendicular to the beam in the horizontal and vertical planes.

7.8.2 Testing and Results

For the new tests, the accelerometer used for the frequency estimation is moved away from the shaker attachment to see how well the technique functions with remote acceleration data. It is relocated to node 9, in the x-direction. The frequency estimation also uses a larger sample period of 1024 samples to improve the frequency resolution. All of the data from the experiments is saved on this occasion to facilitate a more detailed post analysis.

The stepped sinusoidal test is repeated with the automated actuation enabled, and the results are seen in figure 7.39. These are an improvement over the individual results at either 0 N or 3200 N in the horizontal direction. The passive cases have maximum response amplitudes of $2.503 \times 10^{-5}\text{ms}^{-2}$ and $2.001 \times 10^{-5}\text{ms}^{-2}$ over the frequency range, whereas the automated system limits the maximum amplitude to $1.342 \times 10^{-5}\text{ms}^{-2}$, with the peaks also spanning a reduced bandwidth. A poor choice of actuation change points is responsible for the less impressive results in the vertical direction.

In a second test, further gains are made by retesting the passive cases and making a slight adjustment to the lookup table, as seen in figure 7.40. The final test produces the results in figure 7.41, with a horizontal peak magnitude of only $1.543 \times 10^{-5}\text{ms}^{-2}$: a 47% reduction in the peak response. The benefits are emphasized in the linear response plots of figure 7.42.

Despite the success of the latest demonstration, it does not exploit the full potential offered by the technique. In particular, the peak at roughly 52.5 Hz should have been avoidable. Part of the problem is once again a poor choice of actuation change points, but analysis of the saved data reveals some of the responsibility to lie with the frequency estimation.

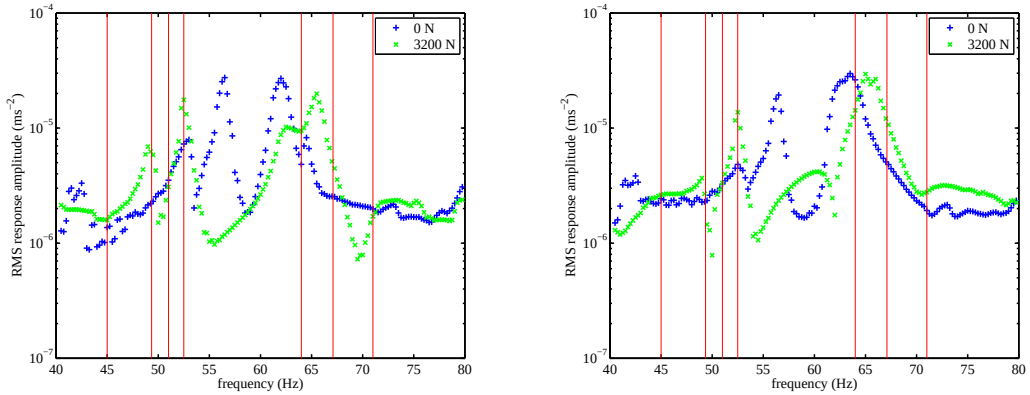

(a) Horizontal plane (b) Vertical plane

Figure 7.40: Passive RMS response measurements for the second binary actuation study on the space frame. Vertical lines indicate the chosen actuation points.

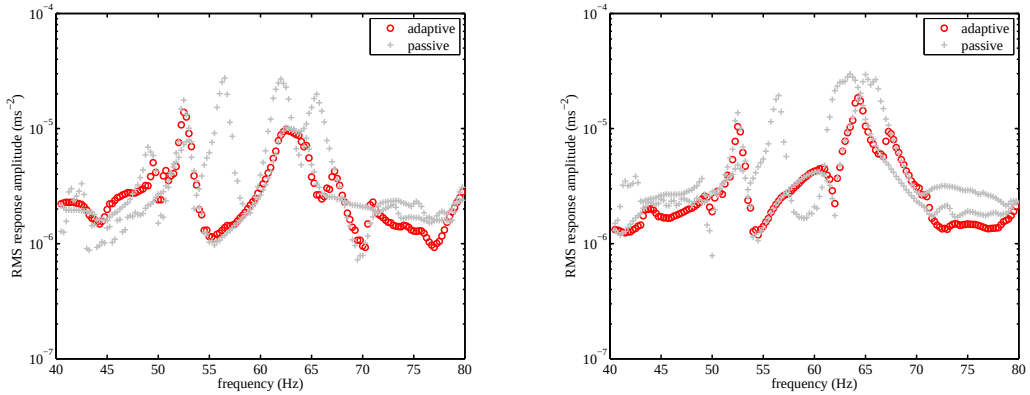

(a) Horizontal plane (b) Vertical plane

Figure 7.41: RMS response measurements for the second binary actuation study on the space frame.

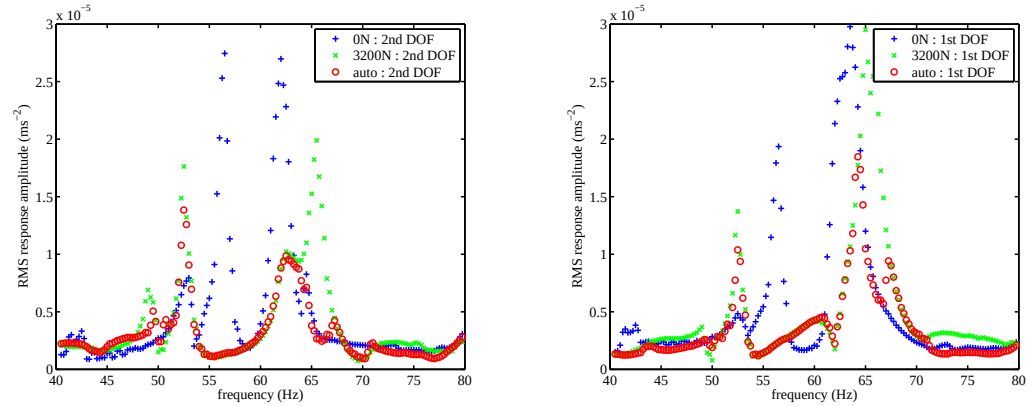

(a) Horizontal plane (b) Vertical plane

Figure 7.42: RMS response measurements for the second binary actuation study on the space frame.

7.9 Frequency Estimation Discussion

The frequency estimation method may now be analysed in further detail. The output of the estimation algorithm throughout the final test is shown in figure 7.43. As previously, the errors in the estimated frequencies are categorised as either *inaccurate* or *misidentified*. The inaccurate estimates are close to the actual excitation frequencies, whereas the misidentified frequencies skip between vastly different values. The misidentified frequencies are now seen to be composed entirely of harmonics of the excitation frequency or 0 Hz. In contrast to the conclusions drawn previously these errors do not seem to be responsible for any fluctuation in the load demand, seen in figure 7.44. This is largely due to the fact that the harmonics and the 0 Hz band lie outside the range of the lookup table for this example. Instead, the fluctuations that are seen in the load demand occur close to 200 s and 600 s on the graph. These correspond with regions of inaccurate frequency estimation in figure 7.43, where the estimate meanders close to the excitation frequency without identifying it precisely.

An analysis of the spectral breakdown over the course of the test provides further insight. This analysis is performed after the test is completed, using saved accelerometer response time histories. Unfortunately, file size restrictions on the data aquisition software led to a reduced sample frequency of 100 Hz in the saved data. As a result, the spectral response chart exhibits aliasing in the frequency range of interest and requires careful interpretation. This chart is seen in figure 7.45. The dominant excitation frequency is clearly seen dropping in 0.5 Hz intervals from 80 Hz to 40 Hz. The aliasing is manifested as a reflection about the Nyquist frequency of 50Hz so there is an equivalent peak seen rising from 20 Hz to 60 Hz. It should be noted that the full sampling frequency of 500Hz used in the real-time estimation algorithm does not suffer from this artefact. Also present in the figure is a weak harmonic peak; this is confusing because of the aliased reflections but it can be seen in the top right corner dropping at twice the rate of the base frequency to a final value of 80Hz, with equivalent reflections throughout the plot. The harmonic generally has a much lower magnitude than the true excitation frequency. The regions where the load demand fluctuates are now seen to correspond with near-resonant conditions, where the full frequency spectrum sees an increased response, manifested as light bands on the spectral chart. Perversely, these regions are exactly those which depend the most on the accuracy of the estimates to avoid exciting the resonances. It is this behaviour which is seen at 550 s, leading to the poor performace observed previously at 52.5 Hz.

Several possibilities present themselves for improving on the estimation algorithm. Firstly, a knowledge of the expected range of drive frequencies can narrow down the scope for error. Limiting the range in this example to 40-80 Hz would not only eliminate the possibility of the frequency being estimated near 0 Hz, but would also rule out the harmonic. This limiting could be performed by applying a band-pass filter prior to the spectral estimation, or more simply by passing only the appropriate data range to the peak-picking routine.

Sporadic fluctuations in the frequency estimation could be tackled by applying a low-pass filter to the output of the frequency estimation routine, or the load demand input. These two options would

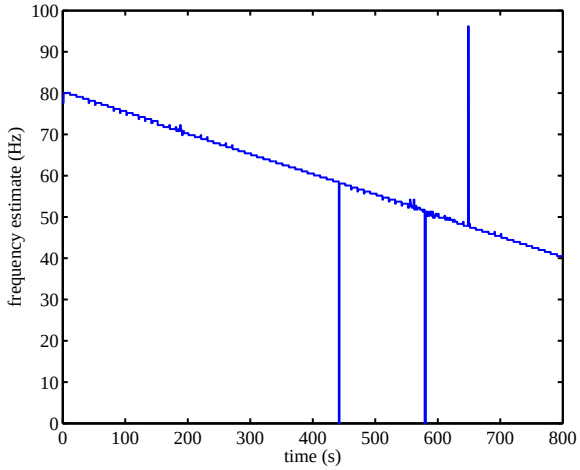

Figure 7.43: The drive frequency estimation as recorded throughout the final test of the space frame.

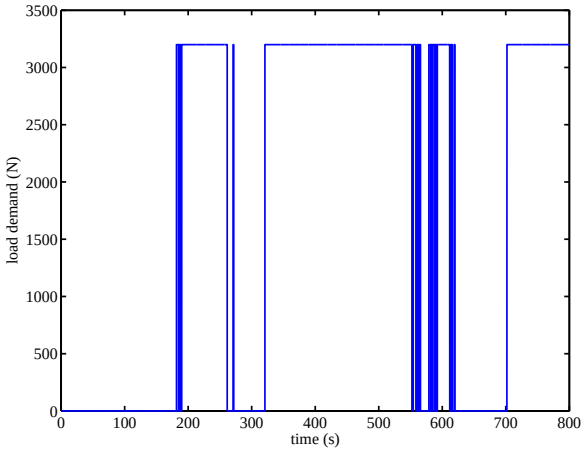

Figure 7.44: The load demand throughout the final test.

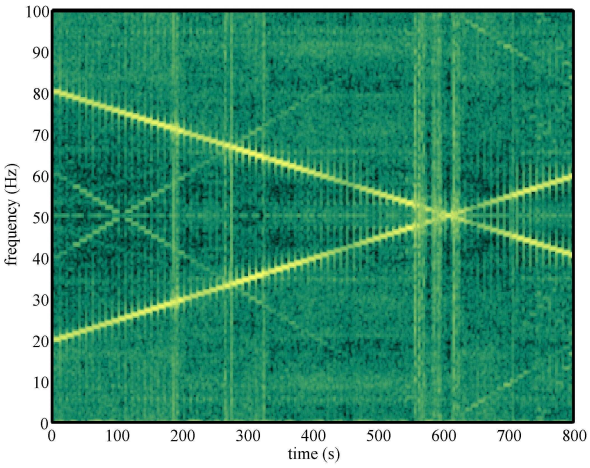

Figure 7.45: The spectral response of the space frame throughout the final test. Light regions represent high response and dark regions low response. Inadequate sampling frequency in the saved data is responsible for the aliasing in this plot.

achieve more or less the same objective, reducing the potentially detrimental tendency of the algorithm to skip between actuation loads. Provided the frequency was identified correctly for the majority of the sampling intervals then the desired outcome would be achieved.

A related development would be concerned with minimising actuation changes, and thus minimising power consumption. Here the paradigm would be to replace the lookup table with a decision-making algorithm. By storing the frequency response surface for the full load range the algorithm could perform an online cost function minimisation, taking into account both the estimated response improvement and the required actuation energy to decide on the appropriate actuation demand.

The most problematic behaviour observed in the tests was the appearance of small inaccuracies resulting from the peak-picking method at resonance. The identification difficulties are thought to be due to non-linearities in the model, creating spurious peaks in the vicinity of the excitation frequency. A better estimate of the driving frequency may be found using curve fitting methods. These could be applied to a frequency spectrum from a single accelerometer as above, or further benefit could be gained by employing measurements from a selection of locations; these would compensate for "dead spots" in any one response spectrum.

Finally, in conjuction with any of the above methods, the drive frequency estimation may be improved by employing a Kalman filter [271, 272]. To be of significant benefit the filter would need to be embued with some understanding of the nature of the variations in the excitation conditions, but in its simplest form this could be comprised of a simple stochastic description of the rate of change of the excitation frequency. Perhaps a better application of the Kalman filter would be in updating the reference response curves used to decide on the optimum actuation load. This approach would allow the system to account for long term structural variability without operator intervention.

7.10 Conclusions

An automated response suppression system has been successfully implemented, demonstrating the reduction of the response of the test structure to narrow-band excitation across a range of frequencies. The improved response is achieved without the use of damping or active control, but using an adaptive technique which requires less power than equivalent active solutions.

The main shortcomings of the scheme are due to the frequency estimation algorithm. Suggestions to improve on this aspect of the system have been made, focusing on band-pass filtering, curve fitting and Kalman filtering. A further weakness in the proposed controller is its reliance on *a priori* measurements of the response curves. Again it has been suggested that a Kalman filter could be employed to permit online updating of the assumed response profile.

An advantage of using stress stiffening to implement the adaptive scheme is its potential for propagating stiffness changes far from the actuation point. Even then, however, the loads are unlikely to

propagate in significant proportions around an entire structure. Answering this doubt, a follow-up study has demonstrated the reduction of vibrations at locations outside of the actuator load path.

While these experiments have focused on compensating for changeable drive frequencies, the technique is equally applicable to case of variable operating conditions. For example, the response of a helicopter tail boom could be manipulated to compensate for changes in the transverse tail rotor loads.

Chapter 8

Lynx Tail Boom Study

8.1 Introduction

In the preceding chapter a clear demonstration of adaptive response tuning has been given, demonstrating the potential of automated internal load adjustment for response suppression. Implementation details for the technique are case specific and for each new structure a thorough analysis must be performed to determine firstly the suitability of the method to the problem in hand, and secondly the approach that must be taken. In this chapter, some analytical tools are developed to address these tasks and a finite element analysis (FEA) of a Lynx tail boom is undertaken. Two methods are investigated: the first consists of manipulating the natural frequencies of the structure as before, while a second approach employs the actuation apparatus as a tuned vibration absorber (TVA). The original intention was to apply the results of the numerical analysis to an experimental demonstration but unfortunately the airframe was unavailable for testing at the time of writing.

8.2 Actuator Placement

When deciding on an appropriate actuator placement the first question that must be answered is, "which mode(s) do you want to control?". The task faced is then that of determining which members must be tensioned in order to influence those modes, and which actuator placement will produce such tensioning. Where several modes should be controlled independently it may prove advantageous to distribute several actuators around the structure.

A set of tools are proposed here for this analysis. The choice of actuator placements in a complex structure is vast, so the first step is to narrow down the possibilities. An algorithm is developed below to aid in this endeavour; the end product is a diagram of the structure indicating the extent to which a given mode will be influenced by unit stress stiffening in each of the members. This information facilitates an informed choice of actuator placements which may then be evaluated in detail. The

detailed evaluation utilises modal FEA sensitivity analyses, performed with respect to loading at each location in turn, giving a clear indication of the extent to which each mode may be controlled by an actuator at that location. Once suitable actuation points are chosen, an inverse method produces a simple control law for placing the poles as desired.

8.2.1 Stress Stiffening Influence Diagram

The first tool offered here provides a means of visualising the sensitivity of each mode to stress stiffening in the component members. It is implemented in an ANSYS macro, following the methods presented below.

The sensitivity of a mode to structural loading is dependent upon the coincidence of axial or in-plane static loading with transverse or out-of-plane dynamic bending. The tools developed below use this premise to illustrate the sensitivity of each mode to the presence of stress stiffening in the individual elements.

As a note of caution for anyone hoping to apply these methods, be aware that the ANSYS terminology differs from that used in this thesis: in ANSYS, the *tangent stiffness* is considered to be the nominal stiffness adjusted to compensate for deflections. That is, it takes into account the structural reconfiguration occuring in nonlinear geometric problems but not the stress stiffening effect. The *consistent stiffness* is the ANSYS term for what is referred to here as the tangent stiffness. For the sake of consistency, the following text will continue with the nomenclature used throughout the rest of the thesis.

The sensitivity of an eigenvalue is given by Fox and Kapoor [206] as

$$\frac{d\lambda}{dp} = \phi^T \left(\frac{d\mathbf{K}_T}{dp} - \lambda \frac{d\mathbf{M}}{dp} \right) \phi. \tag{8.1}$$

From eqn. (2.153),

$$\mathbf{K}_T = \mathbf{K}_E + p\overline{\mathbf{K}}_G \tag{8.2}$$

where $\mathbf{K}_T$ is the tangent stiffness matrix, $\mathbf{K}_E$ is the nominal stiffness matrix and $\overline{\mathbf{K}}_G$ is the unit stress stiffness matrix, or the stress stiffness matrix differentiated with respect to the load. The nominal stiffness is constant by definition and $\overline{\mathbf{K}}_G$ is assumed constant within the linear loading regime so

$$\frac{d\mathbf{K}_T}{dp} = \overline{\mathbf{K}}_G. \tag{8.3}$$

For the case of stress stiffnening,

$$\frac{d\mathbf{M}}{dp} = 0 \tag{8.4}$$

so the eigenvalue sensitivity becomes

$$\frac{d\lambda}{dp} = \phi^T \left(\overline{\mathbf{K}}_G \right) \phi. \tag{8.5}$$

The sensitivity can be expressed as a sum of elemental contributions such that

$$\frac{d\lambda}{dp} = \sum_n \phi^T \left(\overline{\mathbf{K}}_G \big|_n^{(G)} \right) \phi \tag{8.6}$$

where $\overline{\mathbf{K}}_G \big|_n^{(G)}$ is the full global stiffness matrix contribution of the n^{th} element. Including only the elemental DOFs in each term produces

$$\frac{d\lambda}{dp} = \sum_n \phi^T \big|_n^{(g)} \left(\overline{\mathbf{K}}_G \big|_n^{(g)} \right) \phi \big|_n^{(g)} \tag{8.7}$$

where $\phi|_n^{(g)}$ and $\overline{\mathbf{K}}_G \big|_n^{(g)}$ are the reduced-DOF-set elemental displacement vector and elemental stiffness matrix contribution of the n^{th} element, but still in the global coordinate system. A rotational transform $\mathbf{T}_n$ is defined for each element, relating the elemental coordinate system to the global coordinate system such that

$$\phi|_n^{(e)} = \mathbf{T}_n \, \phi|_n^g \tag{8.8}$$

and

$$\overline{\mathbf{K}}_G \big|_n^{(g)} = \mathbf{T}_n^T \, \overline{\mathbf{K}}_G \big|_n^{(e)} \, \mathbf{T}_n \tag{8.9}$$

where $\phi|_n^e$ and $\overline{\mathbf{K}}_G \big|_n^{(e)}$ are the elemental displacement vector and stress stiffness matrix respectively, both in the elemental coordinate system. Combining eqns. (8.8) and (8.9) it can be shown that

$$\phi^T \big|_n^{(g)} \left(\overline{\mathbf{K}}_G \big|_n^{(g)} \right) \phi \big|_n^{(g)} = \phi^T \big|_n^{(e)} \left(\overline{\mathbf{K}}_G \big|_n^{(e)} \right) \phi \big|_n^{(e)} \tag{8.10}$$

and the eigenvalue sensitivity can thus be expressed in terms of the elemental eigenvector components and stress stiffness matrices:

$$\frac{d\lambda}{dp} = \sum_n \frac{d\lambda}{dp}\bigg|_n = \sum_n \phi^T \big|_n^{(e)} \left(\overline{\mathbf{K}}_G \big|_n^{(e)} \right) \phi \big|_n^{(e)}. \tag{8.11}$$

Elemental stress stiffening matrices can not be extracted directly from ANSYS so they must be computed for these purposes. The stress stiffening matrix given for a 2D beam in the ANSYS Theory Guide [152] is the same as that given by Przemieniecki [164] and derived in section 2.4.2. Differentiating with respect to load gives

$$\overline{\mathbf{K}}_G \big|_n^{(e)} = \frac{1}{L} \begin{bmatrix} 0 & 0 & 0 & 0 & 0 & 0 \\ 0 & \frac{6}{5} & \frac{1}{10}L & 0 & -\frac{6}{5} & \frac{1}{10}L \\ 0 & \frac{1}{10}L & \frac{2}{15}L^2 & 0 & -\frac{1}{10}L & -\frac{1}{30}L^2 \\ 0 & 0 & 0 & 0 & 0 & 0 \\ 0 & -\frac{6}{5} & -\frac{1}{10}L & 0 & \frac{6}{5} & -\frac{1}{10}L \\ 0 & \frac{1}{10}L & -\frac{1}{30}L^2 & 0 & -\frac{1}{10}L & \frac{2}{15}L^2 \end{bmatrix}. \tag{8.12}$$

Extrapolating to the 3D beam,

$$\overline{\mathbf{K}}_G\big|_n^{(e)} = \frac{1}{L}\begin{bmatrix}
0 & 0 & 0 & 0 & 0 & 0 & 0 & 0 & 0 & 0 & 0 & 0 \\
0 & \frac{6}{5} & 0 & 0 & 0 & \frac{1}{10}L & 0 & -\frac{6}{5} & 0 & 0 & 0 & \frac{1}{10}L \\
0 & 0 & \frac{6}{5} & 0 & \frac{1}{10}L & 0 & 0 & 0 & -\frac{6}{5} & 0 & \frac{1}{10}L & 0 \\
0 & 0 & 0 & 0 & 0 & 0 & 0 & 0 & 0 & 0 & 0 & 0 \\
0 & 0 & \frac{1}{10}L & 0 & \frac{2}{15}L^2 & 0 & 0 & 0 & -\frac{1}{10}L & 0 & -\frac{1}{30}L^2 & 0 \\
0 & \frac{1}{10}L & 0 & 0 & 0 & \frac{2}{15}L^2 & 0 & -\frac{1}{10}L & 0 & 0 & 0 & -\frac{1}{30}L^2 \\
0 & 0 & 0 & 0 & 0 & 0 & 0 & 0 & 0 & 0 & 0 & 0 \\
0 & -\frac{6}{5} & 0 & 0 & 0 & -\frac{1}{10}L & 0 & \frac{6}{5} & 0 & 0 & 0 & -\frac{1}{10}L \\
0 & 0 & -\frac{6}{5} & 0 & -\frac{1}{10}L & 0 & 0 & 0 & \frac{6}{5} & 0 & -\frac{1}{10}L & 0 \\
0 & 0 & 0 & 0 & 0 & 0 & 0 & 0 & 0 & 0 & 0 & 0 \\
0 & 0 & \frac{1}{10}L & 0 & -\frac{1}{30}L^2 & 0 & 0 & 0 & -\frac{1}{10}L & 0 & \frac{2}{15}L^2 & 0 \\
0 & \frac{1}{10}L & 0 & 0 & 0 & -\frac{1}{30}L^2 & 0 & -\frac{1}{10}L & 0 & 0 & 0 & \frac{2}{15}L^2
\end{bmatrix} \tag{8.13}$$

Putting this into eqn. 8.11 gives

$$\begin{aligned}\left.\frac{d\lambda}{dp}\right|_n =& \frac{6}{5L}[\Delta u_y^2 + \Delta u_z^2] + \frac{1}{5}[\Sigma\theta_z \Delta u_y + \Sigma\theta_y \Delta u_z] \\ &+ \frac{L}{15}[\theta_{y1}^2 + \theta_{y2}^2 + \theta_{z1}^2 + \theta_{z2}^2 + \frac{1}{2}\theta_{y1}\theta_{y2} + \frac{1}{2}\theta_{z1}\theta_{z2}]\end{aligned} \tag{8.14}$$

where

$$\Delta u_y = u_{y1} - u_{y2} \qquad \Delta u_z = u_{z1} - u_{z2} \tag{8.15}$$

$$\Sigma\theta_y = \theta_{y1} + \theta_{y2} \qquad \Sigma\theta_z = \theta_{z1} + \theta_{z2} \tag{8.16}$$

and

$$\phi^T\big|_n^{(e)} = \{\ u_{x1} \quad u_{y1} \quad u_{z1} \quad \theta_{x1} \quad \theta_{y1} \quad \theta_{z1} \quad u_{x2} \quad u_{y2} \quad u_{z2} \quad \theta_{x2} \quad \theta_{y2} \quad \theta_{z2}\ \}^T. \tag{8.17}$$

In order to use eqn. (8.14) to compute the sensitivity of a given mode to each of the beam elements, the components of $\phi^T\big|_n^{(e)}$ in eqn. (8.17) must be known, as well as the element length L. The useful information which may be extracted from the ANSYS database consists of the cartesian node locations for each element, the element rotation α about the elemental x-axis, and the 12 nodal displacements in the global coordinate system. The displacements correspond to the mass-normalised eigenvector DOFs (where care must be taken to stipulate the mass-normalisation prior to solution by setting the relevant ANSYS flag).

The element length is calculated from the node coordinates:

$$L = \sqrt{(x_2 - x_1)^2 + (y_2 - y_1)^2 + (z_2 - z_1)^2}. \tag{8.18}$$

The elemental displacements must be computed from the global DOF displacements of the eigenvector

using eqn. (8.8). The ANSYS Theory Reference [152] describes how to compute the transform $\mathbf{T}_n$ as follows:

$$\mathbf{T}_n = \begin{bmatrix} \mathbf{T} & \mathbf{0} & \mathbf{0} & \mathbf{0} \\ \mathbf{0} & \mathbf{T} & \mathbf{0} & \mathbf{0} \\ \mathbf{0} & \mathbf{0} & \mathbf{T} & \mathbf{0} \\ \mathbf{0} & \mathbf{0} & \mathbf{0} & \mathbf{T} \end{bmatrix} \tag{8.19}$$

where

$$\mathbf{T} = \begin{bmatrix} C_1C_2 & S_1C_2 & S_2 \\ (-C_1S_2S_3 - S_1C_3) & (-S_1S_2S_3 + C_1C_3) & S_3C_2 \\ (-C_1S_2C_3 - S_1S_3) & (-S_1S_2C_3 + C_1S_3) & C_3C_2 \end{bmatrix} \tag{8.20}$$

and

$$S_1 = \begin{cases} \frac{y_2 - y_1}{L_{xy}} & \text{if } L_{xy} > 0.0001L \\ 0 & \text{if } L_{xy} < 0.0001L \end{cases} \tag{8.21}$$

$$S_2 = \frac{z_2 - z_1}{L} \tag{8.22}$$

$$S_3 = \sin(\alpha) \tag{8.23}$$

$$C_1 = \begin{cases} \frac{x_2 - x_1}{L_{xy}} & \text{if } L_{xy} > 0.0001L \\ 1 & \text{if } L_{xy} < 0.0001L \end{cases} \tag{8.24}$$

$$C_2 = \frac{L_{xy}}{L} \tag{8.25}$$

$$C_3 = \cos(\alpha) \tag{8.26}$$

$$L_{xy} = \sqrt{(x_2 - x_1)^2 + (y_2 - y_1)^2}. \tag{8.27}$$

Using this procedure, each beam's potential for affecting the eigenvalue is determined, and subsequently placed in an ANSYS element table allowing it to be displayed pictorially through the ANSYS postprocessor.

Figure 8.1 shows the results of the macro for the first nine modes of the space frame used in chapter 7. As expected, the frequencies of modes 7 and 8 show a strong dependency on the axial loads carried in the cubic diagonal member. Other modes, notably 5 and 9, are most sensitive to loads in the actuated member but the scale on the plots reveals that they are affected to a lesser extent than modes 7 and 8. The other modes show a more even distribution of dependency throughout the structure.

Stress stiffening for shells and solid elements is calculated in ANSYS using numerical integration over the element area or volume. While it is possible to perform this integration in an ANSYS macro, the coding task is prohibitive and for reasons that will be seen in section 8.4 it is not necessary for the task in hand.

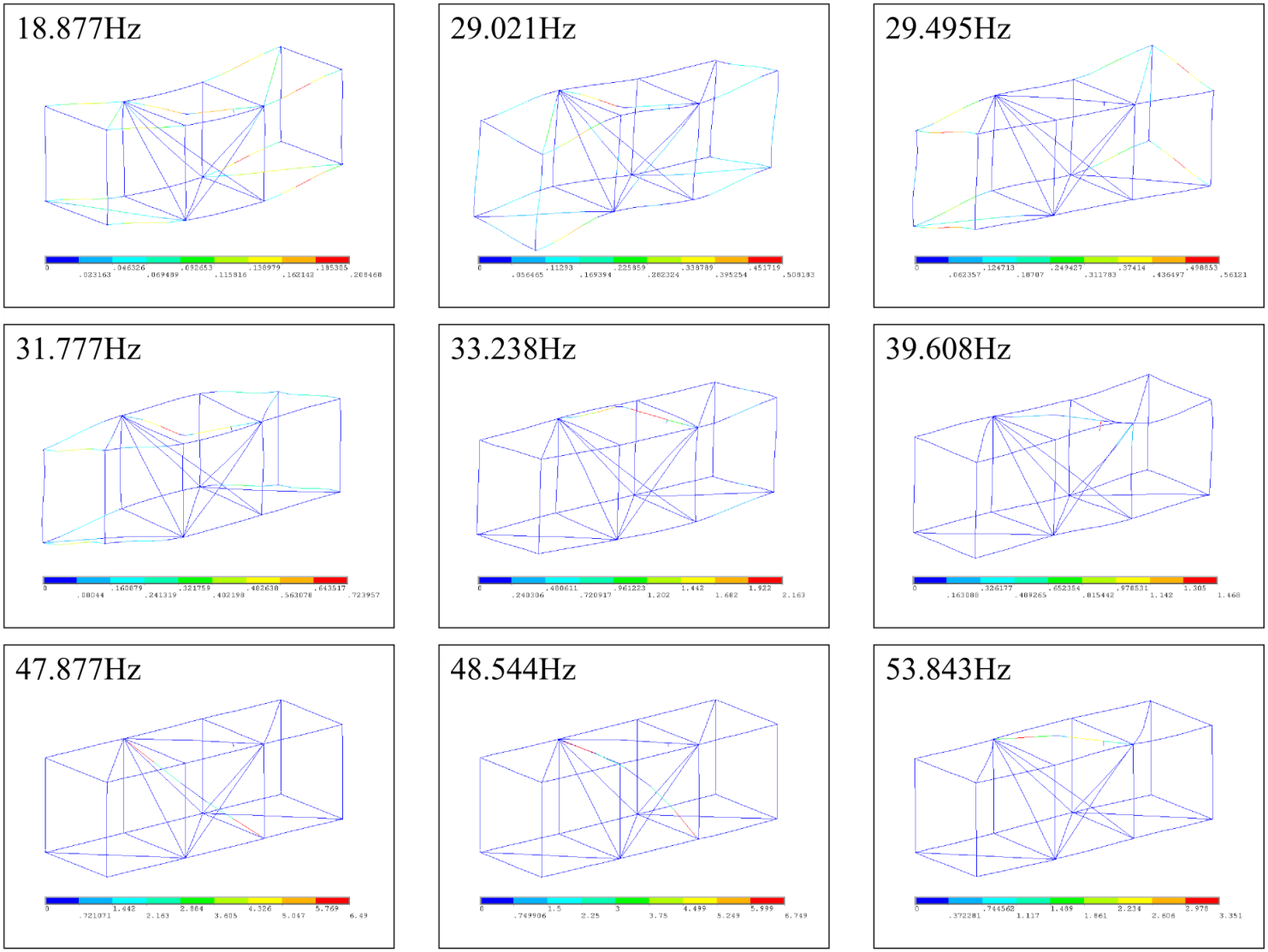

Figure 8.1: Influence of stress stiffening in each of the beam elements on the eigenvalue of each mode.

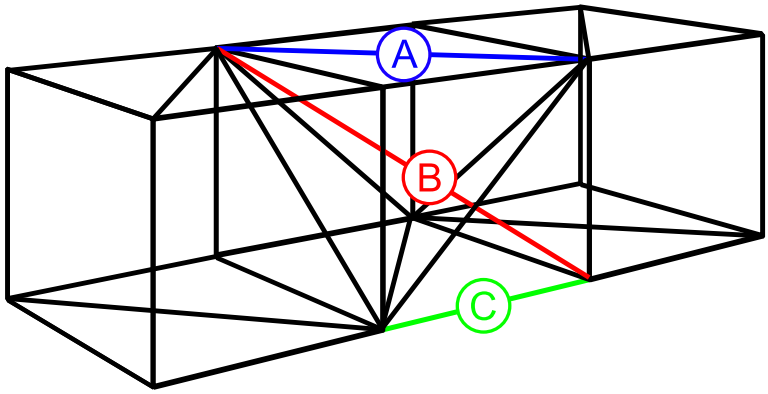

Figure 8.2: Actuator locations in the spaceframe for the sensitivity studies. (A) is the location used for previous studies, (B) is the cubic diagonal member and (C) is the horizontal member at the front centre of the structure.

8.2.2 Modal Sensitivity Analysis

The stress stiffening influence diagram does not directly lead to the identification of an appropriate actuator location; rather, it provides an indication of which members should be subjected to axial or in-plane loading. Equipped with this knowledge, sensible loading points may be selected and evaluated. Provided there is no interaction between modes (low modal coupling and high frequency separations) then the eigenvalues will exhibit approximately linear variation within the linear loading regime and the behaviour is fully described by the eigenvalue sensitivities for the zero load case. Using the ANSYS Gradient method in the Design Optimisation library the sensitivities to loading at each actuation point may be determined with a single run.

As an example, the sensitivities calculated by ANSYS for the space frame of chapter 7 are shown in table 8.1, corresponding to the actuator locations shown in figure 8.2. The values for location A, as used in the previous studies, are seen to match the gradients of the lines in figure 7.29. The sensitivities for other locations about the central cube are seen to be roughly linear permutations of the first load case, on account of the single degree of redundancy.

Mode	Frequency sensitivity to unit load (HzN^{-1})		
	Config A	Config B	Config C
1	3.77×10^{-4}	-1.55×10^{-4}	2.58×10^{-4}
2	3.93×10^{-4}	-1.63×10^{-4}	2.74×10^{-4}
3	-1.42×10^{-5}	-3.04×10^{-6}	1.23×10^{-5}
4	6.64×10^{-4}	-2.81×10^{-4}	4.68×10^{-4}
5	2.09×10^{-3}	-8.55×10^{-4}	1.42×10^{-3}
6	1.57×10^{-4}	-6.09×10^{-5}	9.73×10^{-5}
7	-8.09×10^{-3}	3.71×10^{-3}	-6.26×10^{-3}
8	-8.35×10^{-3}	3.83×10^{-3}	-6.46×10^{-3}
9	1.70×10^{-3}	-6.84×10^{-4}	1.13×10^{-3}

Table 8.1: The first nine frequency sensitivities for the actuator configurations shown in figure 8.2

The significance of the degree of redundancy was touched upon on in chapter 7, and the values presented here support the notion that the internal load distribution in the redundant cube is roughly the same regardless which member contains the actuator. Bahra and Greening [266] describe how rank deficiency of the equilibrium matrix leads to fewer linearly independent load distributions than members in a frame. The consequence of this observation is that any achievable load distribution may be induced using appropriately placed actuators, their number being equal to the rank of the equilibrium matrix.

8.2.3 Inverse Control Law

Depending on circumstances it may be desirable to control several modes independently. This could be useful, for example, in the configuration seen in section 7.8, where three modes with non-negligible modal overlap are seen to vary such that their separation remains roughly constant. In this case it is difficult to find a load configuration using a single actuator that will avoid exciting any of the three modes within that frequency band.

Because of the linear behaviour of the eigenvalues within the linear loading regime, it is possible to develop a simple control algorithm for this purpose. The ability to control modes independently is dependent upon a set of actuator placements which produce linearly independent eigenvalue sensitivities. The number of actuators that can be usefully employed will be determined by the rank of the sensitivity matrix, which will not exceed that of the equilibrium matrix discussed above, and will correspond to the number of linearly independent columns in the sensitivity matrix

$$\mathbf{S} = \begin{bmatrix} \frac{\partial \lambda_1}{\partial p_1} & \frac{\partial \lambda_1}{\partial p_2} & \cdots & \frac{\partial \lambda_1}{\partial p_n} \\ \frac{\partial \lambda_2}{\partial p_1} & \frac{\partial \lambda_2}{\partial p_2} & \cdots & \frac{\partial \lambda_2}{\partial p_n} \\ \vdots & \vdots & \ddots & \vdots \\ \frac{\partial \lambda_m}{\partial p_1} & \frac{\partial \lambda_m}{\partial p_2} & \cdots & \frac{\partial \lambda_m}{\partial p_n} \end{bmatrix} \tag{8.28}$$

where m is the number of eigenvalues to be controlled and n is the number of actuators. The eigenvalue perturbations from their nominal values are given by

$$\boldsymbol{\Delta\Lambda} = \mathbf{S}\boldsymbol{\Delta}\mathbf{p} \tag{8.29}$$

where $\boldsymbol{\Delta}\mathbf{p}$ is the vector of parameter perturbations, in this case the actuator loads. To determine the necessary load inputs for a given set of eigenvalue perturbations, the inverse problem must be solved:

$$\boldsymbol{\Delta}\mathbf{p} = \mathbf{S}^{+}\boldsymbol{\Delta\Lambda} \tag{8.30}$$

where

$$\mathbf{S}^{+} = (\mathbf{S}^{T}\mathbf{S})^{-1}\mathbf{S}^{T} \tag{8.31}$$

is the pseudo-inverse. If $m = n$, an exact solution exists. Where $m > n$, and there are more modes to

be controlled than actuators to control them with, the solution provided is the least squares solution. If some modes are more critical than others then a weighting matrix can be used as in the updating schemes of section 2.7 such that

$$\mathbf{W}\boldsymbol{\Delta\Lambda} = \mathbf{WS}\boldsymbol{\Delta p} \tag{8.32}$$

and

$$\boldsymbol{\Delta p} = (\mathbf{S}^T\mathbf{WS})^{-1}\mathbf{S}^T\mathbf{W}\boldsymbol{\Delta\Lambda} \tag{8.33}$$

where $\mathbf{W}$ is a diagonal matrix of weighting factors.

If $m < n$, and there are fewer modes to be controlled than actuators to control them with, a unique solution does not exist and another method must be used. By minimsing the actuator perturbations the least squares solution becomes

$$\boldsymbol{\Delta p} = \mathbf{S}^T(\mathbf{S}^T\mathbf{S})^{-1}\boldsymbol{\Delta\Lambda} \tag{8.34}$$

and once more a weighting matrix may be used, this time influencing distribution of the actuator load changes:

$$\boldsymbol{\Delta p} = \mathbf{W}^{-1}\mathbf{S}^T(\mathbf{S}^T\mathbf{W}^{-1}\mathbf{S})^{-1}\boldsymbol{\Delta\Lambda}. \tag{8.35}$$

Although admitting exact solutions, this technique does not take into account the permissible load ranges of each of the actuators. As a result, the loading parameters may be unrealistic: they may stray into nonlinear regions, outside the actuator capabilities, or even beyond the structural failure loads. Solutions to this problem could be to limit the eigenvalue perturbations to sensible values, or to incorporate the load boundaries into the penalty function for the control system.

8.3 Tail Boom Model

The Lynx Mk. 7 is pictured in figure 8.3(a). Prior to the commencement of this study an extensive modal testing programme had been performed on the tail boom, identifying frequencies, damping and mode shapes for the first 18 modes. It is pictured in figure 8.3(b) mounted on a reaction wall for the modal tests. While the Lynx itself was not available for new tests, the availability of test data for model validation led to the decision to use an FE model of the tail boom as a test case to explore the potential for response control in a real aerospace structure.

Furthermore, a detailed FE model of the structure was also available. This model had been created for Nastran, but in order to directly apply the tools and techniques developed here an ANSYS model was needed. Several options for converting the model were considered but after some investigation, the most reliable method of those available was deemed to be the creation of a custom script. The script was created in MATLAB.

The first step in the conversion is a parsing routine to interpret the data in the Nastran bulk data file (BDF). This is relatively straightforward as the file format is well defined in the Nastran docu-

(a) Lynx helicopter. (b) Tail boom mounted on reaction wall.

Figure 8.3: Photographs of the Lynx Mk 7 used in preliminary experimental tests.

mentation [273]. Once the command entries have been stored in MATLAB arrays, the next step is to read the model data. The Lynx model was found to contain entries corresponding to coordinate systems, materials, nodes, beam elements, triangular and quadrilateral shell elements, point masses, DOF couplings, constraint equations, and boundary conditions, in addition to the real constants associated with each element type. The final step in the conversion process is to write an ANSYS input file (.lgw extension) containing the commands to recreate the model.

To produce a valid ANSYS model, an additional element processing stage was needed before the final ANSYS input file creation. This was necessary because the element shape restrictions in Nastran were found to be more relaxed than those in ANSYS; some of the highly warped quadrilateral shell elements needed to be substituted with two triangular shells and some of the heavily tapered beams adjusted appropriately. The code was carefully written to produce warnings for any model features which were not reproduced exactly, as well as for unsupported model features in the Nastran BDF file, so that differences in the results could be attributed to the model discrepancies.

The full helicopter model imported to ANSYS is pictured in figure 8.4. The tailboom section is shown in figure 8.5. The tailboom model consists of 2185 nodes, 3519 elements and 13 coupling/constraint equations. Trials with ANSYS showed that the constraint equations led to problems with insufficient memory. This problem seems unusual but after extensive investigation the allocated memory was deemed sufficient, and the constraint equations were seen to be applied correctly, yet the errors were still produced. For want of a better solution the constraint equations were replaced with light, rigid beam elements. For coupled nodes this does not have a significant effect on the solution, but complicated constraint equations such as those used in Nastran's RBE3 elements can not be reproduced accurately in this way. RBE3 elements were used in the Nastran model to attach the tail plane and the point mass representing the tail rotor hub to the fin, as seen in figure 8.6. The effect of the RBE3 constraint equations is to distribute loading realistically between several nodes but without constraining the displacement of the nodes relative to one another. By substituting the RBE3 elements with nearly-rigid beams an artificial rigidity is introduced between the attachment nodes. This transcription inaccuracy was necessarily accepted.

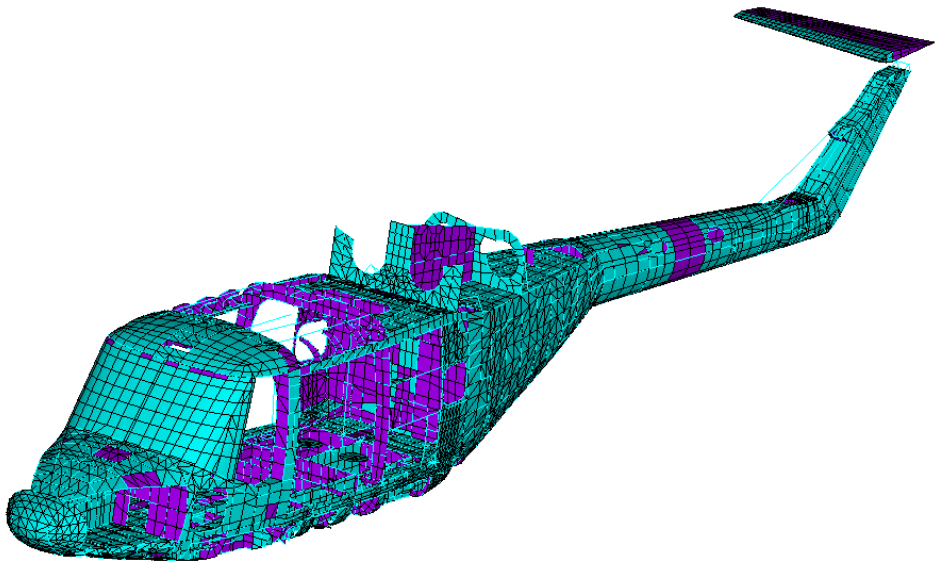

Figure 8.4: Full model of the lynx helicopter airframe, as imported into ANSYS.

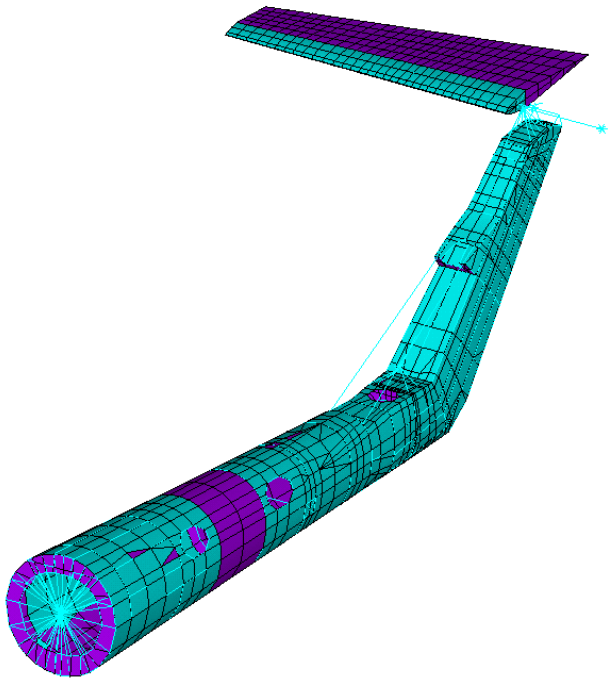

Figure 8.5: The FE model of the Lynx tail boom imported into ANSYS.

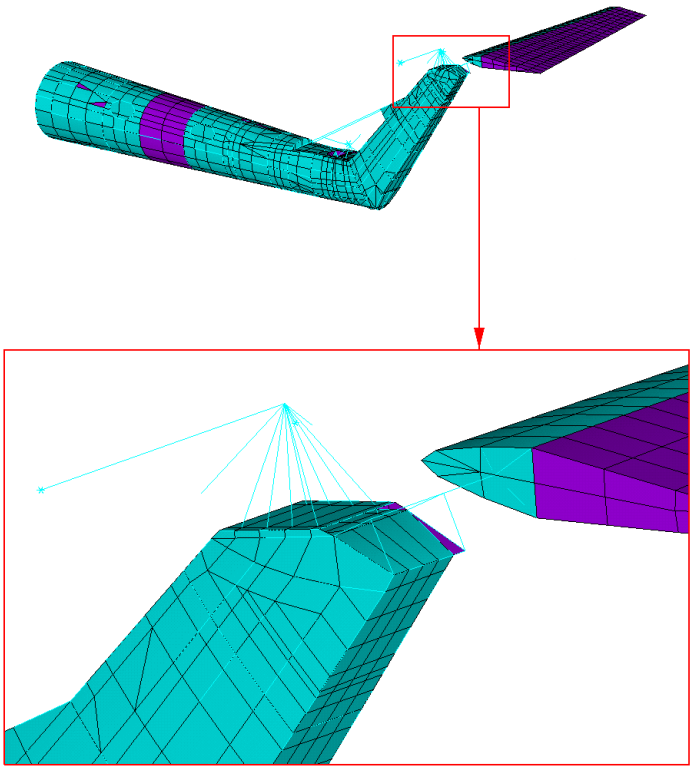

Figure 8.6: Enlarged view of the RBE3 elements connecting the tailplane and the tail rotor hub (modelled as a point mass) to the fin.

The model is constrained at the tail root, mimicking the early experiments on the reaction wall. Using this configuration the modal results from the ANSYS and Nastran models are compared in figure 8.7. The two result sets are by no means identical but the low order modes show consistency up past the rotor excitation frequency of 22Hz. The ANSYS model produces higher frequencies than the Nastran model, possibly due to the increased stiffness at the tailplane and tail rotor hub attachment points. Comparing the two models to the experimental results in figure 8.8, the ANSYS model is in fact seen to give a better mode shape correlation than that of the Nastran model while the frequency correlation for the low order modes is worse. Once again, the high order modes are seen to exhibit a relatively poor correlation. For these reasons the analysis that follows will be confined to the low order modes, focusing on those close to the rotor frequency. The first 9 modes from the ANSYS model are shown in figure 8.9.

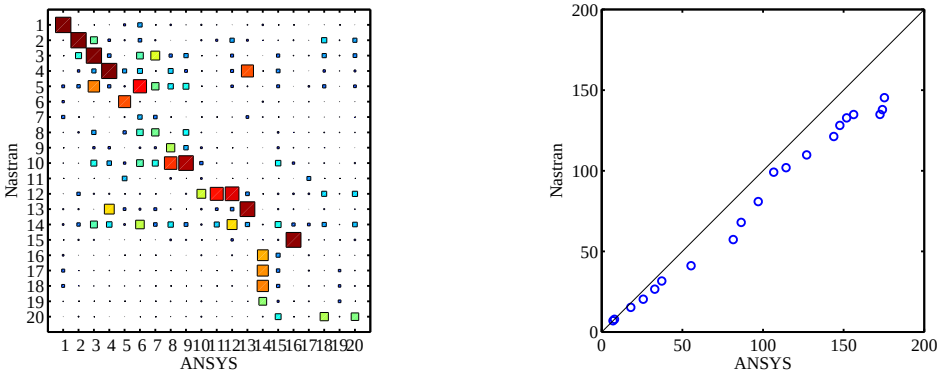

(a) MAC (b) Frequencies (Hz)

Figure 8.7: Comparison of the modal results from the ANSYS and Nastran FE models of the Lynx tail boom.

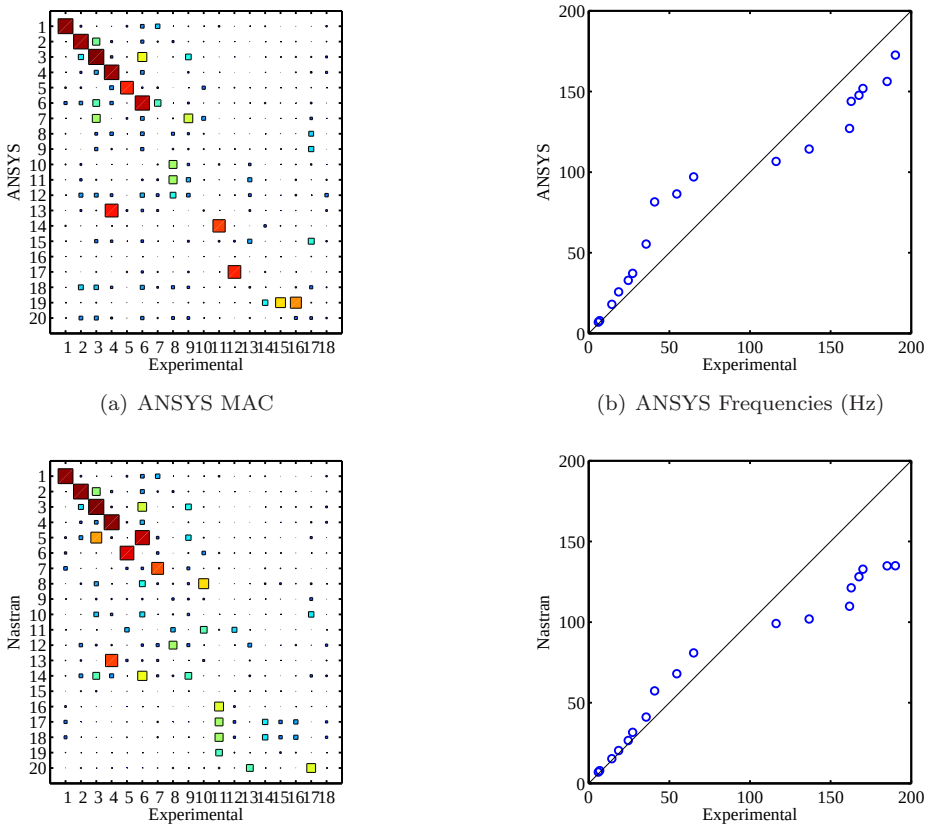

(a) ANSYS MAC (b) ANSYS Frequencies (Hz)

(c) Nastran MAC (d) Nastran Frequencies (Hz)

Figure 8.8: Comparison of the experimental modal results for the Lynx tail boom with the ANSYS and Nastran FE models.

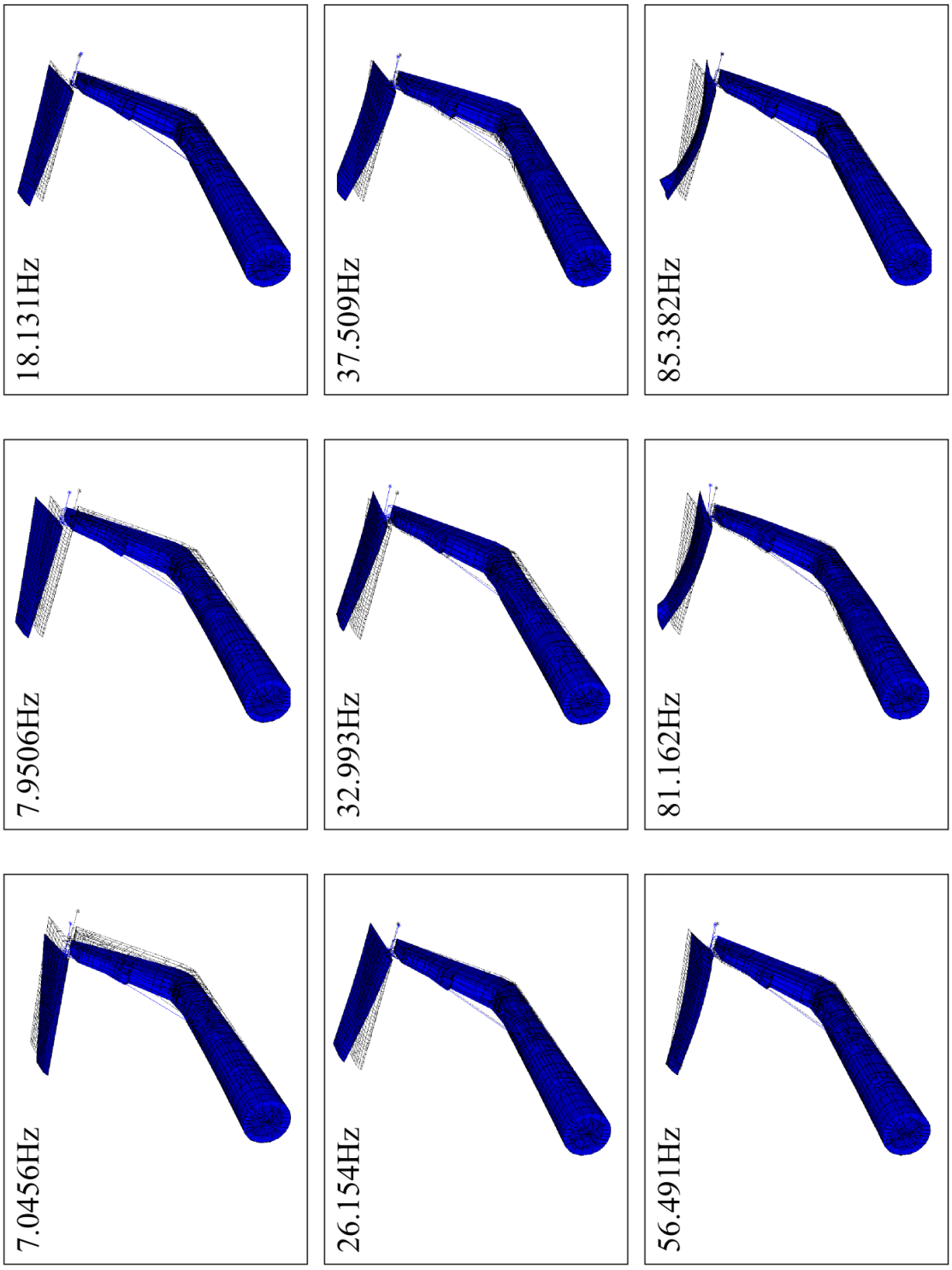

Figure 8.9: Modal results from the ANSYS FE model of the Lynx tail boom.

8.4 Tail Boom Eigenfrequency Control

Examining the mode shapes in figure 8.9 it is clear that the low order modes are the principal bending modes of the tail boom. Consequently, the most effective form of stress stiffening will be that which applies axial loading to the boom, thus reducing the transverse stiffness of these modes as for a simple beam. For these fundamental modes the scheme derived in section 8.2.1 offers little further insight; as all of the elements exhibit transverse motion with respect to the boom axis it would simply confirm that for maximum effect an axial load should be distributed throughout the boom. In contrast, local stresses would serve to soften small sections of the boom but within a safe loading regime this would not have a great effect on the overall stiffness, and thus the effect on the eigenfrequencies would also be small.

In the model the axial loading is established through the attachment of a tensioning wire, or cable, running the length of the tail boom. One end of the wire is attached at the centre of the tail root, with the other attached to a bulkhead toward the aft of the tailboom. The bulkhead has a hole in the centre so to facilitate the wire attachment in the centre a rigid plate is simulated using stiff, light elements spanning the hole. The arrangement is seen in figure 8.10. The tensioning wire is modelled using 10 steel beam elements with a cross sectional area of 0.001m^2 and symmetrical moments of inertia of 10^{-9}m^4; the intention being to simulate a sturdy wire with low bending stiffness. The ends of the wire are pinned at the attachment points.

The first buckling mode is illustrated in figure 8.11. Although hard to discern in the figure, it is found that the failure point is the bulkhead itself, which is not designed to carry loading in this direction. The failure is manifested in the diagram as a deflection in one of the panels connected to the bulkhead. Accordingly, the whole bulkhead is reinforced in the model, transferring the load directly to the cylindrical frame of the boom. The new buckling mode is shown in figure 8.12, where the boom is seen to buckle along its length as expected.

With this configuration, a sensitivity analysis is carried out using the Gradient method of the Design Optimisation tool, discussed in section 2.7.3. The tensioning wire is uncoupled at the root for the static analysis then reattached for the dynamic analysis and two iterations of this procedure are performed for the sensitivity analysis. The results are shown in table 8.2. Examining the mode shapes, it is found that many of the modes are simply localised bending modes for the tensioning wire. Perhaps unsurprisingly, these modes show the greatest sensitivities with respect to the loading.

The ANSYS script was adapted to record iterative modal solutions over successive load steps. Figure 8.13 shows the first 38 frequency loci over a range of loading up to the first buckling load, where the tensioning wire modes are seen to rise steeply while the tail boom modes fall almost imperceptibly. In attempting to separate the two sets of modes, it is found that some modes become coupled where the frequencies are close, such that the sensitivities change rapidly as seen in chapter 4. In such cases the zero-load sensitivities are not representative of the macroscopic behaviour of the tail boom

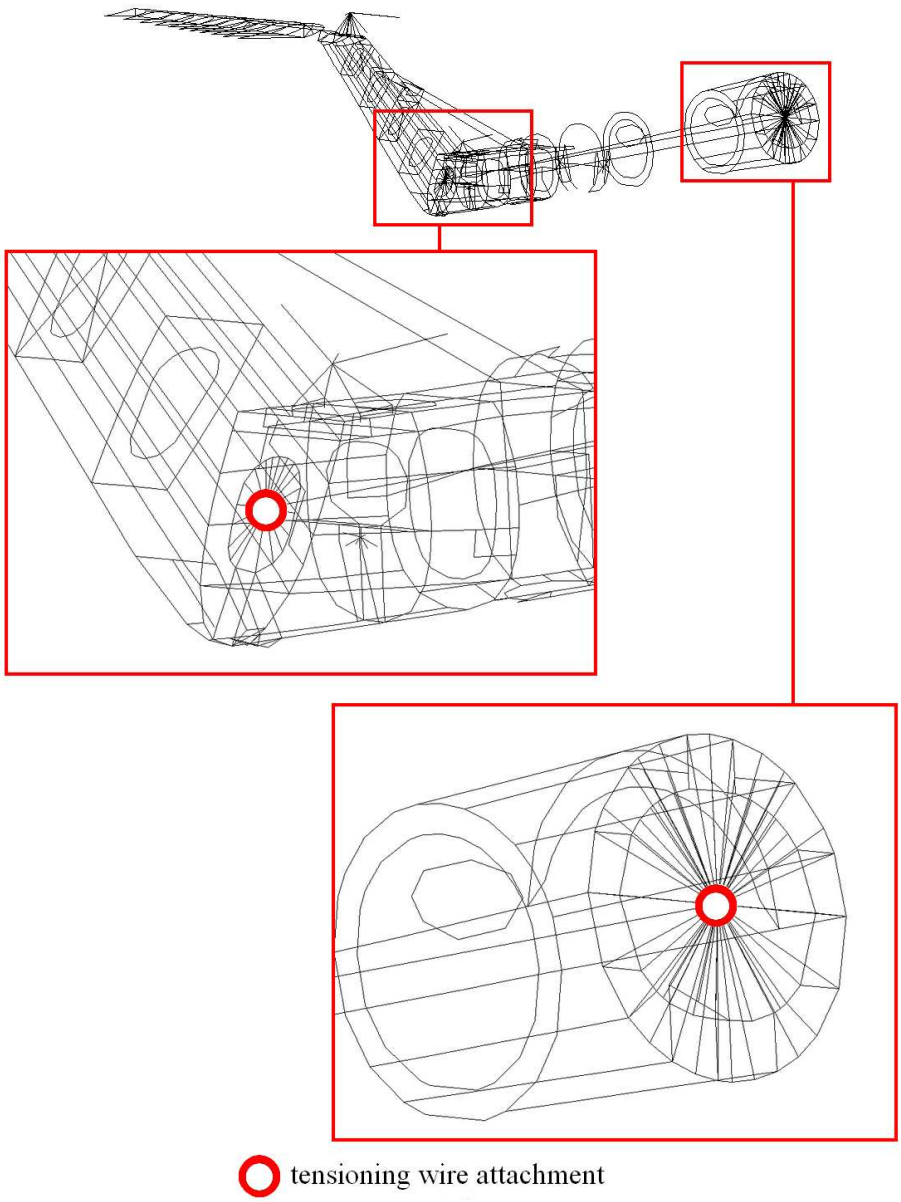

Figure 8.10: Wireframe view of the tail boom model, showing enlargements of the tensioning wire attachment points, at the root centre and reinforced aft bulkhead.

Mode	Freq.(Hz)	Freq. sens.(HzN^{-1})	Mode	Freq.(Hz)	Freq. sens.(HzN^{-1})
1	0.71	1.95×10^{-05}	11	17.68	1.78×10^{-05}
2	0.71	1.95×10^{-05}	12	17.74	1.95×10^{-05}
3	2.83	1.95×10^{-05}	13	18.25	1.66×10^{-06}
4	2.83	1.96×10^{-05}	14	25.52	1.62×10^{-05}
5	6.35	1.91×10^{-05}	15	25.66	1.94×10^{-05}
6	7.13	1.93×10^{-05}	16	26.35	3.17×10^{-06}
7	7.13	4.03×10^{-07}	17	33.48	1.09×10^{-06}
8	7.98	4.82×10^{-07}	18	35.03	1.76×10^{-05}
9	11.32	1.95×10^{-05}	19	35.32	1.84×10^{-05}
10	11.33	1.95×10^{-05}	20	37.79	1.87×10^{-06}

Table 8.2: The first twenty frequency sensitivities for the Lynx tail boom with axial tensioning wire.

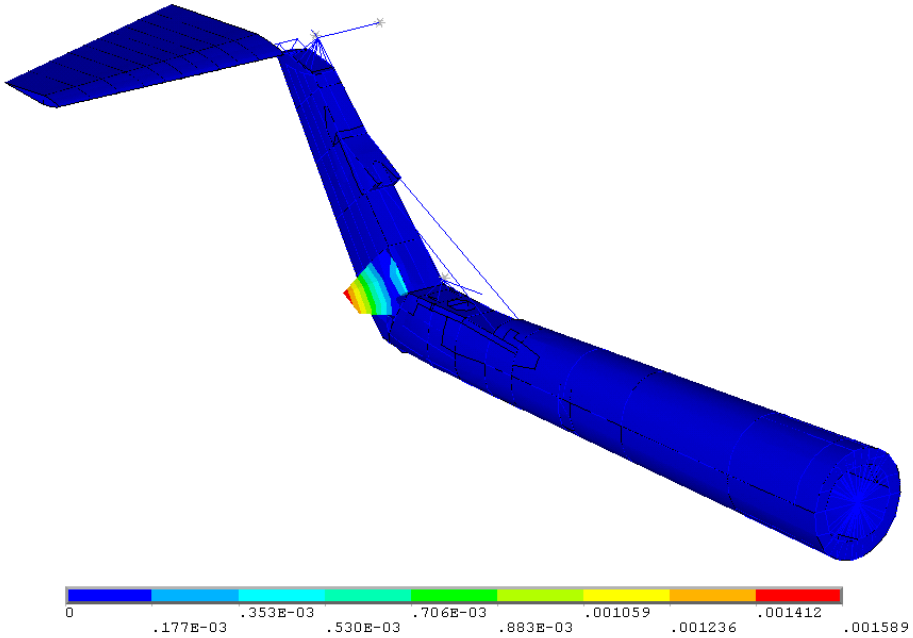

Figure 8.11: First buckling mode of the initial tensioning wire configuration.

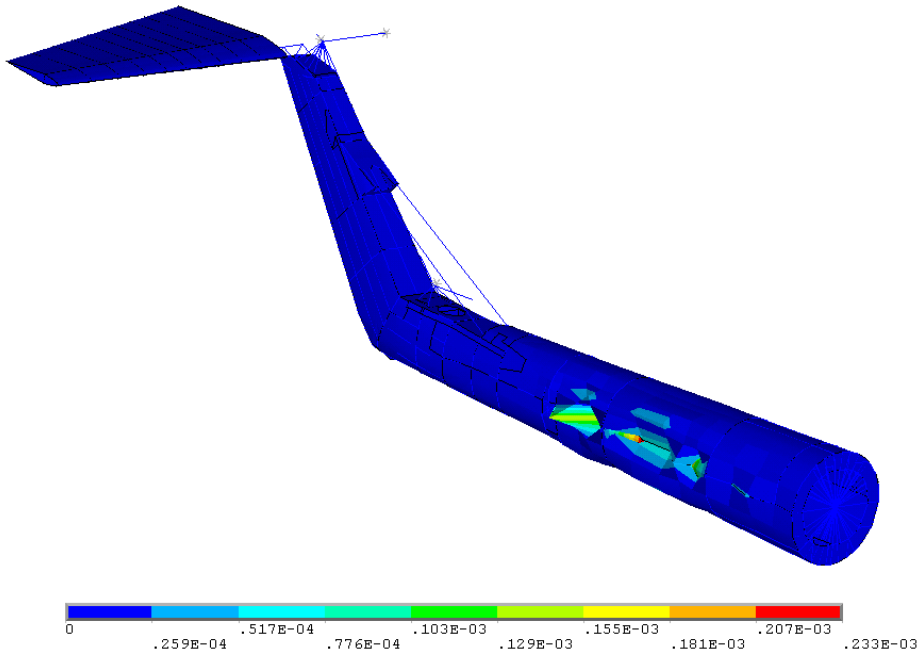

Figure 8.12: First buckling mode of the tail boom with the bulkhead reinforced for the tensioning wire attachment.

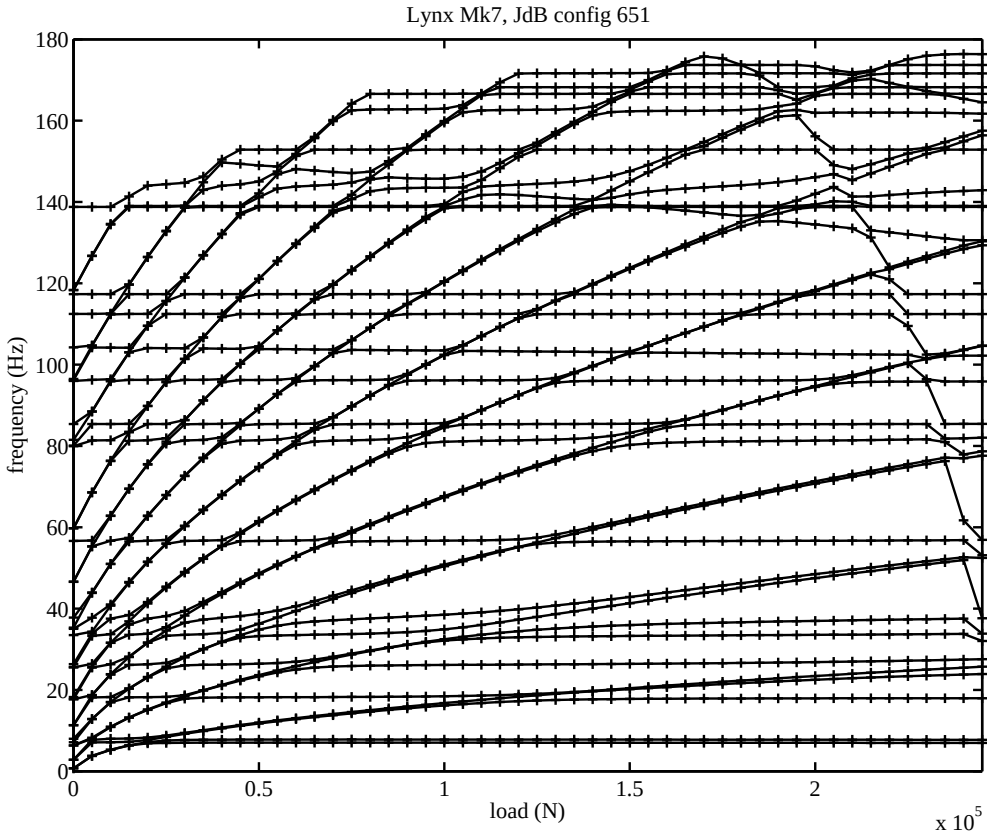

Figure 8.13: The first 38 frequency loci of the tail boom with the axial tensioning wire, loaded up to the first buckling load. Mode tracing has not been employed in the production of this plot.

modes. To quantify the variation of the tail boom modes more reliably, a second sensitivity study is conducted but with the tensioning wire removed from the model and the loads applied directly to the wire attachment points. While the local behaviour at modal intersections can not be modelled this way, the global trends are properly represented. The resulting tail boom frequency sensitivities are shown in table 8.3, along side the loads required to produce 1% and 2% shifts in each frequency (remembering that the eigenvalue perturbations show approximately linear response to the loading).

It is noted that in all of the examples considered, the load required to produce a 1% change in the frequencies is greater than the principal buckling load of 247kN. Examining figure 8.12, the failure mode is seen to be in localised panel buckling. That is, the overall stiffness of the tail boom does not approach zero but instead the stiffness of local sections goes to zero. This is apparent at the right hand side of figure 8.13 where a single frequency locus, representing a localised mode in the buckling region, is seen to drop sharply past the principal bending frequencies of the stucture. Note that mode tracing has not been employed in the production of this figure so the falling mode appears as a series of perturbations to the modes it crosses; whether or not these modes veer is not a question that is addressed here.

The localised failure can be seen as a “weak link” in the buckling behaviour. Unfortunately it imposes severe practical restrictions on the method being implemented here. Several solutions present

Mode	Freq.(Hz)	Freq. sens.(HzN^{-1})	1% shift load (N)	2% shift load (N)
1	7.12	-1.16×10^{-7}	-6.19×10^{5}	-1.24×10^{6}
2	7.98	8.67×10^{-8}	9.25×10^{5}	1.86×10^{6}
3	18.22	-5.17×10^{-8}	-3.54×10^{6}	-7.12×10^{6}
4	26.26	-7.53×10^{-8}	-3.51×10^{6}	-7.05×10^{6}
5	33.47	3.33×10^{-9}	1.01×10^{8}	2.03×10^{8}
6	37.80	-2.51×10^{-7}	-1.51×10^{6}	-3.04×10^{6}
7	56.68	-1.46×10^{-8}	-3.92×10^{7}	-7.87×10^{7}
8	81.37	-2.30×10^{-8}	-3.56×10^{7}	-7.16×10^{7}
9	85.40	-1.42×10^{-9}	-6.04×10^{8}	-1.21×10^{9}

Table 8.3: The frequency sensitivities for the first nine tail boom modes, along with the corresponding loads required to produce 1% and 2% changes in each of the frequencies.

themselves to this problem: firstly, the weak sections could be reinforced. This would likely involve an extensive redesign of the tail, to meet the axial loading requirements of the tensioning scheme. The second solution is to perform a more detailed buckling analysis of each section of the tail and distribute appropriately scaled loading to each section. This could be accomplished with individual actuators or with a mechanical or pneumatic distribution system. The complexity of such a system is, however, beyond the scope of this chapter.

Two further configurations are investigated here: the first is a wire similar to that used previously, but this time applying a compressive axial force to the fin, and the second utilises the existing 8C strut as a tensioning member. The 8C strut is seen in figures 8.14 and 8.15, and was originally introduced to change the torsional stiffness of the tail; thus it was thought that this stiffness may also be sensitive to changes in the tension carried by the strut.

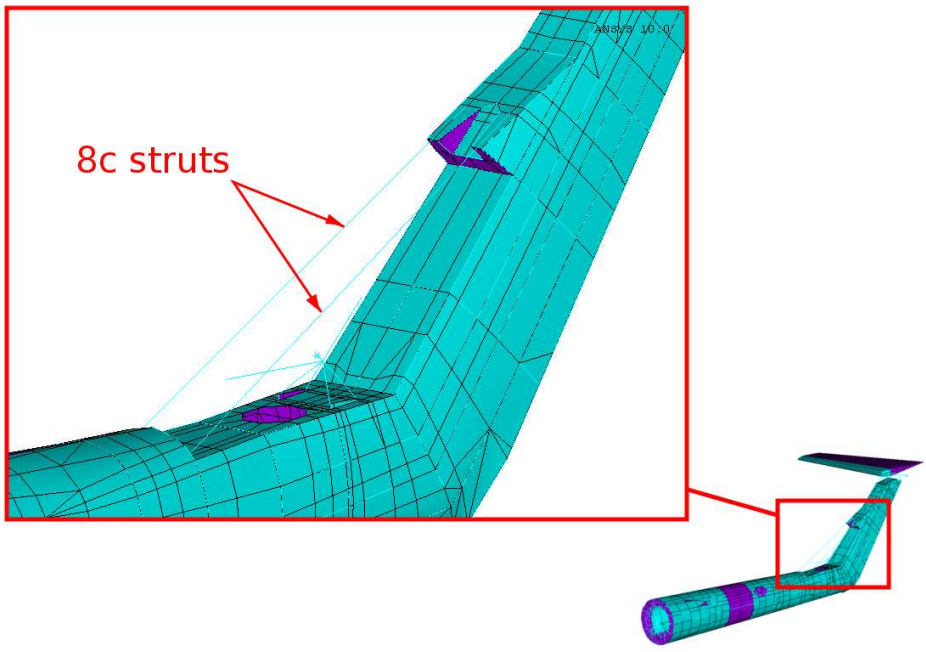

Figure 8.14: The 8c struts connecting the fin to the main tail boom in the FE model.

Figure 8.15: Photograph of the 8c struts spanning the corner between the fin and tailboom.

Mode	Freq.(Hz)	Frequency sensitivity to unit load (HzN^{-1})		
		main boom	fin	8c strut
1	7.05	-1.16×10^{-7}	1.31×10^{-7}	-6.24×10^{-9}
2	7.95	8.67×10^{-8}	-9.42×10^{-7}	-4.77×10^{-6}
3	18.13	-5.17×10^{-8}	-1.20×10^{-8}	-5.61×10^{-7}
4	26.15	-7.53×10^{-8}	-1.43×10^{-8}	-2.59×10^{-6}
5	32.99	3.33×10^{-9}	-5.04×10^{-8}	-3.29×10^{-6}
6	37.51	-2.51×10^{-7}	-8.15×10^{-8}	-5.82×10^{-6}
7	56.49	-1.46×10^{-8}	-1.67×10^{-8}	3.57×10^{-7}
8	81.16	-2.30×10^{-8}	-4.27×10^{-8}	-1.66×10^{-6}
9	85.38	-1.42×10^{-9}	-5.89×10^{-9}	-2.66×10^{-8}
buckling load (N)		246839	117655	7977

Table 8.4: The buckling loads and frequency sensitivities for the first nine tail boom modes, with three different loading configurations. The nominal frequencies listed are those for the baseline tail boom configuration, before adaptation for the attachment of tensioning wires.

The attachment of the wire for the fin loading is shown in figure 8.16. The same approach is taken as before and the same properties used for the wire. As with the first configuration, the buckling mode is seen in figure 8.17 to be comprised of local panel buckling.

For the 8C strut tensioning, the existing member in the FE model is simply uncoupled at one end, the loading applied, and the nodes recoupled for the dynamic analysis. In this case the buckling mode in figure 8.18 is a failure of the 8c strut attachment lug. This occurs at a much lower load than that encountered in the primary load-bearing structures of the fin and main boom.

The buckling loads and sensitivities for all of the schemes in this section are amalgamated in table 8.4. The most effective scheme of those considered is the first, with a tensioning wire running the length of the tail. Using this arrangement, the biggest change in frequency seen before the first buckling load is reached is 0.17% in mode 6.

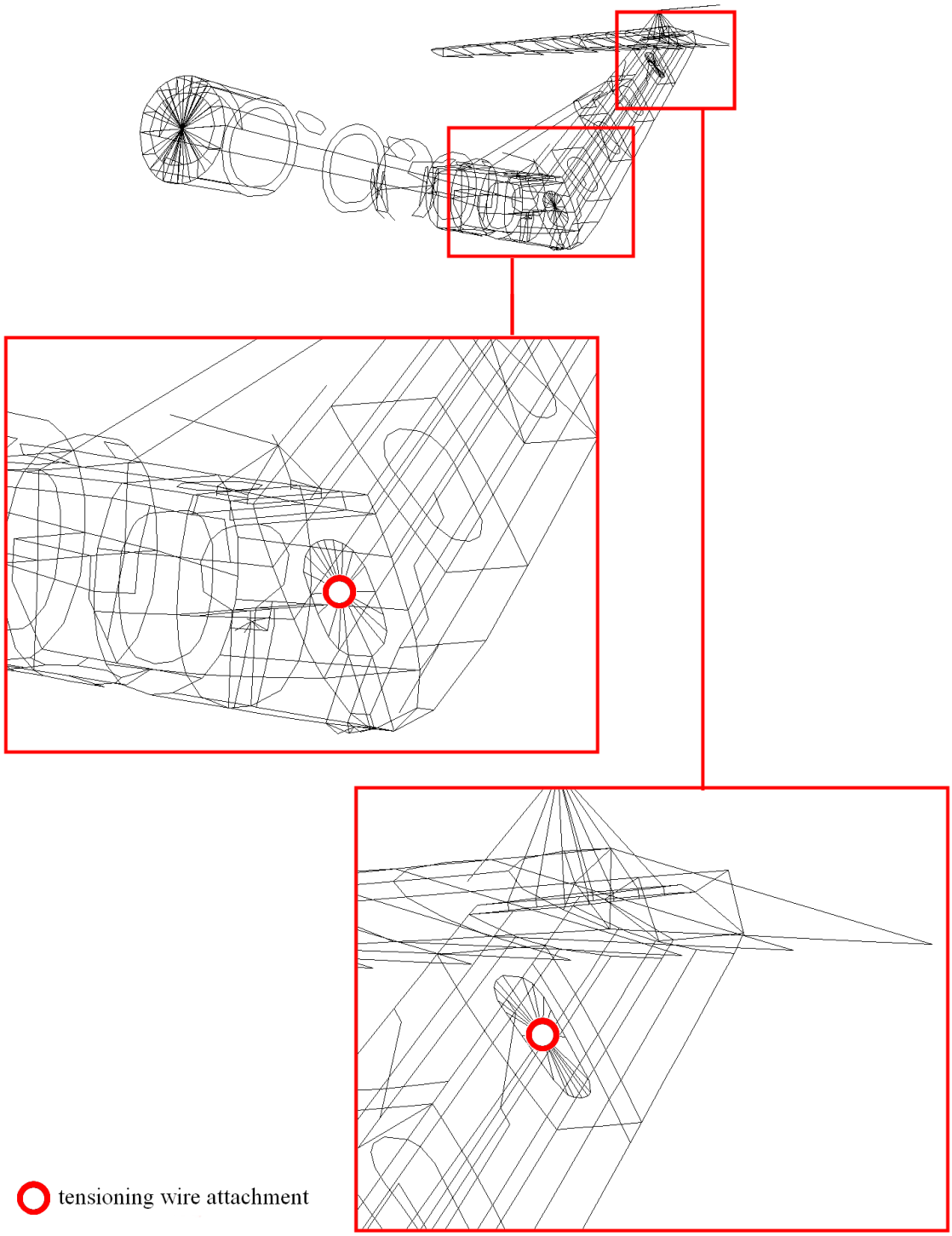

Figure 8.16: Attachment points for the tensioning wire in the fin.

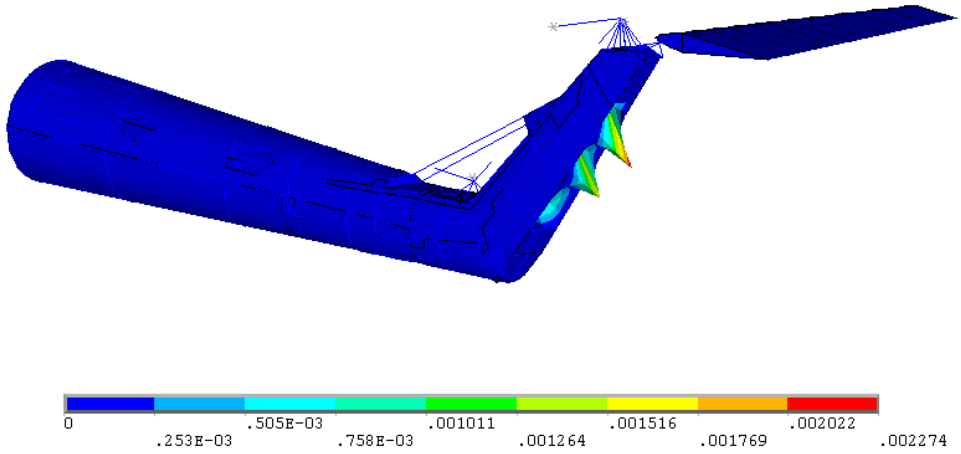

Figure 8.17: First buckling mode for the fin under compression.

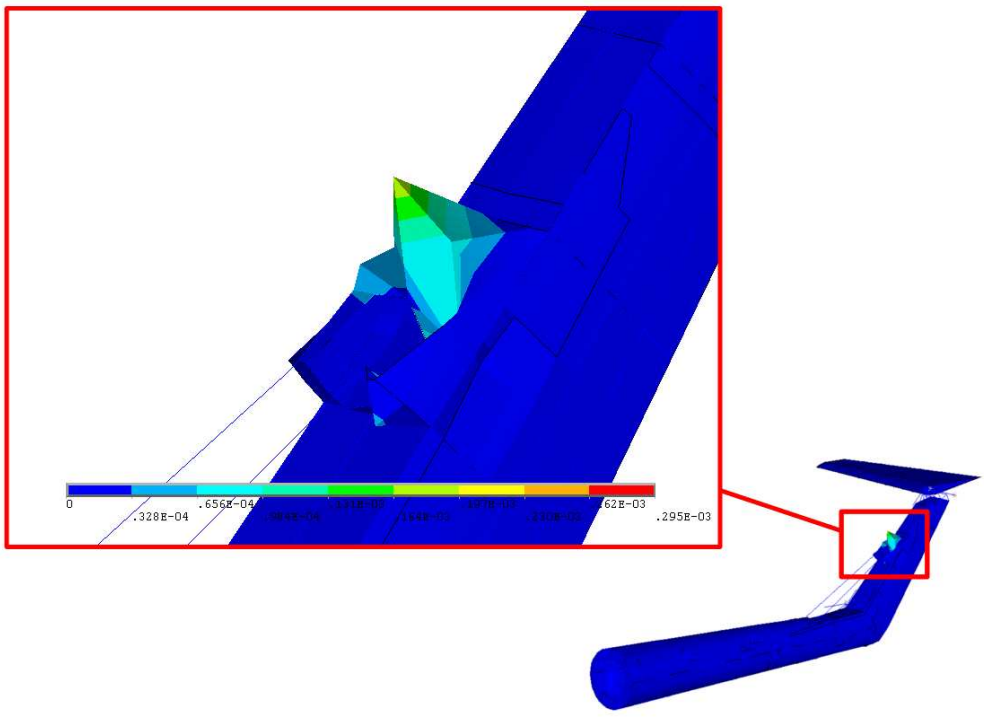

Figure 8.18: First buckling mode with the 8c strut under tension.

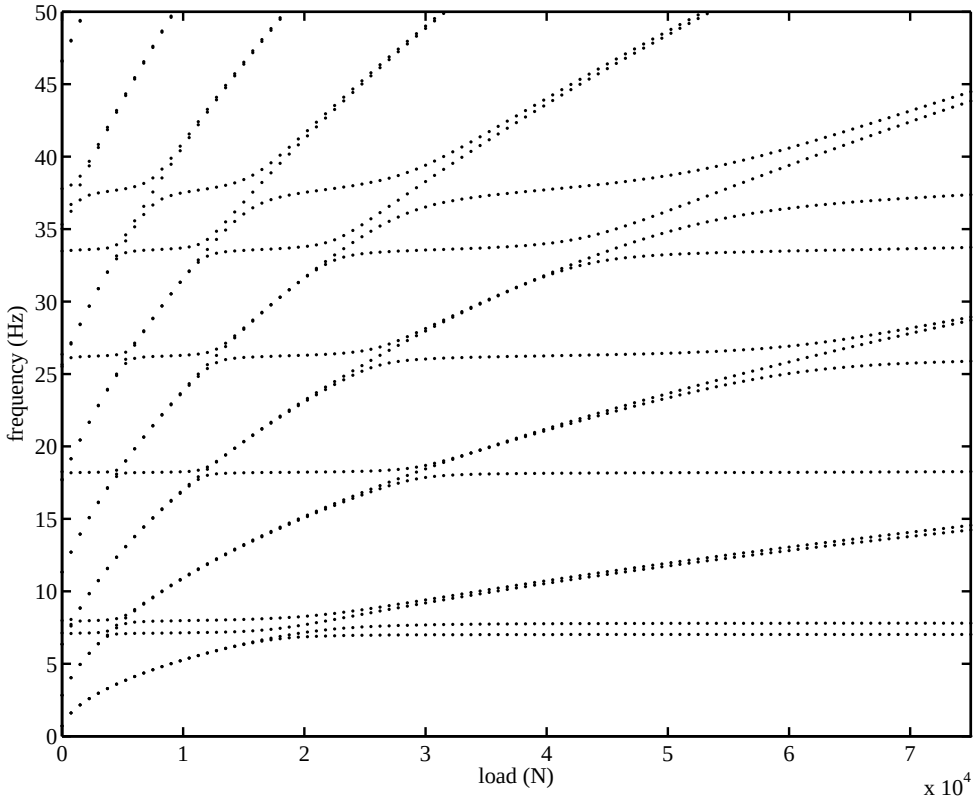

Figure 8.19: Detailed region of the frequency loci for the main tail boom tensioning wire arrangement, with refined load steps.

8.5 Adaptive Tuned Vibration Absorber

Referring once more to figure 8.13, it is noted that the frequency loci intersect in many places. Up until now no efforts have been made to distinguish between veerings and crossings. Focusing on smaller load and frequency ranges, and with greater refinement, figure 8.19 reveals that some of the intersections undoubtedly exhibit veering. It is now clear how the tensioning wire modes interact with the main tail boom modes, altering their sensitivities as noted in the previous section. Following the investigations of chapter 4, it is not uncommon to find antiresonances sandwiched between two resonant eigenvalue curves as they veer, and this section details how this can be exploited for vibration suppression. The technique is effectively that which is applied in tuned vibration absorbers (TVAs), so the section will begin by revisiting this topic.

8.5.1 Tuned Vibration Absorbers: Principles of Operation

Sun *et al.* [274] offer a survey of TVAs, covering passive, active and adaptive systems. In their simplest form, TVAs consist of a supplementary spring mass system attached at a point. The textbook example is that of a single DOF system subject to periodic forcing as shown in figure 8.20. The FRF for the

primary system is seen in figure 8.21, with and without the TVA attached. The mass and stiffness are described by $M = K = 1$ so that without the TVA there is a single resonant peak at $1/2\pi$ Hz. When the spring-mass system of the TVA is tuned such that its own natural freqency matches that of the primary system, the resultant FRF exhibits an antiresonance at that frequency, with two resonant peaks either side. In this example the absorber is described by $m = k = 0.1$.

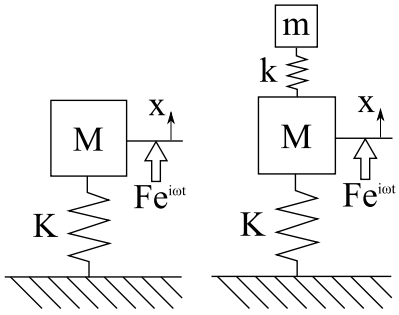

(a) One DOF. (b) TVA added.

Figure 8.20: Textbook tuned vibration absorber example.

The effect of tuning the TVA stiffness is illustrated in figure 8.22(a), where the response of the primary system is seen to vary. As the absorber stiffness is increased the antiresonance is clearly seen rising from 0 Hz to replace the single resonance at $1/2\pi$ Hz. The response of the absorber itself is shown in figure 8.22(b), where there is no antiresonance. Thus, when tuned, the absorber vibrates in place of the primary system. This is not a resonant response, however, and is thus less severe than the vibration it seeks to suppress.

Viewing the 3D FRFs from above while preserving the colour gradient to denote amplitude, the variation of the natural frequencies and antiresonances with the TVA stiffness is easy to distinguish in figures 8.23. From these graphs it is clear that the two frequency curves are veering with respect to one another. Reducing m from 0.1 to 0.01 produces an even clearer demonstration of veering in figure 8.24.

Extrapolating from this system, it is apparent that wherever an antiresonance exists bewteen two modes, if they can be made to veer then the antiresonance will pass between them, thus forming an effective tuned mass damper. This result was highlighted in chapter 4 where figures 3.30(d) and 3.30(e) exhibit instances of the effect. The addition of a dedicated absorber mass to the system is not necessary in this case; one part of the system acts as the absorber, eliminating the vibrations in another. The "sacrificial" part of the structure is not jeopardised because the vibrations are not resonant. It simply constrains the inevitable vibrations to an acceptable locality. This idea is not new: Feng and Mita [275] describe a technique referred to as *Mega Substructure Configuration* where instead of supplementing a building with a spring-mass-damper system, the stiffness and damping properties of an existing substructure are tuned to provide the same effect. The tools of chapters 4 to 6 may offer new approaches to the problem.

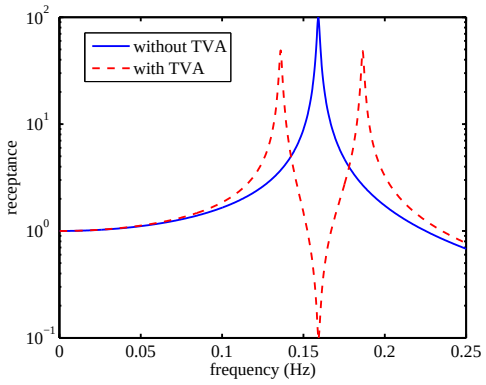

Figure 8.21: FRFs for the primary system.

One of the difficulties with pure undamped vibration absorbers (as opposed to tuned mass dampers, which explicitly include a damping element) is that the device must be tuned accurately to produce optimal results. If the tuning is slightly misaligned, the antires-

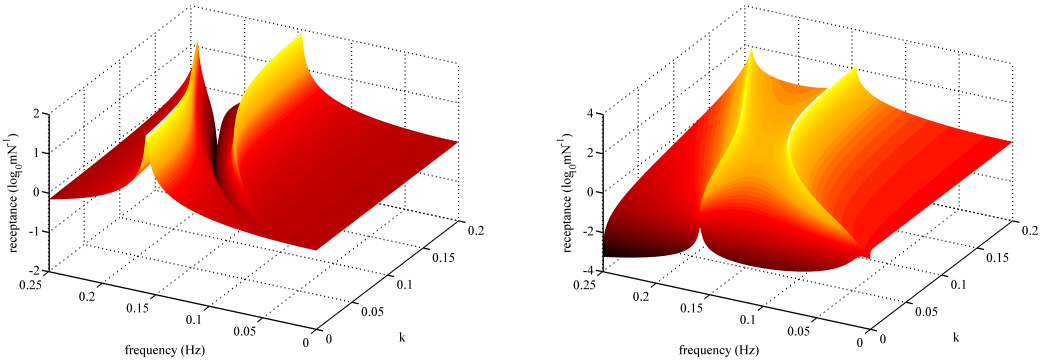

(a) Primary system. (b) TVA response.

Figure 8.22: FRFs for varying TVA stiffness values.

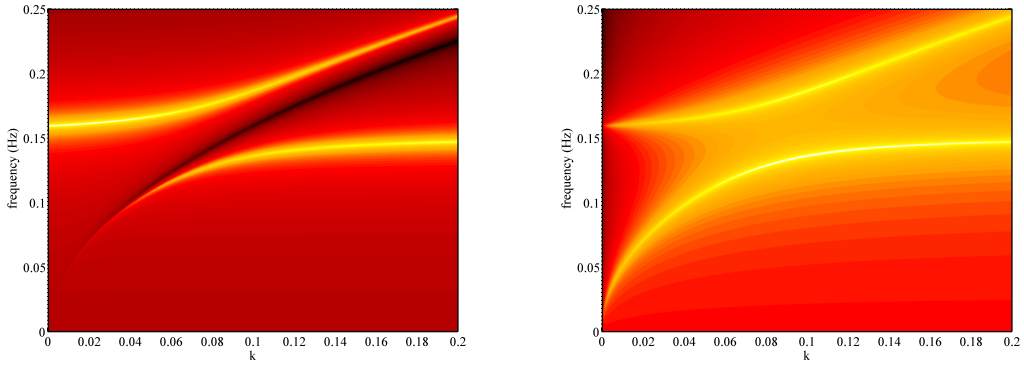

(a) Primary system. (b) TVA response.

Figure 8.23: FRFs for varying TVA stiffness values. TVA mass is 0.1.

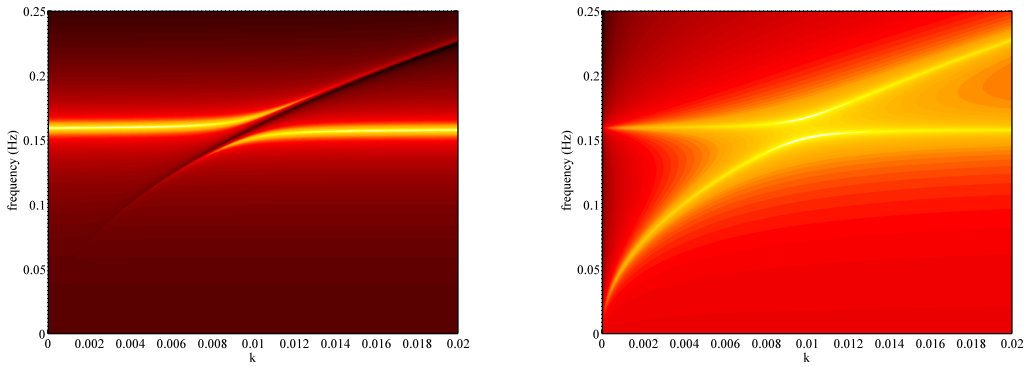

(a) Primary system. (b) TVA response.

Figure 8.24: FRFs for varying TVA stiffness values. TVA mass is 0.01.

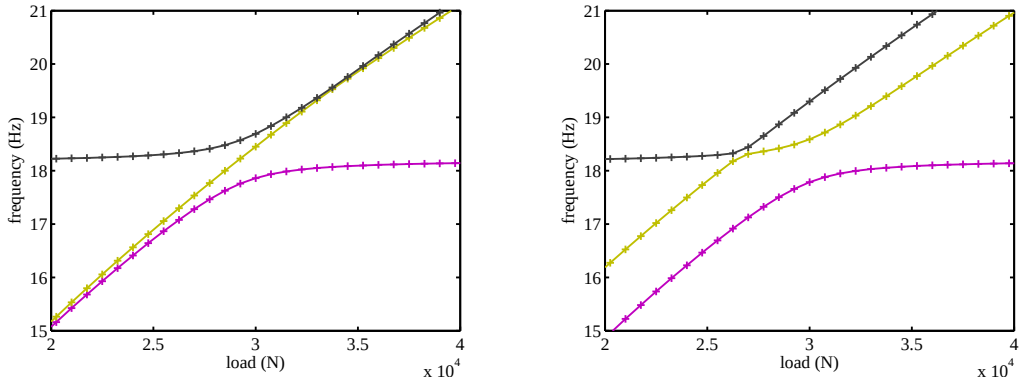

(a) Circular cable.

(b) Eccentric cable.

Figure 8.25: Example of three veering frequency loci, using two different tensioning cable profiles.

onance will not coincide with the excitation frequency. Similarly, if the excitation frequency wanders from the tuned frequency, the response will be adversely affected. In extreme cases the forcing could excite one of the resonances either side of the antiresonance. Recent developments, cited in chapter 1, have explored the concept of adaptive TVAs. Such a device can, in theory, adjust its tuning on line, thus maintaining an optimal response. In figure 8.23(a) the antiresonance is seen to sweep a wide frequency band as the TVA stiffness is adjusted, permitting effective vibration cancellation over a range of excitation conditions.

8.5.2 Adaptive Load Tuning

As loading is applied to the tail boom, it exhibits many veering modes. In contrast to the frames tested in earlier chapters, and the Mega Substructure Configuration method mentioned above, the example considered here *does* involve a dedicated absorber mass. In this case it is not a discrete mass but a distributed mass in the form of the tensioning cable. As with a standard TVA, one of the veering modes is dominated by motion of the absorber mass over the majority of the parameter spectrum (in this case the load range). Thus it is expected that the cable will be capable of functioning as an adaptive TVA, with the axial tension serving to tune the stiffness. The feasibility of this proposition is investigated below.

For the method to be successful it is necessary that an antiresonance runs between two veering modes. Most of the instances of modal interaction observed here are complicated, consisting of at least two concurrent veerings. The resultant effect is one or more loci appearing to "cut across" between two veering loci. An example is framed in figure 8.25(a), showing the veering of the 18 Hz boom mode. The TVAs efforts are hampered by these "double veerings", which place a resonance instead of the desired antiresonance directly between two veering modes. The double veerings occur because the axisymmetric wire has two almost coincident frequencies for each of the principal bending modes. Where these cross another mode, they both veer simultaneously with the third mode and with each other.

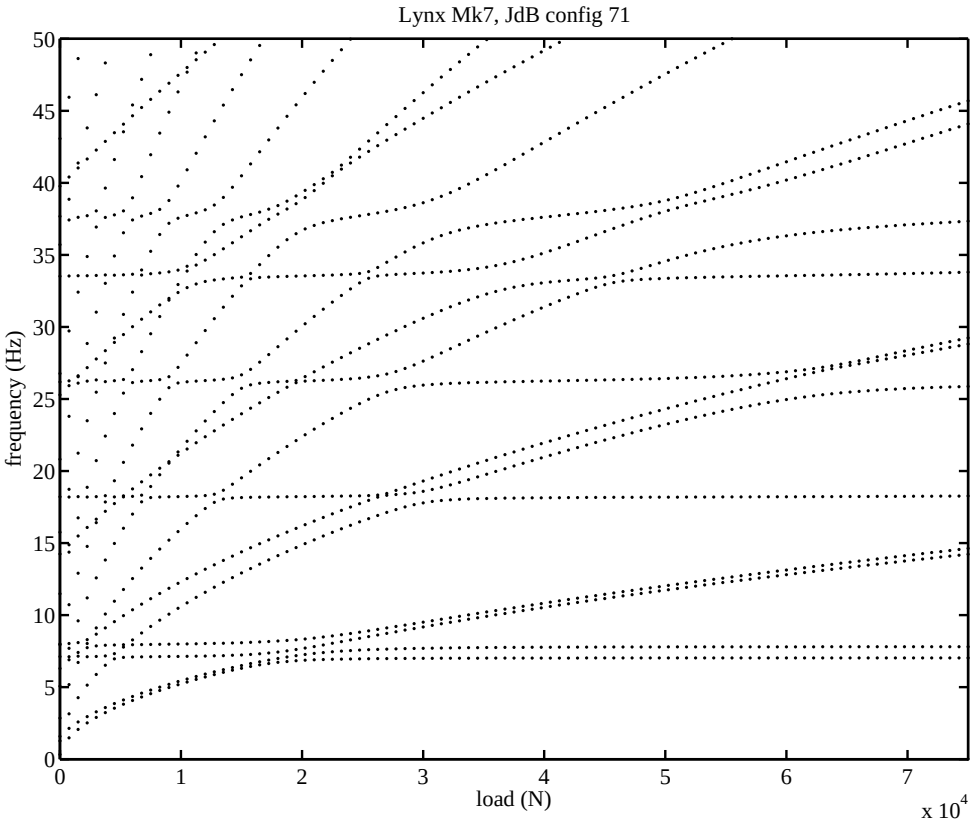

Figure 8.26: Frequency loci of the tail boom with the *eccentric* tensioning wire.

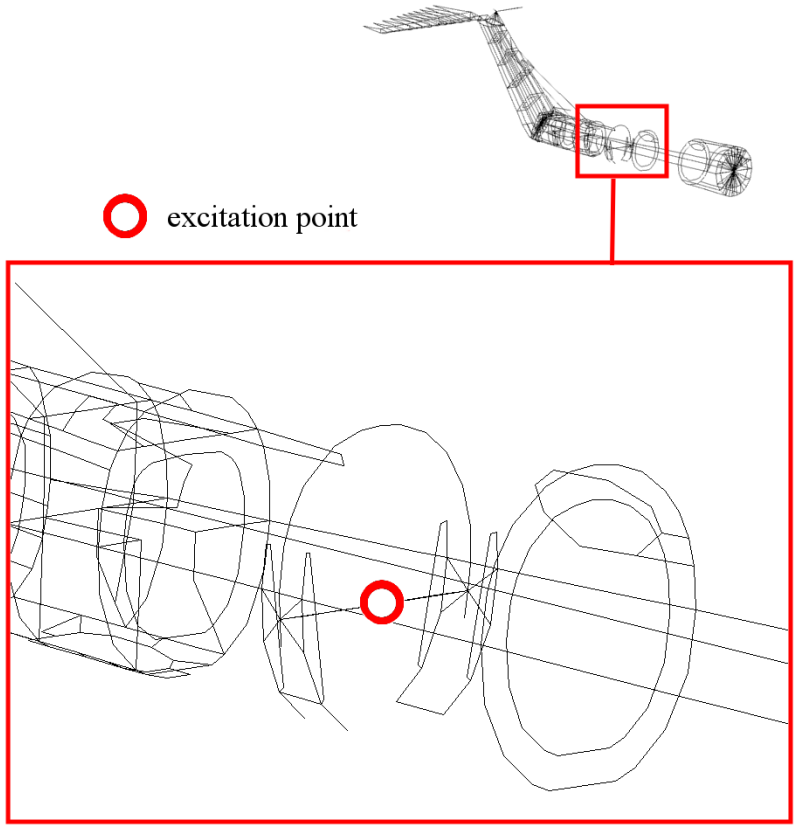

Figure 8.27: The excitation point for the response plots on the lynx tail boom.

To mitigate this behaviour, the symmetry of the wire in the model is broken by quintupling the moment of inertia in the vertical plane and dividing the inertia in the horizontal plane by five. As hoped, there is less interference between the veering modes with each of the wire modes clearly distinguishable in figure 8.26. The 18 Hz example is now seen to produce pure two-mode veering in figure 8.25(b).

Using the asymmetric wire configuration, FRF plots are computed in ANSYS for 100 load steps in the range 0N to 75kN, representing 30% of the buckling load. Point FRFs will inevitably produce antiresonances between all the modes, but the current demonstration is intended to show that the whole tail boom's motion may be repressed. Accordingly, separate response and excitation points are chosen. The excitation is applied at a reinforced section mid-way down the tail, indicated in figure 8.27. The response is measured at the wire attachment point in the aft bulkhead, as described before in figure 8.10.

FRF waterfall plots are seen in figure 8.28 for horizontal and vertical excitation and response measurements. Clearly the interaction of the modes interrupts the resonant ridges. The behaviour of the natural frequencies and antiresonances is better illustrated in the contour plots of figure 8.29. Promisingly, many antiresonances are seen passing between the veering modes. Focusing again on the 18 Hz example, the FRFs can be seen clearly in figures 8.30 and 8.31. Evidently the response can be dramatically reduced by tuning the cable tension, and figure 8.32, shows how the behaviour mimics that of a traditional TVA. Figure 8.33 highlights instances of the effect which could be used to address each of the 6 modes below 50 Hz, all requiring less than 15% of the first axial buckling load of the tail boom. It was hoped that all the modes could be tackled using even lower loading levels, as there are modal intersections at much lower forces, but figure 8.34 shows that the interactions between cable modes and tail boom modes are weaker at lower loads. This is something that could be addressed by increasing the coupling; if the stress stiffening matrices from the FE model are available then the methods of chapter 6 can be used to evaluate changes to the cross section, tapering, and end contstraints of the wire, as well as additional mass or stiffness elements. Unfortunately the stress stiffening matrices are not readily available from ANSYS (hence their re-evaluation for beam elements in the macro described in section 8.2.1). The computation of these matrices and the evaluation of the modal coupling sensitivities would be the starting point for future studies along these lines. As well as reducing the actuation loads required to produce TVA behaviour, another objective could be to reduce the wire mass from the 7.85 kg/m used here.

The system proposed above has an obvious advantage over passive TVAs: the adaptive stiffness provided by the load modulation can maintain optimum tuning in the presence of changeable system configurations, mechanical wear, or variable operating conditions. It also has an apparently unique advantage over other adaptive TVAs on account of the distributed mass and stiffness arrangement. This configuration leads to a theoretically infinite number of absorber modes, each at a different frequency, and each of which can be tuned using the same axial load parameter. As such, the arrangement caters ideally for systems where a selection of modes may be problematic dependent on operating conditions. Using a single system it is possible to address the suppression of any mode in

the primary structure by selecting a nearby absorber load. The use of only one device for this purpose reduces the complexity and weight compared with the combination of adaptive-passive devices that would usually be required to address such a situation.

8.6 Conclusions

This chapter has focused on the application of stress stiffening to response suppression in practical structures. Tools have been developed to determine optimum actuator placements for achieving specific control requirements, and strategies have been proposed for the independent deterministic control of multiple modes.

An FEM analysis of the Lynx tail boom was undertaken with the objective of identifying a means of suppressing response levels for the low frequency modes, close to the rotor frequency of 22 Hz. These were found to be low order bending modes of the tail, making the most effective loading configuration an axial compression of the whole tail boom. The analyses show that significant alterations to the natural frequencies can not be achieved without inducing local panel buckling: a compressive load of 3.5×10^6 N produces a 1% change in the 3th and 4th modes, nominally at 18Hz and 26Hz, but local panel buckling first occurs at 2.5×10^5 N.

An alternative strategy is proposed, employing a tesioning cable running the length of the tail boom as a tuned vibration absorber. The absorber can be adaptively tuned by modulating the tension. A novel aspect of this configuration is that the distributed mass in the cable produces multiple absorber modes, allowing the absorber to be tuned to a selection of tail boom modes using only a narrow force band. The FE model has successfully demonstrated the application of these concepts to suppress the first 6 vibration modes, covering the 0–50 Hz range.

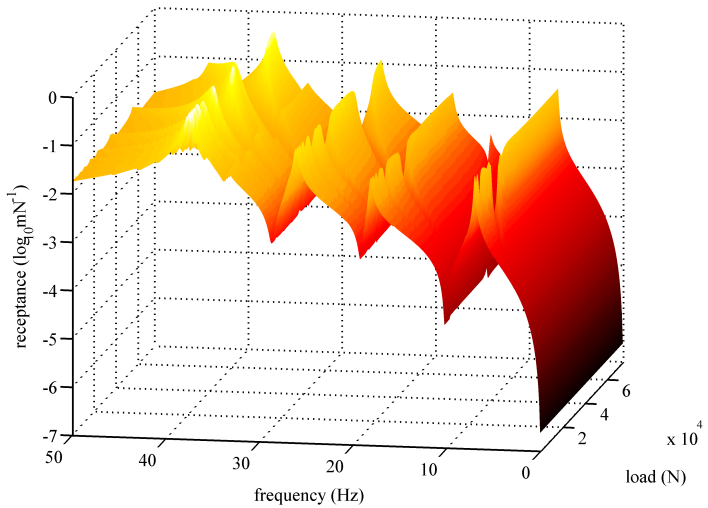

(a) horiz-horiz

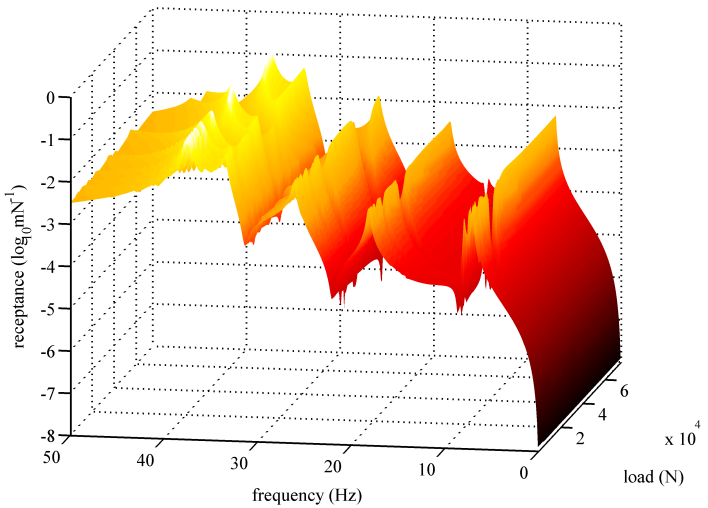

(b) horiz-vert

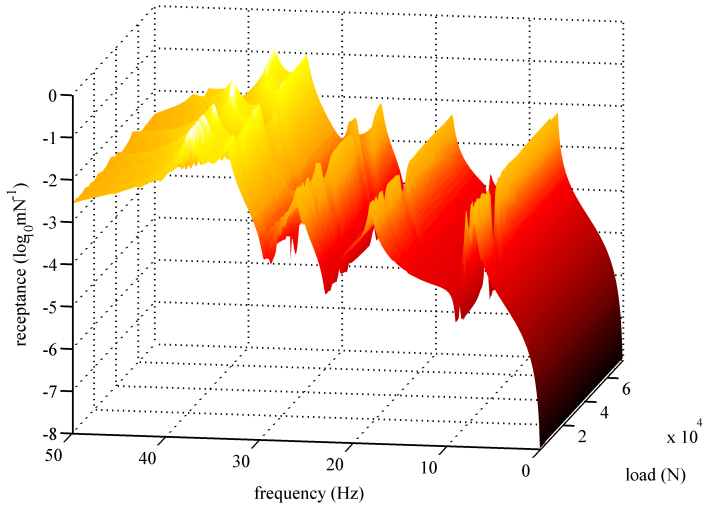

(c) vert-horiz

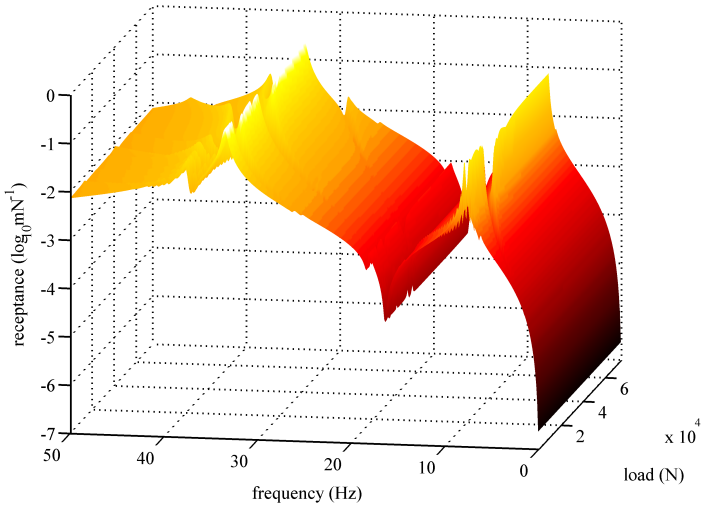

(d) vert-vert

Figure 8.28: Waterfall plots showing the variation of the FRFs with load, up to 30% of the first buckling load. Captions indicate excitation-response.

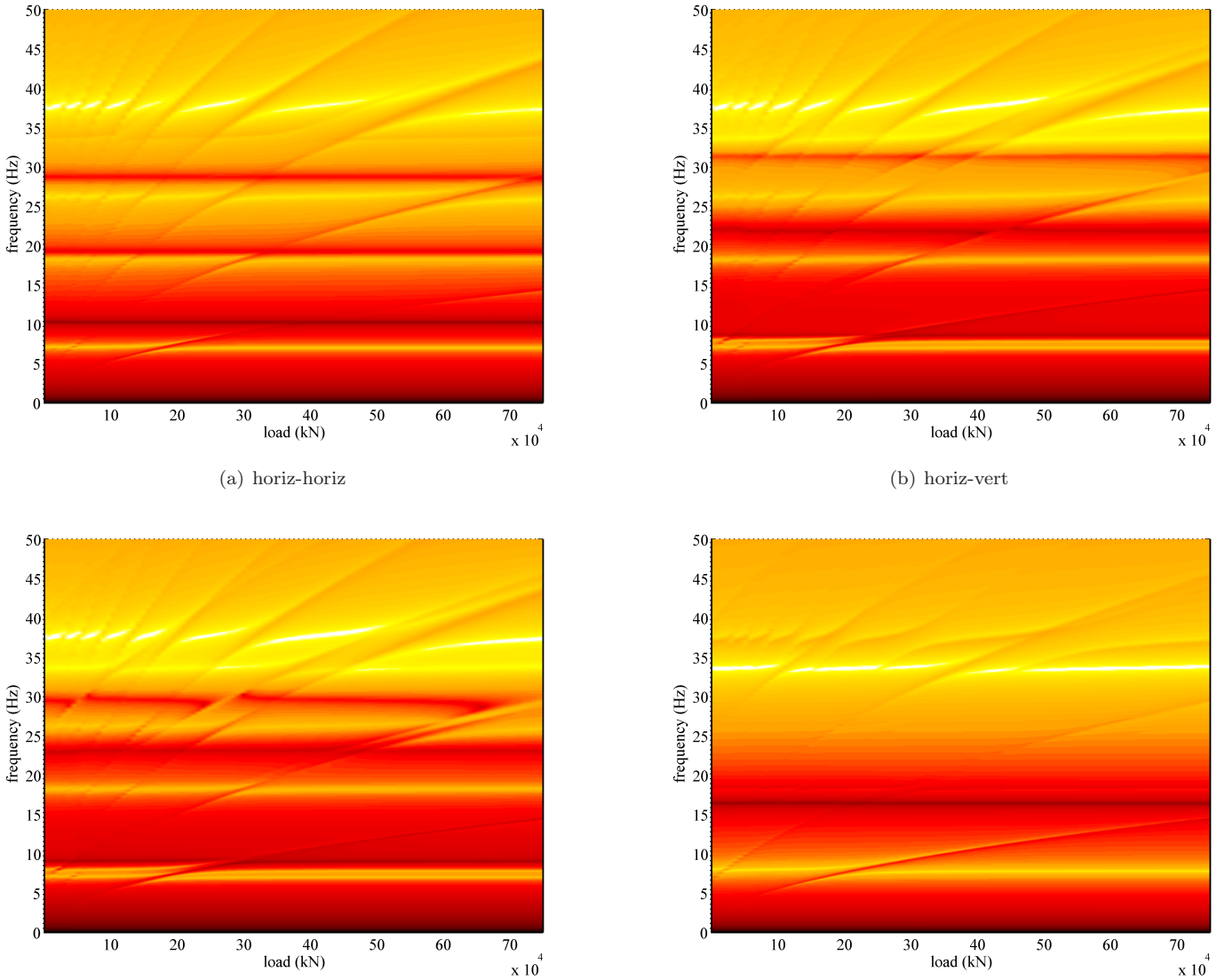

(a) horiz-horiz

(b) horiz-vert

(c) vert-horiz

(d) vert-vert

Figure 8.29: Response contours for the tail boom for loads spanning 30% of the first buckling load. Light regions denote high response. Captions indicate excitation-response.

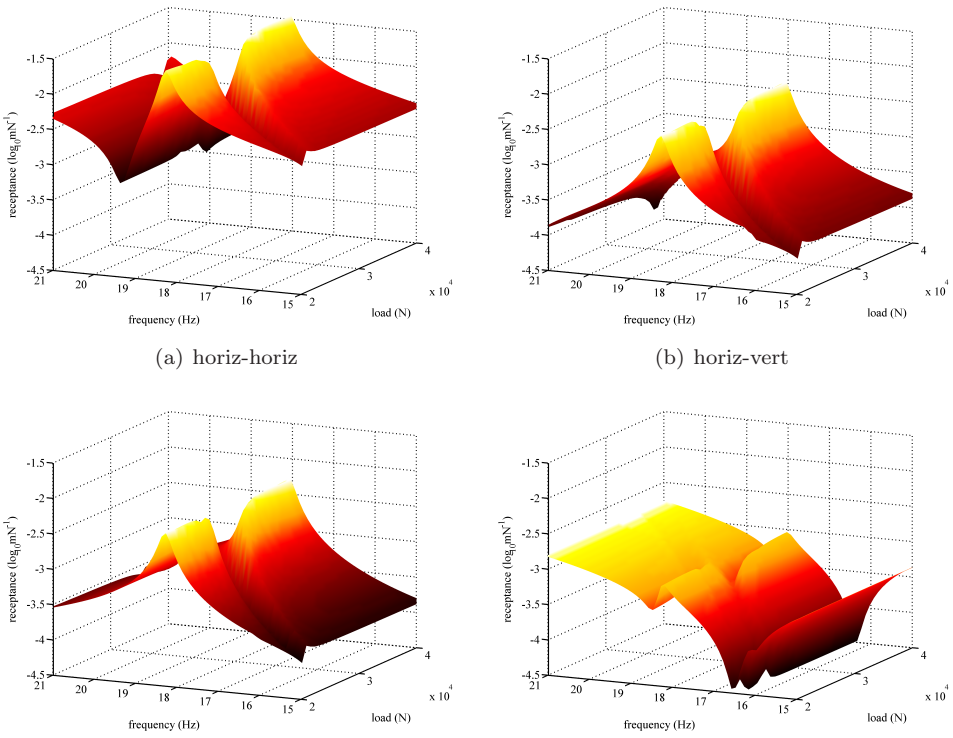

(a) horiz-horiz (b) horiz-vert

(c) vert-horiz (d) vert-vert

Figure 8.30: Waterfall plots for the 18 Hz mode. Captions indicate excitation-response.

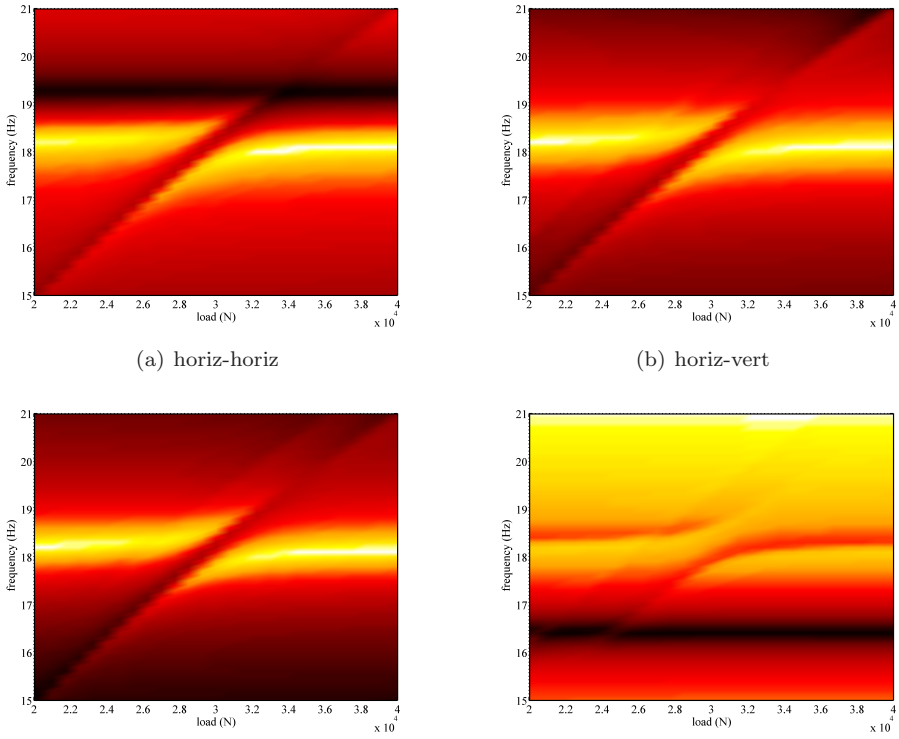

(a) horiz-horiz (b) horiz-vert

(c) vert-horiz (d) vert-vert

Figure 8.31: Response contours for the 18 Hz mode. Light regions denote high response. Captions indicate excitation-response.

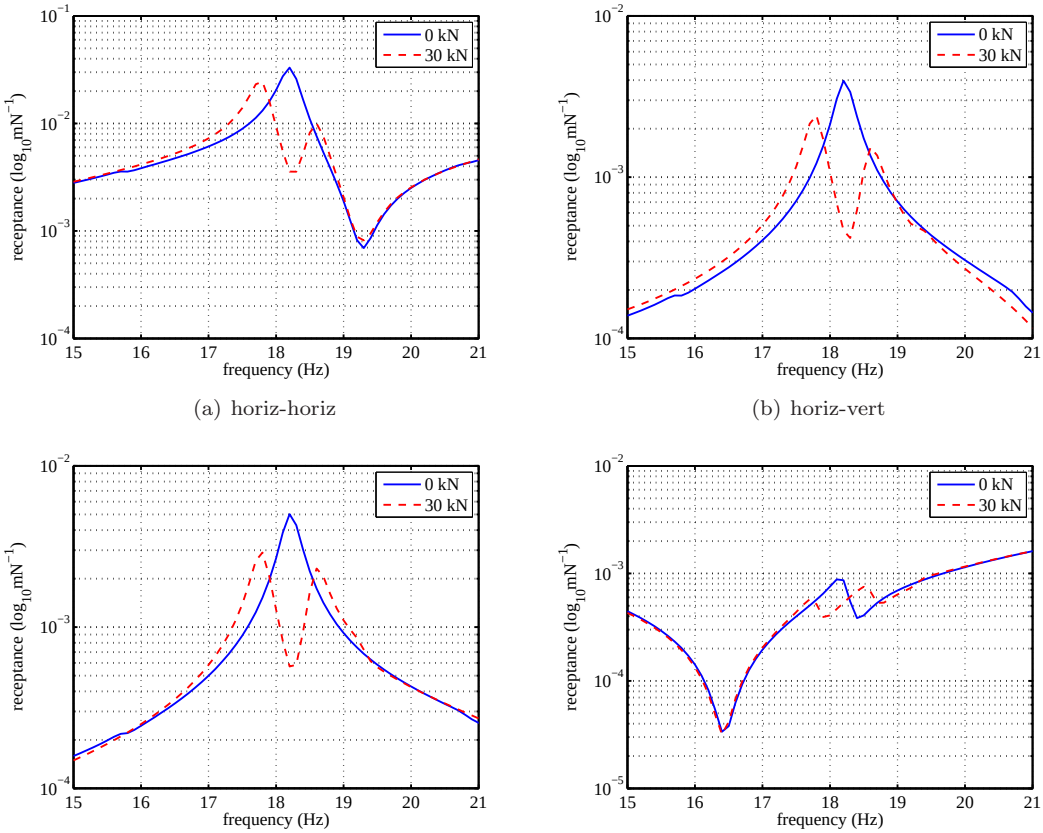

(a) horiz-horiz

(b) horiz-vert

(c) vert-horiz

(d) vert-vert

Figure 8.32: Illustration of the 18 Hz modal interactions mimicking a traditional TVA. Captions indicate excitation-response points.

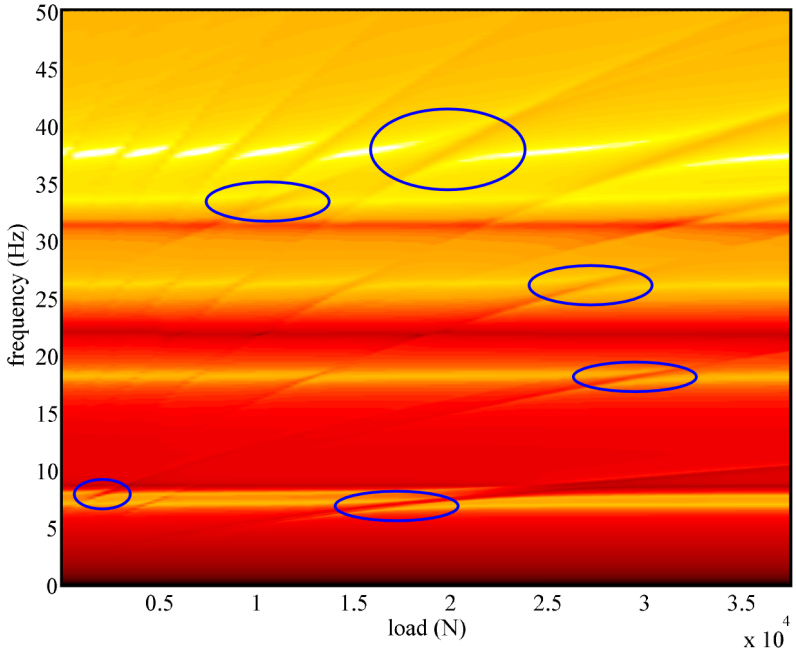

Figure 8.33: Examples of suitable response regions for TVA implementation. Antiresonances bisect the natural frequencies in the highlighted regions.

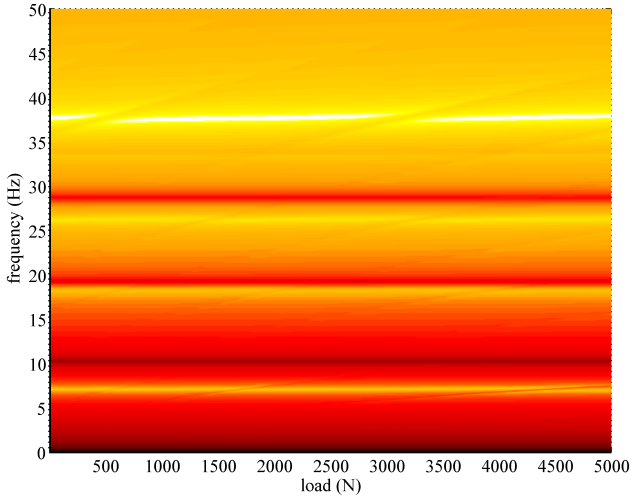

(a) horiz-horiz

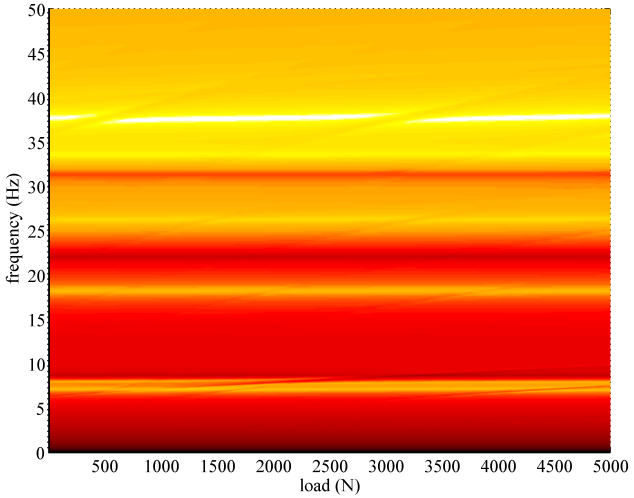

(b) horiz-vert

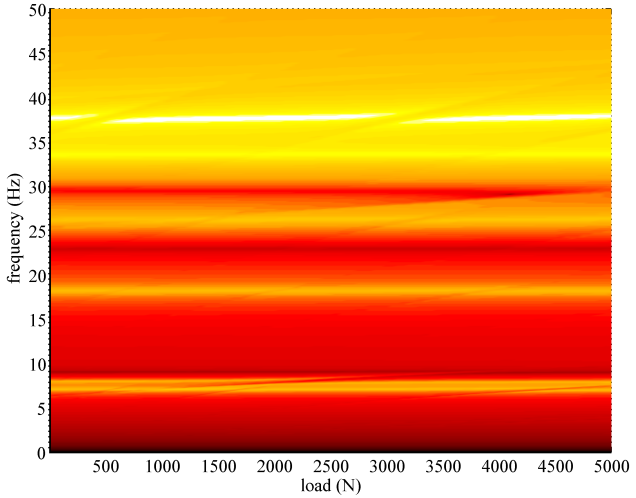

(c) vert-horiz

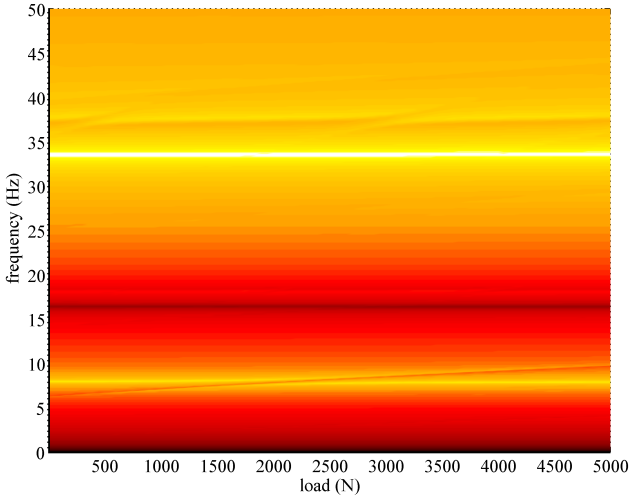

(d) vert-vert

Figure 8.34: Response contours for the 0–5 kN range.

Chapter 9

Conclusions and Future Work

In chapter 1 the goals of this thesis were set out. The objective was to investigate the possibilities of using structural loading to beneficially manipulate dynamic response. The desired outcome was the proposal of methods that could be employed in an adaptive control scheme to reduce vibration levels in rotorcraft.

Existing work in vibration control has focused on three principal methodologies: passive, active and adaptive techniques. The former are the longest standing and designs have evolved close to the performance limitations of the technology. The benefits offered by active methods are already being exploited in today's rotorcraft and much work in the field has been, and continues to be, focused in this area. In comparison, adaptive methods offer the advantages of lower power requirements and greater stablity; as such they have been the subject of recent research in many engineering sectors, but have yet to find favour in aerospace applications. Amongst the myriad adaptive methodologies being investigated, the idea of using internal loading to this end has been largely overlooked. The mechanisms by which loading affects dynamic response are well understood, but the system-wide implications are again something that has received only limited attention.

The approach taken here was to first perform a full investigation of the influence of loading on dynamic response. The preliminary examinations of the behaviour in chapter 3 verify the theoretical models, explore the applicability of several simplifying assumptions, uncover some unforeseen effects and identify charcteristics of the behaviour which may be exploited in novel response control techniques.

In the early studies, modal interactions are identified as an important feature of the response variation, and chapters 4–6 present extensive investigations into the phenomenon of eigenvalue curve veering and the related eigenvector transformations. Experimental and numerical studies are described in chapter 4, which goes on to derive tools for the identification and quantification of the behaviour. Chapter 5 considers the physical manifestations of curve veering, and compares the indices developed in the foregoing work to contemporary metrics. The veering studies are concluded in chapter 6 with a practical exposition of the concepts, applied to the solution of an otherwise onerous class of finite element model updating problems.

Building on the theoretical basis of the early chapters, a proof-of-concept demonstration of an adaptive response suppression system is developed in chapter 7. The analytical and experimental investigations then culminate in the evaluation of adaptive response suppression methodologies for rotorcraft deployment in chapter 8. The finite element studies from the Lynx helicopter tail boom show promising results for an adaptive tuned vibration absorber concept employing a stress-stiffened cable.

A detailed synopsis of the significant findings is given below. The contributions made to the field are grouped under the four main topics of the research: general stress stiffening, eigenvalue curve veering, adaptive response tuning, and rotorcraft-specific implementations. The final section explores directions for future work arising from the thesis.

9.1 Stress Stiffening Investigations

Using simple structures to eliminate sources of uncertainty, a range of numerical methods have been tested. Where mildly nonlinear regions are encountered, the most computationally efficient scheme was found to consist of large load steps and Newton-Raphson iterations. For linear static loading regimes, however, the powerful simplification offered by the assumption of a linear variation in the geometric stiffness has been found to be justifiable. This is important in the application of the analytical tools and control schemes developed in this thesis.

An already well-established concept within structural dynamics is that of uncertainty in the modelling of joints. The studies here have not only highlighted the relevance of these concerns in even the simplest of assemblies, but have undertaken inquiries into a seldom documented fork of this body of research. The investigations relate to the effects of loading on joint parameterisation. It is common practice to represent complex joint interfaces with a reduced set of parameters, and much attention has been devoted to the accurate characterisation of their behaviour in this manner, yet none of the literature sets forth a standard approach for modelling the variation of joint parameters with load. The studies of section 3.3 demonstrate that loading has an important and systematic effect on the joint parameters. The influence of these variations is of comparable significance to stress stiffening in beams, plates and shells, and as such it makes a critical contribution to any dynamic model of a loaded structure. Although not the first of its kind, the work conducted here presents one of few joint loading models in the literature: in this case that of a stressed pin joint. The demonstration invites the development of further joint loading models to form part of a standard approach, complementing the established geometric nonlinear methods.

The most pertinent results from the stress stiffening studies, with respect to the objectives of the thesis, are presented in section 3.4. They establish the viability of manipulating both the resonances and the antiresonances of a structure through internal loading, and highlight some special cases involving curve veering that are exploited in later chapters.

9.2 Eigenvalue Curve Veering

Despite historical doubts over its existence and more recent allusions to its irrelevance, eigenvalue curve veering has found application in niche fields and is beginning to show universal application with the increasing trend towards parametric analyses. Much of the difficulty in understanding its importance is associated with the difficulty in its detection in experimental data. Abrupt instances of the behaviour are easily overlooked or discounted as erroneous, while more gradual instances may appear unremarkable. In contrast, however, its presence has been shown to have a marked effect on system response under certain configurations. In section 4.3, explicit experimental evidence demonstrating its manifestation has been presented for the first time.

Some efforts have been made in the literature to develop methods for the identification of veering, but with no rigorous definition of veering available these methods are ambiguous at best, and often misleading. Section 4.4 considers the factors that contribute to the behaviour, and derives physically meaningful properties to quantify it. Three normalised criteria presented: the *modal dependence factors* (MDFs) quantify the confinement of a mode to the veering subspace, and thus measure the extent to which two modes *can* veer. The *cross-sensitivity quotient* (CSQ) compares the eigenvector alignment with the veering datum vectors to give a measure of the instantaneous intensity of veering. Combining the two MDFs and the CSQ produces a *veering index*, which is the first and only indicator available for definitive identification and quantification of veering.

In chapter 5, the ideas behind the veering index are used to create a set of tools for determining the modal properties at the veering datum. The datum properties can be computed from the results of a single eigensolution, which does not itself need to be computed at the veering datum, and properties such as the datum eigenvalue separation can be used to provide a dimensionalised measure of the modal coupling. Instead of describing the local coupling for an arbitrary parameter configuration, the datum properties give a more meaningful, holistic description of the degree of modal interaction. The chapter finishes with an evaluation of the new veering index and the datum property computations, and compares them to other contemporary metrics. The comparison highlights the clear advantages of the new methods.

One application of these holistic coupling descriptions is in finite element model updating. In particular, the eigenvector rotation rate achieves a maximum at the veering datum and this datum value has been shown to to offer the most complete measure of the modal coupling. The vector rotations, and hence veering, have not only a magnitude but also a sign with respect to a set of reference vectors, and this feature allows the property to differentiate between equivalent parameter perturbations in symmetric systems. Chapter 6 describes a novel updating procedure based on the vector rotation rates. Importantly, the methods use *quantitative* information only from the eigenvalues, which can be determined with relative certainty, and augment this with *qualitative* information from the eigenvectors. The scheme demonstrates robust differentiation between symmetric parameters, and arrives at a unique solution to an otherwise ambiguous updating problem.

9.3 Adaptive Response Tuning

An adaptive response suppression strategy is presented in chapter 7, using an embedded actuator to effect stress stiffening. The reduction in response is achieved by manipulation of the natural frequencies and antiresonances, whose positions are stipulated based on estimates of the narrowband excitation frequency. The required actuation for a given excitation is determined from FRFs obtained in pre-operational tests, and the system is fully automated with the excitation as the only external input. The adaptive system operates at a lower bandwidth than fully active implementations, giving it advantages in terms of reduced power requirements and inherent dynamic stability.

The primary objective of the deployment was resonance avoidance; this target was met in both the preliminary test results of section 7.6 and the final tests in section 7.8. A secondary objective was to position antiresonances to produce further benefits at key locations. This task was found to be difficult to implement in the preliminary tests, due in part to the accuracy of the measurements, and also to the variability in the structural response characteristics over the course of the tests.

The compromises made to the primary objective in trying to meet the secondary objective were not justified by the performance gains, so the final tests were instead focused solely on resonance avoidance. Generalising on the scope of the earlier tests, the results in section 7.8 show that an active element is capable of influencing the response of a structure at locations that are both distant from the actuator and outside the load path of the actuator. The successful proof-of-concept experiments are thought to be the first demonstration of stress stiffening effects applied to the adaptive control of vibration.

9.4 Rotorcraft Implementation

The final chapter of work in this thesis applies all the tools and methods developed in the foregoing studies to the problem of rotorcraft dynamics. The analyses are conducted using an FE model of a Lynx Mk 7 helicopter as a test case.

Before embarking on the helicopter studies, section 8.2 sets out a general methodology for the design of stress-stiffening based adaptive vibration control systems. An important development to come out of the discussions is the *stress stiffening influence diagram*. Section 8.2.1 outlines the method for producing the diagram, which gives a visual representation of the influence of stress stiffening in each of the structural elements on the variation of each of the natural frequencies. The resulting diagram is shown to contribute valuable information to preliminary assessments of actuator placements.

The Lynx studies are confined to the tail boom, in order that existing experimental data from the boom can be used to validate the model. In section 8.3 the low order modes are seen to be well correlated. Three configurations are tested for the load-based response tuning demonstration. Two of these arrangements employ supplementary tensioning wires to apply global compressive forces to large

sections of the tail: firstly to the main boom and secondly to the tail fin. The third arrangement takes advantage of the existing 8C struts between the fin and boom to apply loading. All three methods produce changes in the dynamic response, with the main boom wire effecting the greatest change per unit load. A significant obstacle in the application of this technique, however, is the manifestation of local panel buckling modes. In section 8.4 it is found that the loads required to produce a 1% change in the natural frequencies were generally an order of magnitude higher than these buckling loads. This observation effectively precludes the implementation of the technique, unless a distributed loading system is introduced along with the associated weight penalty.

Instead of pursuing the direct manipulation of the natural frequencies, section 8.5 reports a different approach. A useful discovery emerging from the preceding studies is that the vibration modes of the tensioning wires interact with those of the tail boom itself to produce veering eigenvalue curves at the intersections. These interactions can mimick the effects of a tuned vibration absorber (TVA), with the advantage of being continuously tunable through adaptive tensioning of the cable. Furthermore, and in contrast to traditional TVA configurations, the cable has a distributed mass which results in multiple absorber modes. It was demonstrated that over a load range of less than 15% of the buckling load, all of the modes under 50 Hz can be cancelled by adaptively tuning the nearest cable mode to each natural frequency. Thus the adaptive TVA can ensure a minimal response for any excitation frequency in this band.

9.5 Future Work

The work described in this thesis has opened many lines of inquiry, and finite time constraints have necessarily curtailed the investigations. A selection of the most fruitful prospects for continued development have been identified, and these are outlined in turn below.

9.5.1 Stressed Joint Models

The early studies on stress stiffening in chapter 3 demonstrated a need for sensible loaded joint models. While stress stiffening in beams, plates and shells is well understood, the effects of loading on joints is generally neglected in nonlinear solutions. The new work has shown that the influence of joint loading effects on the dynamic response is important, and the ability to model the dynamics of stressed structures will be contingent on accurate load-sensitive joint modelling. It is suggested that future investigations are focused on creating a standard approach to modelling stress-induced stiffening in joints, such that the effects may be conveniently included in geometric nonlinear solution methods.

9.5.2 Veering Index

The veering index and related criteria developed in chapter 4 have been shown to provide valuable descriptions of the interactions between modes. The current derivation is limited in scope, however, and to provide a universal tool the analysis should be extended to non-self-adjoint eigenproblems, and those involving damping. These generalised methods will need to embrace a new set of modal interactions, including mode coalescence, and modes that veer *with* each other instead of away from one another.

9.5.3 Modal Coupling in Model Updating

The model updating scheme demonstrated in chapter 6 was a success, but there remains work to be done to rigorously prove its advantages over traditional methods. Firstly, where possible, a direct comparison of results from the new scheme should be made with results from methods involving the eigenvectors and antiresonances. This set of tests will require a purpose-built rig where the "unknown" parameters can be pre-determined prior to the model updating trials. Secondly, the new techniques purport to offer advantages in both the quality and quantity of the measurements required to ascertain the same results as the traditional techniques. Using a purpose-built rig once more, it would be instructive to determine how many sensors are required to produce the same quality of parameter estimates as with the eigenvector-based methods, and how much measurement noise is needed to corrupt the estimates for each case.

9.5.4 Model Updating for Multiply Symmetric Structures

Continuing with the model updating, it has been shown in chapter 6 that the behaviour at an intersection of a symmetric and an antisymmetric mode can be used to identify a single set of symmetric parameters. What remains to be demonstrated is how this feature can be extended to determine multiple symmetries, for example those of a bladed disk assembly. Preliminary examinations have revealed that the interactions from a similar symmetric-antisymmetric mode pair do not contribute any new information, so the choice of modal interactions is important. A structured approach to such problems needs to be formulated for future studies.

9.5.5 Adaptive Response Tuning: Frequency Estimation

The adaptive response tuning demonstration in chapter 7 produced a reduced response but this reduction could have been further improved by overcoming shortcomings in the drive frequency estimation. The peak-picking method used for the studies here was seen to produce poor results on occasion, particularly where the excitation was near resonance. Suggestions for improving the frequency estimates involve curve fitting the measured data, incorporating measurement data from multiple locations,

and filtering the estimate with band-pass and Kalman filters. A comparative investigation of these different techniques is proposed as the next step in the development of this system.

9.5.6 Adaptive Response Tuning: Response Profile

Another concern regarding the adaptive system in chapter 7 is its reliance on measured response profiles, which will produce poor results in the presence of structural variability. An improvement on the performance could be obtained once more with a Kalman filter. Using a Kalman filter, the reference response curves for the controller can be continuously updated to match the measured response throughout the operation of the system. Further experiments are needed to evaluate this configuration.

9.5.7 Stress Stiffening Influence Diagram

In section 8.2.1, a methodology was set forth for producing *stress stiffening influence diagrams*, to assist with preliminary actuator placement studies. This tool was implemented for beam elements in an ANSYS macro, and shown to be a useful visual aid. The task that remains is to implement the same functionality for plate and shell elements, so that it is available for a wide range of studies.

9.5.8 Distributed Loading for Natural Frequency Manipulation

The Lynx tail boom studies of chapter 8 showed discouraging results with regard to direct manipulation of the natural frequencies, due to the early onset of local panel buckling. If this method is to be successful it will rely on the application of distributed loading. It is suggested that the implementation of such a scheme is investigated to determine the viability of the approach.

9.5.9 Adaptive Tuned Vibration Absorber

The most promising results to emerge from the Lynx studies in chapter 8 are those of the adaptive tuned vibration absorber. The finite element studies indicate that a cable running the length of the tail can function effectively as a tuned vibration absorber, and that the tension of the cable can be used as an adaptive tuning parameter. It is suggested that experimental demonstrations are undertaken to validate these results. The next step would then be to apply the tools of chapters 4–5 to the design of the cable and attachments, to maximise the coupling between the cable and tail boom modes, and to reduce the loading required to achieve response cancellation at all the natural frequencies.

Appendices

Appendix A

Continuous Analytical Beam Model

The analysis that follows is based upon derivations which can be found in many texts. For example, Euler buckling loads and static stability are discussed by Morley [276] and White *et al.* [277], and the dynamics of loaded and unloaded beams are explored by Warburton [278].

Consider the beam shown in figure A.1(a). It is constrained at either end by pin joints and subject to a compressive axial load, P. The displacement along its length is represented by the function $v(x,t)$. The free body diagram for a small section of the beam, length δx, can be seen in figure A.1(b). The inertial force term is included as $\rho A \delta x \frac{\partial^2 v}{\partial t^2}$, where ρ is the material density, A the beam cross-sectional area, and t is time. Resolving moments about the centre of the section gives

$$S + \frac{1}{2}\frac{\partial S}{\partial x}\delta x = \frac{\partial M}{\partial x} + P\frac{\partial v}{\partial x}$$

where S and M are the internal shear force and moment, respectively. In the limit, as $\delta x \to 0$, this becomes

$$S = \frac{\partial M}{\partial x} + P\frac{\partial v}{\partial x} \tag{A.1}$$

Next, resolving vertically produces

$$\frac{\partial S}{\partial x} + \rho A \frac{\partial^2 v}{\partial t^2} = 0 \tag{A.2}$$

Combining eqns. (A.1) and (A.2) gives

$$\frac{\partial^2 M}{\partial x^2} + P\frac{\partial^2 v}{\partial x^2} + \rho A \frac{\partial^2 v}{\partial t^2} = 0$$

and from Euler-Bernoulli beam bending theory, the moment is defined in terms of the Young's modulus, E, the second moment of area, I, and the curvature by

$$M = EI\frac{\partial^2 v}{\partial x^2}$$

so

$$EI\frac{\partial^4 v}{\partial x^4} + P\frac{\partial^2 v}{\partial x^2} + \rho A \frac{\partial^2 v}{\partial t^2} = 0 \tag{A.3}$$

This is the general equilibrium equation for a Euler-Bernoulli beam. Note that at this stage the end constraints have not been considered so eqn. (A.3) is valid for any boundary conditions.

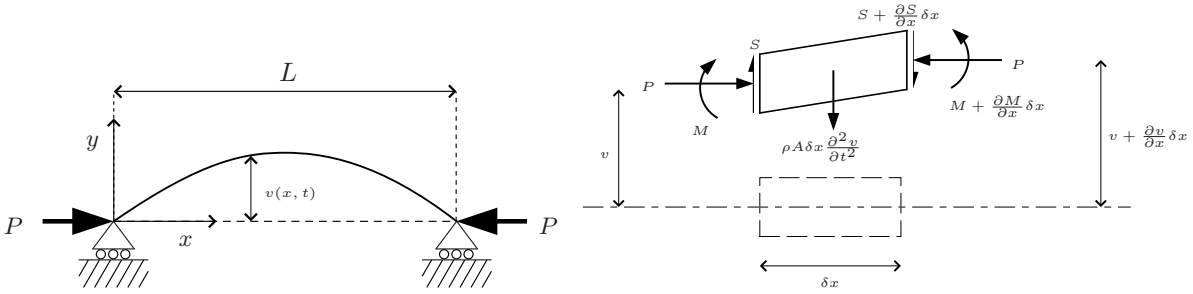

(a) Pinned beam configuration.

(b) Free body diagram, including inertial force.

Figure A.1: Slender beam with pin jointed end constraints, subject to an axial compressive load

A.1 Euler Buckling

Straightforward derivations for the Euler buckling loads of beams with various end constraints are provided by White[277]. The approach taken here is slightly more involved but provides a general solution for any boundary conditions. It also demonstrates more clearly the relationship between the Euler buckling load and the dynamic behaviour of a beam under axial compression.

To obtain the Euler buckling load, the static stability of the beam is considered. There exists a critical axial load P_{crit} for which the beam, when displaced, will not move. At a lesser load the material stiffness will overcome the load and return the beam to its straight, undeformed state. At a greater load the stiffness will be insufficient to support the beam and it will buckle. P_{crit} is therefore a neutral stability point for the structure. It represents the point at which the stiffness of the beam is effectively zero.

The system being considered is time-invariant so all time derivatives are zero. Eqn. (A.3) then becomes

$$EI\frac{\partial^4 v}{\partial x^4} + P\frac{\partial^2 v}{\partial x^2} = 0$$

Integrating twice with respect to x yields

$$EI\frac{\partial^2 v}{\partial x^2} + Pv = Cx + D \tag{A.4}$$

where C and D are constants determined by the boundary conditions. Considering the homogeneous form,

$$EI\frac{\partial^2 v}{\partial x^2} + Pv = 0$$

the complementary function, v_{cf}, is found by substituting $v = Be^{rx} + (Be^{rx})^*$ (where $B \in \mathbb{C}$) to

produce the auxiliary equation

$$EIr^2 + P = 0$$

The roots of this equation are

$$r = \pm\sqrt{-\frac{P}{EI}}$$

so that

$$v_{cf} = Be^{i\lambda x} + B^* e^{-i\lambda x} \tag{A.5}$$

$$= B_1 sin(\lambda x) + B_2 cos(\lambda x) \tag{A.6}$$

where

$$\lambda = \sqrt{\frac{P}{EI}}$$

A particular integral is assumed,

$$v_p = B_3 x + B_4$$

making the general solution to eqn. (A.4)

$$v = B_1 sin(\lambda x) + B_2 cos(\lambda x) + B_3 x + B_4 \tag{A.7}$$

Eqn. (A.7) remains valid for any end constraints. Now using pinned boundary conditions of $v = d^2v/dx^2 = 0$ at $x = 0$ and $x = L$ it is found that $B_2 = B_3 = B_4 = 0$ and

$$B_1 sin(\lambda L) = 0$$

This condition has two solutions: The trivial solution is $B_1 = 0$ where there is no deflection. The second solution is

$$\lambda L = \sqrt{\frac{P}{EI}}\, L = n\pi \quad , \quad n = 1, 2, 3, ...$$

Rearranged, this is seen to be the familiar Euler Buckling result for a pinned beam:

$$P = \frac{n^2\pi^2 EI}{L^2} \quad , \quad n = 1, 2, 3, ... \tag{A.8}$$

Eqn. (A.8) describes all the possible loads for neutral stability of the beam, each with a corresponding mode shape. The critical buckling load, P_{crit}, is given by the lowest of these loads, where $n = 1$.

A.2 Natural Frequencies of an Unloaded Beam

Consider once again the pin-jointed beam shown in figure A.1, this time without the load P but undergoing small unforced lateral oscillations (in the y-direction). If $P = 0$ then the second term of

eqn. (A.3) is omitted, giving

$$EI\frac{d^4v}{dx^4} + \rho A\frac{d^2v}{dt^2} = 0$$

From here the derivation follows the same method used in above, similar to that used by Warburton[278]. The displacement $v(x,t)$ is split into two components, the mode shape $V(x)$ and a time-dependent oscillation, to give $v = Vsin(\omega t + \alpha)$. As before, a mode shape of $V = Be^{rx} + B^*e^{r^*x}$ is assumed. This produces the auxiliary equation

$$EIr^4 - \rho A\omega^2 = 0$$

with roots

$$r = \pm\sqrt{\pm\omega\left[\frac{\rho A}{EI}\right]^{\frac{1}{2}}}$$

The generalised mode shape of the beam for any end conditions is therefore described by

$$\begin{aligned} v &= B_a e^{i\lambda x} + B_a^* e^{-i\lambda x} + B_b e^{\lambda x} + B_c e^{-\lambda x} \\ &= B_1 sin(\lambda x) + B_2 cos(\lambda x) + B_3 sinh(\lambda x) + B_4 cosh(\lambda x) \end{aligned} \tag{A.9}$$

where

$$B_a \in \mathbb{C}$$

$$B_b, B_c \in \mathbb{R}$$

$$\lambda = \left[\frac{\rho A\omega^2}{EI}\right]^{\frac{1}{4}} \tag{A.10}$$

Again using pinned boundary conditions of $v = d^2v/dx^2 = 0$ at $x = 0$ and $x = L$, it is found that $B_2 = B_4 = 0$ so

$$B_1 sin(\lambda L) + B_3 sinh(\lambda L) = 0$$

and

$$-k^2 B_1 sin(\lambda L) + k^2 B_3 sinh(\lambda L) = 0$$

The only nontrivial solution is if B_3=0 and

$$\lambda L = \left[\frac{\rho A\omega^2}{EI}\right]^{\frac{1}{4}} L = n\pi \quad , \quad n = 1, 2, 3, ...$$

This can be arranged to give the *nth* natural frequency,

$$\omega_n = \left(\frac{n\pi}{L}\right)^2 \sqrt{\frac{EI}{\rho A}} \quad , \quad n = 1, 2, 3, ... \tag{A.11}$$

A.3 Natural Frequencies of a Beam Under Axial Loading

The beam from figure A.1 is examined once more, this time under axial load *and* undergoing small unforced lateral oscillations. For this system, all the terms of eqn. (A.3) are included. As before,

$V = Be^{rx} + B^*e^{r^*x}$ is used with $v = Vsin(\omega t + \alpha)$ in eqn. (A.3) to produce the auxilliary equation

$$EIr^4 + Pr^2 - \rho A\omega^2 = 0$$

Solving, the roots are given by

$$r = \pm \left[-\frac{P}{2EI} \pm \sqrt{\left(\frac{P}{2EI}\right)^2 + \frac{\rho A\omega^2}{EI}} \right]^{\frac{1}{2}}$$

so

$$V = B_1 sin(\lambda_1 x) + B_2 cos(\lambda_1 x) + B_3 sinh(\lambda_2 x) + B_4 cosh(\lambda_2 x) \tag{A.12}$$

where

$$\lambda_1 = \left[\sqrt{\left(\frac{P}{2EI}\right)^2 + \frac{\rho A\omega^2}{EI}} + \frac{P}{2EI} \right]^{\frac{1}{2}} \tag{A.13}$$

and

$$\lambda_2 = \left[\sqrt{\left(\frac{P}{2EI}\right)^2 + \frac{\rho A\omega^2}{EI}} - \frac{P}{2EI} \right]^{\frac{1}{2}} \tag{A.14}$$

This is the most general result for a beam with any end conditions. If no axial force is present, $P = 0$ and $\lambda_1 = \lambda_2 = \lambda$, making eqns. (A.12–A.14) the same as eqns. (A.9–A.10).

Continuing with eqn. (A.12), applying pinned end constraints $v = d^2v/dx^2 = 0$ at $x = 0$ and $x = L$ yields $B_2 = B_3 = 0$,

$$B_1 sin(\lambda_1 L) + B_3 sinh(\lambda_2 L) = 0$$

and

$$-\lambda_1^2 B_1 sin(\lambda_1 L) + \lambda_2^2 B_3 sinh(\lambda_2 L) = 0$$

The only nontrivial solution is $B_3 = 0$ and

$$\lambda_1 L = \left[\sqrt{\left(\frac{P}{2EI}\right)^2 + \frac{\rho A\omega^2}{EI}} + \frac{P}{2EI} \right]^{\frac{1}{2}} L = n\pi \quad , \quad n = 1, 2, 3, ...$$

Rearranged, this produces the same result as Warburton[278] for the nth natural frequency of a pinned beam:

$$\omega_n = \left(\frac{n\pi}{L}\right)^2 \sqrt{\frac{EI}{\rho A}\left(1 - \frac{PL^2}{n^2\pi^2 EI}\right)} \quad , \quad n = 1, 2, 3, ... \tag{A.15}$$

Substituting in P_{crit} from eqn. (A.8) for the first mode,

$$\omega_1^2 = \frac{EI}{\rho A}\left(\frac{\pi}{L}\right)^4 \left(1 - \frac{P}{P_{crit}}\right) \tag{A.16}$$

It is seen that, for the pinned-pinned case, the square of the natural frequency has a linear relationship with the ratio $\frac{P}{P_{crit}}$. Using an analogy with the one degree of freedom system in figure 2.1 with natural

frequency given by $\omega_0 = \sqrt{\frac{k}{m}}$, the effective mass of the beam is given by $m = \rho AL$ and the effective stiffness is then

$$k = \frac{\pi^4 EI}{L^3}\left(1 - \frac{P}{P_{crit}}\right)$$

As P approaches P_{crit}, the effective stiffness of the beam drops to zero, and so does the natural frequency.

A.4 End Constraints

It has been shown how the buckling load of a beam is derived from the same equations as the natural frequency and how, for a pinned beam, the two properties are related. The pinned-pinned end conditions form a special case, where the mode shape for both static and dynamic deflections is an identical sine function. For different end conditions, the solutions are not so simple and the static mode shape differs from the dynamic mode shape. For these conditions, the convenient linear relationship in eqn. (A.16) does not apply.

Roark[279] warns that even slight changes in end constraints have a marked effect on the critical buckling loads and, by implication, on the magnitude of the stress stiffening effect. It is noted that this is less important in the case of columns and beams than in the case of thin plates but, despite this, the estimation of constraints remains a significant parameter for theoretical analysis. Blevins [280] offers a thorough treatment of the dynamic solutions for a range of end constraints.

Appendix B

The Wheatstone Bridge

Strain gauges respond to extension with a change in electrical resistance. The changes in resistance are small so appropriate conditioning equipment must be used; the usual choice is a Wheatstone Bridge [281] (which should perhaps be attributed instead to Christie [282]). The bridge is illustrated in figure B.1(a). It consists of four resistors, one of which is the strain gauge. The others are called *dummy* resistors. Together these form a balance such that the voltage measured is zero when all resistances are equal.

Variations in the gauge resistance cause small deviations from zero which can be measured accurately with a sensitive voltmeter. If all the resistors have equal nominal values and the change in gauge resistance is assumed to be negligible compared to the total resistance, the strain is ascertained using the equation

$$\epsilon = \frac{2V_m}{GV_s} \tag{B.1}$$

where V_m is the measured bridge voltage, V_s is the supply voltage and G is the gauge factor which relates the resistance changes to strain.

Because the measurements are sensitive to small changes in resistance, the temperature of the gauges and connecting wires can affect the accuracy of the readings. In particular, long wires connecting the gauge to the bridge should be avoided. Where this is not possible, an alternative arrangement is to connect two wires to one end of the gauge, one of which connects to the voltmeter and the other connects to the dummy resistor as in figure B.1(b). The resistance of the long wire going to the voltmeter is inconsequential as there is negligible current flowing, while equal changes to the resistance of the remaining two wires will now compensate for one another, lying as they do either side of the balance.

A further precaution often employed is to introduce a dummy strain gauge in place of a dummy resistor as seen in figure B.1(c). This is mounted on an unstressed surface of the same material as that of the active gauge, such that both gauges experience similar temperatures. In this manner, most of the inaccuracies introduced by temperature changes are eliminated. If the gauges are intended to

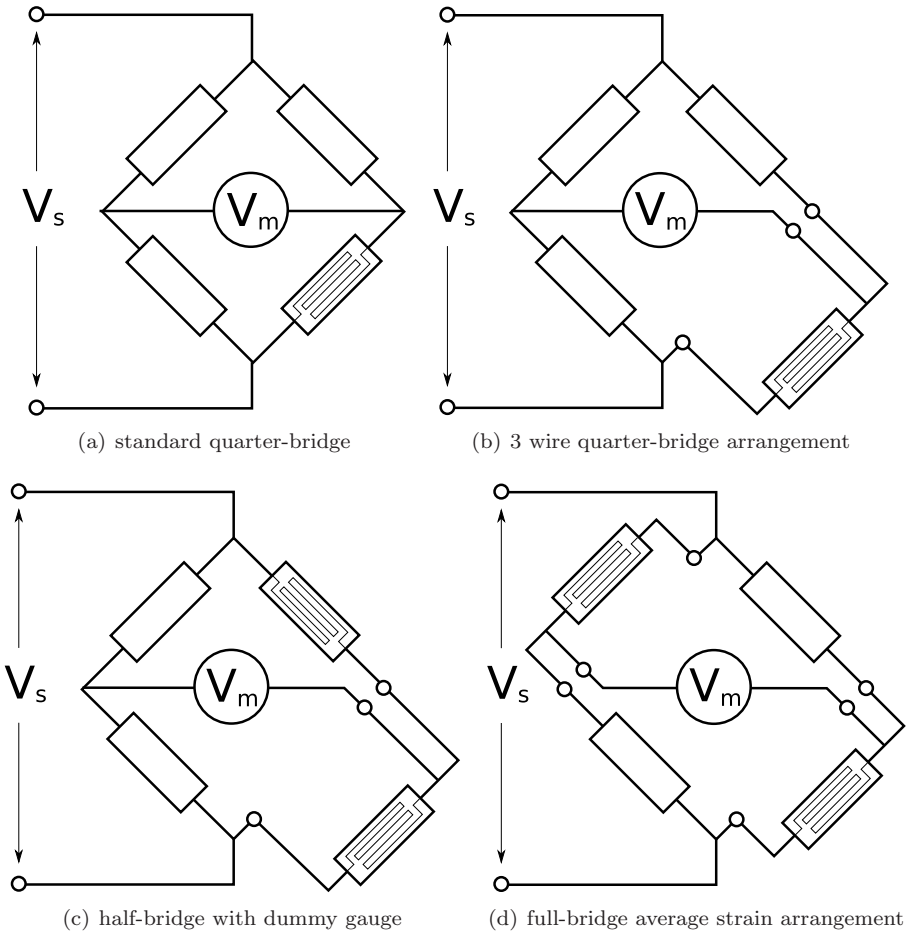

(a) standard quarter-bridge (b) 3 wire quarter-bridge arrangement

(c) half-bridge with dummy gauge (d) full-bridge average strain arrangement

Figure B.1: Wheatstone Bridge configurations. In all cases the bottom right resistor is an an active strain gauge, while the plain boxes represent ordinary dummy resistors.

measure bending, then it is common practice to use the same configuration as figure B.1(c), but now with the two gauges mounted either side of a beam or plate.

One final configuration deserves mention: in the configurations described so far, only one side of the bridge has been used; these are referred to as *half-bridge* configurations. It is sometimes desirable to use a *full-bridge* configuration, one such example being in the measurement of average axial strain. The setup pictured in figure B.1(d) will allow the measurement of the average strain, while compensating for any bending which might distort the reading from a single gauge.

Appendix C

Experimental Mass Property Determination

The mass and inertia properties of a linear ball screw actuator are required for its inclusion in an FE model. The actuator is assumed to be rigid in comparison to the rest of the structure, so that it may be represented in terms of the mass, mass moments of inertia, and the location of the centre of mass (CoM). The mass is measured with a set of weighing scales and the location of the CoM is then determined using moments of inertia. The setup is seen in figure C.1 and the location of the CoM between the two supports is given by the weight distribution:

$$\frac{d_A}{d_A + d_B} = \frac{R_B}{R_A + R_B}, \tag{C.1}$$

where the symbols are defined in figure C.2. To pinpoint the CoM this procedure is repeated for three orientations of the actuator.

The mass moments of inertia are determined using a trifilar pendulum arrangement as shown in figure C.3. The theory behind the method is described by du Bois *et al.* [154]. The pendulum is displaced and released to perform free rotational oscillations about its vertical axis, and the period of oscillation is used to compute the moment of inertia of the actuator. This method is convenient for the calculation of I_{yy} and I_{zz}, as labeled in figure C.4, but not for measurement of the inertia about the actuation axis I_{xx} as it poses difficulties in balancing the actuator on the trifilar plate. The third moment of inertia is instead determined using a compound pendulum method with the actuation arm resting on bearings and the actuator oscillating under gravity.

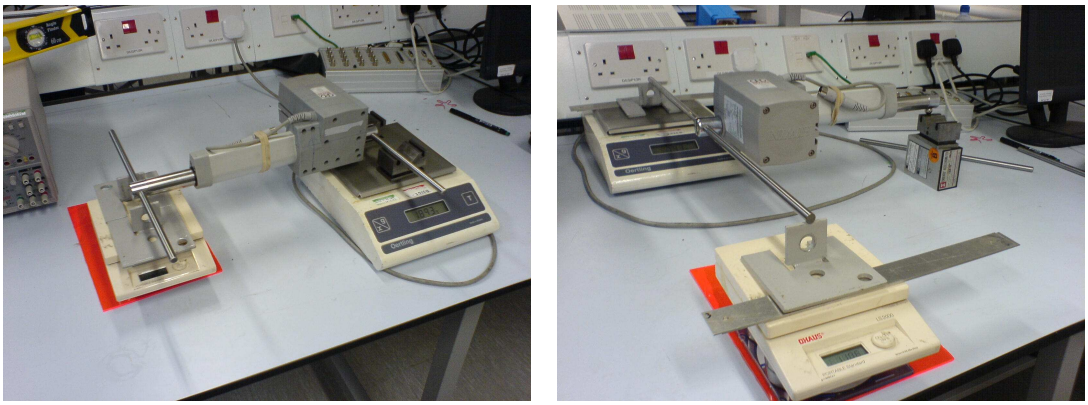

(a) (b)

Figure C.1: Two of the configurations used for determining the location of the centre of mass for the actuator.

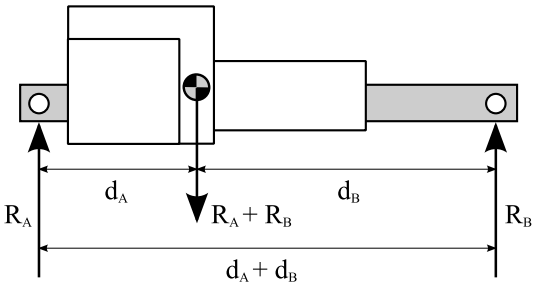

Figure C.2: Illustration of the quantities used in the centre of mass calculation for the actuator.

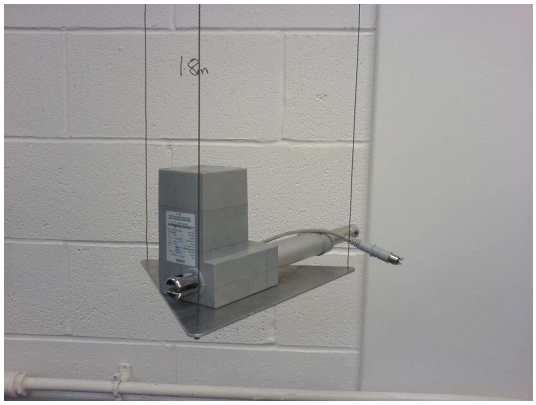

Figure C.3: The actuator sitting on the trifilar plate in the arrangement used for determining the mass moment of inertia.

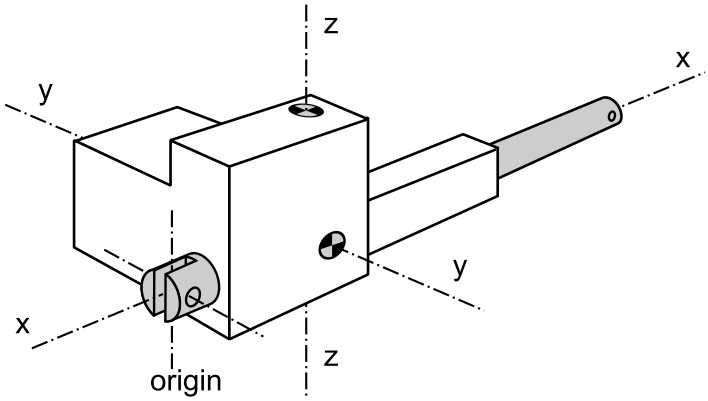

Figure C.4: The coordinate system used for the actuator when defining the inertial properties.

Bibliography

[1] K.Y. Bülah and R.H. Scanlan. Resonance, Tacoma Narrows bridge failure, and undergraduate physics textbooks. *Am, J. Phys*, 59:2, 1991.

[2] AC Lazer and PJ McKenna. Large-amplitude periodic oscillations in suspension bridges: some new connections with nonlinear analysis. *Siam Review*, 32:537, 1990.

[3] M.S.T. de Freitas, R.L. Viana, and C. Grebogi. Erosion of the safe basin for the transversal oscillations of a suspension bridge. *Chaos, Solitons and Fractals*, 18(4):829–841, 2003.

[4] RCT Rainey. Slender-body expressions for the wave load on offshore structures. *Proceedings: Mathematical and Physical Sciences*, pages 391–416, 1995.

[5] I. Langen, O. Skjåstad, and S. Haver. Measured and predicted dynamic behaviour of an offshore gravity platform. *Applied Ocean Research*, 20(1-2):15–26, 1998.

[6] C. Swan, PH Taylor, and H. Van Langen. Observations of wave-structure interaction for a multi-legged concrete platform. *Applied Ocean Research*, 19(5-6):309–327, 1997.

[7] A. Nathanson, P. Haynes, and D. Galanis. Surfing injuries. *American Journal of Emergency Medicine*, 20(3):155–160, 2002.

[8] Young-Ji Park, Alfredo H.-S. Ang, and Yi Kwei Wen. Seismic damage analysis of reinforced concrete buildings. *Journal of Structural Engineering*, 111(4):740–757, 1985.

[9] Alex H. Barbat, Fabricio Yépez Moya, and José A. Canas. Damage scenarios simulation for seismic risk assessment in urban zones. *Earthquake Spectra*, 12(3):371–394, 1996.

[10] Luis Esteva and Sonia E. Ruiz. Seismic failure rates of multistory frames. *Journal of Structural Engineering*, 115(2):268–284, 1989.

[11] Ronald R. Wakefield, Aly S. Nazmy, and David P. Billington. Analysis of seismic failure in skew rc bridge. *Journal of Structural Engineering*, 117(3):972–986, 1991.

[12] P. Dallard, AJ Fitzpatrick, A. Flint, S. Le Bourva, A. Low, RM Ridsdill Smith, and M. Willford. The London millennium footbridge. *Structural Engineer*, 79(22):17–21, 2001.

[13] A. Pavic, T. Armitage, P. Reynolds, and J. Wright. Methodology for modal testing of the Millennium Bridge, London. *Structures & Buildings*, 152(2):111–121, 2002.

[14] D.P. Taylor. Damper Retrofit of the London Millenium Footbridge – A Case Study in Biodynamic Design. In *Proceedings of the 73rd Shock and Vibration Symposium*, 2002.

[15] J. Sim, A. Blakeborough, and MS Williams. Statistical analysis of structural vibrations due to crowd jumping loads. *Structures & Buildings*, 161(2):65–75, 2008.

[16] J. Sim, A. Blakeborough, M. S. Williams, and G. Parkhouse. Statistical model of crowd jumping loads. *Journal of Structural Engineering*, 134(12):1852–1861, 2008.

[17] R. E. Harrison, S. Yao, J. R. Wright, A. Pavic, and P. Reynolds. Human jumping and bobbing forces on flexible structures: Effect of structural properties. *Journal of Engineering Mechanics*, 134(8):663–675, 2008.

[18] Christopher A. Jones and Paul Reynolds. Finite element modelling and updating of a stadium structure using in-service data. In *Proceedings of the 27th International Modal Analysis Conference*, 2009.

[19] D.R. Gaukroger, C.W. Skingle, and K.H. Heron. An application of system identification to flutter testing. *Journal of Sound and Vibration*, 72(2):141 – 150, 1980.

[20] E. Nissim and G.B. Gilyard. Method for experimental determination of flutter speed by parameter identification. Technical Report 2923, United States National Aeronautics and Space Administration. Scientific and Technical Information Division, 1989.

[21] Barry S. Thornton. A bifurcation method to calculate flutter characteristics of a helicopter blade having complex damping. *Journal of the Franklin Institute*, 300(5-6):365 – 375, 1975.

[22] C. Tung, SL Pucci, FX Caradonna, and HA Morse. The structure of trailing vortices generated by model rotor blades. Technical Report TM81316, United States National Aeronautics and Space Administration, 1981.

[23] Yung H. Yu. Rotor blade-vortex interaction noise. *Progress in Aerospace Sciences*, 36(2):97 – 115, 2000.

[24] F.H. Schmitz and Y.H. Yu. Helicopter impulsive noise: Theoretical and experimental status. *Journal of Sound and Vibration*, 109(3):361 – 422, 1986.

[25] A.C. Veca. Vibration Effects on Helicopter Reliability and Maintainability. 1973.

[26] PM Bongers, CTJ Hulshof, L. Dijkstra, HC Boshuizen, HJM Groenhout, and E. Valken. Back pain and exposure to whole body vibration in helicopter pilots. *Ergonomics*, 33(8):1007–1026, 1990.

[27] D.K. Delaney, T.G. Grubb, P. Beier, L.L. Pater, and M.H. Reiser. Effects of helicopter noise on Mexican spotted owls. *The Journal of Wildlife Management*, pages 60–76, 1999.

[28] G. Popov and S. Sankar. Modelling and analysis of non-linear orifice type damping in vibration isolators. *Journal of Sound and Vibration*, 183(5):751 – 764, 1995.

[29] K. L. Shen and T. T. Soong. Modeling of viscoelastic dampers for structural applications. *Journal of Engineering Mechanics*, 121(6):694–701, 1995.

[30] Jennifer Renninger. Understanding damping techniques. Technical report, EAR Speciality Composites, Aearo Company, 7911 Zionsville Road Indianapolis, IN 46268.

[31] Yunhe Yu, Nagi G. Naganathan, and Rao V. Dukkipati. A literature review of automotive vehicle engine mounting systems. *Mechanism and Machine Theory*, 36(1):123 – 142, 2001.

[32] Timothy A. Brungart and Eric T. Riggs. Rotor isolation for vibration and noise reduction. *Journal of Vibration and Acoustics*, 125(3):407–411, 2003.

[33] Ian G. Buckle and Ronald L. Mayes. Seismic isolation: History, application, and performance—a world view. *Earthquake Spectra*, 6(2):161–201, 1990.

[34] H. FRAHM. DEVICE FOR DAMPING VIBRATIONS OF BODIES, 1911. US Patent 989,958.

[35] J. Ormondroyd and JP Den Hartog. The theory of the dynamic vibration absorber. *Trans. ASME*, 49:9–22, 1928.

[36] M.B. Ozer and T.J. Royston. Extending den hartogs vibration absorber technique to multi-degree-of-freedom systems. *Journal of Vibration and Acoustics*, 127:341, 2005.

[37] F. Sadek, B. Mohraz, A.W. Taylor, and R.M. Chung. A method of estimating the parameters of tuned mass dampers for seismic applications. *Earthquake Engineering & Structural Dynamics*, 26(6), 1997.

[38] T. Balendra, C. M. Wang, and H. F. Cheong. Effectiveness of tuned liquid column dampers for vibration control of towers. *Engineering Structures*, 17(9):668 – 675, 1995. Auxiliary damping systems for mitigation of wind-induced vibration.

[39] Kosuke Nagaya, Toshiyuki Fukushima, and Yasuhiro Kosugi. Counteracting moment device for reduction of earthquake-induced excursions of multi-level buildings. *The Journal of the Acoustical Society of America*, 105(5):2695–2703, 1999.

[40] D. Wagg, I. Bond, P. Weaver, and M. Friswell. *Adaptive structures: engineering applications*. Wiley, 2007.

[41] JC Chang and T.T. Soong. Structural control using active tuned mass dampers. *Journal of the Engineering Mechanics Division*, 106(6):1091–1098, 1980.

[42] C. C. Chang and Henry T. Y. Yang. Control of buildings using active tuned mass dampers. *Journal of Engineering Mechanics*, 121(3):355–366, 1995.

[43] R. A. Burdisso and J. D. Heilmann. A new dual-reaction mass dynamic vibration absorber actuator for active vibration control. *Journal of Sound and Vibration*, 214(5):817 – 831, 1998.

[44] N. Olgac and B. T. Holm-Hansen. A novel active vibration absorption technique: Delayed resonator. *Journal of Sound and Vibration*, 176(1):93 – 104, 1994.

[45] Nejat Olgac and Brian Holm-Hansen. Tunable active vibration absorber: The delayed resonator. *Journal of Dynamic Systems, Measurement, and Control*, 117(4):513–519, 1995.

[46] G.J. Lee-Glauser, G. Ahmadi, and L.G. Horta. Integrated Passive/ Active Vibration Absorber for Multistory Buildings. *Journal of Structural Engineering*, 123:499, 1997.

[47] Yohji OKADA and Ryuichi OKASHITA. Adaptive control of an active mass damper to reduce structural vibration. *JSME international journal. Series C, Mechanical systems, machine elements and manufacturing*, 33(3):435–440, 1990.

[48] Ming Gu and Fujun Peng. An experimental study of active control of wind-induced vibration of super-tall buildings. *Journal of Wind Engineering and Industrial Aerodynamics*, 90(12-15):1919 – 1931, 2002.

[49] John E. Mottershead and Yitshak M. Ram. Inverse eigenvalue problems in vibration absorption: Passive modification and active control. *Mechanical Systems and Signal Processing*, 20(1):5 – 44, 2006.

[50] G. S. Miminis and C. C. Paige. An algorithm for pole assignment of time invariant multi-input linear systems. volume 21, pages 62–67, Dec. 1982.

[51] R.V. Patel and P. Misra. Numerical algorithms for eigenvalue assignment by state feedback. *Proceedings of the IEEE*, 72(12):1755–1764, Dec. 1984.

[52] DJ Inman and A. Kress. Eigenstructure assignment using inverse eigenvalue methods. *Journal of Guidance, Control, and Dynamics*, 18(3):625–627, 1995.

[53] J. Tang and K. W. Wang. Vibration confinement via optimal eigenvector assignment and piezoelectric networks. *Journal of Vibration and Acoustics*, 126(1):27–36, 2004.

[54] F. Kerber, S. Hurlebaus, B.M. Beadle, and U. Stöbener. Control concepts for an active vibration isolation system. *Mechanical Systems and Signal Processing*, 21(8):3042 – 3059, 2007.

[55] C. Bohn, A. Cortabarria, V. H?rtel, and K. Kowalczyk. Active control of engine-induced vibrations in automotive vehicles using disturbance observer gain scheduling. *Control Engineering Practice*, 12(8):1029 – 1039, 2004. Special Section on Emerging Technologies for Active Noise and Vibration Control Systems.

[56] S. Daley, F. A. Johnson, J. B. Pearson, and R. Dixon. Active vibration control for marine applications. *Control Engineering Practice*, 12(4):465 – 474, 2004. UKACC Conference Control 2002.

[57] D. Karnopp. Active and semi-active vibration isolation. *Journal of Mechanical Design*, 117(B):177–185, 1995.

[58] D. Karnopp. Design principles for vibration control systems using semi-active dampers. *Journal of Dynamic Systems, Measurement, and Control*, 112(3):448–455, 1990.

[59] Nader Jalili. A comparative study and analysis of semi-active vibration-control systems. *Journal of Vibration and Acoustics*, 124(4):593–605, 2002.

[60] Michael D. Symans and Michael C. Constantinou. Semi-active control systems for seismic protection of structures: a state-of-the-art review. *Engineering Structures*, 21(6):469 – 487, 1999.

[61] D. L. Margolis and D. Baker. The variable fulcrum isolator: A low power, nonlinear, vibration control component. *Journal of Dynamic Systems, Measurement, and Control*, 114(1):148–154, 1992.

[62] P.L. Walsh and J.S. Lamancusa. A variable stiffness vibration absorber for minimization of transient vibrations. *Journal of Sound and Vibration*, 158(2):195 – 211, 1992.

[63] W.V. Fannin and H.C. Buchanan Jr. Hydraulic damper for vehicles with variable orifice piston valving for varying damping force, August 1987. US Patent 4,685,545.

[64] Nader Jalili and Behrooz Fallahi. Design and dynamic analysis of an adjustable inertia absorber for semiactive structural vibration attenuation. *Journal of Engineering Mechanics*, 128(12):1342–1348, 2002.

[65] M.A. Haroun, J.A. Pires, and A.Y.J. Won. Suppression of environmentally-induced vibrations in tall buildings by hybrid liquid column dampers. *The Structural Design of Tall Buildings*, 5(1), 1996.

[66] C. W. Stammers and T. Sireteanu. Vibration control of machines by use of semi-active dry friction damping. *Journal of Sound and Vibration*, 209(4):671 – 684, 1998.

[67] Y. Liu, T. P. Waters, and M. J. Brennan. A comparison of semi-active damping control strategies for vibration isolation of harmonic disturbances. *Journal of Sound and Vibration*, 280(1-2):21 – 39, 2005.

[68] M. Ahmadian. On the isolation properties of semiactive dampers. *Journal of Vibration and Control*, 5(2):217, 1999.

[69] N. Wongprasert and M. D. Symans. Experimental evaluation of adaptive elastomeric base-isolated structures using variable-orifice fluid dampers. *Journal of Structural Engineering*, 131(6):867–877, 2005.

[70] M. A. Franchek, M. W. Ryan, and R. J. Bernhard. Adaptive passive vibration control. *Journal of Sound and Vibration*, 189(5):565 – 585, 1996.

[71] C. Buhr, M. A. Franchek, and R. J. Bernhard. Non-collocated adaptive-passive vibration control. *Journal of Sound and Vibration*, 206(3):371 – 398, 1997.

[72] J. Liu and K. Liu. A tunable electromagnetic vibration absorber: Characterization and application. *Journal of Sound and Vibration*, 295(3-5):708–724, 2006.

[73] K. Liu, L. Liao, and J. Liu. Comparison of two auto-tuning methods for a variable stiffness vibration absorber. *Transactions of the Canadian Society for Mechanical Engineering*, 29(1):81–96, 2005.

[74] P. Bonello, M.J. Brennan, and S.J. Elliott. Vibration control using an adaptive tuned vibration absorber with a variable curvature stiffness element. *Smart Materials and Structures*, 14(5):1055, 2005.

[75] N. Varadarajan and S. Nagarajaiah. Response control of building with variable stiffness tuned mass damper using empirical mode decomposition and Hilbert transform algorithm. In *16th ASCE Engineering Mechanics Conference, Seattle, WA*, 2003.

[76] MJ Brennan and J. Dayou. Global control of vibration using a tunable vibration neutraliser. *Noise & Vibration Worldwide*, 32(5):16–23, 2001.

[77] M.R. Smith, R.J. Pascal, T. Lee, F.B. Stamps, MC van Schoor, BP Masters, C. Blaurock, EF Prechtl, JP Rodgers, and DJ Merkley. Results from the dynamically tailored airframe structures program. In *ANNUAL FORUM PROCEEDINGS-AMERICAN HELICOPTER SOCIETY*, volume 58, pages 2167–2180. AMERICAN HELICOPTER SOCIETY, INC, 2002.

[78] Farshad Khorrami, Jahangir S. Rastegar, and R. Scott Erwin. Three-degree-of-freedom adaptive-passive isolator for launch vehicle payloads. *Smart Structures and Materials 2000: Industrial and Commercial Applications of Smart Structures Technologies*, 3991(1):164–175, 2000.

[79] G. Kim and R. Singh. A study of passive and adaptive hydraulic engine mount systems with emphasis on non-linear characteristics. *Journal of Sound and Vibration*, 179(3):427 – 453, 1995.

[80] Yugang Li, Dan Aron, and Christopher D. Rahn. Adaptive vibration isolation for axially moving strings: theory and experiment. *Automatica*, 38(3):379 – 390, 2002.

[81] B. Azvine, GR Tomlinson, and RJ Wynne. Use of active constrained-layer damping for controlling resonant vibration. *Smart Materials and Structures*, 4:1–6, 1995.

[82] A. Baz and J. Ro. Optimum design and control of active constrained layer damping. *Journal of Mechanical Design*, 117(B):135–144, 1995.

[83] SC Huang, DJ Inman, and EM Austin. Some design considerations for active and passive constrained layer damping treatments. *Smart Materials and Structures*, 5(3):301–313, 1996.

[84] V. Chawla, S. Utka, and BK Wada. Vibration control by limiting the maximum axial forces in space trusses. *Smart Materials and Structures*, 3(2):107–113, 1994.

[85] Kimihiko Nakano, Yoshihiro Suda, and Shigeyuki Nakadai. Self-powered active vibration control using a single electric actuator. *Journal of Sound and Vibration*, 260(2):213 – 235, 2003.

[86] J. T. Scruggs and W. D. Iwan. Control of a civil structure using an electric machine with semiactive capability. *Journal of Structural Engineering*, 129(7):951–959, 2003.

[87] S. Yoshikawa, A. Bogue, and B. Degon. Commercial application of passive and active piezoelectric vibration control. In *Applications of Ferroelectrics, 1998. ISAF 98. Proceedings of the Eleventh IEEE International Symposium on*, pages 293–294, 1998.

[88] B. F. Spencer, Jr. and S. Nagarajaiah. State of the art of structural control. *Journal of Structural Engineering*, 129(7):845–856, 2003.

[89] C. Niezrecki, D. Brei, S. Balakrishnan, and A. Moskalik. Piezoelectric actuation: state of the art. *The shock and vibration digest*, 33(4):269–280, 2001.

[90] Z.J. Geng and L.S. Haynes. Six degree-of-freedom active vibration control using the stewart platforms. *Control Systems Technology, IEEE Transactions on*, 2(1):45–53, Mar 1994.

[91] A. Preumont. *Responsive systems for active vibration control*. Springer, 2002.

[92] S. Burke and Jr. Hubbard, J. Active vibration control of a simply supported beam using a spatially distributed actuator. *Control Systems Magazine, IEEE*, 7(4):25–30, Aug 1987.

[93] A. Baz, K. Imam, and J. McCoy. Active vibration control of flexible beams using shape memory actuators. *Journal of Sound and Vibration*, 140(3):437 – 456, 1990.

[94] Run xin Zhang, Qing-Qing Ni, Arata Masuda, Takahiko Yamamura, and Masuharu Iwamoto. Vibration characteristics of laminated composite plates with embedded shape memory alloys. *Composite Structures*, 74(4):389 – 398, 2006.

[95] J.H. Han, K.H. Rew, and I. Lee. An experimental study of active vibration control of composite structures with a piezo-ceramic actuator and a piezo-film sensor. *Smart Materials and Structures*, 6(5):549–558, 1997.

[96] Yuan H. Guan, Teik C. Lim, and W. Steve Shepard. Experimental study on active vibration control of a gearbox system. *Journal of Sound and Vibration*, 282(3-5):713 – 733, 2005.

[97] SJ Dyke, BF Spencer Jr, MK Sain, and JD Carlson. Modeling and control of magnetorheological dampers for seismic response reduction. *Smart Materials and Structures*, 5(5):565–575, 1996.

[98] Seung-Yong Ok, Dong-Seok Kim, Kwan-Soon Park, and Hyun-Moo Koh. Semi-active fuzzy control of cable-stayed bridges using magneto-rheological dampers. *Engineering Structures*, 29(5):776 – 788, 2007.

[99] Hiroshi Sodeyama, Kohei Suzuki, and Katsuaki Sunakoda. Development of large capacity semi-active seismic damper using magneto-rheological fluid. *Journal of Pressure Vessel Technology*, 126(1):105–109, 2004.

[100] Richard Christenson, Yi Zhong Lin, Andrew Emmons, and Brent Bass. Large-scale experimental verification of semiactive control through real-time hybrid simulation. *Journal of Structural Engineering*, 134(4):522–534, 2008.

[101] SEUNG-BOK CHOI and WAN-KEE KIM. Vibration control of a semi-active suspension featuring electrorheological fluid dampers. *Journal of Sound and Vibration*, 234(3):537 – 546, 2000.

[102] S. B. Choi, H. K. Lee, and E. G. Chang. Field test results of a semi-active er suspension system associated with skyhook controller. *Mechatronics*, 11(3):345 – 353, 2001.

[103] K. A. Williams, G. T. C. Chiu, and R. J. Bernhard. Dynamic modelling of a shape memory alloy adaptive tuned vibration absorber. *Journal of Sound and Vibration*, 280(1-2):211 – 234, 2005.

[104] E. Rustighi, MJ Brennan, and BR Mace. A shape memory alloy adaptive tuned vibration absorber: design and implementation. *Smart Materials and Structures*, 14(1):19–28, 2005.

[105] Alison B. Flatau, Marcelo J. Dapino, and Frederick T. Calkins. High Bandwidth Tunability in a Smart Vibration Absorber. *Journal of Intelligent Material Systems and Structures*, 11(12):923–929, 2000.

[106] Y. Ketema. A viscoelastic dynamic vibration absorber with adaptable suppression band: A feasibility study. *Journal of Sound and Vibration*, 216(1):133 – 145, 1998.

[107] C.E.P. Jackson and W.F. Grimster. Human aspects of vibration and noise in helicopters. *Journal of Sound and Vibration*, 20(3):343 – 344, IN1–IN3, 345–351, 1972.

[108] R. GANGULI. Optimum design of a helicopter rotor for low vibration using aeroelastic analysis and response surface methods. *Journal of Sound and Vibration*, 258(2):327 – 344, 2002.

[109] J.J. Xiong and X. Yu. Helicopter rotor-fuselage aeroelasticity modeling and solution using the partition-iteration method. *Journal of Sound and Vibration*, 302(4-5):821 – 840, 2007.

[110] L. Tauszig and F. Gandhi. Influence of blade-to-blade dissimilarity on alleviation of helicopter blade-vortex interactions. *Mathematical and Computer Modelling*, 33(10-11):1139 – 1154, 2001.

[111] RD Eyres, AR Champneys, and NAJ Lieven. Modelling and dynamic response of a damper with relief valve. *Nonlinear Dynamics*, 40(2):119–147, 2005.

[112] B. Panda, E. Mychalowycz, and F.J. Tarzanin. Application of passive dampers to modern helicopters. *Smart Materials and Structures*, 5(5):509–515, 1996.

[113] Donald L. Kunz. Nonlinear analysis of helicopter ground resonance. *Nonlinear Analysis: Real World Applications*, 3(3):383 – 395, 2002.

[114] William F. Paul and Kenneth C. Mard. Vibration damped helicopter rotor, 1970. US Patent 3,540,809.

[115] M. Yang, I. Chopra, and D.J. Haas. Vibration prediction for rotor system with faults using coupled rotor-fuselage model. *Journal of Aircraft*, 41(2):348–358, 2004.

[116] I.J. Kenigsberg and L.B. Eastman. Helicopter rotor and transmission mounting and vibration isolation system, September 5 1978. US Patent 4,111,386.

[117] R.L. Mouille, G.C.L. Genoux, and P.E. Hege. Antiresonant suspension device for helicopter, July 10 1984. US Patent 4,458,862.

[118] R.A. Desjardins, C.W. Ellis, and V. Sankewitsch. Vibration isolation system, May 9 1978. US Patent 4,088,042.

[119] C. R. Fuller, J. P. Maillard, M. Mercadal, and A. H. von Flotow. Control of aircraft interior noise using globally detuned vibration absorbers. *Journal of Sound and Vibration*, 203(5):745 – 761, 1997.

[120] J. T. Pearson, R. M. Goodall, and I. Lyndon. Active control of helicopter vibration. *Computing and Control Engineering Journal*, 5(6):277–284, Dec 1994.

[121] Yung H. Yu, Bernd Gmelin, Wolf Splettstoesser, Jean J. Philippe, Jean Prieur, and Thomas F. Brooks. Reduction of helicopter blade-vortex interaction noise by active rotor control technology. *Progress in Aerospace Sciences*, 33(9-10):647 – 687, 1997.

[122] C.R. Fuller and A.H. von Flotow. Active control of sound and vibration. *Control Systems Magazine, IEEE*, 15(6):9–19, Dec 1995.

[123] Sergio Bittanti and Francesco A. Cuzzola. Periodic active control of vibrations in helicopters: a gain-scheduled multi-objective approach. *Control Engineering Practice*, 10(10):1043 – 1057, 2002.

[124] S. Daley, J. Hätönen, and D.H. Owens. Active vibration isolation in a smart spring mount using a repetitive control approach. *Control Engineering Practice*, 14(9):991 – 997, 2006.

[125] K. Nguyen and I. Chopra. Application of higher harmonic control (HHC) to hingeless rotor systems. *Vertica*, 14(14):545–556, 1990.

[126] M. Lovera, P. Colanerio, and R. Celi. Periodic analysis of higher harmonic control techniques for helicopter vibration attenuation. volume 2, pages 999–1004, 4-6, 2003.

[127] D. Patt, L. Liu, J. Chandrasekar, DS Bernstein, and PP Friedmann. The HHC Algorithm for Helicopter Vibration Reduction Revis ited. In *Proceedings of the 45 th AIAA/ASME/cE/AHS/ACS Structures, Structural Dynamics and Materials Conference, Palm Springs, CA, April 2004. AIAA Paper No. 2004-1948*.

[128] T.R. Norman, P.M. Shinoda, C. Kitaplioglu, S. Jacklin, and A. Sheikman. Low-Speed Wind Tunnel Investigation of a Full-Scale UH-60 Rotor System. 58(1):1083–1102, 2002.

[129] S.A. Jacklin, A. Haber, G. de Simone, TR Norman, C. Kitaplioglu, and P. Shinoda. Full-scale wind tunnel test of an individual blade control system for a UH-60 helicopter. 58(1):1103–1114, 2002.

[130] M. Nixon, R. Kvaternik, and T. Settle. Tiltrotor Vibration Reduction Through Higher Harmonic Control. In *American Helicopter Society 53rd Annual Forum*, 1997.

[131] N.A. Koratkar and I. Chopra. Wind tunnel testing of a Mach-scaled rotor model with trailing-edge flaps. *Smart Materials and Structures*, 10(1):1–14, 2001.

[132] M.L. Wilbur, P.H. Mirick, W.T. Yeager, C.W. Langston, C.E.S. Cesnik, and S. Shin. Vibratory loads reduction testing of the NASA/Army/MIT active twist rotor. *Journal of the American Helicopter Society*, 47(2):123–133, 2002.

[133] Y. Chen, V. Wickramasinghe, and D. Zimcik. Experimental evaluation of the Smart Spring for helicopter vibration suppression through blade root impedance control. *Smart Materials and Structures*, 14(5):1066, 2005.

[134] P. Anusonti-Inthra and F. Gandhi. Optimal control of helicopter vibration through cyclic variations in blade root stiffness. *Smart Materials and Structures*, 10(1):86–95, 2001.

[135] F. Gandhi, KW Wang, and L. Xia. Magnetorheological fluid damper feedback linearization control for helicopter rotor application. *Smart Materials and Structures*, 10(1):96–103, 2001.

[136] Wang Wei and Xia Pinqi. Adaptive control of helicopter ground resonance with magnetorheological damper. *Chinese Journal of Aeronautics*, 20(6):501 – 510, 2007.

[137] B. Widrow and G. L. Plett. Nonlinear Adaptive Inverse Control. In *Proceedings of the 36th Conference on Decision & Control*, 1997.

[138] W. Hu and N.M. Wereley. Hybrid magnetorheological fluid–elastomeric lag dampers for helicopter stability augmentation. *Smart Materials and Structures*, 17(4):045021, 2008.

[139] Terry D. Scharton and David A. Bies. VIBRATION ISOLATION SYSTEM, 1971. US Patent 3,606,233.

[140] Y.T. Choi, N.M. Wereley, and Y.S. Jeon. Semi-active vibration isolation using magnetorheological isolators. *Journal of Aircraft*, 42(5):1244–1251, 2005.

[141] G.J. Hiemenz, W. Hu, and N.M. Wereley. Semi-Active Magnetorheological Helicopter Crew Seat Suspension for Vibration Isolation. *Journal OF Aircraft*, 45(3):945, 2008.

[142] T. J. Sutton, S. J. Elliott, M. J. Brennan, K. H. Heron, and D. A. C. Jessop. Active isolation of multiple structural waves on a helicopter gearbox support strut. *Journal of Sound and Vibration*, 205(1):81 – 101, 1997.

[143] AE Staple. An evaluation of active control of structural response as a means of reducing helicopter vibration. In *Proceedings of the 15th European Rotorcraft Forum*, pages 3–17, 1989.

[144] Y. Niwa and N. Katayama. Active vibration reduction system for a helicopter. In *Proceedings of the 20th European Rotorcraft Forum*, 1994.

[145] H. Kawaguchi, S. Bandoh, and Y. Niwa. The test results for avr (active vibration reduction) system. In *Presented at the American Helicopter Society 52nd Annual Forum*, 1996.

[146] T. CHIU and PP FRIEDMANN. An analytical model for ACSR approach to vibration reduction in a helicopter rotor-flexible fuselage system. *Aeronautical Journal*, 101(1009):399–408, 1997.

[147] A. Mathews, VR Sule, and C. Venkatesan. Order Reduction and Closed-Loop Vibration Control in Helicopter Fuselages. *Journal of Guidance Control and Dynamics*, 25(2):316–323, 2002.

[148] J.T. Pearson and R.M. Goodall. Adaptive schemes for the active control of helicopter structural response. *Control Systems Technology, IEEE Transactions on*, 2(2):61–72, Jun 1994.

[149] C. T. Huggin, C. Hatch, G. W. Skingle, and T. J. Griffiths. Active vibration control of the lynx helicopter airframe. In *48th AIAA/ASME/ASCE/AHS/ASC Structures, Structural Dynamics, and Materials Conference*, 2007.

[150] *MATLAB version 6.5.1 R13 SP1.* 3 Apple Hill Drive, Natick, MA 01760-2098.

[151] *LMS Test Lab Spectral Aquisition User Manual, Rev 5A.* Interleuvenlaan 68, B-3001 Leuven, Belgium, 2004.

[152] *Release 10.0 Documentation for ANSYS.* Southpointe, 275 Technology Drive, Canonsburg, PA 15317, USA.

[153] John E. Mottershead, Maryam Ghandchi Tehrani, Danut Stancioiu, Simon James, and Hossein Shahverdi. Structural modification of a helicopter tailcone. *Journal of Sound and Vibration*, 298(1-2):366 – 384, 2006.

[154] J. L. du Bois, S. Adhikari, and N. A. J. Lieven. Error analysis in trifilar inertia measurements. *Experimental Mechanics*, 2008. published online, doi:10.1007/s11340-008-9142-4.

[155] J. L. du Bois, S. Adhikari, and N. A. J. Lieven. Eigenvalue curve veering in stressed structures: An experimental study. *Journal of Sound and Vibration*, 2009. published online, doi:10.1016/j.jsv.2008.12.014.

[156] J. L. du Bois, S. Adhikari, and N. A. J. Lieven. Experimental and numerical investigation of mode veering in a stressed structure. In *Proceedings of the 25th International Modal Analysis Conference*, volume XXV, page 233, 2007.

[157] Jonathan Luke du Bois, Nick A. J. Lieven, and Sondipon Adhikari. Localisation and curve veering: A different perspective on modal interactions. In *Proceedings of the 27th International Modal Analysis Conference*, 2009.

[158] Jonathan Luke du Bois, Nick A. J. Lieven, and Sondipon Adhikari. On the role of modal coupling in model updating. In *Proceedings of the 27th International Modal Analysis Conference*, 2009.

[159] Jonathan Luke du Bois, Nick A. J. Lieven, and Sondipon Adhikari. A new approach to model updating in symmetric structures. In *Proceedings of the 50th AIAA/ASME/ASCE/AHS/ASC Structures, Structural Dynamics, and Materials Conference*, 2009.

[160] Jonathan Luke du Bois, Nick A. J. Lieven, and Sondipon Adhikari. Adaptive passive control of dynamic response through structural loading. In *Proceedings of the 48th AIAA/ASME/ASCE/AHS/ASC Structures, Structural Dynamics, and Materials Conference*, 2009.

[161] L. Meirovitch. *Fundamentals of Vibrations*. McGraw-Hill, 2001.

[162] D. J. Ewins. *Modal Testing: Theory, Practice and Application*. Research Studies Press Ltd., second edition, 2000.

[163] R. D. Cook. *Concepts and Applications of Finite Element Analysis*. John Wiley & Sons, Inc., 1974.

[164] J. S. Przemieniecki. *Theory of Matrix Structural Analysis*. McGraw-Hill, 1968.

[165] G.H. Golub and C.F. Van Loan. *Matrix computations*. 1996.

[166] D.L. Brown and R.J. Allemang. The Modern Era of Experimental Modal Analysis. *SOUND AND VIBRATION*, 41(1):16, 2007.

[167] W. Thomson and P. G. Tait. *Treatise on Natural Philosophy*. Cambridge University Press, 1879.

[168] John William Strutt Rayleigh. *The Theory of Sound*, volume 1. MacMillan and Co., second edition, 1894.

[169] Nuno Manual Mendes Maia, Júlio Martins Montalvão e Silva, Jimin He, Nicholas Andrew John Lieven, Rong Ming Lin, Graham William Skingle, Wai-Ming To, and António Paulo Vale Urgueira. *Theoretical and Experimental Modal Analysis*. Research Studies Press, 1997.

[170] CE Gough. The theory of string resonances on musical instruments. *Acustica*, 49(2):124–141, 1981.

[171] B. C. Stephens. Natural vibration frequencies of structural members as an indication of end fixity and magnitude of stress. *Journal of the Aeronautical Sciences*, 4:54–56, 1936.

[172] H. Lurie. Effective end restraint of columns by frequency measurements. *Journal of the Acoustical Society of America*, 19:2122, 1951.

[173] P. D. Greening and N. A. J. Lieven. Identification and updating of loading in frameworks using dynamic measurements. *Journal of Sound and Vibration*, 260(1):101 – 115, 2003.

[174] Nerio Tullini and Ferdinando Laudiero. Dynamic identification of beam axial loads using one flexural mode shape. *Journal of Sound and Vibration*, 318(1-2):131 – 147, 2008.

[175] P.D. Greening. *Dynamic finite element modelling and updating of loaded structures*. PhD thesis, University of Bristol, 1999.

[176] J. Ryu, S.S. Kim, and S.S. Kim. A criterion on inclusion of stress stiffening effects in flexible multibody dynamic system simulation. *Computers and Structures*, 62(6):1035–1048, 1997.

[177] Juana M. Mayo, Daniel García-Vallejo, and Jaime Domínguez. Study of the geometric stiffening effect: Comparison of different formulations. *Multibody System Dynamics*, 11:321–341, 2004.

[178] A. Jennings. Frame analysis including change of geometry. *Proceedings of the ASCE, Journal of the Structural Division*, 94:627–644, 1968.

[179] DW Murray and E.L. Wilson. Finite element large deflection analysis of plates. *J. Eng. Mech. Div. ASCE*, 95:143–165, 1969.

[180] A. D. Crocombe. How to tackle nonlinear finite element analysis. NAFEMS, Glasgow, 2001.

[181] MJ Turner, RW Clough, HC Martin, and LJ Topp. Stiffness and deflection analysis of complex structures. *J. Aero. Sci*, 23(9):805–823, 1956.

[182] O. C. Zienkiewicz. *The Finite Element Method*. McGraw-Hill Book Company, London, third edition, 1977.

[183] D. Di Maio and D.J. Ewins. Measurement and comparison of operational deflection shapes (odss) using a scanning ldv system in step or continuous scanning mode. *Proceedings of the 27th International Modal Analysis Conference*, 2009.

[184] B. P. Lathi. *Signal Processing and Linear Systems*. Berkeley-Cambridge Press, CA, USA, 1998.

[185] J.W. Cooley, P.A.W. Lewis, and P.D. Welch. Historical notes on the fast fourier transform. *Proceedings of the IEEE*, 55(10):1675–1677, October 1967.

[186] G. C. Danielson and C. Lanczos. Some improvements in practical fourier analysis and their application to x-ray scattering from liquids. *Journal of the Franklin Institute*, 233(4):365–380, April 1942.

[187] James W. Cooley and John W. Tukey. An algorithm for the machine calculation of complex fourier series. *Mathematics of Computation*, 19(90):297–301, 1965.

[188] D.J. Inman. *Engineering Vibration*. Prentice Hall, NJ, second edition, 2001.

[189] RJ Allemang and DL Brown. A UNIFIED MATRIX POLYNOMIAL APPROACH TO MODAL IDENTIFICATION. *Journal of Sound and Vibration*, 211(3):301–322, 1998.

[190] M.H. Richardson and D.L. Formenti. Parameter estimation from frequency response measurements using rational fraction polynomials. In *Proceedings of the 1st International Modal Analysis Conference*, pages 167–181, 1982.

[191] DJ Ewins and PT Gleeson. A method for modal identification of lightly damped structures. *Journal of Sound and Vibration*, 84(1), 1982.

[192] LW Schmerr. A New Complex Exponential Frequency Domain Technique for Analyzing Dynamic Response Data. In *Proceedings of the 1st International Modal Analysis Conference (IMAC I), Orlando, FL*, 1982.

[193] B. Peeters, G. Lowet, H. Van der Auweraer, and J. Leuridan. A New Procedure for Modal Parameter Estimation. *SOUND AND VIBRATION*, 38(1):24–29, 2004.

[194] M.H. Richardson and D.L. Formenti. Global curve fitting of frequency response measurements using the rational fraction polynomial method. In *3rd International Modal Analysis Conference,(Orlando, Fl)*, pages 390–397.

[195] M.H. Richardson. Global Frequency & Damping Estimates from Frequency Response Measurements. In *4th International Modal Analysis Conference (IMAC IV),(Los Angeles, California)*, 1986.

[196] SR Ibrahim and EC Mikulcik. A Method for the Direct Identification of Vibration Parameters from the Free Response. *Shock and Vibration Bulletin*, 47(4):183–198, 1977.

[197] J.N. Juang and R.S. Pappa. Eigensystem realization algorithm for modal parameter identification and model reduction. *Journal of Guidance, Control, and Dynamics*, 8(5):620–627, 1985.

[198] DL Brown, RJ Allemang, R. Zimmerman, and M. Mergeay. Parameter estimation techniques for modal analysis. *SAE Paper*, 790221:19–20, 1979.

[199] H. Vold, J. Kundrat, G. T. Rocklin, and R. Russel. Multi-input modal estimation algorithm for minicomputers. *SAE Transactions*, 1982.

[200] H. Vold and T. Rocklin. The Numerical Implementation of a Multi-Input Modal Estimation Algorithm for Mini-Computers. In *Proceedings, International Modal Analysis Conference, Society of Experimental Mechanics (SEM)*, pages 542–548, 1982.

[201] R. Prony. Essai expérimental et analytique sur les lois de la dilatabilité des fluides élastiques et sur celles de la force expansive de la vapeur de l'eau et de la vapeur d'alkool, à différentes températures. In *Journal de l'Ecole Polytechnique*, volume 1, pages 24–76, 1795.

[202] R.J. Guyan. Reduction of stiffness and mass matrices. *AIAA Journal*, 3(2):380, 1965.

[203] Robert L. Kidder. Reduction of structural frequency equations. *AIAA Journal*, 11(6):892, 1973.

[204] M. I. Friswell and J. E. Mottershead. *Finite Element Model Updating in Structural Dynamics*. Kluwer Academic Publishers, 1995.

[205] JE Mottershead and MI Friswell. Model updating in structural dynamics: a survey. *Journal of sound and vibration*, 167(2):347–375, 1993.

[206] R. L. Fox and M. P. Kapoor. Rates of change of eigenvalues and eigenvectors. *AIAA Journal*, 6(12):2426–2429, 1968.

[207] Richard B. Nelson. Simplified calculation of eigenvector derivatives. *AIAA Journal*, 14(9):1201–1205, 1976.

[208] A.M. KABE. Stiffness matrix adjustment using mode data. *AIAA Journal*, 23(9):1431–1436, 1985.

[209] S. SMITH and C. BEATTIE. Secant-method adjustment for structural models. *AIAA Journal*, 29(1):119–126, 1991.

[210] GML Gladwell and H. Ahmadian. Generic element matrices suitable for finite element model updating. *Mechanical Systems and Signal Processing*, 9(6):601–614, 1995.

[211] MJ Terrell, MI Friswell, and NAJ Lieven. Constrained generic substructure transformations in finite element model updating. *Journal of Sound and Vibration*, 300(1-2):265–279, 2007.

[212] Michael I. Friswell, John E. Mottershead, and Hamid Ahmadian. Finite-element model updating using experimental test data: Parametrization and regularization. *Philosophical Transactions: Mathematical, Physical and Engineering Sciences*, 359(1778):169–186, 2001.

[213] RA Ibrahim and CL Pettit. Uncertainties and dynamic problems of bolted joints and other fasteners. *Journal of Sound and Vibration*, 279(3-5):857–936, 2005.

[214] Amar Singh Bahra and Paul David Greening. Identifying axial load patterns using space frame fems and measured vibration data. *Mechanical Systems and Signal Processing*, 23(4):1282 – 1297, 2009.

[215] S.L. Folkman, E.A. Rowsell, and G.D. Ferney. Influence of pinned joints on damping and dynamic behavior of a truss. *Journal of Guidance, Control, and Dynamics*, 18(6):1398–1403, 1995.

[216] JG Bingham and SL Folkman. Measured influence of gravity on the dynamic behavior of a truss using pinned joints. In *37 th AIAA/ASME/ASCE/AHS/ASC Structures, Structural Dynamics and Materials Conference, Salt Lake City*, pages 1043–1053, 1996.

[217] ST Hsu, JH Griffin, and J. Bielak. How gravity and joint scaling affect dynamic response. *AIAA Journal*, 27(9):1280–1287, 1989.

[218] J. E. Mottershead. On the zeros of structural frequency response functions and their sensitivities. *Mechanical Systems and Signal Processing*, 12(5):591–597, 1998.

[219] W. D'ambrogio and A. Fregolent. The use of antiresonances for robust model updating. *Journal of sound and vibration*, 236(2):227–243, 2000.

[220] K. Jones and J. Turcotte. Finite element model updating using antiresonant frequencies. *Journal of Sound and Vibration*, 252(4):717–727, 2002.

[221] R. W. Claassen and C. J. Thorne. Vibrations of a rectangular cantilever plate. *Journal of the Aerospace Sciences*, 29(11):1300–1305, 1962.

[222] Arthur W. Leissa. On a curve veering aberration. *Journal of Applied Mathematics and Physics (ZAMP)*, 25:99–111, 1974.

[223] R. W. Claassen and C. J. Thorne. Vibrations of thin rectangular isotropic plates. *Journal of Applied Mechanics*, 28:304–305, 1961.

[224] R. W. Claassen and C. J. Thorne. Transverse vibrations of thin rectangular isotropic plates. Technical Report 2379, NAVWEPS Report 7016, U.S. Naval Ordnance Test Station, China Lake, California, August 1960.

[225] R. W. Claassen. Vibration of skew cantilever plate. Technical Report PMR-TR-62-1, Pacific Missile Range, May 1963.

[226] R. W. Claassen. Vibrations of skew cantilever plates. *AIAA Journal*, 1:1222, 1963.

[227] G. B. Warburton. The vibration of rectangular plates. *Proceedings of the Institute of Mechanical Engineers*, 168:371–381, 1954.

[228] N. J. Huffington, Jr. On the occurrence of nodal patterns of nonparallel form in rectangular orthotropic plates. *Journal of Applied Mechanics, Brief Notes*, 28:459–460, 1961.

[229] R. D. Mindlin and H. Deresiewicz. Thickness-shear and flexural vibrations of a circular disk. *Journal of Applied Physics*, 25:1329–1332, 1954.

[230] H. Deresiewicz and R. D. Mindlin. Axially symmetric flexural vibrations of a circular disk. *Journal of Applied Mechanics*, 22:86–88, 1955.

[231] H. Deresiewicz. Symmetric flexural vibrations of a clamped circular disk. *Journal of Applied Mechanics*, 23:319, 1956.

[232] R. D. Mindlin, A. Schacknow, and H. Deresiewicz. Flexural vibrations of rectangular plates. *Journal of Applied Mechanics*, 23:430–436, 1956.

[233] J. R. Kuttler and V. G. Sigillito. On curve veering. *Journal of Sound and Vibration*, 75(4):585–588, 1981.

[234] N. C. Perkins and C. D. Mote, Jr. Comments on curve veering in eigenvalue problems. *Journal of Sound and Vibration*, 106(3):451–463, 1986.

[235] G. S. Schajer. The vibration of a rotating circular string relative to a fixed end restraint. *Journal of Sound and Vibration*, 92(1):11–19, 1984.

[236] J. J. Webster. Free vibrations of rectangular curved panels. *International Journal of Mechanical Science*, 10:571–582, 1968.

[237] M. Petyt and C. C. Fleischer. Free vibration of a curved beam. *Journal of Sound and Vibration*, 18(1):17–30, 1971.

[238] M. S. Triantafyllou. The dynamics of taut inclined cables. *Quarterly Journal of Mechanics and applied Mathematics*, 37(3):421–440, 1984.

[239] R. H. Plaut, K. D. Murphy, and L. N. Virgin. Curve and surface veering for a braced column. *Journal of Sound and Vibration*, 187(5):879–885, 1995.

[240] J. J. Webster and G. B. Warburton. Discussion of "approximate methods for the determination of the natural frequencies of stiffened and curveed plates". *Journal of Sound and Vibration*, 18(1):139–145, 1971.

[241] P. S. Nair and S. Durvasula. On quasi-degeneracies in plate vibration problems. *International Journal of Mechanical Sciences*, 15:975–986, 1973.

[242] M. E. McIntyre and J. Woodhouse. On measuring the elastic and damping constants of orthotropic sheet materials. *Acta Metallurgica*, 36(6):1397–1416, 1988.

[243] C. H. Hodges and J. Woodhouse. Vibration isolation from irregularity in a nearly periodic structure: Theory and measurements. *Journal of the Acoustical Society of America*, 74(3):894–905, 1983.

[244] C. H. Hodges. Confinement of vibration by structural irregularity. *Journal of Sound and Vibration*, 82:411–424, 1982.

[245] C. Pierre and E. H. Dowell. Localization of vibrations by structural irregularity. *Journal of Sound and Vibration*, 114(3):549–564, 1987.

[246] C. Pierre. Mode localization and eigenvalue loci veering phenomena in disordered structures. *Journal of Sound and Vibration*, 126(3):485–502, 1988.

[247] M. S. Triantafyllou and G. S. Triantafyllou. Frequency coalescence and mode localisation phenomena: A geometric theory. *Journal of Sound and Vibration*, 150(3):485–500, 1991.

[248] H. C. Chan and J. K. Liu. Mode localization and frequency loci veering in disordered engineering structures. *Chaos, Solitions and Fractals*, 11:1493–1504, 2000.

[249] X. L. Liu. Behaviour of derivatives of eigenvalues and eigenvectors in curve veering and mode localisation and their relation to close eigenvalues. *Journal of Sound and Vibration*, 256(3):551–564, 2002.

[250] A. Muğan. Effects of mode localisation on input-output directional properties of structures. *Journal of Sound and Vibration*, 258(1):45–63, 2002.

[251] W. Lacarbonara, H. N. Arafat, and A. H. Nayfeh. Non-linear interactions in imperfect beams at veering. *International Journal of Non-Linear Mechanics*, 40:987–1003, 2005.

[252] N. Challamel, C. Lanos, and C. Casandjian. Localization in the buckling or in the vibration of a two-span weakened column. *Engineering Structures*, 28:776–782, 2006.

[253] T. Igusa. Critical configurations of systems subjected to wide-band input. *Journal of Sound and Vibration*, 168(3):525–541, 1993.

[254] D. Afolabi and O. Mehmed. On curve veering and flutter of rotating blades. *Journal of Engineering for Gas Turbines and Power*, 116:702–708, 1994.

[255] E. Balmès. High modal density, curve veering, localization: A different perspective on the structural response. *Journal of Sound and Vibration*, 161(2):358–363, 1993.

[256] Francesco Benedettini, Daniele Zulli, and Rocco Alaggio. Frequency-veering and mode hybridization in arch bridges. In *Proceedings of the 27th International Modal Analysis Conference*, 2009.

[257] S. Natsiavas. Mode localization and frequency veering in a non-conservative mechanical system with dissimilar components. *Journal of Sound and Vibration*, 165(1):137 – 147, 1993.

[258] Jim Woodhouse. On the synthesis of guitar plucks. *Acta Acustica united with Acustica*, 90:928–944, 2004.

[259] Sondipon Adhikari. Rates of change of eigenvalues and eigenvectors in damped dynamic system. *AIAA Journal*, 39(11):1452–1457, 1999.

[260] R. Courant and D. Hilbert. *Methods of Mathematical Physics*, volume 1. Interscience Publishers, 1953.

[261] L. D. Landau and E. M. Lifshitz. *Quantum Mechanics*, volume 2. Pergamon Press, 1974.

[262] Pete Avitabile. Modal space back to basics. *Experimental Techniques*, pages 11–12, Jan/Feb 2008.

[263] Yi-Jui Chiu and Shyh-Chin Huang. The influence on coupling vibration of a rotor system due to a mistuned blade length. *International Journal of Mechanical Sciences*, 49:522–532, 2007.

[264] Özgür Turhan and Gökhan Bulut. Linear coupled shaft-torsional and blade-bending vibrations in multi-stage rotor-blade systems. *Journal of Sound and Vibration*, 296:292–318, 2006.

[265] S.W. Doebling and C.R. Farrar. Estimation Of statistical distributions for modal parameters identified from averaged frequency response function data. *Journal of Vibration and Control*, 7(4):603, 2001.

[266] Amar Singh Bahra and Paul David Greening. Mode traces in degenerate eigensystems and augmented assurance. *AIAA Journal*, 43(6):1299–1305, June 2005.

[267] Amar Singh Bahra and Paul David Greening. Particularities of newton's method in space frame force determination, utilising eigenpair functions. *Journal of Sound and Vibration*, 291:462–490, 2006.

[268] K.N. Chen, D.L. Brown, and V.T. Nicolas. Perturbed boundary condition model updating. In *PROCEEDINGS OF THE INTERNATIONAL MODAL ANALYSIS CONFERENCE*, pages 661–661. SEM SOCIETY FOR EXPERIMENTAL MECHANICS INC, 1993.

[269] S. Lammens, W. Heylen, D. Brown, and P. Sas. Model updating and perturbed boundary condition testing. *status: published*.

[270] M. I. Friswell J. E. Mottershead, C. Mares and S. James. Selection and updating of parameters for an aluminium space-frame model. *Mechanical Systems and Signal Processing*, 14(6):923–944, 2000.

[271] Chui G. Chen. *Kalman Filtering with Real-Time Applications*. Springer, third edition, 1999.

[272] R.L. Eubank. *A Kalman filter primer*. CRC Press, 2006.

[273] *Nastran User Guide 2005*. 2 MacArthur Place, Santa Ana, CA 92707, USA.

[274] J. Q. Sun, M. R. Jolly, and M. A. Norris. Passive, adaptive and active tuned vibration absorbers—a survey. *Journal of Vibration and Acoustics*, 117(B):234–242, 1995.

[275] Maria Q. Feng and Akira Mita. Vibration control of tall buildings using mega subconfiguration. *Journal of Engineering Mechanics*, 121(10):1082–1088, 1995.

[276] A. Morley. *Theory of Structures*. Longmans, Green and Company, fifth edition, 1948.

[277] R. N. White, P. Gergely, and R. G. Sexsmith. *Structural Engineering, Volume 3, Behaviour of Members and Systems*. John Wiley & Sons, Inc., 1974.

[278] G. B. Warburton. *The Dynamical Behaviour of Structures*. Pergamon Press, second edition, 1976.

[279] W. C. Young and R. G. Budynas. *Roark's Formulas for Stress and Strain*. McGraw-Hill, seventh edition, 2002.

[280] R. D. Blevins. *Formulas for Natural Frequency and Mode Shape*. Robert E. Krieger Publishing Company, 1986.

[281] Starling. *Electricity and Magnetism*. Longmans, Green and Company, London, 1929.

[282] S. Ekelof. The genesis of the Wheatstone bridge. *Engineering Science and Education Journal*, 10(1):37–40, 2001.